Through the Organism's eyes

The interaction between hydrodynamics and metabolic dynamics in industrial-scale fermentation processes

Haringa, Cees

DOI
10.4233/uuid:441ec955-cd8d-4ae0-b2f0-98fbf91a570a

Publication date
2017

Document Version
Final published version

Citation (APA)
Haringa, C. (2017). *Through the Organism's eyes: The interaction between hydrodynamics and metabolic dynamics in industrial-scale fermentation processes*. [Dissertation (TU Delft), Delft University of Technology]. https://doi.org/10.4233/uuid:441ec955-cd8d-4ae0-b2f0-98fbf91a570a

Through the organism's eyes

The interaction between hydrodynamics and metabolic dynamics in industrial-scale fermentation processes

Through the organism's eyes

The interaction between hydrodynamics and metabolic dynamics in industrial-scale fermentation processes

Proefschrift

ter verkrijging van de graad van doctor
aan de Technische Universiteit Delft,
op gezag van de Rector Magnificus prof. ir. K.C.A.M. Luyben,
voorzitter van het College voor Promoties,
in het openbaar te verdedigen op maandag 11 december 2017 om 15:00 uur

door

Cornelis HARINGA

Master of Science in Chemical Engineering
geboren te Harlingen, Nederland.

Dit proefschrift is goedgekeurd door de

promotor: Prof. dr. R.F. Mudde
promotor: Prof. dr. ir. H.J. Noorman

Samenstelling promotiecommissie:

Rector Magnificus	voorzitter
Prof. dr. R.F. Mudde	Technische Universiteit Delft, promotor
Prof. dr. ir. H.J. Noorman	Technische Universiteit Delft, promotor

Onafhankelijke leden:

Prof. dr. ir. C.R. Kleijn	Technische Universiteit Delft
Prof. dr. ir. H.E.A. van den Akker	Technische Universiteit Delft
Prof. dr. ir. J.A.M. Kuipers	Technische Universiteit Eindhoven
Prof. dr. ir. F. Delvigne	Université de Liège, Gembloux Agro-Bio Tech
Prof. dr. P. Neubauer	Technische Universität Berlin

This work has been conducted within a multi-party research project, among DSM-Sinochem Pharmaceuticals, TU Delft, East China University of Science and Technology and Shanghai Guojia Ltd., funded by NWO and MoST (2013DFG32630).

Printed by: Ridderprint BV | www.ridderprint.nl

ISBN 978-94-6299-793-6

An electronic version of this dissertation is available at
`http://repository.tudelft.nl/`.

Summary

A call for bio-based fuels, materials and the growing antibiotics and food additive market yield an increasing demand for bulk-scale bioprocesses, paired with a demand for larger and more efficient bioreactors. Upscaling bioreactors might induce transport issues, such as an increased mixing time, possibly giving rise to gradients in process conditions (substrate/oxygen concentration, temperature, shear rate, pH). These gradients mean that micro-organisms continuously observe changes in their environment, affecting their metabolism and possibly reducing their performance. This inherent scaling issue is a consequence of the complex interaction between hydrodynamics and kinetics.

The goal of the Hé-project, of which this work is part, is to gain more understanding about this interaction and its quantitative effects. Experimentally, the use of scale-down simulators (lab-scale setups that replicate the large-scale environment) is gaining popularity. Within the scope of the Hé project scale-down experiments considering the effects of substrate and oxygen availability and shear stress on *P. chrysogenum* are conducted at East China University of Science and Technology (ECUST). The results of these and earlier studies are used for the development of a metabolic model for this organism by researchers at ECUST, that currently captures the effect of substrate variations on the penicillin production.

Current scale-down simulators typically impose fluctuations based on the global large-scale mixing time or without industrial reference. While such setups increase our understanding, they may not adequately reflect the environment in large-scale reactors. This thesis focuses on the use of computational fluid dynamics to study mixing in industrial bioreactors, and in particular to study the variations in substrate concentration observed by micro-organisms. The simulation results are translated to input parameters for the design of representative scale-down simulators. This new generation of scale-down simulators has the potential to quantitatively evaluate the effect of heterogeneity in industrial bioreactors on a case specific basis. While the focus is on substrate concentration variations, the outlined methods are equally valid for other process parameters. Using Eulerian (field-based) methods, a penicillin and a yeast fermentation process were simulated. In both cases reasonable agreement with experimental validation data is observed, including the local substrate concentration in the yeast case. Hence, we regard the simulations as a good reflection of the studied processes, within the required assumptions.

The Reynolds-averaged turbulence models used for modeling do not adequately capture all physical phenomena currently. The mixing time in multi-impeller fermentors is structurally over-predicted by improper assessment of the influence of turbulence between impeller compartments; the MRF impeller model additionally ignores the effect of macro-instabilities that were observed in such flows. Fine-tuning of the turbulent Schmidt number, suggested in earlier studies to improve agreement in the global mixing time, limits predictive value. While large-eddy simulations perform superior with respect to mixing time, their computational demands prohibit routine application. Further attention is required for the interaction between turbulence, aeration and rheology; the latter had to be omitted in the current study.

Lagrangian (particle-based) simulations allow to track thousands of micro-organisms, and record substrate fluctuations from their point of view; referred to as lifelines. The observed variations strongly depend on the balance between the mixing and substrate consumption timescale. We analyzed lifelines using three methods: regime analysis, arc-analysis and Fourier analysis. The acquired fluctuation statistics were employed to guide the design of scale-down simulators; both the design of single-vessel, fluctuating feed and multi-vessel simulators is illustrated. Since the concentration fluctuations are influenced by substrate consumption by the organism, the biomass concentration has to be matched between the lab-scale and large scale in order to ensure an equal rate of change between the cases. This can lead to operational complications for lab-scale simulators. The distribution of fluctuation times follows an exponential decay in stirred vessels, with the mean fluctuation timescale in the order of the vessel circulation time - a factor four below the global mixing time, and significantly faster than applied in current scale-down simulators.

Coupling a metabolic model to the Lagrangian simulations allows to predict the impact of substrate variations on the metabolism. For a *P. chrysogenum* fermentation in a 54 m^3 reactor, we predict a yield loss of $18-46\%$ compared to the ideal mixing case. A simple change in the feed location predicts a reduction in loss to 9%, which illustrates the capacities of Lagrangian simulations for design purposes. Similarly, the results can be used to suggest metabolic optimizations. Numerical evaluation of a scale-down simulator design shows a good match in the metabolic response compared to the industrial scale simulation. The performance is unlikely affected by non-ideal lab-scale mixing, and a reduction in biomass concentration by a factor two compared to the industrial value does not compromise performance, despite a reduced rate-of-change. However, these observations are expected to be highly case-dependent. A fed-batch simulation (60 hours flow time) shows that the coupled metabolic-hydrodynamic approach captures industrial growth and production profiles, and furthermore reveals considerable intra-cellular heterogeneity in enzyme and metabolite levels over the population. This provides a target for experimental assessment, for example using fluorescent labeling of the relevant enzymes.

Altogether, the work presented in this thesis shows that Euler-Lagrange computational fluid dynamics can be used to assess the impact of extra-cellular heterogeneity on the metabolism of micro-organisms, from their point of view. The acquired fluctuation statistics can be used for the design of representative-scale down simulators. Combining the experimental verification of these scale-down simulators with simulations, process improvements can be suggested and evaluated, both regarding the reactor and the metabolism. With this, we are one step closer to rational, reliable scale-up of industrial bioprocesses.

Samenvatting

De vraag naar materialen uit hernieuwbare grondstoffen, alsmede de groeiende markt voor antibiotica en voedingsmiddelentechnologie, zorgt voor een toenemende interesse in industriële bioprocessen op bulkschaal, gepaard gaande met een vraag naar grotere, efficiëntere bioreactoren (fermentoren). Schaalvergroting leidt typisch tot een verhoogde mengtijd en andere transportproblemen, die mogelijk leiden tot gradiënten in procescondities (substraatconcentratie, temperatuur, pH,...). Dergelijke gradiënten betekenen dat de micro-organismen continu variaties in hun omgeving waarnemen, die hun metabolisme en daarmee mogelijk productie (negatief) beïnvloeden. Dit inherent schaalafhankelijke effect is een gevolg van de complexe interactie tussen metabolische kinetiek en hydrodynamica in industriële bioreactoren.

De doelstellingen van het hé project, waarbinnen het huidige onderzoek is uitgevoerd, zijn het vergroten van het begrip betreffende hydrodynamisch- kinetische interacties in bioreactoren, en het kwantitatief inschatten van de gevolgen hiervan. Experimenteel zijn er ontwikkelingen gaande op het gebied van neerschaalsimulatoren; reactoren met het doel om fluctuaties, geobserveerd door micro-organismen in industriële reactoren, op labschaal na te bootsen. Binnen het hé project worden de effecten van fluctuaties in substraatconcentratie, zuurstofconcentratie en schuifspanning op het micro-organisme *P. Chrysogenum* met dergelijke technieken bestudeerd aan de East China University of Science and Technology (ECUST). Op basis van de daar behaalde en eerdere resultaten is door onderzoekers van ECUST een metabolisch model voor dit organisme opgesteld, dat momenteel het effect van variaties in substraatconcentratie op de penicillineproductie vangt.

Momenteel zijn de fluctuaties in neerschaalreactoren typisch gebaseerd op globale mengtijden, of zonder referentie naar industriële condities. Hoewel deze reactoren ons begrip betreffende de effecten van extracellulaire fluctuaties vergroten, is de waarde van dergelijke experimenten als industriële afspiegeling discutabel. In het huidige werk wordt numerieke vloeistofdynamica gebruikt om inzicht te verschaffen in het menggedrag in industriële bioreactoren, en met name de substraatvariaties geobserveerd door micro-organismen in deze reactoren. Deze informatie wordt vertaald naar ontwerpparameters voor neerschaalsimulatoren, die de dynamica van de grote schaal weerspiegelen. Deze nieuwe generatie neerschaalsimulatoren heeft de potentie om de metabolische effecten van extra-cellulaire variaties kwantitatief te evalueren, voor een specifieke fermentatie, met een specifieke reactorgeometrie en organisme. Hoewel de huidige focus op substraatfluctuaties ligt, zijn de methoden eveneens toepasbaar voor andere procesparameters zoals de zuurstofconcentratie, pH en temperatuur.

Op basis van Euleriaanse (veldgebaseerde) numerieke methoden zijn een penicilline- en een gistproces gesimuleerd. In beide gevallen is een redelijke overeenkomst met beschikbare validatiedata, zoals de mengtijd en gasfractie, en in het geval van het gistproces zuurstofoverdracht en lokale substraatconcentratie. De simulaties

kunnen worden beschouwd als een goede afspiegeling van de werkelijke processen, binnen de gestelde aannames.

Een aantal aspecten betreffende bioreactor fysica worden met huidige Reynoldsgemiddelde numerieke methoden niet adequaat gevangen. Dergelijke simulaties, specifiek het ”multiple reference frame”(MRF) roerdermodel, overschatten de mengtijd in reactoren met meerdere roerders doordat turbulente dispersie van materiaal tussen de roercompartimenten slecht gevangen wordt. Het MRF model negeert daarnaast de effecten van een macro-instabiliteit in het stromingspatroon. Gesuggereerde fijnstelling van het turbulent Schmidt-getal ten behoeve van het vangen van de globale mengtijd gaat ten koste van de voorspellende waarde. Grote-eddy simulaties presteren beter qua menging, maar de hoge rekentijd weerhoudt routinematige toepassing hiervan. De interactie tussen turbulentie, beluchting en reologie is een punt van aandacht; het laatste aspect is noodzakelijkerwijs buiten beschouwing gelaten in het huidige werk.

Door middel van Lagrangiaanse (deeltjesgebaseerde) simulaties zijn substraatvariaties in de grote-schaal simulaties vastgelegd vanuit het oogpunt van duizenden individuele micro-organismen; de zogenaamde levenslijnen. De geobserveerde variaties blijken sterk afhankelijk van de verhouding tussen de tijdsschaal van substraatopname en de tijdsschaal van menging. De levenslijnen zijn met een drietal methoden geanalyseerd: regime-analyse, trajectanalyse en Fourier-analyse. De hiermee gewonnen fluctuatiestatistieken kunnen worden gebruikt voor het ontwerpen van representatieve neerschaalsimulatoren, zowel op basis van voedingsvariaties als op basis van meerdere reactorcompartimenten. Met name de eerste twee methoden worden in dit werk geïllustreerd. Aangezien de geobserveerde substraatfluctuaties een resultaat zijn van de consumptie door het organisme, dient een neerschaalsimulator met een gelijke biomassaconcentratie te opereren als de industriële schaal om een gelijke fluctuatiesnelheid te bewerkstelligen. Dit kan voor operationele complicaties zorgen op de labschaal, met name voor viskeuze fermentatievloeistof. De spreiding van de fluctuatieduur in geroerde vaten volgt een karakteristieke exponentiële afname, met een gemiddelde tijdsschaal in de ordegrootte van de circulatietijd, circa een kwart van de globale mengtijd en significant sneller dan in huidige neerschaalsimulatoren.

De levenslijnen kunnen verder worden gebruikt om de invloed van extra-cellulaire variaties op het metabolisme te voorspellen, middels het koppelen van metabolische modellen aan de Lagrangiaanse fase in vloeistofsimulaties. Deze koppeling voorspelt een afname van $18 - 46\%$ in de penicillineproductie ten opzichte van de ideale situatie in een 54 m^3 reactor. Een simpele aanpassing in voedingslocatie reduceert deze voorspelde afname tot 9%, waarmee de potentie van de toegepaste simulatiemethode voor ontwerpoptimalisatie wordt geïllustreerd. Op soortgelijke wijze kunnen gewenste metabolische aanpassingen worden gesuggereerd. Numerieke evaluatie van een neerschaalontwerp laat een potentieel goede reflectie van de industriële schaal zien. De numerieke evaluatie toont dat het effect van niet-ideale menging op labschaal waarschijnlijk miniem is, en dat het halveren van de biomassaconcentratie, ondanks het beperken van de overeenstemming in fluctuatiesnelheid, de metabolische respons niet significant aantast. Deze observaties zijn echter situatie-afhankelijk en zullen derhalve als dusdanig geëvalueerd moeten worden. Tot slot laat een simulatie van een 60 uur durend gevoed batchproces zien dat gekoppelde metabolisch-hydrodynamische modellen goed in staat groei en (de afname van) penicilline productie te vangen. In deze simulatie is een significante heterogeniteit in de enzymbeschikbaarheid binnen de populatie geobserveerd. Deze voorspelling kan mogelijk experimenteel getest worden door middel van fluorescentiemarkering.

Al met al toont dit proefschrift dat het met Euleriaans-Lagrangiaanse vloeistofdynamica simulaties mogelijk is de invloed van gradiënten in fermentatieprocessen te beschouwen vanuit het oogpunt van het organisme, deze informatie te benutten voor het winnen van fluctuatiestatistieken, en deze statistieken te gebruiken voor het ontwerp van neerschaalsimulatoren. Gecombineerd met metabolische modellen is het mogelijk voorspellingen te doen betreffende het resulterend productieverlies en populatieheterogeniteit. Gecombineerd met experimentele verificatie in neerschaalreactoren, kunnen op basis hiervan procesverbeteringen, zowel qua reactorontwerp als metabolische aanpassingen, worden voorgesteld, waarmee een nieuwe stap in de richting van betrouwbare opschaling van bioprocessen wordt gezet.

Contents

1

Introduction

> *Many things are known about scale-up. No longer are Rushton impellers the answer. No longer is our concern only in maintaining the same k_La. Environmental stress due to poor mixing and "hidden" auxotrophy are two factors not fully addressed nor appreciated on scale-up. As a consequence, scale-up is still an art not a science.*
>
> Arthur Humphrey, *Shake Flask to Fermentor: What Have We Learned?* [1]

Former EU-chief scientific adviser[1] Anne Glover crowned the 21^{st} century ”the age of biotechnology”. The prediction seems to hold so far: industrial and pharmaceutical biotechnology are going strong [2]. For example, a recent market study by Deloitte reveals a strong consistent growth since 2010 in all life science related fields, despite varying economic conditions, with a predicted sales increase from $289 \cdot 10^9$ USD in 2010 to $445 \cdot 10^9$ USD in 2019 worldwide [3].

The pharmaceutical (life sciences) market traditionally holds a majority share within the total biotechnology market; in a recent market value assessment the pharma market's share (biologics + industrial pharma) was valued at slightly below 50% of the total US biotechnology market [2], mainly due to an explosive rise in modified crops. Albeit less explosive, biotechnological materials production is on the rise as well. Examples include $1,4-$butanediol [4, 5], an industrial solvent and succinic acid [6, 7], both a polymer precursor and dietary supplement. The feasibility of biotechnological production routes depends strongly on the global oil price, and its volatility gives rise to a more cautious investment climate. Still, the increasing push to step away from fossil resources, combined with rapid technological developments in biotechnology (especially considering genetic engineering techniques), virtually ensures that more and more biological production routes will become competitive.

1.1. Bioreactor development and scale-up

The developments in bulk bio-processes, aside from improved control, have been modest over the years. In some ways, the reactor is still more of a black box than the micro-organisms residing inside. Mixing times, consumption rates, temperatures and other process parameters can be determined at the equipment-size level, but there is little data available regarding local conditions inside industrial bioreactors. Since mixing can typically be regarded as instantaneous in lab-scale reactors (but not always, see chapter 7), these equipment-scale measurements typically suffice for laboratory

---

[1] A position sadly abolished under pressure of environmental organizations due to her progressive views on agricultural biotechnology.

experiments. In industrial scale reactors, where mixing is inherently slower, a heterogeneous fermentation environment may develop [8–10]. This translates to temporal variations in the environment *as experienced by micro-organisms*. Experimentally, it is extremely difficult to obtain detailed insight in this *local* fermentation environment on the large scale, and detailed insight in the fermentation environment must be derived from very limited information.

Extra-cellular heterogeneity leads to heterogeneity in the intra-cellular make-up over the microbial population when the timescales of mixing and intra-cellular response are similar. In this case, the organisms are never truly in equilibrium with their surrounding (which would apply if mixing is much slower than metabolic adaptations), nor is the intra-cellular makeup insensitive to the direct surrounding (which applies if mixing is much faster than metabolic adaptation). Consequently, the population inside a fermentor may be globally as well as locally heterogeneous: two organisms residing at the same point in space may have a different metabolic make-up, depending on the history of their trajectory.

Metabolic heterogeneity in turn may influence gene expression and protein synthesis rates [11, 12], even though the associated timescales are orders of magnitude higher than those of extra-cellular variations [13], leading to heterogeneous enzyme levels within the population. The production of the desired end product may in turn be affected, either by the availability of precursor metabolites, or by the availability of (active) enzymes. The complex response to extra-cellular heterogeneity is one of the aspects that makes bio-reactor scale-up a complicated, error-prone practice [1, 14]. An associated problem relates to organism development. Modified organisms are often selected based on their performance in lab-scale experiments, which unlikely represent the industrial fermentation environment; the herein selected strain may not be the one that performs best under production conditions [15]. Preferably, the impact of environmental heterogeneity should be accounted for *during process design and organism selection*, which means that methods are required that can make predictions regarding the environment and the interplay between extra-cellular and intra-cellular conditions.

1.2. The promise of coupled CFD-Metabolic dynamics

Computation has opened the route to detailed, dynamic descriptions of both biological networks and complex flows. This offers possibilities for new computer-aided routes for studying the environment in large scale bio-reactors. Computational Fluid Dynamics (CFD) enables the prediction of *local* flow profiles inside bioreactors in varying levels of detail [8, 10, 16–20]. CFD can be applied to study how flow influences the *local* distribution of substrate, dissolved oxygen and other extra-cellular parameters that may influence micro-organisms. Detailed metabolic models on the other hand provide the means to assess the response of organisms to a certain environment [21, 22]. These fields are inherently coupled: the distribution of extra-cellular reactants will influence the organism's response, the organism's response will influence the distribution of extra-cellular reactants [21, 23].

Combining CFD simulations with metabolic models enables to study this interplay computationally, and in principle, already during process design. Classically, reaction models in CFD simulations are coupled as source/sink terms in the substrate transport equations [16, 24, 25], which implicitly assumes equilibrium between the intra- and extra-cellular domain. This fully Eulerian (field-based) approach does not include the effect of the intra-cellular history on the current state of the metabolism. It is possible to use a population balance model to include the effect of local cellular heterogeneity, an approach developed by Morchain et al. [18, 19, 26–28]. This approach is especially powerful when resolving longer timescales (hours of fermentation time), but it is limited in the intra-cellular details: a single distributed parameter, typically the growth rate μ, is used to describe the intra-cellular state. When multiple interacting intra-cellular pools need to be tracked, this approach may quickly become cumbersome.

An alternative approach towards bioreactor modeling was pioneered by Lapin et al. [21, 23]: Euler-Lagrange CFD [29], where the biomass phase is represented by a large number of discrete particles (parcels) who's motion is computed individually. Each parcel represents a group of organisms following a similar path through the reactor. A vector of intra-cellular conditions is stored for each particle, containing the levels of key metabolites and enzymes. In this way, the degree of heterogeneity can be assessed straightforwardly for many intra-cellular pools. The Euler-Lagrange approach furthermore provides a unique point of view: it is possible to track both the intra-cellular and extra-cellular environment for each individual particle over time [10, 20, 21, 23, 30–32]. Hence, we can study the fermentation environment from the point of view of the organism, which enables to study the duration and magnitude of extra-cellular concentration variations experienced by micro-organisms. A con is that the required time resolution to resolve particle motion leads to high computational demands when simulating long stretches of flow time.

Regardless of the metabolic approach, the complexity of fermentor flows (turbulent, multi-phase and non-Newtonian) is such that many simplifications must be made in its modeling and, while CFD approaches certainly have predictive value, prior validation of the models against experimental data is still required. For small-scale reactors, detailed flow information may be available from experiments which can be used for validation [16, 33–40]. To some extent, this information may be extrapolated to large-scale reactors, based on geometric similarity and dimensionless number scaling. It may, however,be challenging or outright impossible to perform a full experimental scaling experiment, as length- and timescales associated with the metabolism are scale-invariant. Lacking detailed insight into industrial fermentors, large-scale validation mostly relies on integral parameters: mixing times, gas holdups, oxygen transfer rates, and so forth. Combined with the performance of the applied CFD models in well-studied small-scale experiments, the validity of the chosen CFD approach for large-scale processes can be claimed with at least some confidence.

Similarly, metabolic models should be validated by well-defined laboratory scale environments, for example experiments in which the extra-cellular substrate or dissolved oxygen concentration is deliberately varied with a fixed frequency and amplitude [41–45]. The coupling between CFD and metabolic dynamics (MD) is more difficult to validate, as this requires some degree of experimental insight into the environment inside a bio-reactor. There are promising developments in the field of active tracer probes [46] which measure the environment from the perspective of a flow-following particle, but contamination risks and operating costs will likely uphold conservatism in large-scale fermentation experimentation, and these probes are currently not able to measure local dissolved oxygen or glucose levels. Currently, a very limited number of data sets quantifying the environment inside a large scale fermentor is available.

1.3. Scaling down bioreactors

Scale down (SD) simulators are laboratory setups that aim to mimic the environmental heterogeneity of large scale bioreactors to study how this environment affects the organism [12, 43, 47]. This implies that, in order to be industrially representative, a scale-down simulator must reproduce the amplitude and frequency of fluctuations that organisms encounter at the large scale [15]. As discussed earlier, little to no information on these statistics is available experimentally. As an alternative, the design of SD simulators can be based on CFD information; since the device aims to reproduce the temporal variations observed by organisms, information from the organism's point of view is required. By providing time series of the extra-cellular conditions registered by each individual particle, this is exactly what Euler-Lagrange CFD-MD simulations give: *insight in the fermentation environment, from the point of view of the organism*. The condition versus time series gathered in Euler-Lagrange simulations are referred to as organism lifelines, a term coined by Lapin and Reuss [21, 23].

Scale-down simulators may use deliberate variations in the substrate feed to impose extra-cellular substrate variations, or they may use multiple reactors, each operating under different conditions, in a flow-loop. Both approaches have been frequently applied in literature [41, 43, 44, 48–55]. Lacking detailed information on the environment inside the large scale reactor, the magnitude and duration of the imposed extra-cellular variations in these studies were typically based on the global industrial mixing times, or without industrial reference. While these studies were often very useful in gaining insight in the response of organisms to extra-cellular variations, the imposed conditions may not reflect the conditions encountered by organisms in the industrial situation. With the state-of-the-art Euler-Lagrange CFD approach, statistics on industrial scale variations can be derived from the individual organism lifelines. These statistics can then be used as a basis of design for industrially representative scale-down simulators to aid both in the rational scale-up of bioreactors, and in the development of micro-organisms that are more resilient under industrial conditions.

1.4. The Hé project

The above discussion outlines the scope of the Hé project; a research project aimed at combining computational fluid dynamics and metabolic dynamics to study the environment in large scale bioreactors, how this environment influences the metabolism of micro-organisms and how scale-down simulators can be designed based on the acquired information. This project is conducted in a consortium consisting of TU Delft (Transport Phenomena group and Cell Systems Engineering group), East China University of Technology (ECUST, state key laboratory of bioreactor engineering) and DSM Sinochem pharmaceuticals. Within this framework, TU Delft has the lead in large-scale CFD simulations and, if required, hydrodynamic experiments. ECUST has the lead in biological modeling and experimental scale-down studies. DSM Sinochem provides expertise on industrial reactor design and on *Penicillium chrysogenum*, the model organism used in this study. A further discussion of the rationale behind the Hé project has been published by Wang et al. [56].

1.4.1. Project outline

The Hé project is outlined graphically in figure 1.1. Here, the topics within the dashed boundary are the steps conducted within the scope of this thesis. Within these battery limits ”experimental fluid dynamics” has been included. Within the scope of the project, only LDA measurements relating to the multi-impeller mixing were conducted. The rest of the project focused on the implementation and data processing of the Euler-Lagrange method, and not so much on improving the turbulence, multiphase and rheological modeling of large-scale fermentors to increase agreement with experimental flow data. As such, no further experimental studies were conducted.

The light-green sections are experimental studies geared towards further understanding the *P. chrysogenum* fungii, particularly when exposed to extra-cellular variations in glucose availability, oxygen availability and shear rate. These experiments are used as a basis for metabolic modeling, together with data from prior studies conducted at TU Delft. Both the experimental part and the metabolic modeling are executed at the East China University of Science and Technology (ECUST). All white boxes represent project input. The *P. chrysogenum* strain has been donated by DSM Sinochem pharmaceuticals. Furthermore, DSM/Sinochem has supplied data regarding a 60 m^3 and a 120 m^3 fermentor for CFD validation, as well as input for other reactor configurations. Further CFD input (turbulence/multiphase/rheological modeling and validation data) was acquired from academic literature. Dark grey blocks indicate the final project goals, which were not tackled directly within the current work. Future work should aim at actually constructing CFD-based scale-down simulators, verifying the organism response predicted by the metabolic models, and proposing improved scale-up protocols based on the scale-down analysis.

1.4.2. Research questions

Work by Lapin and Reuss provided the foundation of the Euler-Lagrange CFD approach, which forms the basis of this project. We aim to further establish the methodology, and apply it towards industrially relevant problems. The core steps covered in this project are:

- Implementation of the Euler-Lagrange method in commonly used CFD software (ANSYS FLUENT).
- Set up implementation guidelines and best practices for application of the Euler-Lagrange method.
- Application of the Euler-Lagrange method to industrially relevant case studies.

- Data analysis: from organism lifelines to environmental variation statistics.
- Design of representative scale-down simulators based on CFD data.
- Inclusion and evaluation of metabolic coupling in the Euler-Lagrange framework.

In particular, the focus is on the data analysis step, which involves the translation of large amounts of data (individual lifelines) to manageable fluctuation statistics that capture the fermentation environment at the reactor scale, the subsequent scale-down design step, and analysis of the metabolic response to extra-cellular fluctuations. Based on the above, the following research questions have been formulated:

1. What are the set-up requirements for accurate, coupled $CFD - MD$ simulations?

Lapin and Reuss have discussed the numerical implementation of the Euler-Lagrange approach, but left practical questions open. Practically, the reaction field is discretized separately from the background grid by coupling reactions to particles, which means that the accuracy of the simulation depends strongly on the number of particles N_p and timestep size Δt. Other practical aspects consider simplification of the domain by imposing periodicity, and using the multiple-reference frame impeller modeling strategy which can save considerable computation time. The goal of this first part is to set up implementation guidelines, which can be used to estimate the Lagrangian simulation requirements a-priori, rather than by trial-and-error.

2. Which statistical parameters quantitatively characterize the fermentation environment, as experienced by the organisms inside it, and how can these be derived from organism lifelines?

The second part of this project couples to the data processing challenge. Lifelines contain strong fluctuations in, for example, the extra-cellular substrate concentration C_s. While qualitatively clear, quantitatively the lifelines are not directly insightful or useful as a basis of design for scale-down simulation. A set of statistics representing the observations of the population at large needs to be distilled from the lifelines. In this section of the project, multiple methods for lifeline analysis are explored, and for a deeper understanding of the nature of the registered fluctuations, the link between the fluctuation statistics and Eulerian flowfield features is discussed.

3. How can scale-down simulator designs be derived from the statistics acquired in Euler-Lagrange CFD simulations?

Noorman [15] identified fi degrees of freedom that must be fixed to design a scale-down simulator. Here, we use the CFD data to determine the values of these degrees of freedom, to propose designs that are a proper reflection of the large-scale environment. Further issues that are explored in this phase of the project are the practical feasibility of the proposed scale-down design, and comparing the performance of competing designs.

4. How is the metabolism of *P. chrysogenum* predicted to respond to fluctuations in the extra-cellular environment?

In the final part of this thesis, a metabolic model for *P. chrysogenum*, developed by our project partners, is coupled to large-scale CFD simulations to assess the metabolic response to extra-cellular fluctuations. Key parameters are the production rate q_p and mean growth rate $\overline{\mu}$. The emergence of population heterogeneity is also discussed. By coupling the same metabolic model to a scale-down simulator design, we evaluate the expected performance of this simulator in terms of large-scale replication.

Besides these core challenges, several secondary problems were touched upon during the execution of this work to some extent. These problems involve the modeling of turbulence, gas-liquid flow and non-Newtonian flow in stirred tank bioreactors. Most of these issues have been considered as simulation inputs, and do not constitute sufficient material for a separate chapter. An exception that has been studied in more detail is the interaction between multiple impellers in a single-phase stirred reactor. In particular, the exchange of material between the individual stirrers was found to be underestimated in CFD simulations, over-estimating the mixing time. This observation has led to the additional research question:

5. Is the consistent over-estimation of mixing times in $k-\epsilon$ CFD simulations of multi-impeller mixing vessels due to an underestimation of mass exchange between the separate impeller compartments?

This question arose from the unsatisfactory notion that the turbulent Schmidt number in $k-\epsilon$ simulations has to be arbitrarily tuned to agree with experimental mixing data in stirred tanks. A literature study revealed this is mostly the case for multi-impeller simulations; our hypothesis is that this turbulent transport between the impeller compartments is underestimated in RANS simulations of such systems, due to mis-estimation of turbulent dispersion. Additionally, experimental data hints at the presence of a macro-instability that may promote mixing. A wide variety of simulations, combined with experimental LDA data, has been conducted to study how well RANS models capture flow and turbulence in the region between the stirrers.

1.5. Thesis outline

In chapter 2, a treatment of relevant background theory is given, both considering the flow in stirred, aerated fermentors and the organisms used in this study. Chapter 3 focuses on mixing in multi-impeller fermentors. Chapter 4 discusses implementation guidelines for Euler-Lagrange bioreactor simulations, chapter 5 treats the analysis of organism lifelines, chapter 6 outlines CFD-based scale-down strategies and chapter 7 reports on the use of coupled metabolic-hydrodynamic simulations, combining analysis and downscaling. To conclude, chapter 8 provides some future perspectives. Altogether, this thesis proposes a methodology to translate data acquired from CFD-MD simulations to design parameters for industrially representative scale-down simulators, laboratory scale setups with an extracellular environment that reflects that of the large-scale, as seen *through the organism's eyes*.

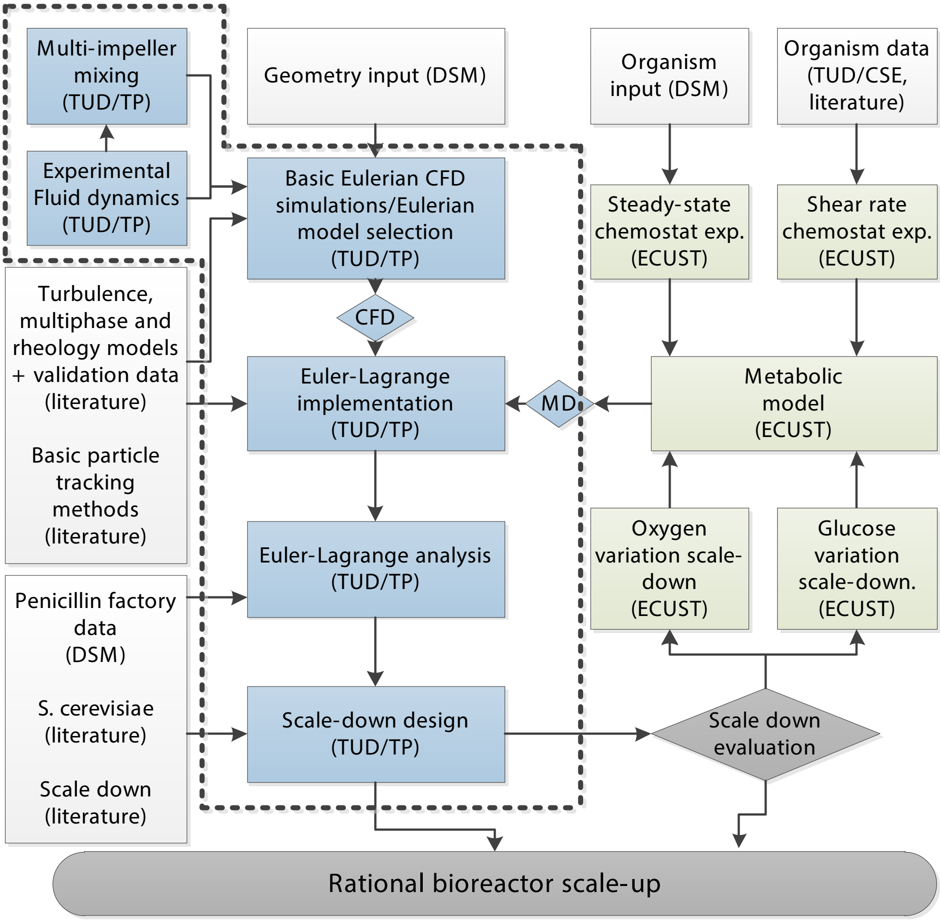

Figure 1.1: Overall project layout in which this work is embedded. The topics within the dashed area are studied within the scope of this thesis. Olive blocks are executed by colleagues at ECUST. White blocks indicate external inputs. Gray parts indicate future project goals.

2

Theory

This chapter provides a treatment of the background theory, to expand upon some modeling choices made in the subsequent chapters. First, fluid dynamic considerations are discussed. The second part focuses on the biological side of the project.

2.1. CFD modeling of stirred fermentors

The flow in industrial scale fermentors is typically turbulent, might be stirred, might be aerated and might be non-Newtonian. All four of these aspects require special treatment within CFD simulations. The first three aspects are treated within this chapter. Non-Newtonian flow simulations were only briefly addressed in this project, and are not discussed in this thesis.

2.1.1. Single phase flow

Industrial stirred tank reactors are commonly operated in the turbulent flow regime ($Re = \frac{u\rho L}{\mu_l} > 10^4$), although highly viscous processes may be operated in the transitional regime. As any flow, the basic fluid motion is described by the *Navier-Stokes and continuity equations*:

$$\rho\left(\frac{\partial u_i}{\partial t} + u_j\frac{\partial u_i}{\partial x_i}\right) = -\frac{\partial p}{\partial x_i} + \frac{\partial}{\partial x_j}\tau_{ij} + f_i \tag{2.1}$$

$$\frac{\partial \rho}{\partial t} + \frac{\partial(\rho u_i)}{\partial x_i} = 0 \tag{2.2}$$

where for Newtonian behavior the stress tensor takes the form:

$$\tau_{ij} = \mu_l\left(\frac{\partial u_i}{\partial x_j} + \frac{\partial u_j}{\partial x_i} - \frac{2}{3}\delta_{ij}\frac{\partial u_i}{\partial x_i}\right) \tag{2.3}$$

These equations typically require a numerical solution [57]. Although other options are available, the versatile finite volume (FV) approach is employed in this project [58], as the inclusion of multiphase behavior and chemical reactions within the FV-framework is well established.

Turbulence modeling

The desire to resolve hours of flow time within at most days of computation time rules out full resolution of the flow, as well as spatially filtered *Large Eddy Simulations* (LES). The latter are used within this project, within the scope of detailed mixing studies (chapter 3). For fermentor simulations, we rely on *Reynols Averaged Navier Stokes* (RANS) methods were the effect of scales of turbulence is modeled, while capturing the global flow patterns and concentration gradients which we are interested in. Furthermore, RANS methods are more established in combination with multiphase flows.

RANS Modeling In the RANS method it is assumed that each property in a turbulent flow can be split into an average and a fluctuating component: $u_i = U_i + u_i'$. Applying this to eq. 2.1, and averaging the resulting equation yields:

$$\rho\left(\frac{\partial U_i}{\partial t} + U_j \frac{\partial U_i}{\partial x_i}\right) = -\frac{\partial p}{\partial x_i} + \frac{\partial}{\partial x_j}\left(\tau_{ij} - \rho\overline{u_i' u_j'}\right) + f_i \tag{2.4}$$

with the Reynolds stress tensor $u_i' u_j'$ nonzero and unknown; closure relations have to be supplied to estimate the Reynolds stresses, which model the impact of (small scale) turbulence on the large scale flow. In *Reynolds Stress Modeling* (RSM) relations for each individual Reynolds stress component are supplied, plus one auxiliary equation for the turbulent energy dissipation rate ϵ [58]. This approach is computationally still relatively intensive, and is only applied in studying single phase flow within this work. Simpler 2-equation models compute the turbulent kinetic energy k_t and turbulent energy dissipation rate ϵ rather than the full Reynolds stress tensor. These methods are significantly cheaper computationally, while showing similar accuracy in the impeller region of a stirred tank [59, 60] In most of this project the two equation standard $k-\epsilon$ or realizable $k-\epsilon$ model is used.

Standard and Realizable k$-\epsilon$ models The $k-\epsilon$ model uses k_t and ϵ to provide closure of the equations. In the standard formulation, the transport equations for k_t and ϵ read:

$$\frac{\partial(\rho k_t)}{\partial t} + \frac{\partial \rho k_t U_i}{\partial x_i} = \frac{\partial}{\partial x_j}\left(\left(\mu_l + \frac{\mu_t}{\sigma_k}\right)\frac{\partial k_t}{\partial x_j}\right) + 2(\mu_l + \mu_t)S_{ij} \cdot S_{ij} - \rho\epsilon \tag{2.5}$$

$$\frac{\partial(\rho\epsilon)}{\partial t} + \frac{\partial \rho\epsilon U_i}{\partial x_j} = \frac{\partial}{\partial x_j}\left(\left(\mu_l + \frac{\mu_t}{\sigma_\epsilon}\right)\frac{\partial \epsilon}{\partial x_j}\right) + C_{1\epsilon}\frac{\epsilon}{k_t}2(\mu_l + \mu_t)S_{ij} \cdot S_{ij} - C_{2\epsilon}\rho\frac{\epsilon^2}{k_t} \tag{2.6}$$

Here μ_t is the turbulent viscosity for the standard $k-\epsilon$ model, $\mu_t = \rho C_\mu k_t^2/\epsilon$; μ_l is the molecular viscosity. Five fitting parameters are required, and by fitting to a wide range of flows it was found that the following set is applicable in the majority of cases: $C_\mu = 0.09$, $\sigma_k = 1.00$, $\sigma_\epsilon = 1.30$, $C_{1\epsilon} = 1.44$ and $C_{2\epsilon} = 1.92$. The Boussinesq assumption [58] is used to close the averaged Navier-Stokes equations:

$$-\rho\overline{u_i'u_j'} = 2\mu_t\left(\frac{\partial U_i}{\partial x_j} + \frac{\partial U_j}{\partial x_i}\right) - \frac{2}{3}\rho k_t \delta_{ij} \tag{2.7}$$

The realizable $k - \epsilon$ model differs from the standard $k - \epsilon$ model in formulation of the turbulent viscosity μ_t and the transport equation for ϵ, which now reads:

$$\frac{\partial(\rho\epsilon)}{\partial t} + \frac{\partial}{\partial x_j}(\rho\epsilon U_i) = \frac{\partial}{\partial x_j}\left(\left(\mu_l + \frac{\mu_t}{\sigma_\epsilon}\right)\frac{\partial\epsilon}{\partial x_j}\right) + \rho C_1 S\epsilon - \rho C_2\frac{\epsilon^2}{k_t + \sqrt{\nu\epsilon}} \tag{2.8}$$

with $C_1 = \max(0.43, \eta/(5+\eta))$, $\eta = Sk_t/\epsilon$ and $S = \sqrt{2S_{ij}\cdot S_{ij}}$

Next to being mathematically consistent, the realizable $k-\epsilon$ model generally performs better in rotating flows [61], which would make it theoretically more applicable for the studied system. The standard $k - \epsilon$ model has been more frequently applied in literature, showing decent results for both flow [59, 62] and mixing [62] in single-impeller mixing tanks.

Reynolds stress modeling RSM models transport of each Reynolds stress component individually, by the transport equation:

$$\begin{aligned}\frac{\partial(\rho\overline{u_i'u_j'})}{\partial t} + \frac{\partial}{\partial x_k}(\rho U_k\overline{u_i'u_j'}) = -\frac{\partial}{\partial x_k}\left(\rho\overline{u_i'u_j'u_k'} + \overline{p'\left(\delta_{kj}u_i' + \delta_{ik}u_j'\right)}\right) + \\ \frac{\partial}{\partial x_k}\left(\mu_l\frac{\partial}{\partial x_k}(\overline{u_i'u_j'})\right) - \rho\left(\overline{u_i'u_k'}\frac{\partial u_j}{\partial x_k} + \overline{u_j'u_k'}\frac{\partial u_i}{\partial x_k}\right) + \\ \overline{p'\left(\frac{\partial u_i'}{\partial x_j} + \frac{\partial u_j'}{\partial x_i}\right)} - \rho\epsilon - 2\rho\Omega_k\left(\overline{u_j'u_m'}\epsilon_{ikm} + \overline{u_i'u_m'}\epsilon_{jkm}\right)\end{aligned} \tag{2.9}$$

The turbulent diffusion, pressure strain and dissipation term must be modeled; the latter is closed by supplying a transport equation for ϵ similar to the $k-\epsilon$ model. For the diffusive term, ANSYS FLUENT uses a simple-gradient approximation because of numerical instabilities with the generalized gradient diffusion model:

$$\frac{\partial}{\partial x_k}\left(\rho\overline{u_i'u_j'u_k'} + \overline{p'\left(\delta_{kj}u_i' + \delta_{ik}u_j'\right)}\right) = \frac{\partial}{\partial x_k}\left(\frac{\mu_t}{\sigma_k}\frac{\partial\overline{u_i'u_j'}}{\partial x_k}\right) \tag{2.10}$$

with $\sigma_k = 0.82$. The pressure strain model can be closed in various ways, the default option is the linear-pressure strain approach which consists of three terms:

$$\overline{p'\left(\frac{\partial u_i'}{\partial x_j} + \frac{\partial u_j'}{\partial x_i}\right)} = \psi_{ij,1} + \psi_{ij,2} + \psi_{ij,3} \tag{2.11}$$

Here, $\psi_{ij,1}$ is the slow pressure-strain term, $\psi_{ij,2}$ the rapid pressure-strain term and $\psi_{ij,3}$ the wall-reflection term. Expressions for these terms can be found in the FLUENT theory guide [63]. As this computationally intensive model did not yield favorable results in previous studies [59], this model has not been applied in fermentor modeling. The Reynolds Stress Model has been used in the single-phase flow section of this study, to investigate the possible role of non-isotropic turbulence on multi-impeller mixing.

Large Eddy Simulations Large eddy simulations employ a spatial filtering procedure rather than an averaging procedure to eq. 2.1, yielding:

$$\frac{\partial \rho \widetilde{u_i}}{\partial t} + \rho \widetilde{u_j} \frac{\partial \widetilde{u_i}}{\partial x_j} = -\frac{\partial \widetilde{p}}{\partial x_i} + \frac{\partial}{\partial x_j} \cdot \left(\widetilde{\tau_{ij}} + \tau_{sg,ij} \right) \tag{2.12}$$

Practically, the applied filtering kernel in FLUENT is based on the local grid size, which is computed as $\Delta = V_c^{1/3}$ [63]. The subgrid stress tensor $\tau_{sg,ij} = \widetilde{u_i}\widetilde{u_j} - \widetilde{u_i u_j}$ results from the filtering procedure and accounts for small-scale (subgrid) turbulence. This term is typically closed via an eddy viscosity formulation, similar to RANS models, but now applicable only for the smaller scales which better abide the isotropy assumptions. The recommended subgrid model is the Dynamic Smagorinsky model [64, 65], which, in contrast to the regular Smagorinsky model, requires no fitted constant; C_S is determined dynamically, with a value between 0 and 0.23. The subgrid turbulent viscosity is calculated as $\mu_t = \rho L_s^2 S$, with $L_s = min(\kappa d, C_s \Delta)$, d being the nearest wall distance and κ the von Karman constant. Combined with $\tau_{sg,ij} - 1/3 \tau_{kk} \delta_{ij} = -2\mu_t \widetilde{S_{ij}}$, this gives (in the bulk):

$$\tau_{sg,ij} = -2 C_S^2 \rho \Delta^2 \tilde{S} \left(\widetilde{S_{ij}} - \frac{1}{3} \widetilde{S_{kk}} \delta_{ij} \right) \tag{2.13}$$

The Smagorinsky model assumes that the production of subgrid turbulent kinetic energy is locally balanced by dissipation. To avoid excessively high mesh requirements in the vicinity of boundaries, standard wall functions are applied [63].

2.1.2. Multiphase modeling

Multiphase flow modeling can be conducted in various ways. For dispersed flows in large scale applications the size difference between the dispersed phase (droplets or bubbles) and simulation domain means that it is impossible to resolve the dispersed entities explicitly. Again, an averaging procedure is applied to avoid fully resolving the dispersed phase, and the interaction between the dispersed and continuous phase has to be modeled [66, 67]. The averaging procedure results in a volume-fraction field α present everywhere in the domain; the two phases are assumed to be inter-penetrating and continuous, leading to the name Euler-Euler modeling.

An alternative option is to treat the dispersed phase as individual point particles, for which the motion is calculated by solving a force balance on each particle, called the Euler-Lagrange approach. As for the Euler-Euler approach, inter-phase interaction is included via (empirical) force models. Literally tracking each individual entity is computationally infeasible for macro-scale flows; a workaround is to assume every computational particle (referred to as parcel) represents a group of individual particles traveling a similar trajectory through the reactor (within the parcel, the true particle size distribution including break-up/coalescence effects can be coupled if desired [68, 69]). In the current work, the Euler-Euler approach is used to model gas-liquid flow. The Euler-Lagrange approach is used to model the biomass phase in this work, as it allows to track the lifelines of parcels of biomass, as well as the internal metabolic state by coupling metabolic reaction networks to each individual parcel.

The Eulerian approach

A two fluid (Euler-Euler) approach requires solving of a separate momentum equation for each fluid, with closure relations modeling inter-phase momentum transfer. A phase indicator $\chi(\mathbf{x},t)$ is introduced into the momentum equation, which is subsequently averaged (using the statistical mean $\overline{f}(\mathbf{x},t) = \int_\Omega f(\mathbf{x},t;\omega)d\mu(\omega)$ [67]). This yields a phase-specific momentum equation with α being the cell phase fraction. For phase a, the equation (in tensor form) reads:

$$\frac{\partial}{\partial t}(\alpha_a\rho_a\overline{\mathbf{U}_a}) + \nabla\cdot(\alpha_a\rho_a\overline{\mathbf{U}_a\mathbf{U}_a}) = \alpha_a\nabla P + \nabla\cdot\alpha_a(\overline{\bar{\bar{\boldsymbol{\tau}}}_a} + \overline{\bar{\bar{\boldsymbol{\tau}}}_{Re,a}}) + \alpha_a\rho_a\mathbf{g} + \mathbf{M}_k \quad (2.14)$$

In this approach individual phase entities such as droplets and particles are averaged out, making it suitable for situations where these entities cannot be practically resolved. (see e.g. [66]). As for single phase flow, $\overline{\bar{\bar{\boldsymbol{\tau}}}_{Re,a}} = -\overline{\rho_a\mathbf{u}'_a\mathbf{u}'_a}$ represents the effect of fluctuating velocities due to (pseudo-) turbulence. Turbulence modeling requires some extra consideration in multi-phase flows. For dispersed applications, the mixture and dispersed formulation of the $k-\epsilon$ are available. In the mixture model, both phases share the same $k-\epsilon$ equations, with a phase averaged density and viscosity. This model is valid for fluids with a similar density ratio, and not advised for gas-liquid flow. The dispersed model is based on Tchen-theory [70] for dispersed phase turbulence, with modified transport equations for the continuous phase to include transfer of turbulent momentum [63]. The term $\mathbf{M}_k$ represents inter-phase momentum exchange, which includes: [71]:

- **Drag force:** Viscous drag resulting from slip velocity
- **Lift force:** Transverse force resulting from vorticity-velocity interaction
- **Virtual mass force:** Results from inertia in the carrier fluid
- **Basset force:** Due to lagging boundary layer formation
- **Turbulent forces:** Phase interaction may influence turbulent behavior

Typically these terms are closed via (semi-) empirical models and the individual contributions of the forces are considered to be additive. In reality, interactions will of course exist as each force depends on and interacts with the bubble/droplet velocity, and the current approach to interaction force modeling can be disputed [72]. In any case, the complexity of the interaction problem means that there is still much ground to gain in the field, and that a general approach is far from available.

In typical stirred tank applications, only the drag force is included. Various drag force formulations are available, as discussed in 2.2. Here, we employ the model of Ishii and Zuber [73] which includes a bubble shape correction, and includes swarm effects based on the Richardson-Zaki correction [74]. In FLUENT, the model is implemented as the 'Universal drag law' with slightly modified coefficients [75], and coupled to the momentum balance via the exchange coefficient K_{ab}.

$$
\begin{aligned}
K_{ab} &= \frac{C_D Re_e \mu_{l,b} A_i}{8 d_p} \\
C_{D,vis} &= \frac{24}{Re_e}(1 + Re_e^{0.75}) \\
C_{D,dis} &= \frac{2}{3}\frac{1}{\sqrt{Eo}}\left(\frac{1 + 17.67(1-\alpha_b)^{1.5}}{18.67(1-\alpha_b)}\right)^2 \\
C_{D,cap} &= \frac{8}{3}(1-\alpha_b)^2 \\
C_D &= \min\left(C_{D,cap},\ \max(C_{D,dis}\ C_{D,vis})\right)
\end{aligned}
\tag{2.15}
$$

Here, $Re_e = \rho_a |u_a - u_b| d_p / \mu_{l,e}$ with $\mu_{l,e} = \mu_{l,a}/(1-\alpha_b)$. $Eo = \Delta\rho g d_p^2/\gamma$ is the Eötvös number, which is related to the Rayleigh-Taylor instability wavelength [76] and associated with the bubble/droplet shape. When coupled to a population balance model, the local Sauter-mean bubble diameter is used as the representative diameter to calculate the drag force.

Population balance modeling Information about the bubble(/particle) size is lost in averaging, and needs to be resupplied. A single (mean) size can be prescribed based on experimental data, but in reality the size is strongly distributed and the mean poorly models bubble behavior throughout the domain. A common approach towards including a size distribution is the use of a population balance model, which prescribes a transport equation for the bubble number density function $n(V,t)$, and may include growth, coalescence and breakup. Neglecting growth/shrinking due to mass transfer and the pressure gradient, this equation reads:

$$
\begin{aligned}
&\frac{\partial}{\partial t}[n(V,t)] + \frac{\partial}{\partial x_i}[u_i n(V,t)] = \\
&\frac{1}{2}\int_0^V a(V-V^*,V^*)n(V-V^*,t)n(V^*,t)dV^* - \int_0^\infty a(V,V^*)n(v,t)n(V^*,t)dV^* \\
&\qquad\qquad + \int_{\Omega v} g(V^*)\beta(V|V^*)n(V^*,t)dV^* - g(V)n(V,t) \qquad (2.16)
\end{aligned}
$$

The first line represents transport, the second line particle death and birth due to aggregation and the third line death and birth due to breakup. Semi-empirical kernels are used to model the different terms. In this project break-up and coalescence were included; ANSYS FLUENT includes several separate break-up and coalescence kernels, but only the Luo and Svendsen [77] kernel is available for *both* break-up and coalescence. Hence, despite superior approaches being described in literature, in this project the Luo and Svendsen kernels were used for both breakup (eq. 2.17) and coalescence (eq. 2.18). It is not advised to mix-and-match different kernels, as the predicted rates may differ significantly between them and they may only balance properly when used with their associated counterpart [78]. The breakup kernel usually requires a frequency term $g(V^*)$ and breakage pdf $\beta(V|V^*)$; in the Luo and Svendsen model these two terms are integrated in the breakage rate Ω_{br}.

$$
\Omega_{br}(V,V^*) = K\int_{\xi,min}^1 \frac{(1+\xi)^2}{\xi^n}\exp(-b\xi^m)d\xi \qquad (2.17)
$$

with $K = 0.9238\epsilon^{1/3}d^{-2/3}\alpha$, $n = 11/3$, $b = 12[f^{2/3} + (1-f)^{2/3} - 1]\gamma/\rho \cdot \epsilon^{-2/3}d^{-5/3}\beta^{-1}$, $m = -11/3$ and $\beta = 2.047$. Furthermore, $\xi = \lambda/d$ where λ is the integral eddy size and d is the particle diameter and f the bin fraction.

$$
\begin{aligned}
a_{ag} &= \omega_{ag}(V_i,V_j)P_{ag}(V_i,V_j) \\
\omega_{ag}(V_i,V_j) &= \frac{\pi}{4}(d_i+d_j)^2\overline{u_{ij}} \\
P_{ag} &= \exp\left[-c_1\frac{\left(0.75(1+x_{ij}^2)(1+x_{ij}^3)\right)^{1/2}}{(\rho_2/\rho_1+0.5)^{1/2}\cdot(1+x_{ij})^3}\cdot\left(\frac{\rho_1 d_i\overline{u_{ij}}^2}{\gamma}\right)^{1/2}\right] \qquad (2.18) \\
\overline{u_{ij}} &= \sqrt{\left(1.43(\epsilon d_i)^{1/3}\right)^2 + \left(1.43(\epsilon d_j)^{1/3}\right)^2}
\end{aligned}
$$

It was attempted to implement alternative models via user defined functions, including the Prince and Blanch [79], Lehr [80] and Wang model [78]. While these models may perform superior to the Luo and Svendsen kernel, implementation proved numerically unstable, however, and constituting side-tracks from the core questions of this work, these issues were not further addressed.

Practical implementation of PBM There are multiple solution procedures for the population balance model, the most popular ones being the discrete method and quadrature method of moments (QMOM) [81–83]. In the discrete method, a number of bins of fixed particle diameter is prescribed, the population balance model computes the local size distribution between these bins. This approach has the advantage of having an easily retrievable size distribution, but possibly requires a large number of bins leading to steep computational demands. Since the bubble size distribution in a stirred tank is relatively narrow ($0.5\text{mm} - 16\text{mm}$ [37–39, 84]), the number of bins ($O(10)$) is manageable.

In the QMOM method, the moments of the size distribution are tracked. Typically $4-8$ moments suffice [81, 85], making the computational cost manageable. The Sauter mean bubble size, by definition, follows from the 3^{rd} and 2^{nd} moment as $d_b = m_3/m_2$; the size distribution on the other hand is not straightforwardly retrieved, since multiple distributions may fit the available set of moments. In this work, the discrete method was applied. Runs with the QMOM method yielded stability issues, and the relatively narrow size distribution does not make the use of the discrete method prohibitively expensive.

2.1.3. Modeling the impeller

In the presence of baffles, a moving wall approach cannot be used to model the impeller, and motion must be imposed otherwise. Early stirred tank simulations resorted to impeller boundary conditions derived from experimental data [86–89], limiting their predictive value; these are further omitted here. For fixed bodies with prescribed motion, the most suitable approach is to mesh *around* the solid body, and add forces to impose motion either at the impeller or in the surrounding domain. Such approaches include the multiple-reference frame model (MRF) [90], the sliding mesh model (SM) [91], the inner-outer model (IO) [92] and the computational snapshot model (CS) [93]. The MRF, IO and CS approach all fix the position of the impeller compared to the baffles, yielding a steady state solution valid for this particular position, whereas the impeller position varies in SM. In the CS approach, forces exerted by the impeller on the fluid are modeled. Both the IO and MRF method separate the mesh in two zones - rotating and stationary - with the Coriolis and centrifugal force imposed in the rotor-domain. In contrast to MRF, the zones overlap slightly in IO; the MRF has been favored in recent years and is frequently included in CFD packages. Using the absolute velocity formulation, the conservation of momentum in a moving reference frame becomes:

$$\frac{\partial}{\partial t}\rho\mathbf{u} + \nabla\cdot(\rho\mathbf{u_r}\mathbf{u}) + \rho[\mathbf{u}\times\omega] = -\nabla p + \nabla\cdot\overline{\overline{\boldsymbol{\tau}}} \tag{2.19}$$

2.2. Stirred tank CFD: literature study

Stirred tanks studies with various turbulence models, multiphase approaches and degrees of success have been conducted over the past $20+$ years. This section provides an overview of such studies, serving as a basis for the CFD modeling conducted within this work. Although some references to older work are made, the focus is on literature from the past 10 years. Furthermore, the focus is on Rushton turbines as they are most frequently used in this work. A wide body of literature regarding impellers designed for superior performance in specific situations (gassed blending, viscous blending, ...) exists, consult e.g. Gogate et al. [94] for a discussion of such systems.

2.2.1. Single phase flow

The impeller discharge stream Most hydrodynamic research in stirred tanks is focused on the impeller discharge stream and trailing vortices, being the regions where the hydrodynamic action happens. Several experimental studies quantified k_t and discharge stream velocities by Laser Doppler Anemometry (LDA) [34, 95–101] or Particle Image Velocimetry (PIV) [35, 102–108]. The dissipation rate ϵ is difficult to measure directly; some authors instead report integral length scales length-scale and compute ϵ on dimensional grounds as $\epsilon = A \cdot k_t^{3/2}/L_{res}$ with A some constant. Recent studies using both LDA and PIV were conducted with sufficient resolution to probe ϵ directly [35, 106, 107]. The results showed that the dimensional methods provided proper values further from the impeller, but underestimated ϵ close to the blade, where assumptions of the dimensional method break down [109].

Inter-impeller flow The flow in multi-impeller systems is strongly dependent on the inter-impeller clearance [110]. We focus on systems that exhibit parallel flow, meaning the individual impellers act as single impeller systems. The exact transition is geometry dependent, but parallel flow is typically ensured for $C/T > 0.5$ [110, 111]. We are particularly interested in the horizontal plane between the impellers which segregates the compartments. Here the flow is dominantly radial, and little axial mass exchange is expected by the mean convective flow. This presents a rate-limiting step in the mixing process, as can be concluded from the mixing times reported in section 2.2.2. Hydro-dynamically, this region is under-studied, being part of the relatively quiescent bulk region. In (PIV) studies where k and ϵ are reported for the whole tank cross-section, details of the inter-compartment plane typically drown in comparison to the peak values near the stirrer [112]. Micale et al. [113] showed sliding mesh and IO-impeller simulations could capture parallel, merging and divergent flow, but their very early simulations strongly underestimated k_t everywhere. At $0.18T$ from the impeller tip, their LDA results showed a small increase in k_t in the inter-compartment plane. Because of its importance in multi-impeller mixing behavior, this domain is the focus of our study.

Macro-instabilities Macro-instabilities (MIs) in stirred tanks have been extensively studied for single-phase, single-impeller geometries, both experimentally and numerically [109, 114, 115]. Nikiforaki et al. [116] suggested that for a fixed agitation rate and geometrical properties, jet instabilities or instabilities by precessing vortices are the dominant cause. An in-depth review and analysis by Paglianti et al. [117, 118] using pressure measurements suggests both phenomena occur in Rushton-stirred tanks, and relate to the Strouthal number $L_c f/V$, f a characteristic frequency. For jet instabilities, the discharge velocity scale $V = C \cdot N_s \cdot D \cdot F_Q$ with C a constant and

F_Q the pumping number is used, while length-scale $L_c = T$. Precessing vortices relate to the mean bulk velocity $V = 2F_Q \cdot N_s D^3/(\pi T^2)$ for a single Rushton impeller with a dual-loop flow structure. In both cases, f scales linear with agitation rate N_s, hence MIs are reported in f/N_s. Follow-up work with 2 impellers revealed a precessing vortex frequency of $f/N_s \approx 0.02$ and jet oscillation frequency of $f/N_s \approx 0.055$, measured in the discharge stream. Guillard et al. similarly identified instabilities with $f/N_s \approx 0.08 - 0.05$ above the top impeller by PLIF. [119, 120]

RANS modeling

The aforementioned impeller discharge profiles are frequently used to validate CFD studies. Nearly all such studies report good agreement with the mean discharge velocities [59, 92, 95, 121–124], while the turbulent kinetic energy k_t and dissipation rate ϵ yield less universal agreement. Brucato reported an underestimation of k_t using the standard $k - \epsilon$ (*SKE*) model, for both *IO* and *SM* impeller modeling. Jenne and Reuss [124] relied on experimental boundary conditions, but made a noteworthy contribution by comparing many $k - \epsilon$ formulations. They observed good performance with a modified Chen-Kim $k - \epsilon$ model and reasonable performance of the *SKE* model, while standard Chen-Kim and Renormalization group $k - \epsilon$ (*RNG-KE*) performed significantly worse. Gunyol and Mudde [59] found good agreement in k_t with the *SKE* and the realizable $k - \epsilon$ (*RKE*) while the results for Reynolds Stress model (*RSM*) were less satisfactory, and poor results were found for *RNG-KE*.

Some studies report an underestimation of ϵ of up to 50% [95, 96]; they all included the full $3D$ impeller geometry, including disc and blade thickness. This typically yields $1 - 3$ cells across the blade thickness, resulting in a poorly resolved flow around the blade. In contrast, studies using sheet bodies for the impeller and baffle do not observe a strong under-prediction of ϵ [59, 60, 62] although significant mesh densities (10^6+ cells for a single impeller and $360°$ domain) are required to yield mesh-independent ϵ profiles [62]. Both the *SKE* and *RKE* model yield good agreement with the dimensional assessment of ϵ by Wu and Patterson [59]. This is perhaps unsurprising, as the $k - \epsilon$ method is built largely on the same assumptions (isotropy and a single turbulent length-scale $L_{res} = Ak_t^{3/2}/\epsilon$). One sidenote is that Gunyol and Mudde [59] report instantaneous outflow profiles for a fixed impeller position using the MRF impeller modeling approach, while LDA data used for comparison is phase-averaged over all positions. Singh et al. [60] used SM impeller modeling, yielding phase-averaged results. Their results still show a decent agreement in k_t and ϵ further from the impeller for the *SKE* model, but the agreement breaks down near the blade, especially compared to direct ϵ measurements. This hints at a breakdown of the $k - \epsilon$ assumptions close to the impeller, and a consequent error in the prediction of trailing vortex behavior; a qualitative comparison of trailing vortex behavior by Singh et al. shows the $k - \epsilon$ model predicts short vortices trailing close to the shaft, whereas more elaborate models predict longer vortices bulging outward from the blade, more in line with experimental assessments [101, 103, 105].

LES

Revstedt et al. [125] used finite volume LES (FV-LES) with an implicit closure model and momentum source terms for impeller modeling. They found decent results for U and k_t in the bulk, with poorer agreement near the impeller, with $2.12 \cdot 10^5$ gridcells. Yeoh et al. [126, 127] (FV-LES, SGS ($C_S = 0.1$), $4.9 \cdot 10^5$ cells,sliding-deforming grid) and Zhang et al. [128] (FV-LES, SGS ($C_S = 0.1$), inner-outer impeller method, $1.7 \cdot 10^6$ cells) both found good results for U and k_t, none of them report on ϵ. A lattice-Boltzmann approach (LB-LES) has been frequently applied in LES studies [129]. Eggels applied the Smagorinsky (SGS) subgrid model with constant $C_S = 0.1$, combined with a force field method to include impeller motion. Aside from a local under-prediction of U_{ax}, overall good agreement in velocities was observed compared to experimental data. Derksen and van de Akker (SGS-model, $C_S = 0.12$) used a grid of $6 \cdot 10^6$ nodes [130]. The impeller discharge stream velocities, k_t, and trailing vortex behavior were accurately captured. The phase-averaged maximum energy dissipation in the impeller discharge stream was $\overline{\epsilon_{max}}/N_S^3 D^2 \approx 4.6$, over 50% lower than measured experimentally [35]. Hartmann et al. [109] observed that the Voke subgrid model predicted a higher eddy viscosity in the bulk regions than SGS; equal values were observed in the discharge stream. The velocities were well captured, while k_t was locally overestimated. Hartmann found Values of ϵ similar to Derksen and van den Akker [130], which is supported by Micheletti et al. [131] (SGS, ($C_S = 0.1$)) with finite-volume LES.

Delafosse et al. [132, 133] (sliding mesh, 10^6 cells, FV-LES, SGS model) were the first to note explicitly that setting $C_S = 0.1$ leads to a significant under-prediction of ϵ in the discharge stream. This value of C_S was selected after testing for a wide range of flows, with higher values of C_S leading to excessive turbulence dampening [63]. Still, Delafosse et al. observed good results with $C_S = 0.2$, without significantly affecting the predictions for velocity and k_t. Soos et al. [134] (sliding mesh, $1.6 \cdot 10^6$ cells) also used $C_S = 0.2$. Compared to the data of both Escudié and Liné [105], and Wu and Patterson [34], they report a mild under-prediction of the velocities and the periodic kinetic energy, while k_t was well predicted. The values for ϵ are in accordance with Delafosse et al.

The work of Delafosse et al. and Soos et al. indicates a case-by-case tuning of C_S may be required, which is undesirable from the perspective of predictive capabilities. Murthy and Joshi [97] used the dynamic kinetic energy subgrid model, which expands upon the dynamic Smagorinsky model by introducing a subgrid-kinetic energy transport equation (FV-LES, $1.3 \cdot 10^6$ cells, sliding mesh). They good results for the dissipation based power number Po_ϵ, but reported no profiles of ϵ or values of C_S were reported to judge why such good agreement was achieved. Jahoda et al. [65] applied the dynamic Smagorinsky model for mixing in 1 and 2 impeller geometries but did not report ϵ or Po_ϵ. They did show local values of C_S, which were in the range of $0.05 - 0.1$, below the default $C_S = 0.1$. A direct computation of C_S based on direct numerical simulation by Gillissen and van den Akker [64] yielded $C_S \approx 0.1$, in agreement with their own dynamic LES. This indicates that the proposed C_S tuning is not in accordance with physical observations, and the authors note that the under-prediction in ϵ may be the result of an under-predicted k_t production due to insufficient mesh resolution in the vicinity of walls.

DES

As noted by Gillissen [64], under-resolution of the wall-bound flow may be related to the observed under-prediction of ϵ in LES simulations, and may consequently affect micro-mixing behavior. Detached eddy simulations (DES) blend a LES approach in the free-stream with RANS in under-resolved (wall) regions, and may thereby reduce any dependence of the bulk flow on wall effects. Of course, the accuracy of the wall flow itself will still be limited, due to the inherent assumptions of the RANS methodology. Gimbun et al. [135] conducted Spalart-Allmaras-DES simulations in a Rushton-stirred tank, and extensively compared the results with both *SKE-RANS* and *FV-LES* (SGS, $C_S = 0.1$). The bulk velocity prediction was very similar between the models. DES generally yielded the best agreement with experimental k_t data of Derksen et al [101], predicting slightly higher values than *SKE* and LES. LES and DES were nearly equal in assessing the qualitative trailing vortex behavior, with the *SKE* model predicting significantly lower radial spreading of the vortex core, similar to the study of Singh et al. [60]. DES compared favorable to the other models in predicting velocities and k_t in the vortex core. Overall, DES outperformed RANS, and outperformed LES in regions where wall effects are significant.

Chara et al. [136] came to similar conclusions, observing good agreement in discharge velocities and trailing vortex behavior. They did note that the tangential spread of the trailing vortex is slightly narrower than experimental (PIV) results show. Lane [137] studied the energy dissipation behavior of various turbulence models with an A-310 impeller. A power recovery of 69% was observed, i.e. $P_{des} = \int(\mu + \mu_t)S_{ij}^2 dV$ is 69% of the power input. The DES-mesh contained $13.1 \cdot 10^6$ cells. For various SST and KE formulations, the energy recovery was $68-91\%$ and strongly mesh dependent, supporting the observations by Coroneo et al. [62]. The low energy recovery for DES, at the finest mesh used, does hint that the wall treatment of DES does not provide a significant improvement over LES in terms of resolving ϵ. Clearly, a comprehensive comparison of LES and DES with various levels of wall resolution, possibly supported by DNS, is required to provide further insight in the reported under-predictions of ϵ.

2.2.2. Single phase mixing

We report the 95% mixing time in dimensionless form; $\theta_{95} = N_s \cdot \tau_{95}$ with τ_{95} the mixing time in s and N_s the agitation rate in s^{-1}.

Mixing: definition Various not necessarily inter-comparable definitions of θ_{95} are used in literature. Frequently applied point-measurements ($0D$) typically establish τ_{95} as the time where the normalized tracer concentration $C_s/\overline{C_s}$ is between 0.95 and 1.05 ($\overline{C_s}$ the vessel average) [65, 138–144]. The local dynamics resolved by probes make them favorable for comparison with CFD, but individual point-probes might not represent mixing in the entire vessel properly. For multiple probes, θ_{95-MP} is the arithmetic average θ_{95} of the points [145, 146]. Probe based measurements are here referred to as: 0D-xP, X being the number of points.

Line ($1D$) methods were not encountered in literature for the studied setups. Plane laser induced fluorescence (P-LIF) measures mixing in a $2D$ cross-section [62]; every pixel can be regarded as a probe to calculate an arithmetic average, or mixing can be quantified by the coefficient of mixing (CoM) [147−149] (alternatively called Coefficient of Variation (CoV)), which is also applicable to $3D$ domains. This approach is especially suitable for CFD techniques. As meshes are typically non-uniform, volume-weighing should be applied in the determination of the CoM [149]:

$$CoM = \sqrt{\left(\frac{\Sigma_i \left(\frac{c_i - \bar{c}}{\bar{c}} \right)^2 \Delta V_i}{\Sigma_i \Delta V_i} \right)} \tag{2.20}$$

Kukukova et al. [147] set $CoM = 0.05$ as the 95% mixing limit, while Hartmann et al. [149] report $CoM = 0.0283$ being where 95% of the volume is 95% mixed, based on numerical experiments. We apply the limit of Hartmann, but do not consider either indicator to be superior provided consistency is applied. Studies which quantify mixing with the CoM are labeled $2D$-CoM or $3D$-CoM. For decolorization methods, the 95% mixing time was declared when 95% of the volume was decolored ($3D$-C) [150]. Lee et al. [151] suspended thermally sensitive liquid-crystal particles ($3D$-T) and applied a heat pulse, measuring θ_{95} when 95% of the particles had the same hue.

Single impeller mixing

Experimental: 1 impeller

Single-impeller mixing times from literature are reported in table 2.1. The mixing time correlation of Fasano et al. yields $\theta_{95} = 30.7$ for a single Rushton turbine, with $D = T/3,\ H = T$. The Ruszkowski-Grenville correlation, valid for various impeller types [152], predicts $\theta_{95} = 27.5$. Table 2.1 shows considerable spread in experimental measurements and CFD results (in part due to different mixing definitions), but overall $\theta_{95} \approx 30 - 40$, in agreement with the correlation estimates.

The 0-D measurements reasonably agree between studies, with Raghav Rao et al. [153] being a notable outlier. This may be a probe location issue, although Jahoda et al. [65] and Kukukova et al. [138] yield lower θ_{95} with similar placement. The thermal particle method of Lee [151] gives a significantly lower θ_{95}, while the colorization method of Moo-Young [150] is in agreement with $0D$ results. Lacking detailed information on the thermal sensitivity of the particles of Lee, it is difficult to judge the exact cause of their lower θ_{95}, but we expect it to be method-related.

Considering the CFD methods, LES methods typically agree with experimental data, albeit with significant spread. This may result from different quantification techniques: Jahoda et al. use a single probe, Yeoh et al. average a number of probes and Hartmann et al. use the 3D-CoM, which appears to yield a generally higher θ_{95}, possibly due to the inclusion poorly mixed regions (close to the walls) which are not sufficiently accounted for in $0D$ measurements.

The *SM-SKE* approach of Jahoda over-predicts θ_{95} compared to their measurements. Zadghaffari et al. do not explicitly quantify θ_{95} for their *SKE* simulation, but show similar results. In contrast, the *MRF-SKE* approach of Jahoda et al. and Kukukova et al. underestimates θ_{95} compared with their measurements. The experimental agreement in $0D$ measurements means this is unlikely to result from experimental flow disturbance by the probe. More likely, the mesh resolution was insufficient, or *MRF-SKE* is inherently unsuitable. Results by Coroneo et al. (different geometry: $D = T/3,\ C = T/2,\ H = T$) hint at the first option: both the quantitative mixing dynamics (2D-CoM, *MRF-SKE* and PLIF-experiment) and qualitative mixing dynamics (concentration snapshots) were in good agreement between simulation and experiment. However, a fine mesh ($\pm\ 2000k$ cells) was required, compared to much cruder domains used in earlier $RANS$ studies.

Jahoda et al. and Kukukova et al. evaluated mesh quality based on velocity profiles and torque-based power numbers (Po_τ), which are rather insensitive to mesh details [62]. Coroneo et al. found Po_ϵ to be a better indicator of mesh dependency. Javed et al. report surprising agreement between simulation and experiment at low mesh resolution. Inspection of their individual probe results reveals large local differences, yielding local under- and overestimates of θ_{95}, that average out overall.

2+ impellers

Because of the larger number of geometrical variations, we only report cases where both experimental and CFD data are available (table 2.2). All employed $0-D$ measurement techniques, typically using 1 probe per impeller compartment. All cases were top-injected, meaning the bottom probe yields the highest τ_{95}. In all cases, this value was reported.

2-impeller: Kukukova et al. [138] and Jahoda et al. [65] studied the same geometry, with $C/T = D/T = 1/3$ (table 2.2), but with slightly differing probe locations, explaining the different τ_{95}. Their LES simulations are in agreement with the probe dynamics, but the higher degree of experimental noise leads to a higher θ_{95} experimentally. Both *SM-SKE* and *MRF-SKE* over-estimate θ_{95}; the similar MRF assessment between Jahoda and Kukukova hints the probe location dependence is more significant experimentally than numerically.

Zadghaffari et al. reported good agreement for LES with their own experimental results in a geometry with $C = T/4$ and $D = T/2$. Oddly, they compared a $2D$ experiment with a $0D$ numerical measurement. Both Bujalski et al. and Jaworski et al. ($C = T/4$ and $D = T/2$) reported up to a factor 2 overestimation of θ_{95}, using *SM-SKE* and *MRF-SKE*. Both of these were very early studies with limited mesh resolution, which can explain part of the offset.

3+ impellers:

For 3 impellers (table 2.3), Mostek et al. [159] (*MRF-SKE*) report a 20% overestimation in θ_{95} compared to their measurement with $C = T/2$, which is a 40% over-estimation compared to measurements by Jahoda et al. [158] in the same geometry. Similar observations apply to $C = T/3$. With 4 impellers, Montante et al. require a strongly lower turbulent Schmidt number, $Sc_t = 0.1$ [160], to yield agreement with experiments. Delafosse et al. [112] required $Sc_t = 0.2$ rather than the default 0.7 for proper

Table 2.1: An overview of mixing times for a single impeller geometry ($D = T/3,\ C = T/3,\ H = T$): experimental ($t_{95}$).

Author	θ_{95}	Measure	Re	Method	Sc_t	Mesh	ref.
Kukukova et al.	33	0D-1P	46667	conductivity	–	–	[138]
Jahoda et al.	34	0D-1P	46667	conductivity	–	–	[65]
Lee et al.	21.6	2.5D-T	40000	thermal	–	–	[151]
Distelhoff et al	36	0D - 8P avg.	24000	LIF	–	–	[146]
Javed et al	32	0D - 32P	24000	LIF	–	–	[145]
Moo-Young et al.	36	3D-C	24000	decolorization	–	–	[150]
Raghav Rao et al.	48.2 $(avg.)$	0D-1P	> 100000	conductivity	–	–	[153]
Rewatkar et al.	39.5 $(avg.)$	0D-1P	> 200000	conductivity	–	–	[154]
Nere et al.	35.3	3D-MM	46722	$B.C.\ k-\epsilon$	?	?	[155]
Kukukova et al.	23.5	0D-P	46722	$MRF\ k-\epsilon$	0.7	$330k$	[138]
Jahoda et al.	13.5	0D-P	46722	$MRF\ k-\epsilon$	0.7	$615k$	[65]
Jahoda et al.	50	0D-P	46722	$SM\ k-\epsilon$	0.7	$615k$	[65]
Javed et al	27	0D - 32P	24000	$SM\ k-\epsilon$	0.7	$112k$	[145]
Zadghaffari et al	$40-80$	0D - 1P	41667	$SM\ LES$	0.7	$971k$	[156]
Jahoda et al.	26	0D-P	46722	$SM-LES$	0.7	$615k$	[65]
Yeoh et al.	33.2	0D-48+P	4000	$SM-LES$	0.7	$330k$	[127]
Hartmann et al.	$39.8-54.7$	3D-CoM	24000	$SM-LES$	0.7	$13824k$	[149]

Table 2.2: An overview of mixing results with 2 impeller geometries: CFD and experimental data. Unless otherwise stated, $D = T/3$ and $\Delta C = T$.

Author	$Geometry$	θ_{95}	Measure	Re	Method	Sc_t	Mesh	ref.
Kukukova et al.	$C = T/3$	104.5	0D-P	46722	conductivity	–	–	[138]
Kukukova et al.	$C = T/3$	113.5	0D-P	46722	$MRF\ k - \epsilon$	0.7	$286k$	[138]
Jahoda et al.	$C = T/3$	92	0D-P	46722	conductivity	0.7	–	[65]
Jahoda et al.	$C = T/3$	110	0D-P	46722	$MRF\ k - \epsilon$	0.7	$1230k$	[65]
Jahoda et al.	$C = T/3$	116	0D-P	46722	$SM\ k - \epsilon$	0.7	$1230k$	[65]
Jahoda et al.	$C = T/3$	81.5	0D-P	46722	$SM\ LES$	0.7	$1230k$	[65]
Jaworski et al.	$C = T/4,\ D = T/2$	46.6	0D-6P	162000	conductivity	–	–	[142, 143]
Jaworski et al.	$C = T/4,\ D = T/2$	48.9	0D-6P	216000	conductivity	–	–	[142, 143]
Jaworski et al.	$C = T/4,\ D = T/2$	137.5	0D-6P	162000	$SM\ k - \epsilon$	?	$70k/180^o$	[142, 143]
Jaworski et al.	$C = T/4,\ D = T/2$	125.2	0D-6P	216000	$SM\ k - \epsilon$	?	$70k/180^o$	[142, 143]
Jaworski et al.	$C = T/4,\ D = T/2$	140	0D-6P	324000	$SM\ k - \epsilon$	?	$70k/180^o$	[142, 143]
Bujalski et al.	$C = T/4,\ D = T/2$	176	0D-6P	216000	$MRF\ k - \epsilon$	?	$115k$	[139, 141]
Zadghaffari et al.	$C = 0.55T,\ \Delta C = 0.7T$	41.3	2D-A	37500	plif	–	–	[157]
Zadghaffari et al.	$C = 0.55T,\ \Delta C = 0.7T$	52.5	2D-A	50000	plif	–	–	[157]
Zadghaffari et al.	$C = 0.55T,\ \Delta C = 0.7T$	58.7	2D-A	66667	plif	–	–	[157]
Zadghaffari et al.	$C = 0.55T,\ \Delta C = 0.7T$	43.9	0D-P	37500	$SM\ LES$	0.7	$610k$	[157]
Zadghaffari et al.	$C = 0.55T,\ \Delta C = 0.7T$	54.5	0D-P	50000	$SM\ LES$	0.7	$610k$	[157]
Zadghaffari et al.	$C = 0.55T,\ \Delta C = 0.7T$	63.3	0D-P	66667	$SM\ LES$	0.7	$610k$	[157]

Table 2.3: An overview of mixing results for 3 and 4 impeller geometries. In all cases, $H = n \cdot T$ where n is the number of impellers, $\Delta C = T$ and $D = T/3$.

Author	$Geometry$	θ_{95}	Measure	Re	Method	Sc_t	Mesh	ref.
Jahoda et al.	$3\ Imp.,\ C = T/2$	197	0D-P	21000	conductivity	–	–	[158]
Jahoda et al.	$3\ Imp.,\ C = T/2$	186	0D-P	25210	conductivity	–	–	[158]
Jahoda et al.	$3\ Imp.,\ C = T/2$	212	0D-P	33610	conductivity	–	–	[158]
Jahoda et al.	$3\ Imp.,\ C = T/2$	210	0D-P	42015	conductivity	–	–	[158]
Jahoda et al.	$3\ Imp.,\ C = T/2$	204	0D-P	50415	conductivity	–	–	[158]
Mostek et al.	$3\ Imp.,\ C = T/2$	239	0D-P	46722	conductivity	–	–	[159]
Mostek et al.	$3\ Imp.,\ C = T/2$	286	0D-P	46722	$MRF\ k - \epsilon$	0.7	1537k	[159]
Mostek et al.	$3\ Imp.,\ C = T/3$	236	0D-P	46722	conductivity	–	–	[159]
Mostek et al.	$3\ Imp.,\ C = T/3$	273	0D-P	46722	$MRF\ k - \epsilon$	0.7	1537k	[159]
Jahoda et al.1994	$4\ Imp.,\ C = T/2$	400	0D-P	21000	conductivity	–	–	[158]
Jahoda et al.1994	$4\ Imp.,\ C = T/2$	387	0D-P	25210	conductivity	–	–	[158]
Jahoda et al.1994	$4\ Imp.,\ C = T/2$	392	0D-P	33610	conductivity	–	–	[158]
Jahoda et al.1994	$4\ Imp.,\ C = T/2$	405	0D-P	42015	conductivity	–	–	[158]
Jahoda et al.1994	$4\ Imp.,\ C = T/2$	402	0D-P	50415	conductivity	–	–	[158]
Montante et al.	$4\ Imp.,\ C = T/2$	461	0D-P	37500	conductivity	–	–	[160]
Mostek et al.	$4\ Imp.,\ C = T/2$	437	0D-P	46722	conductivity	–	–	[159]
Montante et al.	$4\ Imp.,\ C = T/2$	476	0D-P	37500	$SM\ k - \epsilon$	0.1	350k	[160]
Mostek et al.	$4\ Imp.,\ C = T/2$	466	0D-P	46722	$MRF\ k - \epsilon$	0.7	1984k	[159]
Mostek et al.	$4\ Imp.,\ C = T/3$	439	0D-P	46722	conductivity	–	–	[159]
Mostek et al.	$4\ Imp.,\ C = T/3$	477	0D-P	37500	$MRF\ k - \epsilon$	0.7	1984k	[159]

prediction of θ_{95} with two 4-blade impellers, as did Gunyol et al. [84] in a 4-impeller fermentor. Mostek et al. [159] found decent agreement in 4 impeller systems without any Sc_t compared to their experiments, but again Jahoda et al. [158] reported lower experimental θ_{95}. In the work of Mostek, increasing mesh density *increases* θ_{95}. This applies to 2, 3 and 4 impeller systems; the increase in with θ_{95} and mesh requirements that were reported for mesh-independent single-impeller results [62] hint that mesh-independence was not reached by Mostek et al., implying a significant over-estimation in θ_{95} when the mesh density is further increased. The decent agreement in θ_{95} observed for 3 and 4 impellers may be an incidental negation of an inherent over-estimation of θ_{95} by *MRF-SKE* by insufficient resolution, rather than inherently good model performance.

Single phase mixing: observations Significant spread is visible within the single-impeller mixing results, but no consistent over- or under-prediction of the θ_{95} by CFD simulations is observed. Coroneo et al. [62] show that, while requiring dense meshes, good qualitative (mixing motion contours) and quantitative (mixing time) agreement *can* be achieved with RANS methods. For multi-impeller simulations, the situation is very different: there are strong indications that the results of Mostek et al. [159] were not mesh independent, and that further refinement will lead to a significant over-estimation of θ_{95}. Several authors resort to ad-hoc tuning of the turbulent Schmidt number, $Sc_t = \nu_t/\mathcal{D}_t$ to $Sc_t = 0.1 - 0.2$ in order to repair this over-prediction [84, 112, 160], compromising the predictive value of their simulations. The default value of $Sc_t = 0.7$ is based on boundary layer studies [161].

We pose the hypothesis that the overestimation of θ_{95} is a consequence of the zero-shear layer in-between individual impeller compartments, that form for high inter-impeller spacing [110, 113]. As a result of Reynolds Averaging, there is no convective axial flow between the compartments, and all material exchange is governed by turbulent diffusion. Due to the zero-shear layer, we expect the turbulence intensity to be underestimated in this region, leading to an under-prediction of mass exchange. While the turbulent Schmidt number may vary in value depending on local flow features, it is more likely that values as low as 0.1 are used to patch inadequate turbulence predictions, as was observed in cross-flow jet spreading [161]. However, this tuning will affect mixing in *all* of the vessel, and the data of Coroneo et al. [62] shows no tuning is required *within* the individual impeller compartments. Improving agreement in the overall mixing time will hence lead to a poorer prediction of tracer dispersion in the bulk. In chapter 3 we explore the flow behavior in the inter-compartment plane to support our hypothesis of turbulence underestimation.

2.2.3. Gas-liquid flows

Multiphase flows are considerably more complex than single phase flows, both in their nature and in modeling. Several regimes are distinguished in stirred gas-liquid flow, classified based on the Froude number $Fr = N_s^2 D/g$ and gas flow number $Gs = Q_g/(N_s D^3)$ with Q_g the gas flow rate in m^3/s [33, 162]. For low Fr/high Gs, the impeller hardly influences bubble motion, inducing flooding. Increasing N_s or decreasing Q_g leads to the loading regime, wherein gas is partially dispersed, and a further increase of N_s/decrease of Q_g will lead to complete dispersion; the regime boundaries are geometry dependent. Gas accumulates in a low pressure zone behind the blade, which reduces the power transmission from the stirrer to the fluid [33, 163]. In the complete dispersion regime the accumulation is minor, leading to trailing or clinging cavities and a power drop sensitive to the cavity size [33]. When Q_g increases, a 3-3 structure with 3 major and 3 minor cavities may exist [162]. The power drop is significant for a Rushton turbine ($> 30\%$), but becomes less sensitive to a further increase in Q_g. Still, a power drop as large as 60% can occur at high Q_g [33]. When flooded, large ragged gas cavities occur, with power drop of around 50% for Rushton turbines. [33] Impellers that have been designed specifically for gassed operation may show significantly different power dynamics [164–168].

Deen et al. [36] used PIV to study the velocity field of both phases, observing an up to 50% reduction of the liquid radial velocity in the impeller discharge stream compared to single phase flow for a gas flow number $Gs = Q_g/N_sD^3 = 0.029$. Radial velocity fluctuations were enhanced under aerated conditions, with the highly turbulent zone being shifted upward in the axial direction; a clear effect of buoyancy on the discharge stream. The 36% power drop hints that sizable cavities had formed behind the blades, which causes the two distinct trailing vortices observed in single-phase flow to vanish. The gas flow will cause a reactor-scale circulation due to the buoyant gas dragging liquid up in regions of strong axial gas-flow. This additional circulation can affect the mixing times; Groen et al. [169] observed that in case of impeller flooding mixing is *more rapid* than in single phase flow; the reactor basically acts as a bubble column. In the $3-3$ cavity regime the mixing time was equal to a single phase case with the same power input, and in the clinging cavity regime, θ_{95} may be negatively affected by gas flow. The results of Groen have been widely confirmed [164, 170–174]. It is well known that for single-phase mixing θ_{95} reduces as a function of Re in the laminar/transitional regime, reaching a constant value under fully turbulent conditions. Under aerated conditions, for a given Q_g, the situation may be different: at low N_s, flooding leads to a low dimension-carrying mixing time τ_{95} (θ_{95} is an ill indicator here, since at very low N_s the vessel acts more as a bubble column). In the loading regime τ_{95} *increases* with Re and, as N_s increases too, θ_{95} increases strongly. When the 3-3 cavity regime is reached, the behavior is similar to single phase, and θ_{95} may increase again somewhat at very high stirring speeds, in the clinging cavity regime [172]. Oddly, Hadjiev et al. [175] reported an increase in θ_{95} with increasing Re even in single-phase flow, in a 3 L lab scale fermentor vessel. While they did observe an analogy between single- and multiphase mixing, these results are at odds with other mixing literature. Guillard [176] used the single-multiphase analogy to develop a model that favorably compared to experimental results in large-scale multi-impeller vessels.

Oxygen transfer from the gas to the liquid phase plays an important role in aerated fermentors; in large-scale vessels the availability of oxygen can be a limiting factor, leading to yield losses and unintended by-products. The overall rate of mass transfer depends on the bubble area concentration, a, and mass transfer coefficient, k_l. The individual contributions and local transfer rates are difficult to measure and experimental assessments frequently report equipment-integral k_La values, rather than the local mass transfer rate [177–184]. In stirred tanks, the specific power consumption and gas flow rate appear to have the biggest $k_L a$-influence [178], although impeller types and other process parameters may play some role, too. A systematic review of this literature is currently out of scope. Alves et al. showed that under mildly turbulent conditions, film diffusion limits interfacial mass transfer [185] and Higbie's penetration theory is valid to predict local mass-transfer [186]. Under highly turbulent conditions, better predictions follow from models based on Danckwerts surface renewal theory [61, 187] such as the eddy-cell model of Lamont and Scott [188].

The different flow regimes existing in gas-liquid stirred tanks pose additional modeling challenges; a robust CFD model should be able to predict the correct flow profile for a given Fr and Gs. Additionally, the fact that the bubble size information needs to be supplied in dispersed Euler-Euler simulations adds complexity. Experimental studies have determined typical bubble sizes in the range of $2-5$ mm in gas-water, lab scale tanks [37–39, 189]. Data on bubble sizes at the industrial scale is, however, scarce. The work of Hinze et al. [70] relates the maximum stable bubble size to a critical Weber number $We = \rho u^2 l/\gamma$, but the value of this critical number ranges widely between studies [190]. Add to this that in real fermentations parameters such as the effective viscosity and gas-liquid surface tension may deviate strongly from water (and over time), and it is clear that capturing multiphase behavior in 2-phase fermentors is far from a settled issue, both experimentally and numerically.

Euler-Euler gas-liquid modeling

Khopkar [191] studied the relative importance of several inter-phase forces in stirred vessel applications, concluding that the virtual mass force is not significant in the bulk of the vessel, and that the lift and Basset force are typically an order of magnitude smaller than the drag force. Hence, they recommended include only the drag force in CFD modeling. Scargiali et al. [192] reached similar conclusions considering lift, virtual mass and turbulent dispersion forces (the latter accounts for bubble re-distribution by turbulence). As noted before in this chapter, the interphase forces need to be closed with (empirical) closure relations. The frequently used Schiller and Naumann model [193] has been developed for a rigid particle in a stagnant liquid. In turbulent, bubbly flows shape deformation, swarm effects and drag modification by turbulence interaction play a significant role. The first two of these effects are especially significant in dense bubbly flows, and are, for example, included in the aforementioned Ishii-Zuber drag model applied in this study. Turbulence attenuation seems to be particularly prominent at lower gas fractions [84, 192, 194, 195]. Many CFD simulations, focusing on $\alpha < 5\%$ (for which most validation data is available), include some form of drag modification to account for the effect of turbulence. Bakker and van den Akker [196] employed a modified Reynolds number based on the bubble slip velocity and an effective viscosity $\mu_{eff} = \mu_l + C^* \rho_l k_t^2/\epsilon$. Brucato et al. [195] developed a drag correction by dropping solid particles through a turbulent Taylor-Couette flow, where they noted that the settling velocity reduced, i.e. C_D increased, yielding eq. 2.21:

$$\frac{C_D - C_{D,0}}{C_{D,0}} = K\left(d_p/\lambda_k\right)^3 \tag{2.21}$$

Here, λ_k is the Kolmogorov lengthscale. Lane et al. [197] applied the model of Brucato with a lower K to account for the different nature of bubbles. Khopkar [198] used the Brucato/Lane correction to compare CFD simulations (4 mm bubbles) with experimental Computer-automated radioactive particle tracking (CARPT) and computed tomography (CT) data in the flooding and 3-3 cavity regime. The radial and tangential velocity over the height of the domain were predicted reasonably well, with some over-estimation of $U_{rad,l}$ in the discharge stream. Gunyol et al. [84] noted that the Brucato/Lane correction improved agreement for low α, but led to strong over-estimations of α in high hold-up cases, using both Schiller-Naumann and Ishii-Zuber drag as a basis. Van den Akker [72] noted that the basis of Brucato's approach, using the ratio of the particle to Kolmogorov eddies, is questionable. Furthermore, specific aspects of the Taylor-Couette setup such as the presence of Taylor vortices were not accounted for. Using the relevant timescales as a basis for drag attenuation is instead recommended. Lane et al. [197] suggested a drag modification based on the ratio between the particle relaxation time and integral eddy timescale, τ_p/T_L. Drag is modified as $\overline{C_D}/C_{D,0} = (U_S/U_T)^{-2}$, where U_S/U_T follows from eq. 2.22:

$$\frac{U_S}{U_T} = 1 - 1.4\left(\frac{\tau_p}{T_L}\right)^{0.7} \exp\left(-0.6\frac{\tau_p}{T_L}\right) \tag{2.22}$$

Their model shows good agreement with terminal velocity datasets for bubbles and droplets in turbulent flow. Lane et al. combined their approach with a transport equation for the number density that allowed the local mean bubble diameter to vary (without requiring a full population balance approach), additional corrections for drag in very high holdups regions ($\alpha > 0.3$), and inclusion of liquid turbulence attenuation via the model of Sato et al. [199]. Their model well-predicted the bubble diameter and gas-holdup for several cases, although fitting to the data was required to find the model constants, and the combination of models makes it difficult to evaluate individual model contributions. Karimi et al. [200] compared the drag coefficient modifications of Lane, Bakker and Brucato (with Lane's value of K in eq. 2.21), and showed that all models work reasonably when α is low, while strongly overestimating α in high hold-up cases. The model of Lane performed best with a stable 20% α over-estimation compared to data of Newell [201, 202], while the Brucato model doubled α and introduced strong transient oscillations. Montante [203] et al. decided upon a more simple approach, prescribing a maximum terminal velocity of 0.12 m/s (considerably lower than the > 0.2 m/s in quiescent flow) rather than C_D, a method later adopted by Petitti et al. [85, 204] and Buffo et al. [82]. The axial and radial velocity were well predicted with this approach, although the gas hold-up was low ($< 2\%$), which makes the relevance for highly aerated systems questionable.

Balachandar and Eaton [194] note in a review on dispersed multiphase flows that turbulent drag attenuation has been observed to be both positive and negative, depending on the attenuation mechanism. Besides drag attenuation, continuous phase turbulence is attenuated by the presence of the dispersed entities. Balachandar and Eaton describe a strong dependence of turbulence attenuation on the particle Stokes number St, with maximum attenuation around $St = 50$. Further dependencies on Re

and the holdup α were observed, both towards dampening and augmentation. In any case, the effect of turbulence modulation is poorly understood, and rarely included in gas-liquid stirred tank simulations. Sliding mesh simulations conducted by Deen et al. [36] included turbulence modulation of the liquid phase using the model of Sato et al. [199]. The liquid velocities (mean and fluctuating) in the two phase simulation are in good agreement with their own experiments, the axial mean gas velocity is strongly over-predicted, while the fluctuating gas velocity is under-predicted. Unfortunately, no results without the Sato model are presented, making it difficult to assess the importance of including turbulence modulation. Assuming a mean bubble size of 4 mm, it is noted that the bubble deformation of the Ishii-Zuber drag model improves the agreement in axial velocity, although it is still far from perfect.

Population balance modeling

Early approaches aimed at including bubble size distributions assumed the bubble to reach a local mean equilibrium size, based on the local flow properties [197] this introduces global but not local size distributions at modest computational costs. Venneker et al. [205] were among the first to engage in population balance modeling of bubble distributions in stirred tanks, wherein bubble size is transported and does not need to be in equilibrium with local flow properties. They employed their own kernels and modeled aeration of a viscous 0.075 % Keltrol solution. The prediction of the gas holdup was promising. Chen et al. [206] employed a bin-based population balance model in a bubble column to test the influence of the number of size classes, yielding very similar results using 9 or 16 classes, with a distribution between $1 - 40$ mm. The comparatively narrow size distribution observed in gas-liquid flows means the class-based population balance approach does not seem to be prohibitive in terms of computation time, which is promising for simulations with large meshes.

Wang et al. noted that the energy constraint employed by Luo to guide break-up is unsatisfactory [78, 207]. Lehr et al. [80] replaced the energy constraint with a capillary pressure constraint, while Wang et al. [207] combined both approaches. Wang et al. [78] compared their own kernel to those of Lehr et al. [80], Luo and Svendsen [77] and Prince and Blanch [79]. The break-up rate of the Prince and Blanch kernel exceeded that of Lehr et al. and Wang et al. by approximately two orders of magnitude for a fixed energy dissipation rate; the model of Luo and Svendsen predicts higher breakup rates than Lehr et al. and Wang et al. for small bubbles ($d_b < 4$ mm), and significantly lower breakup rates for larger bubbles. The difference in break-up rates between the approaches shows why it is likely a bad idea to mix coalescence and break-up models; mixing models may easily lead to unrealistic size distributions. Wang et al. next compared the axial bubble size evolution in a bubble column. The model of Prince and Blanch under-predicts the bubble size; especially for high gas flow rates the distribution is too narrow, and the mean too small. The Kernel of Luo et al. yields a heavily skewed distribution with many small bubbles due to the high break-up rate at small sizes, and an unrealistically long tail in the large bubble region, due to the low break-up rate for large bubbles. In some cases, bi-modality is even observed. Both lehr et al. and Wang et al. show good agreement with experimental data; the model of Wang et al. better captures the axial evolution of their own data, while the model of Lehr et al. shows better agreement with distributions at different gas flow rates (data by Lehr et al.). In conclusion, the models of Lehr et al. and Wang et al. are preferred when it comes to predicting the size distribution (the Luo and Svendsen may still yield similar Sauter mean diameters, which in most CFD packages are used for $k_l a$ and interphase force calculations). Wang et al. furthermore showed their own model had the capability of predicting the transition of the homogeneous to the heterogeneous flow regime in a bubble column [208, 209]. However, only the Luo and Svendsen kernel is fully included in ANSYS FLUENT, currently.

Laakkonen et al. [210, 211] recognized that the integral terms in the break-up model of Wang et al. may be computationally prohibitive, and proposed a new kernel without such terms. Combined with a drag modification model based on a modified version of the Bakker-van den Akker approach, their CFD simulations reasonably well computed the gas hold-up (albeit with some over-estimation, on a crude grid) in a 14 and 200 L tank. Laakkonen et al. compared the predictions of their own model with the model of Lehr et al., and observed that the model of Lehr under-predicts bubble sizes in stirred tanks. Moilanen et al. [212] applied the method of Laakkonen to a shear-thinning, viscous xanthan fermentation with the drag model of Tzounakos et al. [213]. The gas hold-up was reasonably well predicted, the energy input heavily under-predicted, as was the $k_l a$ in all but the most viscous simulation. Mixing times were strongly over-estimated due to the formation of stagnant zones in the CFD simulations, showing that modeling of viscous fermentations requires significant improvement. Gimbun et al. [61] modeled the experiments of Laakkonen et al. [37, 38] using the QMOM population balance approach, employing the kernels of Prince and Blanch [79] and drag model of Ishii and Zuber [73]. The velocity profiles in their simulation were in decent accordance experiments by Deen et al. [36], agreeing well with experimental bubble sizes. For the $k_l a$, the eddy-cell model [188], taking ϵ into account, yielded better agreement than the penetration model [186], although the difference was small. Petitti et al. [85, 204] combined QMOM with the kernels of Laakkonen. They did note that parameter C_1 in these kernels may be scale-dependent, which could lead to unreliable results for different scales. Additional care was taken in stabilizing the moment equations, correcting for possible corruption of the moment set due to spatial discretization in the momentum transport equations. The terminal velocity approach of Montante was selected for drag modeling. Globally, the gas hold-up was slightly over-predicted, but never more than 20% . The accuracy of the bubble size prediction was found to depend on the value of C_1, which was fitted to the data. Buffo et al. [82] expanded the work of Petitti et al. to the multidimensional direct quadrature method of moments (DQMOM). In this approach, the distribution in velocity, size and composition can be tracked separately, while regular QMOM only accounts for size differences. As in the work of Petitti, good agreement with the data of Laakkonen was observed.

Kálal et al. [214] mixed the break-up model of Luo et al. and the coalescence model of Prince and Blanch, and used the terminal velocity of Montante et al. [203]. Despite the strongly different formulations, a reasonable agreement with data by Laakkonen was observed; high mesh resolutions ($2 \cdot 10^6$) were required for mesh-independence results. The authors noted significant formation of small bubbles, and recommended exploring different kernels. Montante et al. [215] used the same kernels (discrete method, 16 bins) and compared the CFD flowfields with their own PIV results. The velocity components were well predicted (based on two axial profiles), but the liquid phase velocity differed little from the predictions made with a mono-disperse bubble assumption. A larger difference with mono-disperse bubbles was registered for the gas phase velocity. The Sauter mean diameter poorly agreed with experimental data, but the number average was properly assessed. Liu et al. [216] simulated several values of N_s and Q_g with the same kernels (20 classes, $0.1 - 10$ mm), such that flooding, loading and dispersion were captured. The CFD model further used Schiller-Naumann drag and the added mass force. The overall hold-up reasonably reflected experimental CT data, but the strong radial hold-up variations could not be reproduced. Sarkar et al. [217] used the break-up and coalescence method of Luo and Svendsen in a 3-stirrer fermentor, observing good agreement with the experimental $k_l a$ using the Higbie penetration model.

Zhang et al. [218] combined the Eulerian multiphase model with a large eddy approach using a fixed bubble size and relatively crude mesh. This approach is questionable both due to the insufficient mesh resolution for proper mesh modeling, and because LES seems incompatible with the underlying assumptions of Euler-Euler modeling. Still, the results are better than for a RANS approach on the same grid in terms of gas-holdup; although locally strong deviations from the hold-up are found with either model.

Mixing in gas-liquid flows

Khopkar et al. [198] used Lagrangian particle tracking to compare circulation time distributions from their CFD simulations with CARPT data, observing generally good agreement with log-normal circulation behavior, with a slight skew to long circulation times for the CFD work. This could be a result of the tendency of particles to stick in low-turbulence zones when the dynamic random walk model is used to model turbulent dispersion of particles [21, 23, 219, 220]. They furthermore studied the influence of the gas flow regime in a multi-impeller system on the circulation time distribution. While there was no experimental circulation distribution data to compare in this case, the mean CFD circulation time τ_c was in good agreement with the experimentally determined mixing time, using the rule of thumb $\tau_{95} \approx 4\tau_c$. Jahoda et al. [221] studied mixing in a vessel with a single pitch blade impeller, for $Q_g = 1 - 7.5$ L/min and $N = 300$ RPM. The liquid velocity for $Q_g = 1$ L/min equaled that of single phase flow using MRF impeller modeling, while for SM the impeller discharge stream was clearly pushed upward. For $Q_g = 4$ L/min, the approaches gave similar results. In all cases, flooding was predicted by the CFD simulations (Schiller-Naumann drag, 4 mm bubbles). A variable level of agreement was observed for mixing. For $Q_g = 1$ L/min both methods under-predicted τ_{95}, while for $Q_g = 4$ L/min MRF over-predicted the τ_{95} and SM agreed with experiments. For $Q_g = 6 - 7.5$ L/min, both methods yielded decent results within the experimental margin of error, with SM predicting faster mixing than MRF. The applied strategy likely under-predicted the drag coefficient for low gassing rates (no correction was applied), leading to an untimely flooding transition. Under flooding conditions, both the mixing time and power drop were reasonably well predicted.

Multiphase stirred flows: observations

CFD simulations of multi-phase stirred flows have led to promising results, but there is still a clear gap in literature. The interaction between the two phases remains a complex modeling issue. It has been reasonably established that virtual mass, turbulent bubble dispersion, the lift force and the Basset force can be neglected, although for a more general conclusion this should be checked for a wider range of conditions. The interplay between turbulence and the dispersed phase has been poorly studied for stirred tank applications. Although it is well known that drag modification by turbulence is significant, it's effect on the macro-scale flow has only been included via empirical correlations with limited validity and questionable theoretical basis [72], or ad-hoc adjustment of the terminal velocity [203]. The development of a more robust approach to this issue is among the most urgent problems in multiphase modeling. Turbulence attenuation in the presence of a dispersed phase is a lively field of research [194], but the effect of this phenomena in dense bubbly flows in stirred tanks is poorly studied. Population balance modeling has improved the predictive capabilities of multi-phase simulations, still their application has been limited to relatively low gas hold-ups so far. Generally speaking, high hold-up ($5 - 20\%$) stirred tanks have been understudied, with and without population balances. Swarm effects and the effects of bubble deformation on the drag force have been included in some cases by using the drag model of Ishii and Zuber [73], but rarely so. For high-hold up simulations, these considerations seem to be essential [84]. Clearly, there is room for a thorough comparative study of gas-liquid stirred tank simulations, considering:

- The effect of different inter-phase forces, in combination with the population balance approach, on $u_l,\ u_g,\ k_t,\ \alpha,\ d_b$. Specifically, drag attenuation by turbulence at a range of gas fraction demands further study.
- The effect of liquid-phase turbulence attenuation
- The capability to predict flooding/loading/dispersion transitions
- The model performance for high gas hold-up cases

2.2.4. RANS modeling: Setup

Based on the above discussions, we have opted to model all internals as sheet bodies for better agreement in ϵ. The standard $k-\epsilon$ model was used for turbulence modeling due to decent agreement with flow and mixing literature [59, 62]. Later multi-impeller work showed that the realizable $k-\epsilon$ model yielded (somewhat) better predictions of θ_{95}, and this model is recommended for consideration in future work. In any case, θ_{95} in multi-impeller vessels is still over-predicted for single phase flows (chapter 3), and the turbulent Schmidt number was evaluated case-by-case for the fermentor modeling conducted in this thesis. In multi-impeller simulations the MRF and sliding mesh model yield comparable mixing behavior (chapter 3); in terms of computational demand, the MRF model is strongly preferred and hence applied for fermentor modeling.

The multi-phase simulations conducted in chapter 5 consider high-holdup cases. The Ishii-Zuber drag law (implemented in FLUENT as Universal Drag) was selected to account for deformation and swarm effects, no turbulent drag modification was required at high gas-holdup values [84], and no additional inter-phase forces were applied [192, 198]. The coalescence and break-up model of Luo and Svendsen [77] were used in population balance modeling due to their default availability in ANSYS FLUENT. In this work the mean diameter is of greater importance, and the Luo/Svendsen model appears to predict this reasonably. Still, for future work, implementation and consideration of other models is recommended to yield better agreement in size distributions [78]. UDF implementations of the Laakkonen and Lehr coalescence kernels were attempted, but they proved numerically unstable, and solving these issues was not considered to be within the scope of this project. The relatively low number of bins (max. 16) made computational demands of the discrete approach manageable; this approach showed better computational stability. Expansion of the bubbles due to the hydro-static pressure was not accounted for in this work. To calculate the $k_l a$, the eddy-cell approach of Lamont and Scott was used [188], based on the results of Gimbun et al. [61].

2.3. Biological modeling

In this work, reaction dynamics for two different organisms have been coupled to CFD simulations of fermentors. The metabolic modeling part of the Hé-project is conducted by a team from East China University of Science and Technology, and biological modeling in itself not the focus of the current thesis. Still, the application of metabolic models (*S. cerevisiae* and *P. chrysogenum*) in CFD simulations means some background on the metabolic features is required for analysis and discussion.In this section, a brief overview of the key metabolic features is provided for both organisms, combined with some typical industrial practices.

The coupling of chemical reactions to CFD simulations has been frequently conducted. Biological reactions are often modeled with unstructured, hyperbolic Monod kinetics [222] for biomass specific substrate uptake:

$$q_s = q_{s,max} \cdot \frac{C_s}{K_s + C_s} \text{ (mol/g}_{dw}\text{/h)} \tag{2.23}$$

Here, $q_{s,max}$ is the transport capacity, and K_s the substrate affinity; the values vary strongly between different transport mechanisms and hence between organisms. While it is often assumed in practice that both parameters are constant for a given organism, this may not be the case [223]. Organisms may have the capacity to synthesize several transporters with different affinities, the expression of which may depend on the extra-cellular conditions. Hence, the observed affinity may depend on the conditions [224, 225], and q_s may be the result of multiple transporters acting in parallel. The transport capacity may similarly vary; *P. chrysogenum* experiments conducted within the scope of this project [226] indicate that $q_{s,max}$ is reduced at low biomass specific growth rates (μ), hinting at a lower availability of transporters. Postma et al. [227, 228], reported strong deviations from Monod kinetics for *S. cerevisiae* at different steady states, hinting at the presence of 2 transporters, with the amount of each transporter depending on μ. Experiments by De Jonge et al. [44] for *P. chrysogenum* and Suarez-Mendez et al. [45] for *S. cerevisiae* reveal that Monod kinetics do properly model the substrate uptake rate in feast-famine cycles, c.q. at a timescale of minutes. This agrees with the notion that transporter adaptation occurs by controlling the synthesis rate of transporter enzymes, a process taking place at hour timescales. For simulated flowtimes of < 1 h, the kinetic parameters can typically be assumed constant. However, the dependence of the kinetic parameters on the reaction conditions means that literature values for $q_{s,max}$ and K_s can not be used straightforwardly; the reported values may not be representative for the simulated conditions. Lacking a better alternative, in this work values of $q_{s,max}$ and K_s from literature are used when using Monod kinetics, with the notion that these may be acquired under unrepresentative conditions. When a structured metabolic model is used (chapter 7), $q_{s,max}$ varies depending on conditions.

2.3.1. Penicillium chrysogenum

Penicillium Chrysogenum is a fungus (eukaryote) known for its capability to produce $\beta - lactam$ antibiotics, including *penicillin-G* (Pen-G). In this project strain DS17690, a high *pen-G* producer, is applied.

The penicillin production pathway Penicillin in produced by condensing amino acids α-aminoadipate (AAA), L-cysteine (CYS) and L-valine (VAL) to form a backbone, followed by enzymatic ring closure at the sulfur atom, and exchange of the AAA section for phenylacetic acid (PAA) [229]. The total synthesis pathway is presented in figure 2.1. The amino acids AAA, CYS and VAL are synthesized in abundance; external addition of AAA had no positive effect on penicillin production [229]. The backbone is formed when the three acids are condensed to α-aminoadipyl-L-cysteinyl-D-valine (ACV) by the enzyme ACVS, consuming ATP. ACV is transferred to IPNS, where it is oxidized to isopenicillin-N (IPN). IPN is transported to the peroxisomes where the enzyme *AT* is located. This enzyme has multiple functions; The high-affinity route is the 'IAT' route: AAA is exchanged for Coenzyme-A (CoA) activated PAA, producing Pen-G and releasing the CoA [230]. Alternatively, when PAA is absent the IAH route is taken: IPN is converted to 6-aminopenicillanic acid (6-APA) by releasing AAA. 6-APA reacts to 8-HPA under addition of CO_2. PAA-CoA can still be added to 6-APA by the AAT functionality of the AT enzyme; the IAH-AAT route also contributes to Pen-G formation. The PAA used in the above reactions has to be supplied externally. It has been shown that uptake of PAA occurs through passive diffusion of the non-dissociated acid [229, 231]. However, an active (ATP driven) exporter of PAA is also present, resulting in a so-called 'futile cycle' of PAA in- and export, consuming a considerable amount of ATP [231, 232].

It has been shown that, under regular glucose-limited conditions, ACVS controls 94% of the flux through the penicillin biosynthesis pathway, and that this enzyme's activity degenerates over the period of cultivation [229, 230]. Van Gulik et al. reported that the central carbon metabolism is not limiting for penicillin production, but NADPH availability was limited when an increased NADPH demand was imposed by changing carbon/nitrogen substrate [233]. Nasution et al. [234] reported an influence of cysteine supply on the penicillin production rate, attributed to the NADPH demand in

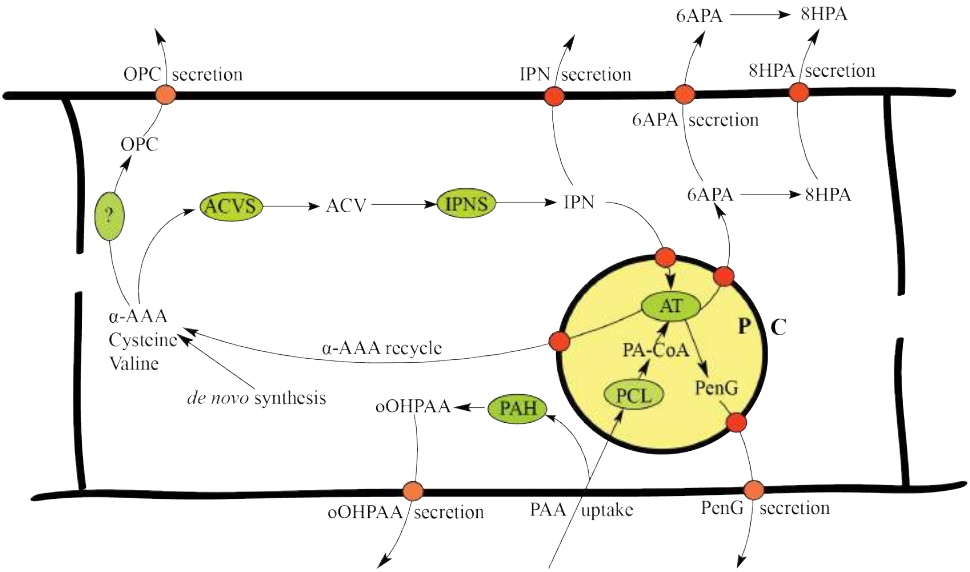

Figure 2.1: Synthesis pathway of *Penicillin-G* in *P. chrysogenum* (reproduced from [229] with permission).

cysteine synthesis. A high q_p furthermore correlated with high ATP levels. Kleijn et al. [235] observed a strongly increased flux through the pentose phosphate pathway to fulfill the increased NADPH demand. Douma et al. [236] formulated a model (the dynamic gene regulation model, DRW) describing the dependence of the biomass specific penicillin production rate q_p, on μ and the extra-cellular substrate concentration C_s; q_p was found to be suppressed by substrate excess conditions. De Jonge et al. [44] imposed 6 min feast-famine cycles, with the same time averaged $\overline{C_s}$ as a steady state chemostat. This reduced q_p by approximately a factor 2, but also reduced degradation in q_p over time.

From the production pathway it is clear that a lack of PAA will drive the pathway fluxes away from Pen-G, towards 6-APA and IPN as the main end products [229]. The total production of $\beta-$lactams (which includes both these compounds and Pen-G) was 50% of the normal production under PAA starvation conditions. After a step supply of PAA, the PenG production rate briefly exceeds the regular pathway flux, consuming stored IPN and 6-APA. As a result, the oxygen uptake rate peaked as well. The rapid response shows all relevant enzymes were expressed already, despite PAA absence. In this case, the activity of AT was rate limiting [229, 230].

Oxygen dependency of P. chrysogenum In lab-scale fermentations the dissolved oxygen concentration DO is typically saturated, however, in industrial fermentations oxygen transfer may be limiting. Oxygen is required for the conversion from ACV to IPN and oxygen starvation therefore limits IPNS activity; de Noronha Pissara et al. assumed a first order activity of IPNS for $DO < 70\ \%$ [237], which is supported by Bainbridge et al. [238]. According to the model of de Noronha Pissara et al. for penicillin-V production, IPNS was found to be rate limiting at low DO, while for $DO > 50\%$ control shifted to ACVS. Although both the strain and product are different, this is consistent with the observations of Deshmukh et al. that ACVS is limiting when oxygen is abundant [229]. It also indicates that a metabolic model for industrial penicillin fermentation should include a shift in pathway control if oxygen is considered; over the course of a fed-batch process the oxygen demand will increase due to an increase in biomass concentration, while the associated increase in rheology will reduce oxygen transfer. Most oxygen will be required by the central metabolism, hence lack of oxygen may reduce the energy availability, introducing significant stress on the cell. The effect of oxygen starvation was studied by Enfors and Larsson [239, 240] using a scale-down simulator. They revealed that $< 2\text{min}$ of oxygen limitation has no irreversible effect, but a first-order irreversible decrease in respiration capacity is observed for longer starvation periods. Although the circulation time in large fermentors is typically below $2\ \text{min}$, individual organisms may occasionally reside in oxygen-limited regions of the reactor for such periods. McIntyre et al. [241] commented that oxygen starvation (like carbon starvation) may result in cell autolysis. Their study furthermore revealed some ethanol production, indicating that *P. Chrysogenum* has some capacity to consume substrate under oxygen starvation conditions [241]. No data regarding effects on q_p is reported. Vardar and Lilly [54] cycled DO-levels in a 7 liter fermentor and observed a steep decrease in penicillin formation for a DO $< 30\%$ and an irreversible impairment in production below 10%, an observation supported by Henriksen et al. [242]. Surprisingly, the oxygen uptake itself was affected significantly only at a DOT of 7%. They used the Pen-V producing strain *P1*. Cycling the DO concentration around $30 \pm 7\%$ with a period of 2min showed the same reduced production (with a steady flux) as a constant 26% DO, possibly due to differences in dynamics between inhibition and release from inhibition. Whether similar effects occur in the DS17690 strain for *Pen-G* production is currently not known, nor are there any metabolic models available that include the effect of oxygen limitations on μ, q_s and q_p. In any case, the effects of oxygen starvation on the intra-cellular state, which is a prerequisite for comprehensive metabolic modeling, are poorly known and require additional attention.

Morphological effects The mycelial nature of *P. chrysogenum* gives rise to the complex rheology of penicillin broths [243–245]. Cells may tangle to form pellets, which lead to comparatively low viscosities [246]; within the pellets the (near) absence of convective transport may lead to local substrate- and oxygen limitations [247], however. It is therefore preferential to conduct industrial fermentation with dispersed or clumped cells [246, 248], even though this may complicate the rheology. Smith et al. [249] report that the use of very high agitation rates reduces the mean hyphal length and penicillin production rate, which indicates that (on the lab scale) the loss of production due to shear damage outweighs the improved oxygen transfer. They found the decrease correlated not just with power input, but also the circulation rate. These observations were further developed by Jüsten et al. into the *Eddy Dissipation Circulation Function* (EDCF) concept, posing that the product of the energy dissipation rate (causing shear damage) and the frequency of exposure to high-dissipation conditions correlates well with the mean hyphal length [250, 251].

Structured metabolic model for penicillin production

Previous models for penicillin production were often mechanistic and acted at the reactor scale. These models may include several of the observations outlined above, including substrate repression, oxygen limitation [252–254], pH, temperature, power input [253, 254], morphology and rheology [254]. These models, however, do not take the intra-cellular environment and reactor heterogeneity into account, making them unsuitable for CFD coupling and scale-down simulator design.

One of the aims of the Hé project is to develop a structured metabolic model for penicillin production, relating the production rate to the intracellular state of the cell. To allow coupling of metabolic models and CFD simulations, compact models of O(10) equations are highly desired from the perspective of computation speed and memory requirements. These are a far cry from full-scale models such as those published by Agren et al. [22]. Nikerel et al. [255] discuss how the use of pseudo-equilibrium and quasi-steady state assumptions, lumping of similar metabolites and removal of insignificant byproducts can be used to reduce a model of 155 metabolites and 156 reactions [233] to 52 metabolites with 48 rates, while maintaining the essential metabolic responses. The metabolic response model of Nikerel et al. [255], combined with the work gene regulation model of Douma et al. [236], the production pathway study of Deshmukh et al. [229] and the substrate oscillation study of De Jonge et al. [44], forms the basis of the metabolic model developed by the ECUST team in the scope of this project.

Compared to the model of Nikerel, the number of equations in this metabolic model is further reduced, and some enzyme pools have been introduced in order to assess performance at the timescale of hours. Currently, the model includes 5 metabolite and 4 enzymes pools. The most significant effects that are captured with the current model are:

- The effect of PAA on the metabolism. Although PAA limitation is not expected on the large scale, futile cycling of PAA costs a significant amount of ATP.
- Storage/release kinetics: excess substrate is stored as trehalose at times of substrate excess, and is released back to the glycolytic pathway under substrate starvation conditions.
- Penicillin production dependency on μ and glycolytic intermediates; q_p controlled by the amount of available enzyme, the enzyme dynamics are governed by the DRW model of Douma, but with intracellular glycolytic intermediates assuming control instead of extra-cellular substrate.
- Intracellular carbon pools (amino acid, glycolytic intermediates) and ATP influence the growth rate.
- The availability of substrate transporter enzymes is dynamic, and relates to the growth rate. This implies that $q_{s,max}$ in the Monod uptake model is dynamic on long timescales, while at short times Monod kinetics are retrieved.

A full description of the model can be found in *appendix A*. Further model extensions may consider oxygen starvation and shear effects. Currently, these phenomena are insufficiently quantified for the current strain to be included in a structured, dynamic model at the cellular level; investigations into shear and oxygen starvation effects are conducted at ECUST within the scope of this project. As noted earlier, the current model has 4 enzyme pools in total, which can be assumed to be in quasi-steady state within the timespan of several mixing times, although they may vary strongly over the process timescale, and their level may be heterogeneous within the population. Assuming the enzyme level to be in steady-state when simulating mixing timescales reduces the computational load; this does mean that the value of these parameters under fluctuating conditions needs to be estimated a-priori, or assessed iteratively.

2.3.2. Saccharomyces cerevisiae

Saccharomyces cerevisiae, colloquially known as baker's yeast, is one of the workhorses of the biotechnology industry, used in baking and brewing, but also as model organism in biological research. In contrast to the *P. chrysogenum*, the cells are typically smooth ovoids, giving rise to low viscosity broths that behave in a reasonably Newtonian fashion. Strain $CBS8066$ is used in this project.

S. cerevisiae can be grown both aerobically and anaerobically. Anaerobic fermentation typically has to goal of ethanol production; in absence of oxygen, glucose substrate is metabolized to form 2 pyruvate, which is turned into 2 ethanol $+ 2\ CO_2$. The net production of ATP under anaerobic conditions is 2 ATP/glucose; the low energy gain of anaerobic growth leads to a low growth rate [256]. Under aerobic conditions, glucose is metabolized in the Krebs cycle which has a yield of 32 ATP/glucose in case the substrate is completely combusted, leading to much higher growth rates; the objective of aerated yeast processes is typically to produce large amounts of biomass. The product may either be the yeast itself (for backing applications), or yeast extracts (used as taste enhancers).

The Crabtree effect Aiming at the production of biomass, it is desirable to avoid production of ethanol in aerobic yeast processes, meaning that (local) deficiencies in dissolved oxygen are to be avoided. However, ethanol production can also occur under glucose excess conditions, even if high levels of dissolved oxygen are available, called the Crabtree effect [257]. Publications often discriminate between a short-term and long-term Crabtree effect; the short-term effect is more interesting from the point of view of the dynamic environment in industrial bioreactors. Initially, the effect was often regarded as resulting from a saturated oxygen uptake capacity, but later reports showed that the rate limitations instead occur in the capacity to oxidize pyruvate to acetyl-CoA [258, 259], rather than oxygen availability itself. The oxidation of pyruvate to acetyl-CoA can occur directly, by action of pyruvate dehydrogenase, or via a bypass route which utilizes pyruvate reduction to acetaldehyde via pyruvate decarboxylase; a notable difference between Crabtree-positive and negative yeast is the higher level of this enzyme in the former [260]. The pyruvate affinity of the first route is much higher [261], and at low dilution rates the direct route is dominant; at higher dilution rates the contribution of the bypass becomes significant [258]. In the bypass route, acetaldehyde is converted to acetate and then acetyl-CoA. Alternatively, acetaldehyde can be metabolized to ethanol, but the affinity of this route is much lower [262]. Taken together, these observations lead to the hypothesis that the Crabtree effect sets in when the pyruvate to acetyl-CoA bypass saturates, driving the conversion of acetaldehyde to ethanol [228, 262, 263]. The production of ethanol is paired with significant excretion of acetate. Verduyn et al. [257, 264] reported measurable quantities of ethanol within 2 minutes after a glucose pulse, showing that the Crabtree-effect is metabolically controlled. Kresnowati et al. [265] showed a peak in the intracellular pyruvate level around $5 - 10$ s after a glucose pulse, for strain CEN.PK 113-7D, supporting a rapid intracellular response.

In pulse studies a large amount of substrate is introduced instantaneously, leading to strong excess and making it difficult to comment on the exact conditions at which the Crabtree effect sets in. Studies which explicitly considered the onset were conducted in steady-state chemostats. The exact onset of the Crabtree effect depends on the applied strain, but several studies report the onset to occur at dilution rates of $D_r = 0.35 - 0.4$ h^{-1}, with $D_{r,crit} = 0.38 - 0.39$ h^{-1} reported for *S. cerevisiae* CBS8066 [227]. Postma et al. [227] reported a residual substrate concentration *independent* of the dilution rate for a series of steady-state chemostats with $D_r < D_{r,crit}$, which means that substrate uptake does not follow Monod kinetics at long timescales. A strong elevation in residual glucose concentration was observed when $D_r > D_{r,crit}$ Postma et al. attribute this uptake behavior to the presence of 2 transporters with different affinities, the total capacity of which varies with the dilution rate. The above considerations make it challenging to introduce the Crabtree effect into an unstructured metabolic framework, as is required for more traditional CFD simulations. The observations of Postma et al. reveal that the onset of the ethanol production links to the growth rate μ, which in turn can be related to the substrate uptake rate q_s. Using Monod kinetics to determined q_s based on C_s will introduce errors, however, as $q_{s,max}$ and K_s vary depending on the growth rate. The value of the kinetic parameters can be estimated under steady-state conditions, but it is unknown whether these agree with the statistical steady-state values under highly dynamic conditions. Correct inclusion of the substrate uptake rate within structured metabolic models will be challenging, as the adaptation of the capacity of the different transporters still needs to be predicted based on the extra-cellular environment. The pyruvate node is a logical basis for a simple metabolic model; based on the above observations inclusion of acetadelhyde is also recommended.

More recent work focused on further quantification of the intra-cellular environment after the admission of a glucose pulse. Wu et al. [266] report a highly increased substrate uptake after the pulse, directly followed by a dip - possibly caused by $G6P$ inhibition, reaching a minimum at $t = 50$ s, and leveling off at a somewhat higher level over the next 100 s. A 50 s time-lag followed by a 100 s transient is seen in the ethanol production. During the first phase, acetate production increases, indicating that acetaldehyde is first driven towards acetate, and ethanol production only sets in once this route is saturated. Importantly, the response timescales are relatively close to the circulation time of a large fermentor, which means the extra- and intra-cellular environment in such reactors will almost certainly be out-of-equilibrium locally. The consequence may be that ethanol formation is suppressed due to the brevity of exposures to excess conditions, or that ethanol formation may be continuously active to some extent.

Suarez-Mendez et al. [45] reported a consistent reduction in the pyruvate level in scale-down experiments compared to steady state conditions, although their oscillations were of insufficient amplitude to invoke a Crabtree response. Still, these extra-cellular variations could change the ratio of substrate pushed through the bypass route, possibly affecting the biomass yield on substrate. Experiments with successive rapid oscillations of sufficient amplitude are required to provide additional information. In the experiments of Wu, the pyruvate pool follows the dynamics of q_s: a strong peak, followed by a dip, and gradual settling; the settling concentration exceeds the level prior to the pulse by a factor 2. Kresnowati et al. [267] focused on transcriptome dynamics, but also included several metabolic pools. A rapid drop in ATP as well as the total AXP was observed immediately following the pulse. The NADH/NAD ratio peaked immediately, all studied glycolytic and TCA intermediates responded with short lag times (< 100 s), in accordance with the observations of Wu et al.

In the large-scale experiments conducted at the former Statoil plant in Stavanger (Norway), ethanol was measured to be present during the exponential growth phase of the fermentation [16]. The presence of a glucose gradient during later stages implies that there may still be zones in the reactor where glucose excess occurs. Noorman [15] reports that the respiration quotient (RQ) in the bottom of the reactor was below 1, which hints at co-consumption of ethanol and glucose in this region of the reactor. In the bulk of the vessel, $RQ \approx 1$, indicating solely glucose consumption. While no quantifications are made, the data indicates that despite low ethanol levels overall, there may be some local production and re-consumption due to the large-scale glucose gradient.

Current models for S. cerevisiae Several models for S. cerevisiae have been developed previously. Lapin et al. coupled a model for anaerobic fermentation to Euler-Lagrange CFD [21]. Aerobic models are more rare. Sonnleitner and Käppeli [268] assumed oxygen limitations caused the onset of Crabtree fermentation. Pham et al. [42] proposed a model in which the oxidative and total substrate fluxes are separately calculated, and $q_{ferm} = q_s - q_{ox}$. A Monod model is used to determine q_s, ethanol re-assimilation is included in parallel to glucose uptake. The model was capable of correctly assessing the dynamics of C_x, C_s, C_e and q_{o2} in a fed batch fermentation, and an oscillating feed experiment with an oscillation period of 0.5 h. The model does not consider the intra-cellular environment, limiting its applicability for metabolic coupling to CFD simulations. Lei et al. [263] proposed an intracellular model including pyruvate, acetaldehyde and acetate, based on the bypass saturation hypothesis of Postma et al. [228]. The presence of two substrate uptake systems was taken into account (albeit with fixed $q_{s,max}$), with an extra acetaldehyde-based term to include the rapid rise in q_s under Crabtree conditions. The level of acetaldehyde was used to control the Crabtree onset. The model compared favorably with the data of Postma et al. [227] for steady state chemostats, although the presence of acetate and acetaldehyde at high dilution rates was overestimated. In a dynamic batch simulation, the agreement is mostly qualitative, with a strong over-prediction for the pyruvate and under-prediction for the acetate pool. Similar qualitatively correct, but quantitatively incorrect tendencies were observed for fed-batch, glucose pulse and dilution rate-shift experiments. While intracellular in its basis, equilibrium between the intra- and extra-cellular domain was assumed, and all balance equations are written in extracellular form; this makes the model as published unsuitable to study heterogeneity at the metabolic timescale. Rizzi et al. [269] proposed an elaborate model of the glycolytic pathway, and studied short-timescale dynamics. They found satisfactory results for the production of several components, including excreted acetate, ethanol and intra-cellular G6P, F6P, FBP, GAP and PEP. The pyruvate pool was strongly over-estimated after the pulse, as was ADP while NADH was under-estimated. The over-estimation of pyruvate was attributed to an incomplete understanding of the pyruvate decarboxylase enzyme. The model of Rizzi et al. [269] provides a step towards a dynamic metabolic model suitable for CFD coupling, although it is desired that the number of model equations is further reduced and the model performance is more widely checked. The availability of intra-cellular response data to glucose pulses should facilitate the development of such a model in the future.

3

Mixing in multi-impeller reactors

Stirred industrial fermentors frequently contain multiple impellers. For accurate assessment of extra-cellular gradients in these fermentors, the mixing behavior in such vessels must be accurately captured. A review of literature reveals that RANS models currently perform poorly in this respect, even for the comparatively simple case of single-phase, Newtonian flow. Compartment formation around the individual impellers is often observed in multi-impeller vessels, especially in the case of radial mixers and high inter-impeller clearance. Since mixing in single-impeller systems is reasonably captured by RANS models, our hypothesis is that the interaction between these compartments is not adequately captured in multi-impeller RANS simulations.

In this chapter, we use a combination of experimental LDA data, RANS simulations and large eddy simulations to assess the role of turbulence and macro-instabilities in the exchange of fluid between the compartments formed around individual impellers, in a single-phase mixing process with two Rushton turbines. LDA results confirm the presence of macro-instabilities (MIs), which locally account for up to half of the fluctuating kinetic energy. While unsteady sliding mesh simulations do capture the influence of a macro-instability on mixing between the compartments to a reasonable degree, they under-estimate the production of turbulence in the region of convergent flow between the impellers, which leads to a mixing time over-estimation of approx. 17%*. By virtue of their steady state nature, multiple reference frame simulations do not capture the effect of the macro-instability , nor do they correctly assess the turbulent kinetic energy. The combined effect leads to over-estimations in the mixing time of up to* 100% *depending on the used turbulence model and mesh density. Furthermore, variation in the predicted flow-pattern between the meshes led to deviations from typical mesh-dependence behavior, which reduces reliability. Large eddy simulations, even at very crude meshes, performed significantly better in assessing the mixing dynamics in two-impeller stirred vessels, although the frequency of the experimentally observed macro-instability was not fully reproduced, and the energy dissipation rate* ϵ *was poorly assessed.*

3.1. Introduction

CFD simulations offer a relatively cheap and fast approach towards evaluating the mixing performance of a range of impeller configurations, without requiring a lengthy experimental campaign. This of course requires that CFD simulations sufficiently capture the true mixing behavior, which gave rise to a significant body of validation literature. A review of literature focusing on single phase flows with Rushton turbines (chapter 2, section 2.2) shows that Reynolds Averaged Navier Stokes (RANS) simulations yield decent results for single-impeller geometries [62], but appear to consistently overestimate mixing times in multi-impeller geometries [65, 138, 159, 160]; this over-estimation may hold for other impeller types at large spacing [160]. LES simulations appear to adequately capture mixing behavior, but the required computation time prohibits routine application.

We assess this overestimation of the mixing time in Rushton-stirred tanks with large impeller spacing by RANS simulations. Our original hypothesis was that of RANS simulations under-estimating μ_t in the horizontal plane segregating the compartments formed around the individual impellers, hence under-estimating the mass exchange between them. During our investigation, we additionally observed a macro-instability (MI) in the inter-compartment plane itself, which significantly contributed to mass exchange. In several prior publications, inter-compartment mass exchange was boosted by tuning of the turbulent Schmidt number, $Sc_t = \nu_t/(\mathcal{D}_t)$. We pose that this tuning is not based on physical reasoning. Instead, it is a patchwork solution to cover under-predicted turbulent exchange, as Tominaga and Stathopoulos [161] similarly discussed for mispredicted scalar spreading in jets, as well as exchange by virtue of MIs. Such an an ad-hoc correction compromises the predictive capabilities of stirred tank simulations.

Whereas other publications on multi-impeller mixing focus primarily on overall mixing behavior, we study the flow in the inter-compartment plane in detail, using a combination of LDA experiments, RANS and LES simulations. With this, we attempt to describe which physical phenomena underlay inter-compartment mass transfer, their assessment by CFD simulations, and answer as to why RANS simulations poorly capture mixing in multi-impeller tanks.

3.2. Materials and Methods

3.2.1. CFD setup

The focus for RANS simulations is on the realizable $k-\epsilon$ (RKE) and Reynolds Stress Model (RSM) with linear-pressure strain formulation. For the LES simulations, the dynamic Smagorinsky model is employed, based on the favorable mixing results obtained by Jahoda et al. [65]. An overview of the model formulations is given in chapter 2, sec. 2.1.1. Both the steady-state multiple reference frame (MRF) and transient slid-

Table 3.1: Meshes used in this work. $2IF$ represents a $360°$ domain and $2IP$ represents the $60°$ domain. The last letter(s) represent the mesh quality (C = crude, M = medium, F = fine, SF = super-fine).

Name	Cells	Domain	Methods
2IP-C	$94k$	60°	RKE, RSM
2IP-M	$506k$	60°	RKE, RSM
2IP-F	$812k$	60°	RKE, RSM, SM-RKE
2IF-C	$648k$	360°	RKE, RSM, SM-RKE, LES
2IF-M	$1997k$	360°	RKE, RSM, SM-RKE, SM-RSM, LES
2IF-F	$5884k$	360°	RKE, RSM, SM-RKE
2IF-SF	$10584k$	360°	RKE, RSM, LES

ing mesh (SM) impeller model are used in RANS simulations. For LES, only the latter is employed.

A 2-impeller stirred tank with height $H = 2T$, impeller diameter $D = T/3$, off-bottom clearance $C = T/3$ and inter-impeller clearance $\Delta C = T$ was modeled. Here, tank diameter $T = 0.29$ m, as used by Jahoda et al. The tank contains 4 baffles with width $T/10$. All internals were modeled as sheet bodies [59, 62]. Simulations were conducted both in a 360° domain and 60° domain to assess the influence of a symmetry assumption [10, 20, 59, 84]. Using a 60° section introduces 6 baffles; the effect of this additional baffling was found to be small [59]. As in Jahoda et al. [65], the tracer concentration probe is placed at $T/4$ from the bottom, between the baffles, at $T/20$ from the wall, and the agitation rate $N_s = 5$ s^{-1}.

Spatial discretization was set to 2^{nd} order upwind [59, 62] for RANS models and bounded central differences with for LES. Standard wall functions were employed. The vessel top was set to no-shear to mimic a free surface, all other walls were no-slip. Convergence of the flowfield was declared when the residuals were $< 10^{-5}$ and the mean velocity remained within 0.1% over 1000 iterations. With transient simulations (SM and LES), only the residuals were considered. We report the used meshes in table 3.1, with the *2IF* series being the full domain, and the *2IP* series representing a 60° slice. We set $\Delta t = 0.00333$s in the sliding mesh simulations and the crudest LES simulation, *2IF-C*. The finest LES simulation, *2IF-SF*, was conducted with $\Delta t = 0.001667$s, and medium resolution simulation (*2IF-M*) with both Δt values for comparison. Temporal discretization was second order implicit. With the MRF model, the flowfield was resolved in steady state. During mixing, we used a timestep size of $\Delta t = 0.005$ s with MRF, while the velocity and turbulence fields remained frozen. Second order implicit time discretization was used in all cases.

Tracer was introduced as a passive scalar in a spherical volume ($r = 0.0125$m), at $Y = 0.551$m from the bottom, at $r/R = 0.5$, in the baffle plane, with $R = 0.5T$ the tank radius. The tracer and bulk fluid had equal properties, $\rho = 1000$ kg/m^3 and $\mu_l = 0.001$ Pa s, such that the tracer will not disturb the flowfield. The FLUENT default simple gradient diffusion hypothesis (SGDH) was used to determine turbulent scalar diffusion, modeling the diffusive flux as $J_i = -(\rho_l \mathcal{D}_m + \mu_t/Sc_t)\nabla C_i$ with $\mathcal{D}_m = 10^{-9}$ m^2/s the molecular diffusion coefficient, μ_t the turbulent viscosity, C_i the scalar concentration. $Sc_t = 0.7$ is the turbulent Schmidt number. A simulation with generalized gradient diffusion hypothesis (GGDH) yielded no significant change in θ_{95}.

3.2.2. LDA setup

We used a 2-probe TSI powersight laser system (150mW) with $\lambda_1 = 561$ nm (axial) and $\lambda_2 = 532$ nm (radial), operated in backward scattering mode. A glass tank ($T = 0.26$ m, $H = 2T,\ C = T/3,\ \Delta C = T$, 4 aluminum baffles of $T/10$) was placed in a water-filled rectangular glass box for refractive index matching. Two standard Rushton turbines were mounted on a centered shaft of diameter $d_s = 0.02$ m. All experiments were conducted at $N_s = 5.78$ s^{-1}, to match the Reynolds number with Jahoda et al. [65]. Hollow glass seeding ($d_p = 8 - 12$ μm, Stokes number $St = 0.03$) was used.

Verification measurements were conducted in the impeller outflow, at the height

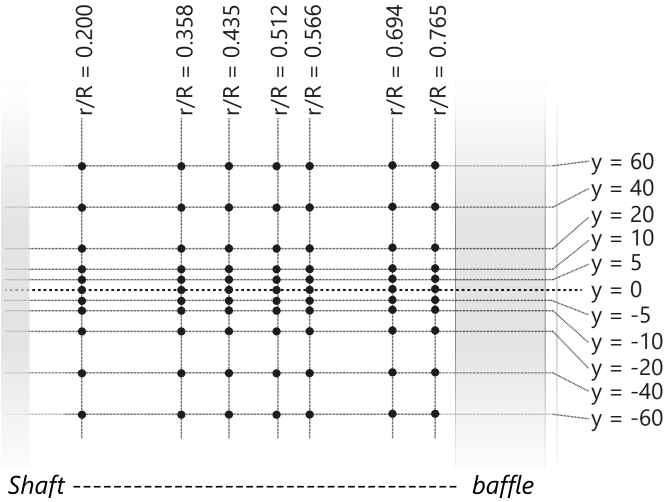

Figure 3.1: Measurement grid for the LDA-experiments in the mid-compartment plane. All axial values are given in mm, with $y = 0$ the central position between the impeller, and $r = 0$ the impeller shaft.

of the impeller disc, at radial positions were $r = [50,\ 60,\ 70,\ 77,\ 90,\ 102]$ mm, in the baffle plane. The average data rate was $340 - 500$ Hz (axial) and $830 - 850$Hz (radial). Data around the inter-compartment plane was recorded at $r = 7\ *\ y = 11$ (radial * axial) positions, specified in figure 3.1. Each measurement 50000 data-points were collected, measurements were done in $5-$fold. The average data rates were 289 Hz (axial) and 343Hz (radial). These are insufficient to resolve the full turbulence spectrum, but suffice to measure the energy-carrying motions which are expected to be relevant for inter-compartment mass exchange.

Data processing

LDA data processing was conducted in MATLAB 8.6.0. The setup contained a burst counter to remove false registrations, the velocity bias was corrected using gate-time weighing. The mean velocity is retrieved by time-averaging the velocity signal; subtracting the mean yields the fluctuating velocity. The contribution of noise and periodic flow components was assessed via the slotted auto-correlation method with local variance normalization [270–272], with the auto-correlation $\hat{\rho}$ computed as:

$$\hat{\rho}(k\Delta\tau_{lag}) = \frac{\Sigma u'(t_i)u'(t_j)}{\sqrt{\Sigma u'^2(t_i)\Sigma u'^2(t_j)}} \tag{3.1}$$

Ideally, at zero lag-time $\hat{\rho} = 1$; (white) noise causes a lower value in practice, the difference is used to assess the noise contribution Ψ. To segregate periodic flow contributions, van Maanen [273] proposed fitting the auto-correlation function with a series of damped cosines, eq. 3.2:

$$\hat{\rho}_{fit}(\tau) = b + c_0 e^{-\alpha_0 \tau} + \Sigma_{n=1}^{i} c_n e^{-\alpha_n \tau} \cos(2 \cdot n f \pi \tau) \tag{3.2}$$

Summing the amplitudes Σc_n then gives the contribution of periodic motions to the fluctuating kinetic energy. Alternatively, the kinetic energy contribution of periodic flow can be estimated from the spectral density function eq. 3.3:

$$S(f) = \frac{\Delta t}{\pi} \left[\frac{1}{2} \hat{\rho}(k \Delta \tau_{lag}) w(k \Delta \tau_{lag}) \cos(k f \Delta \tau_{lag}) \right] \tag{3.3}$$

With w a Tukey-Hanning window [271] with width $t_m(f) = t_{max} \kappa f_0 / f$, where lower κ decreases low-frequency resolution, but high κ can induce modulation. We found $\kappa = 5$ provided a good trade-off. The relative contribution of periodic components follows from integrating eq. 3.3 over the relevant frequencies, which was done using trapezoidal integration.

With these methods, the RMS velocity $u_{rms} = \sqrt{(u'u')}$ can be corrected for the periodic components, by eq. 3.4 when periodic fitting is used and eq. 3.5 when using spectral integration:

$$u'_t = u' \cdot \sqrt{1 - \Psi - \Sigma(c_n)} \tag{3.4}$$

$$u'_t = u' \cdot \sqrt{1 - \Psi - E_{per}/E_{tot}} \tag{3.5}$$

Since the tangential component of U and u' is unknown, isotropy is assumed in order to calculate the turbulent kinetic energy as $k_t = 3/4(\overline{u'^2_{t,ax}} + \overline{u'^2_{t,rad}})$.

In the impeller outflow $\hat{\rho}$ was evaluated for $\tau_{lag} = 250$ ms using 500 slots, which sufficed to capture noise and blade passages. The well-defined impeller-induced periodicity gave preference to eq. 3.4 for periodic estimation, taking the first 3 harmonics into account. There was no discernible influence of MIs in the outflow. In the mid-plane, $\hat{\rho}$ was evaluated first for $\tau_{lag} = 250$ ms using 500 slots to estimate noise (no impeller influence was discernible here), and next at $\tau_{lag} = 40$ s with 1600 slots to evaluate MI-induced periodicity. As a high-resolution, long lag time computation was unfeasible, we estimated the total spectral density function by matching the spectrum of both lag time ranges in the overlapping frequency range to construct a single spectrum.

In the mid-plane, $\hat{\rho}$ was fitted with 4 cosines with frequencies $f_{i.j}$: $i = 1, 2$ indicates the two fitted frequencies, $j = 1$ the base frequency and $j = 2$ the first harmonic. Spectral density integration requires a cut-off between turbulent and MI components. We considered the range $f/N_s < 0.1$ (10 impeller revolutions) as MI-components, based on visual assessment of the spectra. Of course, the cutoff point can be debated, but as we use the same definition between experiment and CFD changing the cut-off should not affect the comparison. In the mid-plane, we report k_t as the MI-free turbulent kinetic energy, k_{MI} as the kinetic energy of macro-instabilities and k_{t*} as their sum.

3.3. Results and Discussion

3.3.1. Experimental

LDA verification

Ranade and Joshi [274] summarized a range impeller outflow measurements, visualized in the gray band of figure 3.2. Our data coincides with the upper bound, we observe a somewhat slower decline in U_{rad} with radial position. The differences may arise because of variations in signal processing, LDA setup, and sensitivity of U_{rad} to the axial position, and because varying measurement angles compared to the baffle. The rapid drop at $r = 102$mm is attributed to the vicinity of the baffle. A good agreement in turbulent kinetic energy k_t is observed compared to Wu and Patterson [34]; Murthy and Joshi [97] reported a higher k_t near the tip, likely since they measured all three velocity components and avoided the isotropy assumption.

Mid-plane dynamics

We define the mid-plane $y = 0$ as the axial location exactly between the two impellers. U_{rad} shows mirror symmetry in the mid-plane, with some deviation near the baffle (the results are shown together with the CFD results, e.g. figure 3.8). U_{ax} switches from convergent to divergent behavior between $r/R = 0.617$ and $r/R = 0.489$. Below $r/R = 0.489$, this flow divergence leads to a deceleration in U_{rad}. The total fluctuating kinetic energy k_t peaks at $y = 0$, and increases in strength with increasing r/R,

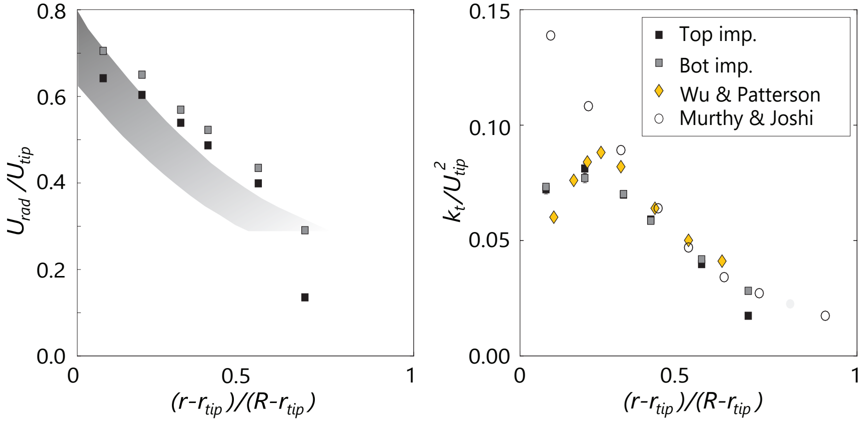

Figure 3.2: LDA results: current data (top and bottom impeller outflow) compared with earlier studies. The gray band (U_{rad}) represents the studies summarized by [274]. For k_t, we compare with Wu and Patterson [34] and Murthy and Joshi [97]. The position is scaled with tank radius R and impeller tip radius r_{tip} and k_t with the tip speed U_{tip}.

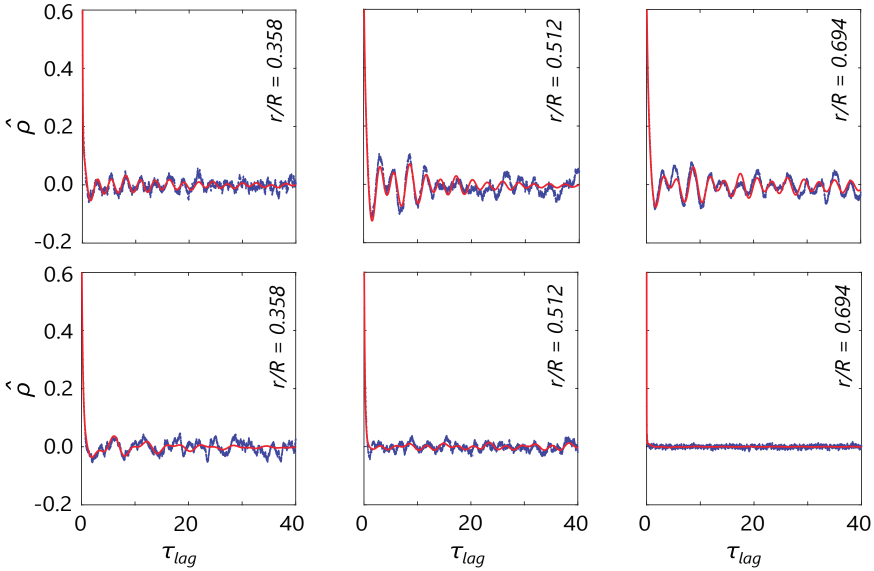

Figure 3.3: Fitted auto-correlation functions of u'_{ax} (top) and u'_{rad} (bottom) at 3 radial locations, in the plane $y = 0$. Blue: LDA data. Red: fitted function with 4 damped cosines, at 2 base frequencies and their first harmonic.

again with the exception of the point closest to the baffle. To discriminate whether this k_t-peak at $y = 0$ is evidence of MIs, or whether it represents regular turbulence generated by the collision of the converging flow, we have to assess the influence of low-frequency oscillations.

Fitting $\hat{\rho}$ with dampened cosines (fig. 3.3) consistently yielded frequencies around $f_{1.1}/N_s = 0.020 \pm 0.001$ and $f_2/N_s = 0.061 \pm 0.003$ axially and $f_{1.1}/N_s = 0.015 \pm 0.007$ and $f_{2.1}/N_s = 0.052 \pm 0.015$ radially. These values agree well the reports of Paglianti et al. [117] for the precessing vortex and jet instability effect, respectively. The MI energy was maximum at $y = 0$. An overview of parameters at $y = 0$ is presented in table 3.2. Radially, the oscillations are comparatively weak: $\Sigma c_{n,rad} < 0.075$ at all locations except at $r/R = 0.0694$. The latter seems to be a fitting error caused by excessive damping; there are hardly fluctuations visible in fig. 3.3 (bottom right), and the damping coefficients are all at the constraint value $a_n = 0.33$. For the axial component, $\Sigma c_{n,ax}$ varies between 0.1 at the shaft to 0.22 at $r/R = 0.694$. For fluctuations in U_{rad}, frequencies $f_{1.1,rad}/N_s = 0.015$ and $f_{2.1,rad}/N_s = 0.052$ both contribute more than their respective harmonics, while for U_{ax} the contributions vary with location. Close to the shaft $f_{1.1,ax}$ has twice the amplitude of its harmonic $f_{1.2,ax}/N_s = 0.040$, but in for $r/R > 0.359$, $f_{1.2,ax}/N_s$ is by far the stronger contribution. $f_{2.1,ax}/N_s = 0.061$ exceeds $f_{2.2,ax}/N_s$ by a factor $1.5 - 2$, except at $r/R = 0.2$.

The noise Ψ lies below 6% at all points, except $r/R = 0.765$. This was consistent at all axial positions, and the correlation function showed a much more rapid decay at this position. We have not been able to pinpoint the exact reason for this higher noise

Table 3.2: RMS-velocity, noise factor Ψ, MI-correction factor, oscillation frequencies and kinetic energy in the plane $y = 0$ at different radial positions, using the periodic-fitting approach (eq. 3.4). The coefficient c represent the contribution to the Reynolds stress $\overline{u'u'}$, with $c_{i.j}$ the j^{th} harmonic of frequency component i.

r/R	0.200	0.358	0.435	0.512	0.566	0.694	0.765
u'_{rad} (m/s)	0.149	0.135	0.127	0.115	0.107	0.091	0.083
Ψ_{rad}	0.015	0.017	0.022	0.032	0.037	0.064	0.317
$c_{1.1,rad}$	0	0.006	0.016	0.017	0.006	0.032	0.010
$c_{1.2,rad}$	0.037	0.048	0.040	0.007	0.003	0.002	0.001
$c_{2.1,rad}$	0	0.015	0.075	0.009	0.012	0.045	0.006
$c_{2.2,rad}$	0.032	0.005	0.028	0.016	0.011	0.039	0.012
$f_{1.1,rad}/N_s$	0.020	0.001	0.015	0.015	0.022	0.017	0.017
$f_{2.1,rad}/N_s$	0.049	0.058	0.056	0.053	0.050	0.043	0.062
u'_{ax} (m/s)	0.082	0.098	0.112	0.134	0.154	0.194	0.151
Ψ_{ax}	0.063	0.054	0.045	0.041	0.033	0.027	0.192
$c_{1.1,ax}$	0.049	0.022	0.029	0.031	0	0	0
$c_{1.2,ax}$	0.022	0.005	0.052	0.095	0.064	0.070	0.055
$c_{2.1,ax}$	0.027	0.044	0.043	0.102	0.113	0.135	0.073
$c_{2.2,ax}$	0.003	0.007	0.009	0.014	0	0.011	0
$f_{1.1,ax}/N_s$	0.020	0.017	0.021	0.020	0.021	0.020	0.020
$f_{2.1,ax}/N_s$	0.053	0.062	0.065	0.062	0.062	0.061	0.061
$10^3 \cdot k_{t,1}/U_{tip}^2$	7.73	7.63	7.49	7.54	8.85	10.80	6.17
$10^3 \cdot k_{MI,1}/U_{tip}^2$	0.62	0.41	0.78	1.36	1.23	2.40	0.70

level; it could be that the presence of the baffle leads to relatively dominant small-scale turbulence, meaning the data-rate was insufficient. Furthermore, imperfections in refractive-index matching are most pronounced at this position, and the vicinity of the baffle may lead to higher background noise by reflection effects.

The fitted frequencies contribute $8-20\%$ to the fluctuating kinetic energy at $y = 0$. MIs have a less well defined frequency than stirrer blade passages; their contribution may be under-estimated by rapid dampening and not all frequencies may be accounted for. This makes it likely the MI-energy is underestimated by eq. 3.4. Using the spectral density function (fig. 3.4) and determining the MI contribution with eq. 3.5, the kinetic energy contained in the range $f/N_s < 0.1$ lies between $28-49\%$ at $y = 0$. However, this method does not discriminate MI frequencies from other large-scale contributions, and is considered over-estimative. The non-discriminatory nature of the spectral density method does make comparison with large eddy simulation spectra more straightforward, as they were found to be more erratic. Hence, the MI energies reported in the CFD comparison were obtained by the spectral density method, with the notion that the true MI energy is likely to lie in between the estimates of eq. 3.4 and 3.5. The features observed in fig. 3.4 are in agreement with the fitted cosine frequencies, with a clear bi-modal peak representing $f_{1.2}/N_s$ and $f_{2.1}/N_s$ at the outer radial positions.

Since we are interested in inter-compartment mixing, $u'_{ax,MI}$ is of particular interest; in this direction the jet instability MI_j (f_2) contributes most. Whether MIs

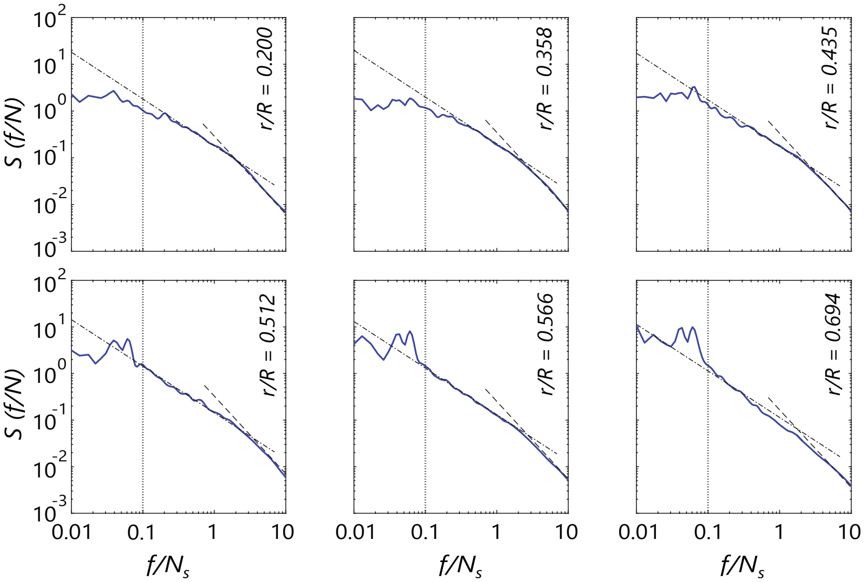

Figure 3.4: Experimental spectral density functions of $\hat{\rho}_{uax}$ at various radial positions and $y = 0$. Dashed line: $S(f/N_s) \propto (f/N_s)^{-5/3}$. Dash-dot line: $S(f/N_s) \propto (f/N_s)^{-1}$. Dotted line: cut-off frequency between MI and turbulence.

will strongly affect mixing depends on whether the observed oscillations represent a cross-flow between the compartments, or the segregation between the compartments moving up and down as a whole. The unsteady CFD results presented later suggest compartment cross-flow only occurs close to the shaft. However, we first focus on the performance of MRF simulations, which are inherently unable to capture MIs by their steady state nature.

3.3.2. CFD validation: the impeller outflow

Figure 3.5 shows U_{rad}, k_t and ϵ in the top impeller outflow for the MRF simulations (360°, *MRF-RKE* (top) and *MRF-RSM* (bottom)). The profiles were tangentially averaged in order to account for all impeller angles. In our view, this is a fairer comparison with LDA data than the instantaneous outflow profile directly from the impeller tip,

Table 3.3: MI-correction factor and kinetic energy in the plane $y = 0$ at different radial positions, using the spectral integration approach (eq. 3.5). The RMS velocity and noise factor are as in table 3.2.

r/R	0.200	0.2358	0.3435	0.512	0.566	0.694	0.765
$(E_p/E_t)_{rad}$ (eq. 3.5)	0.409	0.380	0.337	0.267	0.222	0.140	0.029
$(E_p/E_t)_{ax}$ (eq. 3.5)	0.164	0.140	0.200	0.288	0.391	0.546	0.318
$10^3 \cdot k_{t,2}/U_{tip}^2$	5.38	5.57	5.91	6.32	6.60	6.77	4.67
$10^3 \cdot k_{MI,2}/U_{tip}^2$	3.04	2.47	2.35	2.58	3.52	6.45	2.22

although it reduces agreement near the baffle where the flow is not rotor-dominated.

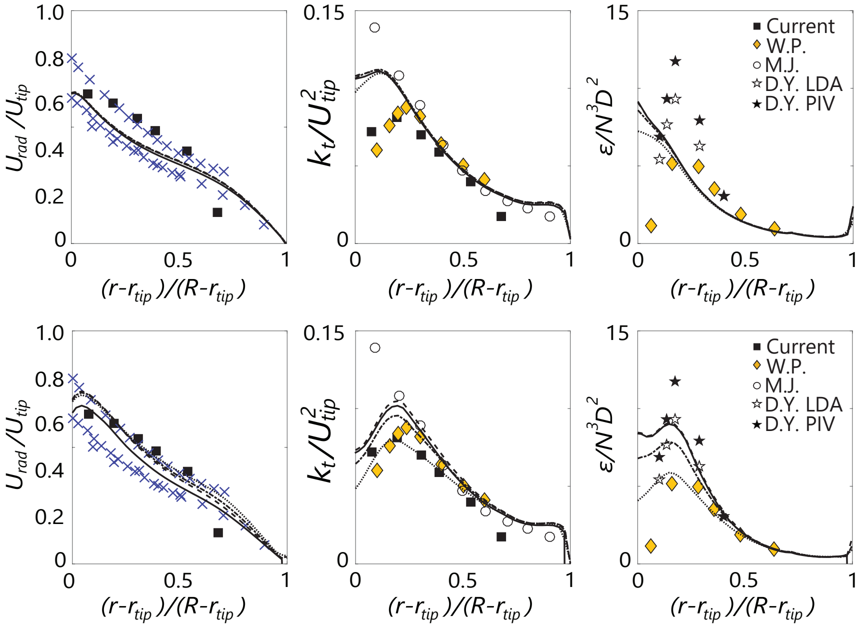

Figure 3.5: Tangentially averaged profiles of U_{rad}, k_t and ϵ in the top impeller outflow compared with phase-averaged LDA data, for *MRF* simulations. Top row: realizable $k-\epsilon$, 360° domain. Bottom row: *RSM*, 360° domain. Lines represent CFD data; dotted line: *2IF-C*, dash-dot line: *2IF-M*, dashed line: *2IF-F*, solid line: *2IF-SF*. Symbols represent experimental data. Abbreviations: W.P. Wu and Patterson [34], MJ. = Murthy and Joshi [97], D.Y. = Ducci and Yianneskis [35]. The crosses in the U_{rad} plot represent the upper- and lower bound of the studies reviewed by Ranade and Joshi [274].

Both models predict U_{rad} and k_t well within the LDA data range; k_t does deviate close to the impeller, where the isotropic turbulence assumption breaks down (note that experimentally the impeller influence is removed from k_t; MI energy is included but negligible). Interestingly, the non-isotropic *RSM* predicts a k_t decrease at the tip, which is in better agreement with our data and Wu and Patterson [34] than with Murthy and Joshi [97], while only the latter measured all velocity components. *RSM* yields a superior assessment for ϵ; at the highest mesh density the peak dissipation rate recorded by Baldi et al. and Ducci et al. [35, 106, 107] is reasonably captured. The *RKE* model agrees with the dimensional assessment of Wu and Patterson [34], likely arising from the similar underlying assumptions. The *RSM* model is more mesh sensitive, but based on impeller outflow data, both models perform satisfactory. Due to similarity the bottom impeller profiles and profiles for the 60° mesh are omitted.

The SM simulations show good agreement with experimental data (fig. 3.6). Again, the *RSM* simulation predicts a decrease in k_t and ϵ near the blade tip, where the *RKE* model does not. In the bulk of the outflow, *RKE* and *RSM* are in excellent agreement. LES is well capable of capturing U_{rad}, but performs poor for k_t and ϵ. Only the turbu-

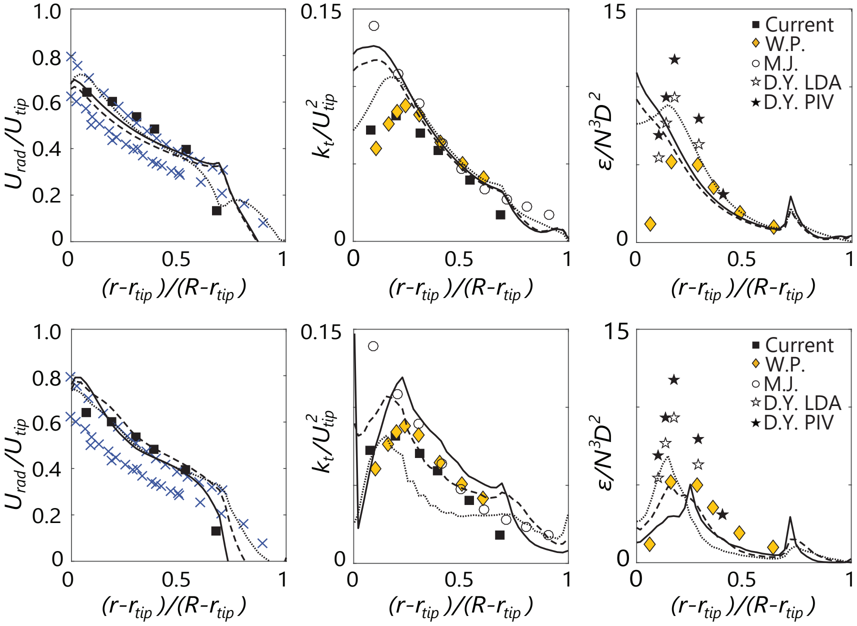

Figure 3.6: Profiles of U_{rad}, k_t and ϵ in the top impeller outflow compared with LDA data. Results are recorded in the baffle plane, which causes erroneous behavior for $(r - r_{tip})/(R - r_{tip}) > 0.7$, the baffle location. Bottom impeller results are omitted due to similarity. Top row: SM simulations. Solid line: *2IF-F*, *SM-RKE*. Dashed line: *2IF-M*, *SM-RKE*. Dotted line: *2IF-M*, *SM-RSM*. Bottom row: LES simulations. Solid line: *2IF-SF*. Dashed line: *2IF-M*. Dotted line: *2IF-C*. Symbols represent experimental data. Abbreviations: W.P. Wu and Patterson [34], M.J. = Murthy and Joshi [97], D.Y. = Ducci and Yianneskis [35]. The crosses in the U_{rad} plot represent the upper- and lower bound of the studies reviewed by Ranade and Joshi [274].

lent kinetic energy of the resolved scales is shown in figure 3.6, which means *2IF-SF* is expected to yield higher k_t than *2IF-C* and *2IF-M*, as observed. However, *2IF-SF*, which is still insufficiently fine to capture all energy carrying eddies, already over-estimates the experimental k_t. The dissipation rate ϵ on the other hand is strongly underestimated. Hartmann et al. [109] and Derksen et al. [130] reported an under-estimation of ϵ with the standard Smagorninsky model using constant $C_s = 0.1$. Delafosse et al. [132] and Soos et al. [134] found that setting $C_s = 0.2$ increased agreement; ϵ is highly sensitive to C_s. Following Jahoda et al. [65], we applied the dynamic Smagorinsky model where C_s is determined dynamically. This gave values between $0.01 - 0.06$, as observed by Jahoda et al. [65]. These low C_s values explain the strong underprediction of ϵ, and may well be related to the over-prediction in k_t. Unfortunately, Jahoda et al. do not report k_t and ϵ for verification.

3.3.3. Mixing times

We quantify θ_{95} by two methods; a probe at the same location as used by Jahoda et al. [65] for direct comparison, and the CoM as used by Hartmann et al. [149]. There is no verification data for the latter, meaning it is reported for mutual comparison only.

Table 3.4: Comparison of dimensionless mixing times θ_{95} for the MRF method: models and mesh dependency. Methods: P = bottom probe, C = coefficient of mixing. The work of Hartmann is followed to set the CoM-boundary.

Mesh	Method	*RKE*	*RSM*
2IF-C	**P**/C	**133.5**/148.5	**138.1**/152.0
2IF-M	**P**/C	**146.1**/162.0	**157.8**/173.0
2IF-F	**P**/C	**145.2**/160.5	**145.2**/159.5
2IF-SF	**P**/C	**180.9**/200.0	n.m. /172.5
2IP-C	**P**/C	**96.2**/106.5	**113.0**/129.0
2IP-M	**P**/C	**117.1**/129.0	**166.4**/161.5
2IP-F	**P**/C	**135.9**/152.0	**176.5**/161.0

n.m. = not measured.

MRF simulations

θ_{95} for both *RKE* and *RSM* exceed the experimental result ($\theta_{95} = 92$) substantially. As observed in Mostek et al. [159], θ_{95} increases with mesh density. There are outliers; particularly mesh *2IF-F* yields a comparatively low θ_{95} with both turbulence models. The CoM-based θ_{95} structurally exceeds probe measurements, but shows a similar trend with mesh density. In all cases, $\theta_P \approx 0.9\theta_C$, which indicates the probe is a representative albeit slightly under-estimative measurement of mixing in the total volume.

2IF-F-RKE is an outlier in terms of mixing time. In table 3.5 we report the integral downward flowrate Q_{ax} through the plane $y = 0$ as an estimate of convective inter-compartment exchange, which is typically seen to decrease with mesh density. It is significantly increased for *2IF-F-RKE*, which appears to be related to the exact velocity field in the plane segregating the compartments, and thereby the magnitude of convective exchange between the compartments. If the segregation plane is tilted compared to the plane $y = 0$, leading to a higher Q_{ax}, convective mixing between the compartments is stronger (hence θ_{95} is lower). As the flowfield in MRF simulations is fixed, this leads to pronounced differences between simulations. This is discussed further in sec. 3.3.4. The observed decrease of $Q_{ax,y=0}$ with increasing mesh density likely causes the trend of increasing θ_{95} with increasing mesh density. Hence, the increasing mixing time is not a typical numerical diffusion issue, and the typical ”cure” of increasing mesh resolution does not lead to better agreement with experimental data. Note that an increased Q_{ax} through $y = 0$ does not necessarily mean increased exchange between the compartments, the segregation plane could be skewed without increased exchange, but there does appear to be a correlation between the two.

The 60° mesh yields a lower θ_{95} when using the *RKE* model. When considering the mid-plane hydrodynamics, we observed this was not a direct result of the smaller domain (which would indicate limiting intra-compartment mixing), but was rather caused by increased axial exchange (Q_{ax}) between the compartments, as reported in table 3.5. *RSM* in the 60° yields similar CoM figures as in the 360° mesh, but while the CoM becomes constant, the probe value keeps increasing. This does indicate different mixing behavior *within* the compartments for the *RSM* model.

SM and LES simulations

SM simulations predict a probe-based $\theta_{95} \approx 110$ for *RKE*, in agreement with the SM simulation of Jahoda et al. [65], and 15% above the experimental value. Interestingly, no mesh dependence is observed in the results of *SM-RKE*. This contrasts the MRF simulations, where θ_{95} was strongly mesh dependent, depending on the predicted axial exchange Q_{ax} between the compartments which in turn depended strongly in the predicted position of the segregation plane between the compartments. As this plane was fixed in MRF simulations, the exact fixed position could strongly influence θ_{95}. In SM simulations, the segregation plane location is dynamic, making the results much less sensitive. These results hint the *SM-RKE* simulations capture convective axial exchange due to MIs with a magnitude that is consistent between the different meshes. The *SM-RSM* model predicts a higher θ_{95} of 133.

The LES simulations with *2IF-C* and *2IF-M* yield mixing times of $\theta_{95} \approx 80$, in agreement with $\theta_{95} = 81.5$ observed in the LES simulations by Jahoda et al., using a similar mesh density. There was no difference between $\Delta t = 0.00333$ and $\Delta t = 0.00167$ for simulations with mesh *2IF-M*. Simulation *2IF-SF* yielded $\theta_{95} = 94$, in very good agreement with the experimental value $\theta_{95} = 96$ reported by Jahoda et al. [65].

Mixing profiles

Probe profiles for a selection of the simulations are shown in figure 3.7. The top figure compares *SM-RKE* with *MRF-RKE*. The SM simulations reasonably capture the lag time and general trend observed experimentally, although the weaker slope in the late stage causes an over-estimated θ_{95} overall. The lower lag time for *2IF-F* is a sign of slightly faster intra-compartment mixing, possibly due to the higher mesh density [62]; the *MRF* simulations show a higher lag time for the denser mesh, however. Both SM curves show some slight wiggling, indicating MIs indeed introduce temporal variations in axial exchange. For LES, *2IF-SF* slightly over-estimates the lag-time, but better approximates the mid and end-stage of the experimental mixing curve. It must be kept in mind that the figures show single realizations, while both the experimental and LES data will vary between repetitions.

3.3.4. Inter-compartment flow

Table 3.5: Axial flow-rate (downward) through the mid-impeller plane $y = 0$ in L/s (MRF simulations). For the 60° mesh, the value is multiplied by 6.

Mesh	*RKE* 360°	*RSM* 360°	*RKE* 60°	*RSM* 60°
X-C	1.36	1.58	3.04	2.45
X-M	1.14	1.28	2.72	1.34
X-F	1.48	1.31	1.10	2.25
X-SF	0.74	1.46	–	–

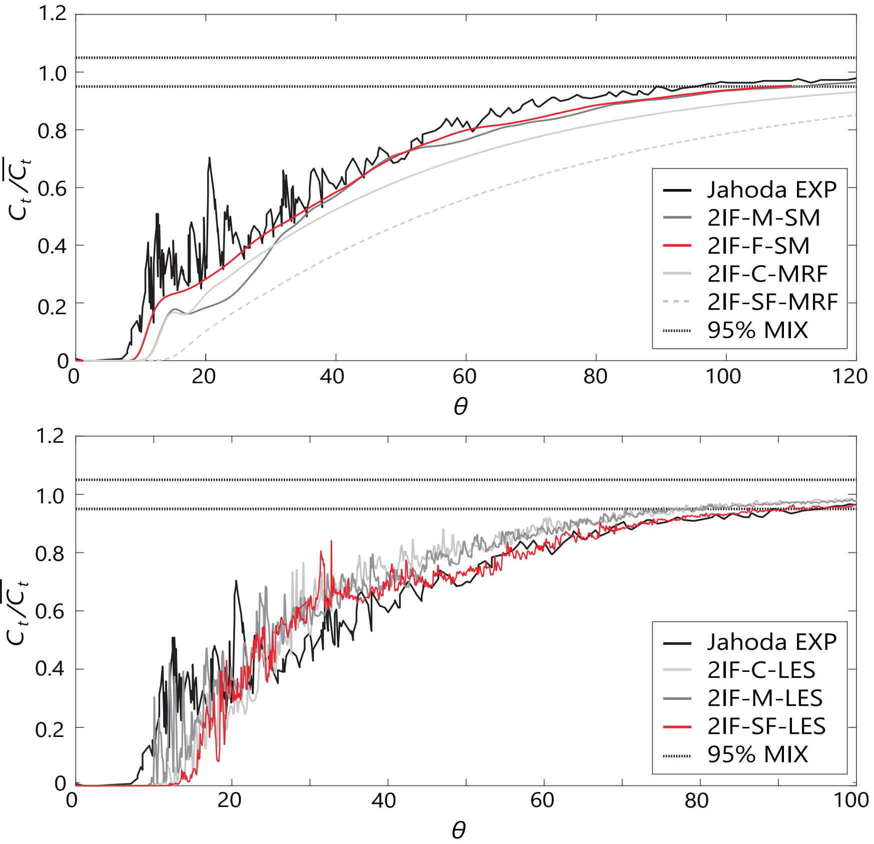

Figure 3.7: Mixing profiles for different simulations. Black: typical experimental data, Jahoda et al. [65]. Top: RANS simulations, including 2 MRF simulations. Bottom: LES simulations.

Table 3.6: Comparison of dimensionless mixing times θ_{95} for the sliding mesh and LES simulations. Methods: P = bottom probe, C = coefficient of mixing. The work of Hartmann is followed to set the CoM-boundary at $CoM = 0.0283$.

Mesh	Method	θ_{95}
2IF-M-SMRKE	**P**/C	**112.7**/126.5
2IF-F-SMRKE	**P**/C	**110.1**/122.0
2IF-M-SMRSM	**P**/C	**133.3**/147.0
2IF-C	**P**/C	**80.0**/86.0
2IF-M ($\Delta t = 1.67$ ms)	**P**/C	**80.7**/88.0
2IF-M ($\Delta t = 3.33$ ms)	**P**/C	**81.6**/$n.m.$
2IF-SF	**P**/C	**94.0**/99.0
Jahoda (LES)	**P**	**81.5**
Jahoda (EXP)	**P**	**96.0**

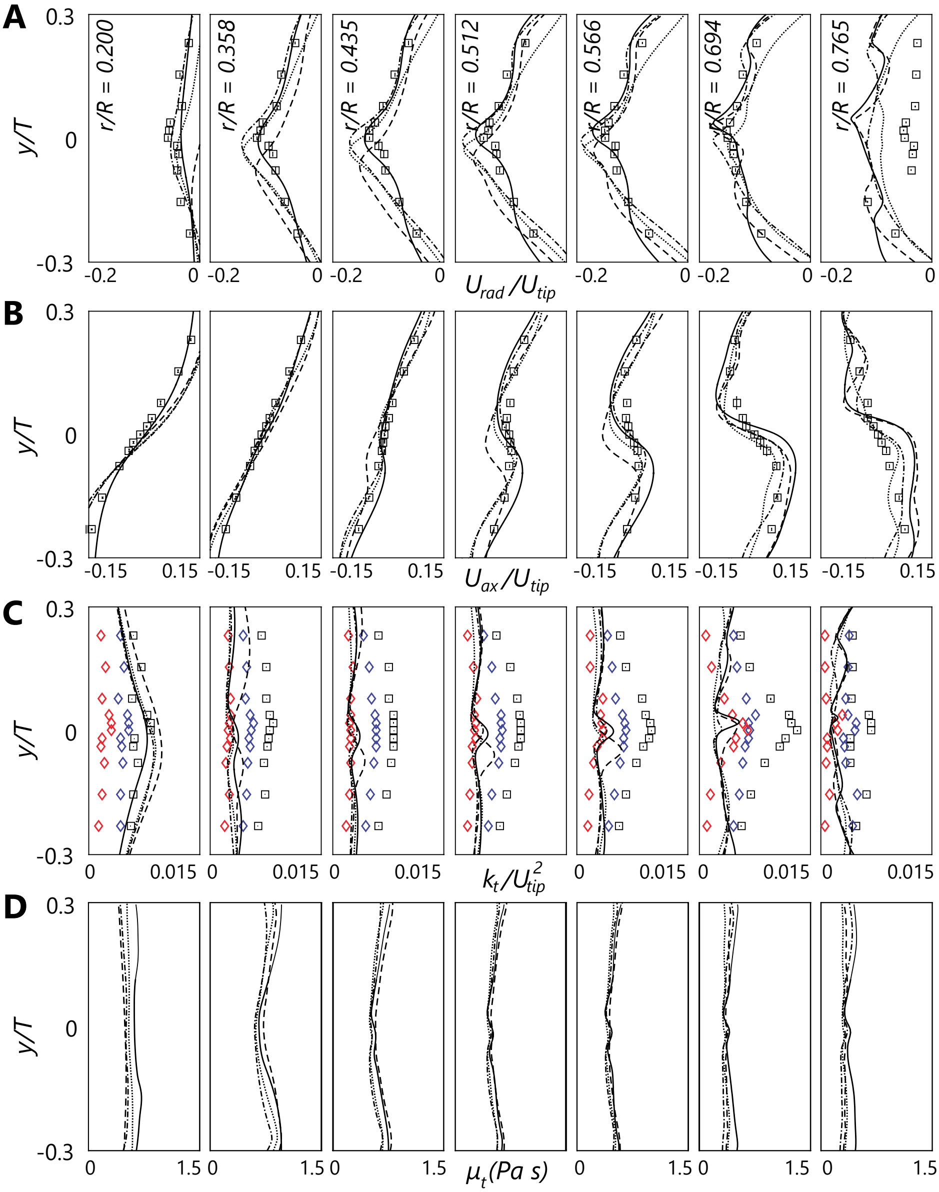

Figure 3.8: Axial profiles of **A:** U_{rad}, **B:** U_{ax} **C:** k_t with *RKE* in baffle plane of the 360° domain. Black rectangles: LDA data. For k_t, the black rectangles represent the total kinetic energy k_{t*}, the blue diamonds the turbulent kinetic energy k_t, and the red diamonds the MI energy k_{MI}. Lines: CFD results at different mesh densities (dotted: *2IF-C* , dash-dot: *2IF-M*, dashed: *2IF-F*, solid: *2IF-SF*). Row **D** shows the tangential average of μ_t acquired from the CFD simulations.

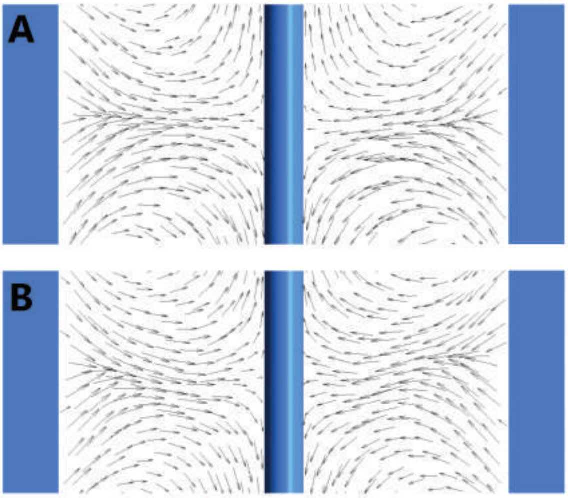

Figure 3.9: Flow structures around the inter-compartment plane (360° domain, $MRF - REA$). **A**: *2IF-M*, **B**: *2IF-F*. In the latter case, flow in the segregation plane is pointed slightly downward, increasing axial exchange.

Midplane dynamics: MRF

Full domain U_{rad} and U_{ax} are reasonably well predicted in the baffle plane using *RKE* (fig. 3.8, row **A** and **B**), although both are over-predicted close to the baffle, probably due to the use of a $2D$ baffle geometry. The change from converging to diverging axial flow is well captured. Some mesh differences can be detected, but aside from *2IF-F* no mesh performs particularly better or worse.

For *2IF-F*, the peak U_{rad} and inflection point of U_{ax} lie slightly below $y = 0$. This indicates the compartment segregation plane is shifted. Qualitative inspection of the vector fields furthermore shows a slightly downward pointed flow in the mid-plane for *2IF-F* (fig. 3.9), which enhances axial exchange. This explains why Q_{ax} is high and θ_{95} is comparatively low in *2IF-F*, despite k_t and tangentially-averaged turbulent viscosity $\langle \mu_t \rangle$ (fig. 3.8 **D**) being similar to the other cases.

The U_{rad} and U_{ax} profiles for *RSM* (fig. 3.10) are in lesser agreement with experimental data. For *2IF-M* the velocity profiles favorably match the LDA measurements, but for both *2IF-F* and *2IF-SF* the U_{rad} peak shows strange asymmetric behavior. As for the *RKE* case, the skewed inter-compartment plane increases Q_{ax} in the $y = 0$ plane (table 3.5), explaining why θ_{95} is nearly similar for *2IF-M*, *2IF-F* and *2IF-SF* with *MRF-RSM*, whereas a large jump in mixing time is observed between *2IF-M* and *2IF-SF* with *MRF-RKE*.

Reduced domain In contrast to the full domain, U_{rad} and U_{ax} are poorly predicted in the 60° domain (fig. 3.11, rows **A, B**). The magnitude of U_{rad} is strongly underestimated everywhere except close to the baffle, while reversal from converging to diverging axial flow is not at all captured within the measured region. The peak U_{rad}

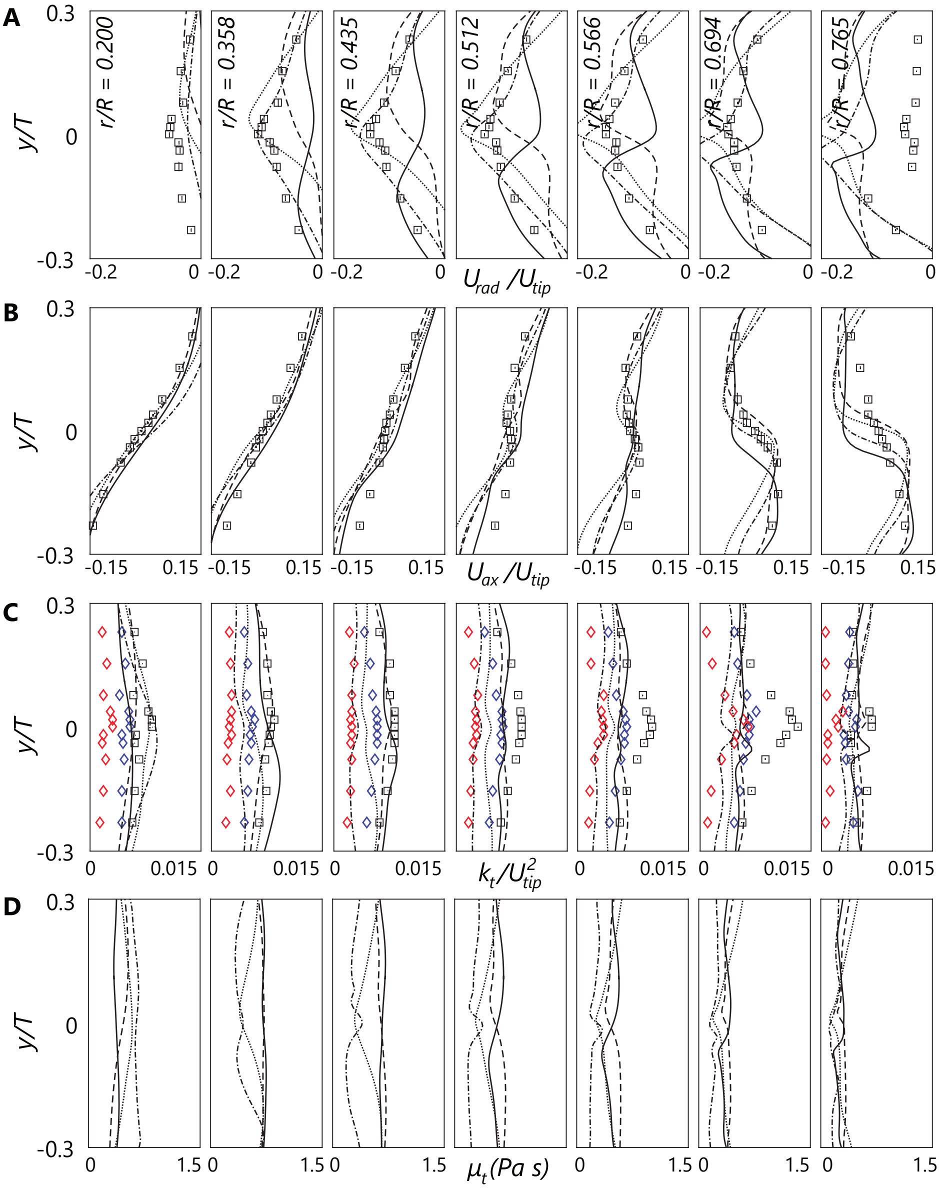

Figure 3.10: Axial profiles of **A:** U_{rad}, **B:** U_{ax} **C:** k_t with, with *MRF-RSM* in the $360°$ domain. Squares: phase-averaged LDA experimental data, recorded in the baffle plane. For k_t, the black rectangles represent the total kinetic energy k_{t*}, the blue diamonds the turbulent kinetic energy k_t, and the red diamonds the MI energy k_{MI}. Lines: CFD results at different mesh densities (dotted: *2IF-C*, dash-dot: *2IF-M*, dashed: *2IF-F*, solid: *2IF-SF*). Row **D** shows the tangential average of μ_t acquired from the CFD simulations.

is predicted at a lower axial position than measured experimentally. The *MRF-RKE* model does yield a comparatively good estimation of k_t for the *2IP-SF* mesh, resulting in a higher tangentially averaged μ_t (fig. 3.11, row **E**). Furthermore Q_{ax} is significantly higher in the 60° domain (table 3.5). Combined, the high μ_t and Q_{ax} explain the low θ_{95} observed for *RKE* in the 60° domain. Compared to *RKE*, *RSM* simulations in the 60° mesh show a higher degree of mesh dependency, with odd U_{rad} peaks. k_t is reasonably assessed for $r/R < 0.5$. Overall, μ_t and Q_{ax} are similar between the 360° and 60° domain for *RSM*, explaining the similarity in θ_{95} between them. As was the case with the full-domain, there seems to be a shift in plane position compared to the experimental data for the denser meshes.

3.3.5. Midplane dynamics: Sliding mesh

SM simulations predict a lower θ_{95} than MRF, although they still over-estimate the experimental value. The wiggles in fig. 3.7 hint the difference lies in the inclusion of MIs. Mid-plane data (fig. 3.12) indeed shows k_t is captured to a similar degree as in the *MRF* case, and under-estimated compared to LDA data, especially in the converging flow region. The data for *2IF-F* shows a slightly higher peak k_t near the baffle than *2IF-M* with the RKE model.

For SM simulations, all fluctuating kinetic energy of the resolved motions is attributed to MIs (not just $f/N_s < 0.1$ as done for the *LDA* and *LES* data). *2IF-M* yields a slightly higher k_{MI} compared to *2IF-F*; k_{t*} is similar between the meshes. The overall MI energy is still lower than reported experimentally. U_{rad} is well captured for *SM-RKE*, although the *MRF* simulations performed slightly better in quantitatively capturing U_{ax}. Still, the reversal from converging to diverging flow is qualitatively reasonably captured with *SM-RKE*. *SM-RSM* performs poorly: a shift in midplane position is clearly observed in all three profiles. In contrast to the *MRF* simulations, this leads to a *higher* θ_{95} for *SM-RSM*. In general, the inclusion of turbulence anisotropy does not seem to improve the agreement with experimental data, in the SM simulations, MRF simulations, and single-impeller work of Gunyol et al. [59]. Hence, there appears to be little reason to opt for the more computationally expensive RSM model Rushton-stirred tank applications.

Probing U_{ax} as a function of time at several points in the mid-plane, *(SM-RKE)* shows strong periodic motions (figure 3.13). For *2IF-M*, these are well defined, with the Fourier spectrum showing a dominant frequency at $f/N_s = 0.058$ (and its harmonics). This is in excellent agreement with the jet instability frequency reported by Paglianti et al. [275], and the experimentally observed values. Experimentally, we also observed a weak contribution of $f/N_s = 0.02$, and strong contribution of $f/N_s \approx 0.04$ in the parallel flow region. In *2IF-M*, a weak peak can be observed at $f/N_s = 0.02$, while $f/N_s = 0.04$ is absent. Case *2IF-F* shows more scatter, the dominant peak now is at $f/N_s = 0.045$ with a strong shoulder at $f/N_s = 0.06$ for $r/R = 0.512$ and $r/R = 0.694$. This is qualitatively more in line with experimental observations, although the contribution of $f/N_s = 0.06$ is too low in the simulation. At $r/R = 0.694$, an additional peak is observed at $f/N_s \approx 0.01$, which represents the very slow oscillation visible in 3.13 **B** that is absent in 3.13 **A**.

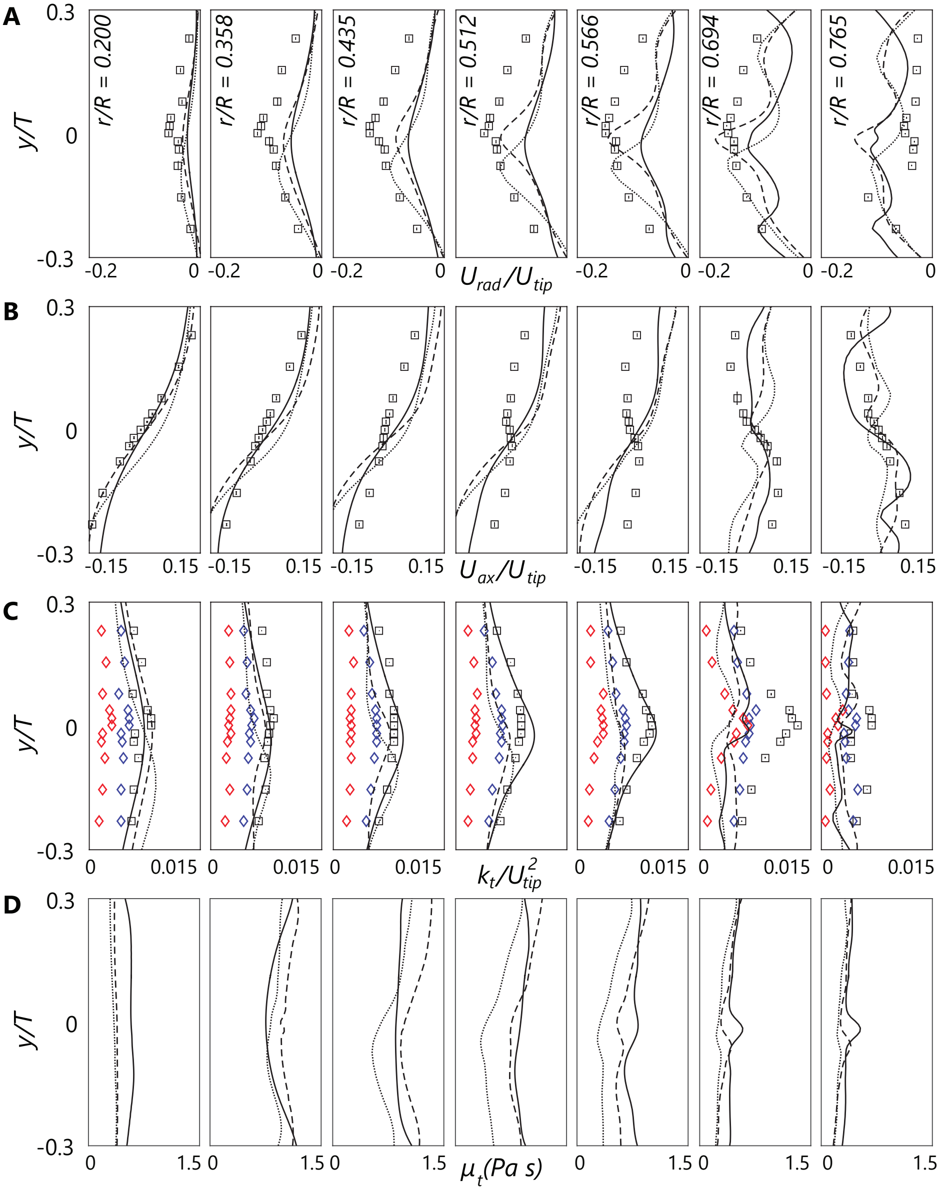

Figure 3.11: Comparison of axial profiles for **A:** U_{rad}, **B:** U_{ax}, **C:** k_t, with *MRF-RKE* in the 60° domain. Squares: phase-averaged LDA experimental data, recorded in the baffle plane. For k_t, the black rectangles represent the total kinetic energy k_{t*}, the blue diamonds the turbulent kinetic energy k_t, and the red diamonds the MI energy k_{MI}. Lines: CFD results at different mesh densities (dotted: *2IF-C*, dash-dot: *2IF-M*, dashed: *2IF-F*, solid: *2IF-SF*). Row **D** shows the tangential average of μ_t acquired from the CFD simulations.

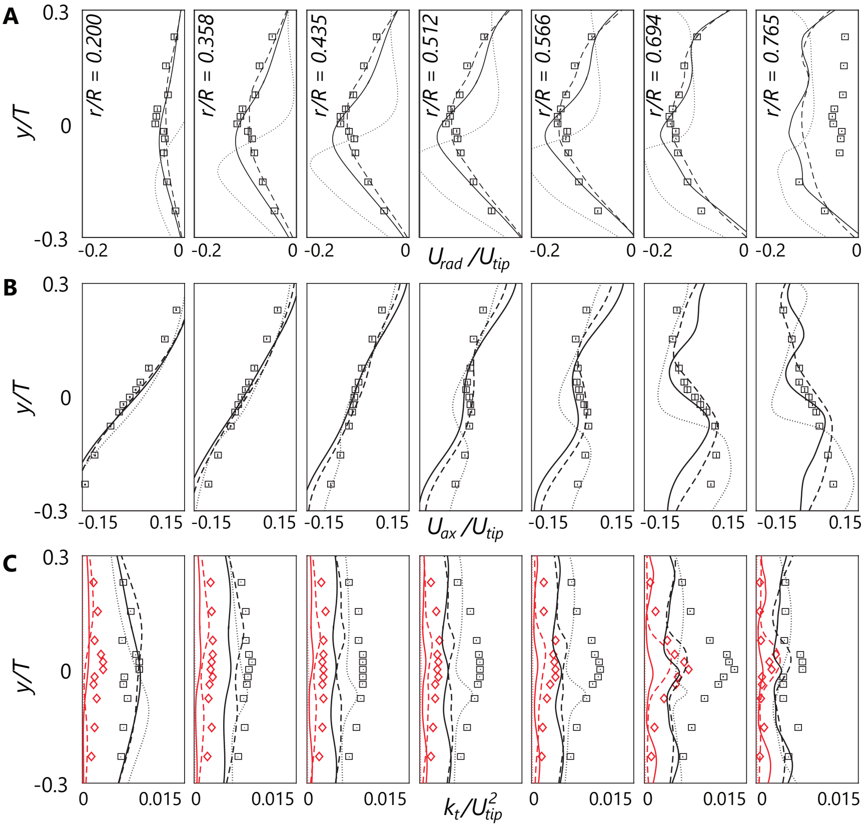

Figure 3.12: Comparison of axial profiles for **A:** U_{rad}, **B:** U_{ax}, **C:** k_t, with *SM* simulations in the 360° domain. Squares: phase-averaged LDA experimental data, recorded in the baffle plane. For k_t, the black rectangles represent the total kinetic energy k_{t*}, the red diamonds show the MI energy k_{MI}. Lines: CFD results at different mesh densities (dotted: *2IF-M-RSM*, dashed: *2IF-M-RKE*, solid: *2IF-F-RKE*).

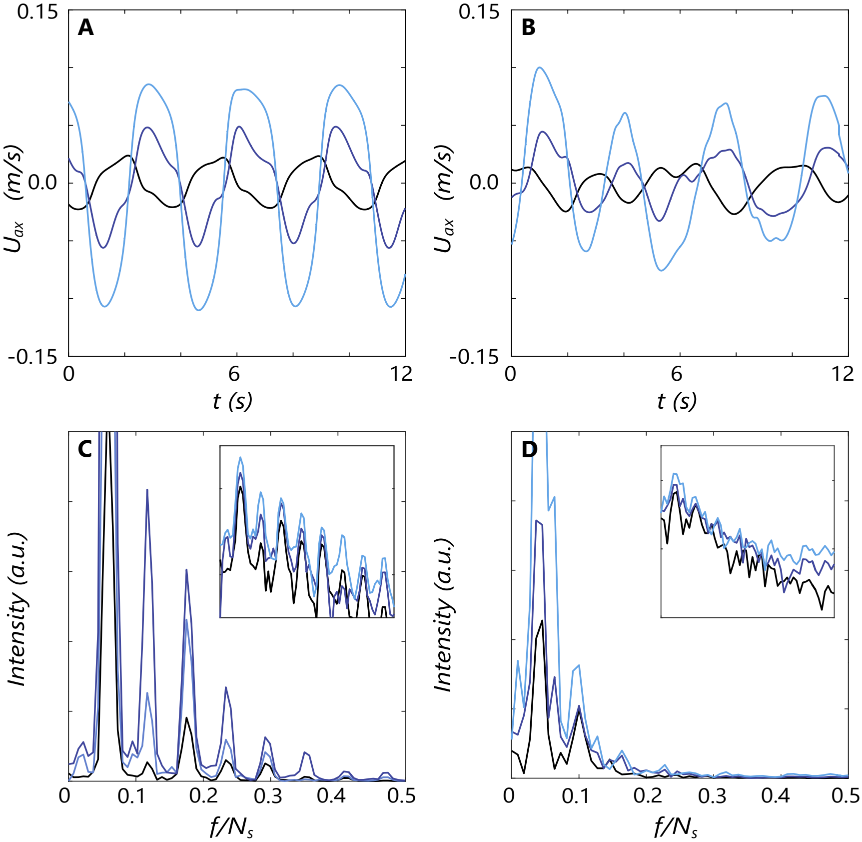

Figure 3.13: **A:** Axial velocity at $y = 0$ versus time, *2IF-M SM-RKE*. **B:** Axial velocity at $y = 0$ versus time, *2IF-F SM-RKE*. **C:** Fourier transform of **A**; inset shows the same graph with a log-y axis. **D:** Fourier transform of **B**; inset shows the same graph with a log-y axis. Black line: $r/R = 0.2$. Dark blue line: $r/R = 0.512$. Light blue line: $r/R = 0.694$.

The qualitative observation that axial oscillations increase with increasing radial position is captured by SM simulations. To some degree, U_{rad} and U_{tan} (not shown) exhibit the opposite trend. The next question is how strongly MIs contribute to mixing. As seen in the snapshots of the velocity vectors (fig. 3.14) and tracer concentration (fig. 3.16), the axial variations result in limited cross-flow between the compartments. Rather, the parallel-flow plane segregating the compartments is displaced as a whole.

Plotting the tracer concentration C_t at fixed monitor points (fig. 3.15) confirms this; the registered concentration oscillates between two levels. This agrees with the segregation plane oscillating as a whole, meaning that the measurement point keeps switching between the compartments. While C_t converges between the compartments eventually, as expected, there is no evidence of significant convective tracer transport at the monitored points; only $r/R = 0.2$ shows some superposed wiggles which hint at some exchange. Snapshots of mixing (fig. 3.16) show that significant carry-over is

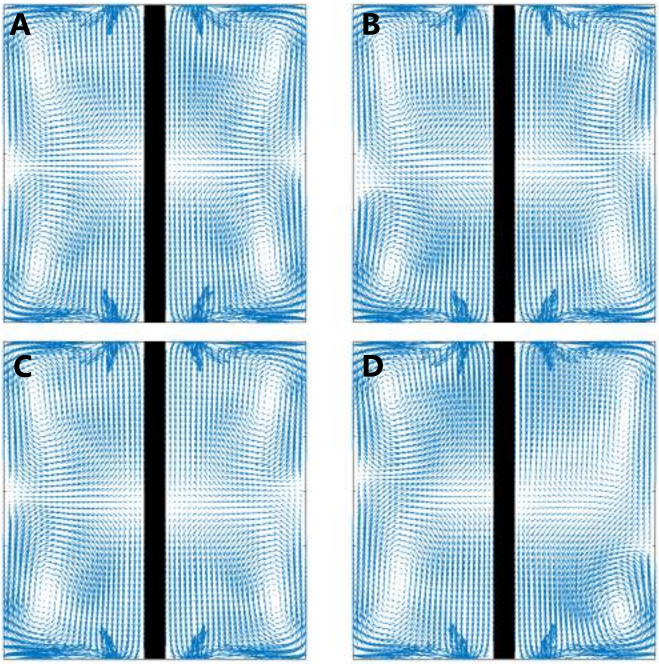

Figure 3.14: Vector fields ($2IM - RKE$) during four stages of a macro-oscillation.

indeed only observed in the divergent flow region near the shaft, and that the imposed MI dynamics do enhance carry-over in this region. There is indeed convective exchange between the compartments due to MIs, but only in the vicinity of the shaft.

3.3.6. Midplane dynamics: Large Eddy Simulations

The velocity components resolved in LES span a much wider range of frequencies, well into the turbulent domain. Hence, we analyze them with the same methods as the LDA data in part I; details on the calculations can be found there. For consistency, the cut-off between MIs and turbulence was set at $f/N_s = 0.1$ when employing spectral integration, with the energy contained in the range $f/N_s < 0.1$ being fully attributed to k_{MI}. This may be an over-estimation of the true MI energy, but because the same cut-off was used in LDA, this method provides the most direct comparison. For *2IF-M*, the reported results were obtained with $\Delta t = 0.0033$, as a larger timespan was resolved for this case.

The frequencies observed with auto-correlation fitting differ between the meshes (table 3.7). As noted earlier, we fit 2 frequency components ($f_{1.1}$ and $f_{2.1}$) and their first harmonics ($f_{1.2}$ and $f_{2.2}$). $2IF - SF$ gives $f_{1.1}/N_s \approx 0.023$ and $f_{2.1}/N_s \approx 0.039$, with strong scatter. The first value agrees well with experimental data for the precessing vortex ($f_{1.1}/N_s \approx 0.02$). The second value underestimates the experimentally observed frequency for the jet instability ($f_{2.1}/N_s \approx 0.06$). In the simulation,

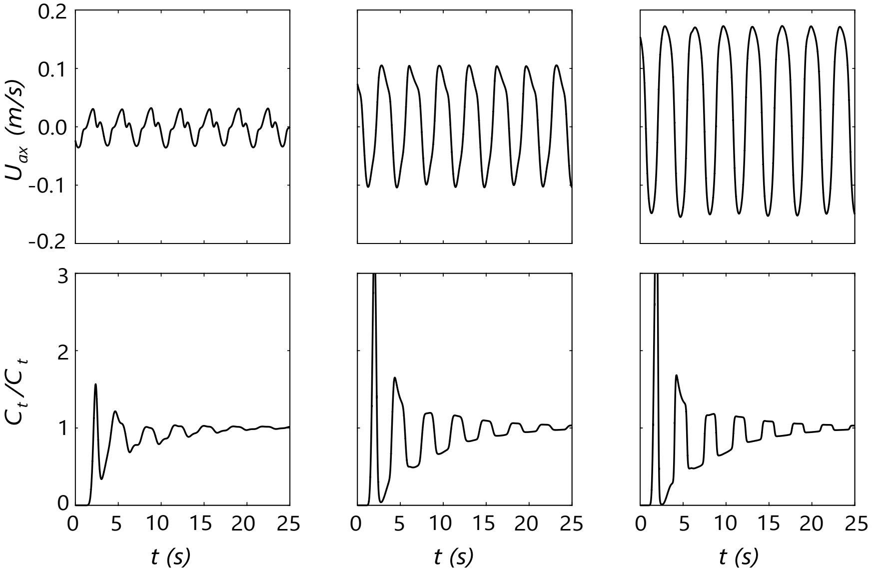

Figure 3.15: Oscillation profiles (*2IF-M*) for U_{ax} (top) and C_t (bottom) at $r/R = 0.2$ (left), $r/R = 0.512$ (middle) and $r/R = 0.6942$ (right) in the place $y = 0$, using the *SM-RKE* approach.

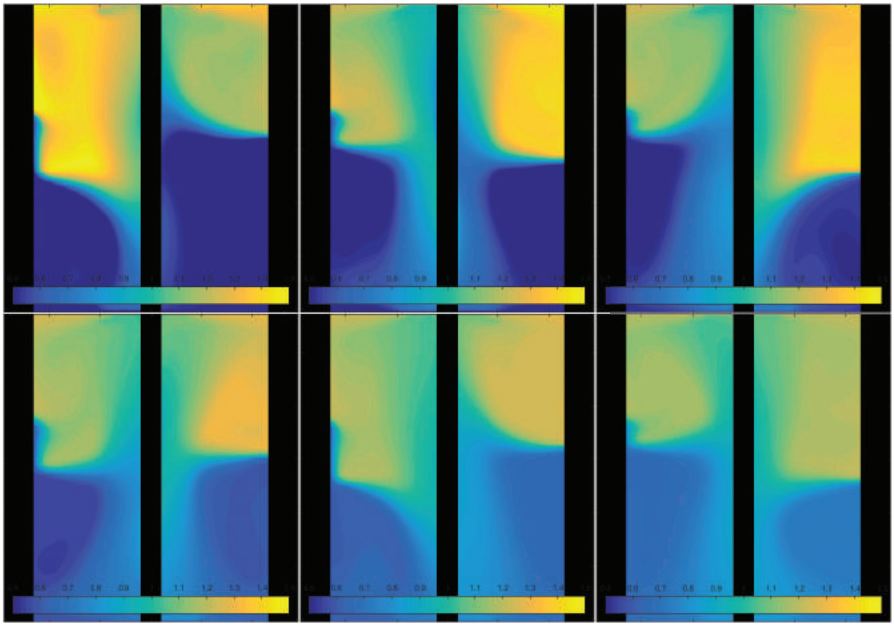

Figure 3.16: Snapshots of mixing at 6 timepoints, $2IF - M - SM$, showing tracer exchange along the shaft is influenced by MIs.

most energy is actually contained in the harmonic frequency, $f_{2.2}/N_s \approx 0.078$, hence $f_{2.1}$ and its harmonic $f_{2.2}$ lie around the experimental jet instability frequency. The quality of the fits (fig. 3.17) is poorer than observed for the experimental data. The data further suggests several higher frequency contributions are present; the current autocorrelation-fit routine leaves these unaccounted for.

$2IF - M$, $f_{1.2}/N_s \approx 0.024$ (which roughly coincides with $f_{2.1}$) and $f_{2.2}/N_s \approx 0.04$ contribute most. While the latter frequency was relatively prominent experimentally, the strongest experimental component $f/N_s = 0.06$ is not observed in the simulation data. As with the SM simulations, the radial correlations show relatively strong oscillations near the shaft (stronger than experimentally observed), while they dampen with radial position. (not shown for brevity).

The spectral density functions (fig. 3.18) show a f^{-1} scaling for $0.1 < f/N_s < 1$, and a $f^{-5/3}$ scaling for $f/N_s > 1$, in line with experimental observations. The moderate spatial resolution of the meshes results in a quick deviation from $-5/3$ scaling at the high-frequency end of the spectra. For the $2IF - SF$ simulations, the filter length ratio was around $\Delta/\eta = 10 - 25$ with η the Kolmogorov lengthscale; the lower value existed near the shaft, the higher near the baffle. A finer mesh may be desired, but for routine use without super-computing facilities, $2IF - SF$ is already much too demanding.

In the low frequency range, the spectral density functions show features around the frequencies that were observed in the auto-correlation fits. The spectrum for $2IF - M$ does show the bi-modal peak observed experimentally, but at frequencies $f_{1.1}/N_s \approx 0.024$ and $f_{2.2}/N_s \approx 0.04$, whereas experimentally $f/N_s = 0.040$ and 0.062 were observed. In $2IF - SF$ the peaks are further apart. Here $f_{1.1}/N_s \approx 0.026$ and $f_{2.2}/N_s \approx 0.078$ contribute most, while $f/N_s \approx 0.040$ is absent. These observations are consistent with the auto-correlation observations.

According to the auto-correlation method, the kinetic energy contained in the MIs is $10 - 30\%$ at $y = 0$ for $2IF - M$, with the maximum at $r/R = 0.512$. For $2IF - SF$, the MI contribution is $5 - 40\%$ with the maximum at $r/R = 0.694$; for comparison, experimental data yielded a contribution of $8 - 20\%$ with the maximum at $r/R = 0.694$. Spectral integration gave a MI kinetic energy contribution of $25 - 30\%$ for $2IF - M$ and $25 - 40\%$ for $2IF - SF$, compared to $25 - 50\%$ experimentally. Overall, we conclude the agreement between LES simulations and experiments is decent in terms of MI-energy. This is supported by the profiles in fig. 3.19. We now further discuss the profiles of velocity and kinetic energy in the mid plane. Again, the spectral integration method is used to assess the MI contribution

Aside from the baffle position, U_{rad} is well captured (fig. 3.19), this is again attributed to the $2D$ baffle geometry. The change from converging to diverging flow in U_{ax} is excellently assessed by all but the crudest mesh. Overall good agreement in k_t is observed, with *2IF-M* over-estimative near the shaft, whereas *2IF-SF* is over-estimative near the baffle. Both simulations reasonably capture k_{MI} near the shaft, but only *2IF-SF* properly captures the peak at $r/R = 0.694$. Even though the frequency distribution does not completely agree with experiments, the overall k_{MI} and k_t are well captured by *2IF-SF*, in line with the good assessment of θ_{95}. The slight under-

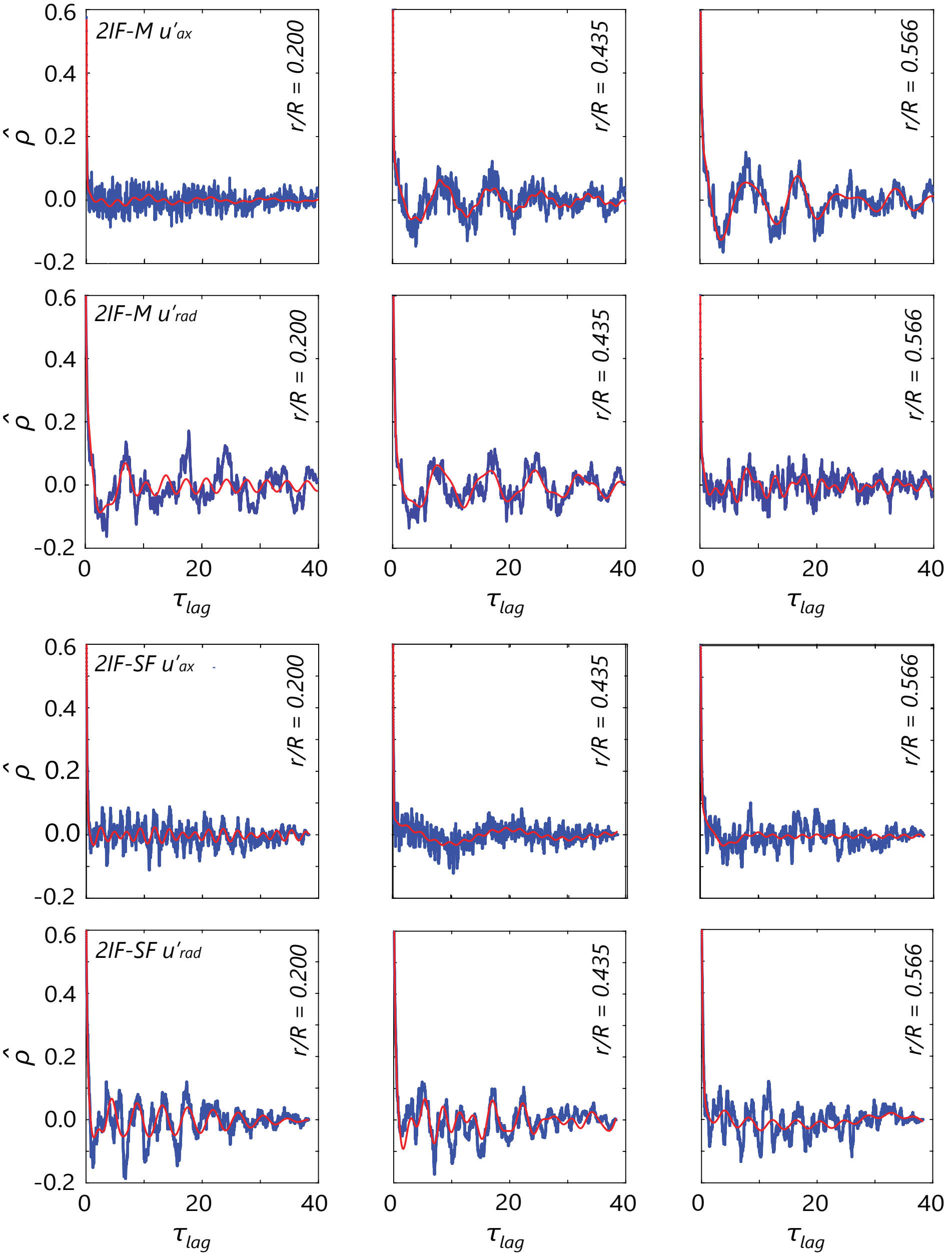

Figure 3.17: Fitted auto-correlation functions for $2IF-M-LES$ (top) and $2IF-SF-LES$ (bottom) at $y=0$, at 3 radial positions. Blue line: raw data. Red line: fitted damped cosine function.

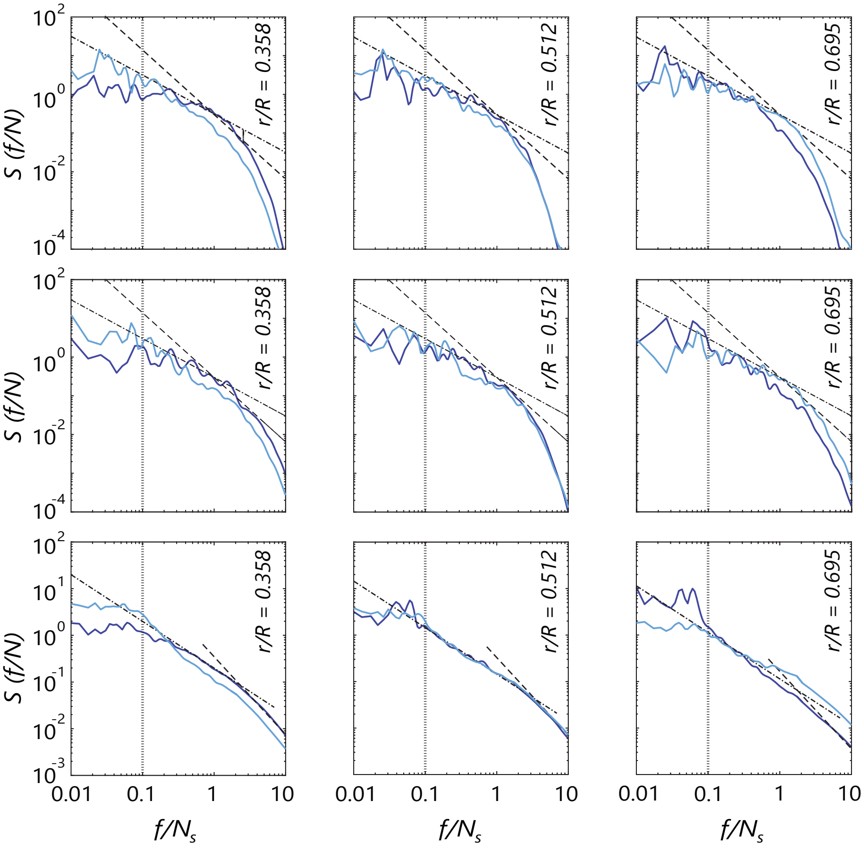

Figure 3.18: Spectral density functions of u'_{ax} (dark blue) and u'_{rad} (light blue) at 3 radial positions, at $y = 0$. **A:** *2IF-M* LES . **B:** *2IF-SF-LES*. **C:** Experimental results. Dashed line: $S(f/N_s) \propto (f/N_s)^{-5/3}$. Dash-dot line: $S(f/N_s) \propto (f/N_s)^{-1}$. Dotted line: cut-off frequency between MI and turbulence.

estimation of θ_{95} by the cruder meshes may be by virtue of their higher k_t near the shaft, which due to its diverging axial flow is the region contributing most to exchange between the compartments.

3.4. Concluding remarks

Multi-Rushton stirred tanks are prone to compartment formation around the impellers, which introduces a rate limiting step for mixing. The mixing time θ_{95} depends strongly on 2 factors: turbulent exchange between the compartments, and the effect of macro-instabilities (MIs) on inter-compartment dynamics. Using *LDA*, we find evidence of MIs at $f/N_s = 0.020$ and $f/N_s = 0.062$, in agreement with earlier reported values for the precessing vortex and jet instability [275]. Depending on the method of estimation, the MIs contain at between 15% (from auto-correlation) and 30% (from spectral integration) of the kinetic energy, although close to the baffle this may be as high as

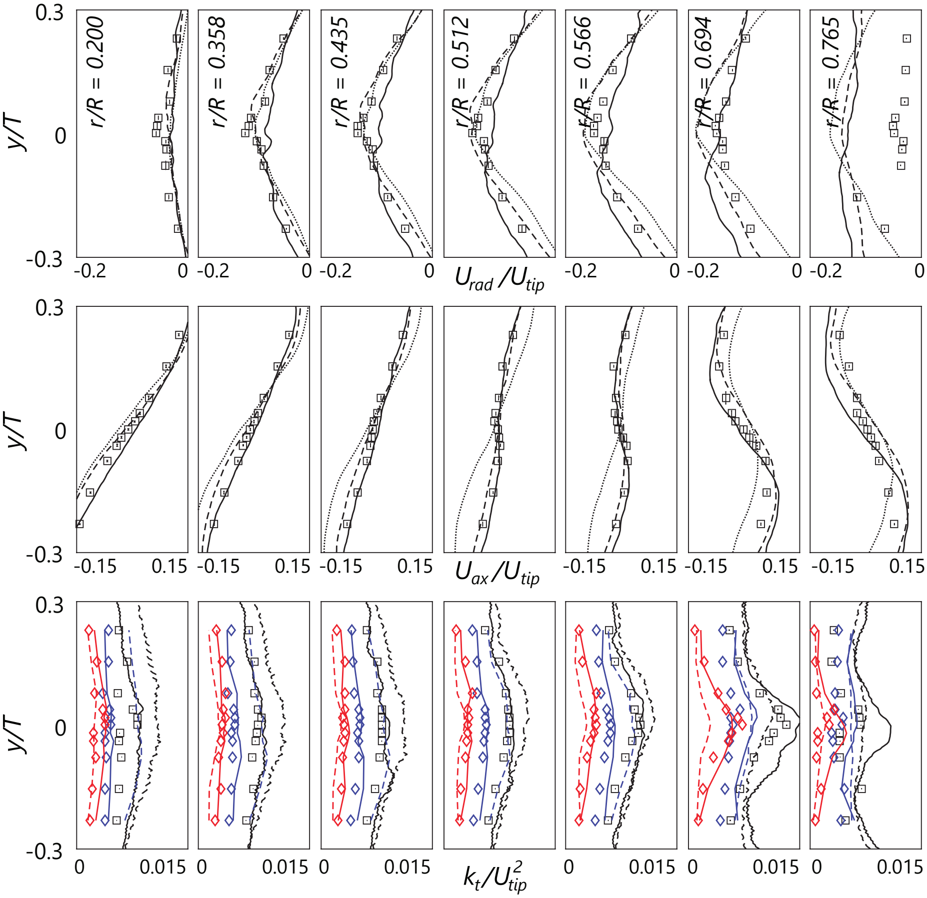

Figure 3.19: Comparison of axial profiles for **A:** U_{rad}, **B:** U_{ax}, **C:** k_t in the baffle plane, for *LES* simulations. Black squares: LDA data. For k_t, the black squares show the total energy k_{t*}, the blue diamonds the turbulent kinetic energy k_t, and the red diamonds the MI energy k_{MI}. Black, blue and red lines show the simulation results for k_{t*}, k_t and k_{MI}, respectively. Dotted line: $2IF-C-LES$ Dashed line: $2IF-M-LES$, Solid line: $2IF-SF-LES$.

$20 - 50\%$, mostly in the axial velocity fluctuations.

Multiple reference frame (MRF) simulations consistently over-predict θ_{95}. In part, this is due to the inability to capture transient MIs. Furthermore, Reynolds Averaging of the inter-compartment flow yields a parallel, largely shear-free flow, which seems to inadequately capture the generation of turbulent kinetic energy (k_t) in the converging flow region, yielding a local under-estimation of k_t. θ_{95} was progressively over-estimated with mesh density, with a 100% over-estimation at the finest mesh. Some cases deviated from typical mesh convergence due to a shift in the predicted mid-plane position, which increased convective transport between the impeller compartments. Possibly the presence of MIs allows for some ambiguity in the segregation plane position when forced into a steady-state solution, which makes the simulations sensitive to the mesh layout and initial conditions. Modeling a $60°$ section of the domain yielded very poor flow agreement around the midplane, in contrast to good agreement around the impeller. Typically, Q_{ax} was higher yielding lower θ_{95}; not as the result of better flow prediction, but due to forcing an inherently unstable plane into a $6-$fold periodic position.

SM simulations perform better than MRF due to their ability to capture MIs, although the MI energy was underestimated compared to experiments. As for MRF, the peak in k_t near the baffle was not resolved. Together, these observations explain why SM outperforms MRF, but still over-estimates θ_{95} by approx. 20%. Some mesh dependency was observed for the MI frequency, but with a frequency around $f/N_s = 0.04 - 0.06$ agreement with experimental data was very reasonable. It was observed the MIs did not strongly disturb the segregation between the compartments, rather the segregation plane moved up and down as a whole. Only near the shaft, where the flow is strongly diverging, mass exchange was significantly affected by MIs. As for the MRF simulations, using the Reynolds Stress Model yielded no advantage over realizable $k - \epsilon$. In fact, the latter compared favorable here.

LES simulations exhibited a wider range of MIs than were observed experimentally, including some higher frequency components, and a less sharp distinction of the low-frequency peaks. The observed frequencies were mesh dependent, with the medium mesh ($2M$ cells) yielding $f/N_s \approx 0.024,\ 0.040$ and the finer mesh ($10M$ cells) $f/N_s \approx 0.026,\ 0.078$. Experimentally, $f/N_s = 0.040$ and $f/N_s = 0.061$ dominated. The MI energy k_{MI} was under-predicted by the medium mesh, while the total kinetic energy was over-predicted near the shaft. As this is the region mostly contributing to mass exchange, it may explain why θ_{95} is under-predicted by LES on the crude and medium resolution mesh. The finer mesh yields a generally good prediction of both k_{MI} and k_t, while θ_{95} was in excellent agreement with experiments.

The applied LES approach did somewhat over-predict k_t and strongly under-predict ϵ in the impeller discharge stream. The employed dynamic Smagorinsky model predicts low values of constant C_s to which this is attributable. While taking C_s constant and fine-tuning it may increase agreement [112], a more universal approach is desired. As such, there is room for further exploration of alternative subgrid models and other transient simulation approaches ((ID)DES, hybrid LES-RANS) in stirred tank applications. Strictly speaking, the finest current LES study was under-resolved, especially in

Table 3.7: Axial RMS-velocity, oscillation frequencies and their contributions for $2IF-M-LES$ and $2IF-SF-LES$ in the plane $y=0$ at different radial positions, using the periodic-fitting approach. The coefficient c represent the contribution to the Reynolds stress $\overline{u'u'}$, with $c_{i.j}$ the j^{th} harmonic of frequency component i. For brevity, only u'_{ax} is reported. Top rows: $2IF-M$. Bottom rows: $2IF-SF$.

r/R	0.200	0.2358	0.3435	0.512	0.566	0.694	0.765
$u'_{ax,M}$ (m/s)	0.089	0.111	0.126	0.147	0.164	0.181	0.148
$c_{1.1,ax,M}$	0	0.026	0	0.001	0.022	0	0
$c_{1.2,ax,M}$	0.033	0.011	0.033	0.08	0.117	0.110	0.049
$c_{2.1,ax,M}$	0.002	0.005	0	0.007	0	0.015	0.023
$c_{2.2,ax,M}$	0.003	0.071	0.017	0.141	0.065	0.045	0.039
$f_{1.1,ax,M}/N_s$	0.014	0.010	0.012	0.012	0.012	0.012	0.013
$f_{2.1,ax,M}/N_s$	0.019	0.022	0.017	0.021	0.018	0.022	0.023
$u'_{ax,SF}$ (m/s)	0.088	0.106	0.117	0.132	0.148	0.208	0.174
$c_{1.1,ax,SF}$	0	0	0.042	0.068	0.086	0.135	0.088
$c_{1.2,ax,SF}$	0.011	0.007	0	0.014	0	0	0.039
$c_{2.1,ax,SF}$	0	0	0.005	0	0	0.013	0
$c_{2.2,ax,SF}$	0.022	0.09	0.006	0.030	0.006	0.210	0.108
$f_{1.1,ax,SF}/N_s$	0.034	0.026	0.010	0.024	0.020	0.022	0.023
$f_{2.1,ax,SF}/N_s$	0.043	0.042	0.042	0.036	0.040	0.036	0.035

the impeller region. Higher resolution studies may be desirable for further fundamental studies, but already the current fine mesh is considered too demanding for routine mixing studies. Despite these shortcomings, LES performed well in terms of mixing assessment, even on the crudest meshes which far from resolve all energy carrying turbulence scales. As both SM and LES mispredict (θ_{95}) to a similar degree at the crude meshes, and both have similar computational demands, both are currently considered to be reasonably options for mixing assessment provided their degree of error is kept in account; both are clearly preferred above MRF. However, if computational facilities allow for finer meshes, LES is the preferred choice.

In applications like long-term modeling of (bio)chemical dynamics in mixing tanks, the use of transient simulation models is highly undesirable from the perspective of computation time, and some degree of mismatch in the mixing time may be tolerable. Here, Sc_t tuning can be used to improve agreement in mixing behavior; it should be considered to adjust Sc_t only in the mid-plane region to avoid an unrealistic increase in mixing in the bulk domain. Such tuning does require the availability of experimental data (or high resolution simulation data) to tune against, reducing the predictive value of such an approach.

4

Practical guidelines for Euler-Lagrange simulations of bioreactors

Lapin et al. [23] proposed an Euler-Lagrange CFD method to study the impact of extra-cellular gradients in industrial bioreactors from the microbial point of view. The discrete representation of the biomass phase yields an advantageous perspective for studying the impact of extra-cellular variations on the metabolism, but at significant computational cost. In particular, the tracked number of particles and the applied time resolution have a large impact on both the accuracy and the runtime of the simulation. In this chapter we study the influence of these parameters on both the accuracy of the simulation and the computation time. Furthermore, reaction coupling schemes for practical implementation in ANSYS FLUENT are treated. We provide guidelines for accurate Euler-Lagrange bioreactor simulations in ANSYS FLUENT at minimal computational cost.

4.1. Introduction

In many (bio)chemical reactors, reaction takes place inside a discrete phase such as micro-organisms or catalysts particles, with transport occurring in the bulk phase. If the timescale of bulk mixing is in the range of or longer than the reaction timescale, the competition between reaction and bulk mixing will result in spatial substrate heterogeneity. When the discrete phase is mobile, such as in a slurry reactor or fermentor, micro-organisms/particles will see continuous changes in their environment as they move around. The spatial substrate gradients inside the reactor, translate to temporal substrate variations from the organism's, catalyst's or particle's reference frame [29].

Focusing now on a bioreactor, the biomass specific production rate q_p of the desired component is typically governed by a complex metabolic reaction network, with the reaction rates depending both on the availability of extra-cellular substrates (such as sugar and oxygen) and intra-cellular components (such as amino acids and ATP). The adaptation of organisms to their surroundings does not occur instantaneously [276], meaning that the intra-cellular and extra-cellular conditions will typically not be in equilibrium. Consequently, q_p may vary in time, and is a function of the organism's trajectory through space: the history of the particle's extracellular exposure influences its intracellular state. As a result, the observed production rate of the entire population may differ considerably from an ideal mixing situation [16]. Second, there may be considerable heterogeneity *within* the population [13].

Published as: C. Haringa, H.J. Noorman and R.F. Mudde. Lagrangian modeling of hydrodynamic–kinetic interactions in (bio)chemical reactors: Practical implementation and setup guidelines, *Chemical Engineering Science*, 157:159-168, 2017

Lapin et al. [21, 23] proposed to study the response of organisms to extra-cellular variations computationally, by combining Euler-Lagrange computational fluid dynamics (CFD) with metabolic models to incorporate metabolic (reaction) dynamics (MD). In their work, they explored synchronized NAD/NADH oscillations in yeast, coupling a metabolic model of $O(10)$ reactions, and successfully reproduced the amplitude and frequency of such oscillations, as well as the eventual de-synchronization. Although this particular reaction has no direct industrial significance, capturing this out-of-equilibrium interplay between the extra- and intra-cellular domain shows the efficacy of the method. However, Lapin et al. left several computational details that may influence the accuracy of the computation undiscussed. Furthermore, their implementation considered an in-house code, while many users rely on commercial or open-source software packages. Here, we show that the proposed methodology can easily be incorporated in a commercial code, discuss a range of implementation aspects, and set up guidelines for accurate 2—way coupled Euler-Lagrange bioreactor studies.

4.1.1. CFD-MD coupling

Due to computational constraints, early CFD-MD work related to bioreactors often remained limited to the application of unstructured kinetic models (i.e. [16]), simulating only the uptake of substrate, or linking growth and production rate directly to the substrate uptake rate via a Herbert-Pirt equation. As such models assume an instantaneous adaptation of the metabolism to the extra-cellular conditions, they are unsuitable when the intra- and extra-cellular conditions are not in equilibrium.

More recently, the adaptation of the metabolism to environmental fluctuations has been included via two approaches: the population balance approach and Euler-Lagrange (EL) approach. In the population balance approach, micro-organisms are modeled as a component of the liquid phase. The biomass specific growth rate μ is typically applied to describe population heterogeneity [18, 19, 26], using empirical relations to specify how μ adapts to the local extracellular environment. This method is suitable for situations where all relevant processes can be described as a function of μ. However, metabolic fluctuations may take place on shorter timescales than growth rate fluctuations, and complex mutual interaction between metabolite- and enzyme levels may mean that solely considering μ to describe population heterogeneity may be too limited. Extending the population balance approach to several mutually interacting intra-cellular species may, however, quickly become cumbersome.

In the EL-approaches the biomass phase is represented by a large number of virtual particles carrying an internal parameter vector describing their state [21, 23]. These virtual particles are further referred to as parcels, to distinguish between computational and physical biomass particles. A large number of intra-cellular components and their mutual interactions can be tracked for each parcel via a structured metabolic model. This makes the EL method specifically suitable to study the effect of reactor heterogeneity on metabolic timescales, and to study how the variations in multiple metabolites lead to heterogeneity in (among others) μ and q_p [21]. In our opinion, coupling complex metabolic models in which the intra-cellular response is governed

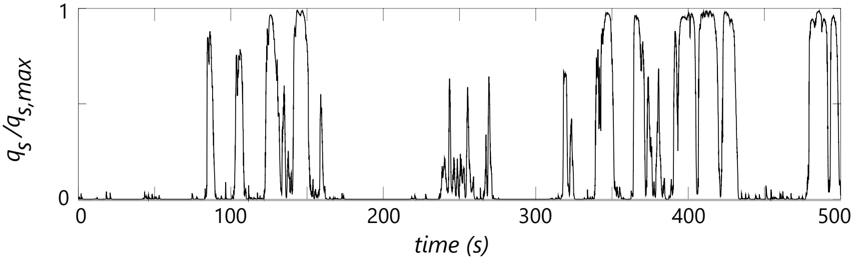

Figure 4.1: Example of an uptake rate signal (lifeline) as experienced by a single parcel in an Euler-Lagrange simulation (scaled with maximum biomass specific substrate uptake rate $q_{s,max}$. This time-series is a result of a spatial gradient as observed from the organism's point of view.

by more parameters than just μ, is more straightforward in the Euler-Lagrange approach.

Besides the easy coupling of complex metabolic models, a second advantage is the viewpoint that the EL method offers. The use of parcels makes it straightforward to study the observed extra-cellular conditions over time for each parcel, and to monitor the intra-cellular response to these conditions. From this viewpoint, it is straightforward to construct 'parameter versus time' series for each parcel, for example the biomass specific uptake rate q_s versus t series shown in figure 4.1. We refer to such timeseries as lifelines, in this case the q_s-lifeline. Statistical processing lifelines, which we will discuss in later chapters, provides direct insight in the response of the metabolism to extra-cellular variations and distributions of the magnitude and duration of extra-cellular variations can easily be collected. Since experimental scale-down simulators should replicate such variations to test organisms under industrially representative conditions, these statistics are a valuable basis of scale-down design. In our opinion, these advantages make the EL-approach the preferred approach to study the impact of substrate gradients on the microbial metabolism, and to provide a basis of design for scale-down simulators.

A major challenge of the EL method is the significant computational burden. First, the large range of timescales in the problem leads to the requirement to simulate a significant period of flow time, while a high temporal resolution is required to compute the parcel trajectories. Second, a large number of parcels (N_p) may be required to obtain an accurate solution, in case the metabolic model is coupled to the parcel phase. In case the uptake rate of extra-cellular compounds is fully determined by the extra-cellular conditions, the rates can be coupled to the Eulerian phase, which means the parcels act solely as tracers and N_p does not affect the Eulerian solution. With fully Eulerian kinetics, N_p and t_{flow} (the total simulated flow time) should be sufficient to obtain converged lifeline statistics, but there is no minimum N_p requirement. In any case the timestep size Δt_c should still be significantly shorter than the timescale of the smallest flow features, for successful particle tracking.

Here, we focus on metabolic-coupled EL simulation, where the value of N_p will affect the solution, and a minimum N_p requirement exists. The local q_s may be influenced by the internal state of the organisms, which means the local q_s is determined by the biomass-carrying Lagrangian phase rather than the Eulerian phase. This means uptake of substrate from the liquid phase becomes an inter-phase exchange effect, only occurring in grid cells where parcels are present. Due to the point-like nature of parcels, the amount of biomass in a given volume element is directly proportional to the number of parcels in that volume element. An insufficient number of parcels leads to artificial spatial variations in the biomass concentration, C_x, and consequently to artificial spatial variations in q_s and C_s. As will be discussed in section 4.1.2, the computation time depends strongly on the number of tracked parcels N_p, and on the required time resolution Δt. In this work, we consider what the minimum number of parcels N_p and maximum allowed timestep size Δt is to provide a good trade-off between accuracy and computational costs for a metabolically coupled Euler-Lagrange simulation. Based on an evaluation of timescales involved in the problem, we present how these values can be predicted based on simulation parameters. These guidelines provide a basis for the computationally efficient application of Euler-Lagrange CFD to study the effects of non-ideal mixing on the performance of industrial scale bioreactors.

4.1.2. Problem outline

With agitation speeds of $N_s > 1$ s^{-1}, the time resolution Δt required to resolve the parcel motion is in the order $\Delta t \approx 5 - 50$ ms. A similar time resolution is required to explicitly model fast reactions such as substrate assimilation and ATP consumption [276]. The 95 % mixing time τ_{95} is typically in the order of one or several minutes [277], and several (approx. 10) mixing times should be simulated to properly resolve the magnitude- and duration distributions for extra-cellular substrate fluctuations. This means in the order of 30 min flow time must be resolved for a typical industrial case. Reactions related to (for example) enzyme production may act on the timescales of hours [236]. If the goal is to study a fermentation including the influence of enzyme dynamics on biomass specific growth, production and uptake rates, the resolved flowtime requirement may be in the order of hours to days, with $O(10)$ ms time resolution. Clearly, such simulations will be computationally demanding especially due to the large number of timesteps, and the computational burden per timestep must be kept to a minimum.

Efficient modeling of stirred tank flows in a fully Eulerian fashion already received considerable interest in literature. Hence, we focus here on the Lagrangian aspects of the simulation. These aspects have received less interest as, in the conventional applications of Euler-Lagrange methods, the parcel computations are typically a minor contribution to the total computation time. In our particular application this is not the case. Under the simplification that the flowfield is in steady state, it is not required to update the flowfield every timestep, leaving operations related to parcel tracking as the major contributor to the total computation time. It must be noted that if this steady-flowfield simplification cannot be made (when the sliding mesh model is used to model the impeller, for example), Eulerian updating is indeed the dominant contribution to the computation time. This assumption, and other aspects related to the Eulerian implementation, are presented in section 4.3.1.

Computational demands of parcel tracking Typically, the Stokes number for a microorganism $St < 0.01$ and massless parcel tracking may be used. This means parcels immediately adapt to the local flow velocity and no force balance has to be solved, reducing the computation time considerably. We will briefly consider computational cost. Running parcel tracking-only simulations on one core of a 2.4GHz XEON E5-2665 established that in ANSYS FLUENT 15.07 the computation time per parcel $t_{comp} \approx 5 - 10 \cdot 10^{-6}$ s, without file output. Here, t_{comp} became independent of N_p for $N_p > 10^5$, meaning the total calculation time scales linearly with N_p for such values. In the case of file output, $t_{comp} \approx 20 - 30 \cdot 10^{-6}$ s when writing 5 tracking parameters to file for each parcel, each timestep. Clearly, file output contributes significantly to the total computation time. In many cases, writing data on only a subset of the total parcel population suffices for the study of metabolic statistics, and it may not be necessary to write data with the same temporal resolution as the simulation time-stepping. Taking this in consideration and writing only the necessary data can save considerable computation time. The specifics will be highly case-dependent however, and are therefore out of the scope of this chapter.

Assuming an average computational demand of $t_{comp} = 10 \cdot 10^{-6}$ s/particle (including optimized file output) and a fairly typical time resolution of $\Delta t = 30$ ms per timestep, the total computation time is 67 h per hour flow-time for $2 \cdot 10^5$ parcels on a single processor; resolving one day of flowtime on a 16-core machine, assuming perfect scalability, would take around 4 days wall-clock time with the applied models. As the runtime scales (approximately) linearly with N_p and inversely with Δt, the benefit of optimizing these two parameters is clear. This leads to the questions: What is the minimum required number of parcels N_p and the maximum allowed timestep size Δt to achieve accurate results? In this case, accurate means the simulation outcome is independent of N_p and Δt and, for a simple reaction model, comparable to results for an Eulerian simulation with a homogeneous biomass concentration C_x, using the same mesh. Preferably, we want to be able to determine the required N_p and Δt for a given simulation problem a priori, rather than resorting to trial and error. Therefore, we first turn to a theoretical approach for the prediction of N_p.

4.2. Setting the number of particles

4.2.1. Artificial concentration variations

A typical CFD mesh of a reactor contains $N_c = O(10^5 - 10^6)$ grid cells where a factor $100 - 1000$ volume difference between cells is common due to local refinement. When $N_p \approx N_c$, large grid cells at all times contain tens of parcels while the smallest cells rarely contain one, inducing artificial spatial biomass concentration gradients. Taking $N_p >>> N_c$ gives an approximately homogeneous biomass distribution, but at excessive computational demands in all but a few applications. Since q_s is directly coupled to the biomass availability, artificial biomass variations inherently give rise to artificial substrate concentration gradients in the vicinity of the parcel, as indicated in figure 4.2 **A**. This need not be a problem if mixing in the direct surrounding of the parcel is sufficiently fast compared to reaction, such that the magnitude of artificial substrate gradients is kept small. In order to estimate how many parcels are required

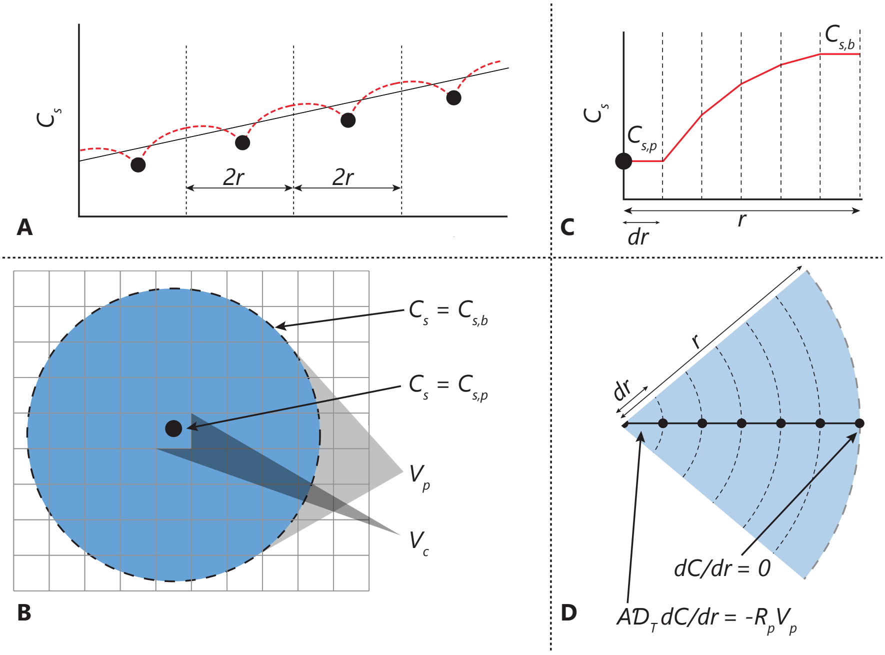

Figure 4.2: An outline of the computational problem: **A:** 1-D representation of computational substrate gradients. The black line represents the physical concentration profile. The dashed red line illustrates the concentration profile that might be found with parcel-coupled reactions. **B:** Hypothetical picture of a single parcel in a fine 2-D grid, outlining the defined volumes and concentrations. **C:** Enlarged view of the substrate concentration profile around a single spherical parcel assuming radial symmetry. The dashed lines indicate the grid cells. **D:** translation from the hypothetical image to the numerical implementation, including boundary conditions.

to make the effect of artificial substrate gradients negligible, we first need to estimate the magnitude of the gradient around the particle as a function of process parameters.

4.2.2. Predicting artificial gradients

Consider a $3-$D domain with volume V_T containing N_p point-like biomass parcels with an equidistant particle spacing. Although the point parcels themselves have no true volume, each parcel has an associated volume $V_p = V_T/N_p$; the parcel represents the amount of biomass that is contained within this associated volume V_p. We study the concentration field in this volume V_p which, for simplicity, we assume a spherical domain with radius r (figure 4.2 **B**). In reality spherical volumes cannot fill the entire domain of course, but we ignore this fact for the sake of the derivation. The background domain is discretized in grid cells with $V_c < V_p$. Because all biomass inside the volume V_p is concentrated in the central gridcell containing the parcel, substrate uptake only occurs inside this gridcell. The substrate concentration at the edge of V_p is assumed constant and homogeneous with a value $C_{s,b}$. Due to uptake, the concentration in the center $C_{s,p} < C_{s,b}$, causing a substrate flux from the domain edge to the center, eventually resulting in a steady concentration gradient within V_p. This is the artificial concentration gradient arising from the point-like biomass distribution; the situation is sketched in figure 4.2 **C**.

We relate concentrations at the edge and center of V_p as $C_{s,b} = (1+\beta)C_{s,p}$, and use β to quantify the magnitude of the artificial gradient. Below, we will relate β to hydrodynamic and metabolic parameters. Subsequently, we consider that in reality the parcels are not stationary and homogeneously distributed. The random fluctuation of the number of parcels in a cell, $N_{p,c}$, is accounted for by the standard deviation of the binomial distribution. Now, we turn to predicting the value of β.

Predicting β The substrate gradient around a parcel depends on the balance between local mixing and reaction; we assume β is a function of the timescales describing these phenomena. Assuming mixing within V_p is governed by turbulent diffusion, $\mathcal{D}_t$, penetration theory dictates $r_p = \sqrt{\pi \mathcal{D}_t \tau_m}$; rewriting in terms of V_p and solving for τ_m gives eq. 4.1 for a parcel p. The reaction timescale in gridcell c containing $N_{p,c}$ parcels, with parcel-bound reaction rate $r_{s,p}$ is given in eq. 4.2.

$$\tau_{m,p} = \left(\frac{3}{4\pi}\right)^{2/3} \frac{1}{\pi \mathcal{D}_t} V_p^{2/3} \tag{4.1}$$

$$\tau_{r,c} = \frac{C_{s,c} V_c}{N_{p,c} r_{s,p} V_p} \tag{4.2}$$

Since we now study a single parcel, $N_{p,c} = 1$. We apply Monod kinetics with C_x being the biomass concentration: $r_{s,p} = q_{s,max} C_x \cdot [C_{s,p}/(K_s + C_{s,p})]$ [222]. When $C_{s,p} << K_s$, Monod kinetics reduce to 1^{st} order kinetics. Computations showed that β becomes independent of $C_{s,p}$ in this regime. For higher $C_{s,p}$, we find that β decreases as $C_{s,p}$ increases, converging to $\beta = 0$ for $C_{s,p} \to \infty$. Hence, we can consider the 1^{st} order regime where β reaches a maximum ($\beta = \beta_m$) as a worst case-scenario to derive a criterion for N_p. Any N_p criterion that holds for $C_{s,p} << K_s$ also holds for higher values of $C_{s,p}$.

To study how β_m depends on the mentioned timescales, we solve the 1-D diffusion equation in MATLAB (version 8.2); A schematic view of the implementation is shown in figure 4.2 **D**. Reaction takes place at the central node, leading to a boundary condition $A\mathcal{D}_t \frac{dC_s}{dr}(t,0) = -r_{p,c}V_p$. Two different boundary conditions have been applied at the domain edge. Simulations were conducted with fixed $C_{s,b}$ - yielding a steady-state solution - or symmetry boundary condition $\frac{dC_s}{dr}(t,r_p) = 0$. The latter gives a transient batch process. As β_m is independent of C_s, both yielded similar results. Based on a large number of simulations with varying domain volume, hydrodynamic parameters and kinetic parameters, we find the relation of eq. 4.3 from the data shown in figure 4.3 **A**. The different symbols correspond with different numbers of nodes between simulations, their relative offset is attributed to the crude discretization.

$$\beta_m = \frac{4\pi^2}{3}\left(\frac{V_c}{V_p}\right)^{2/3} \cdot \frac{\tau_{m,p}}{\tau_{r,c}} \tag{4.3}$$

4.2.3. Distribution of parcels in a volume

Because of turbulent motion, the distribution of parcels inside the volume V_T is not equidistant, but more or less random and the probability of finding $N_{p,c}$ parcels in a volume V_c follows from the binomial distribution. For the magnitude of artificial gradients the absolute number $N_{p,c}$ is not relevant; we have to consider the number of parcels inside a cell, compared to neighboring cells. This number will fluctuate as the parcels are in constant motion. Therefore we use the standard deviation of the binomial distribution, eq. 4.4 to describe the effect of non-homogeneous distribution and parcel motion.

$$\sigma_{p,c} = \left(N_p \frac{V_c}{V_T}\left(1 - \frac{V_c}{V_T}\right)\right)^{1/2} \tag{4.4}$$

4.2.4. Quantifying artificial gradients in CFD simulations

In CFD software we cannot observe the artificial gradients surrounding a parcel directly (unless N_p is really small). Due to these gradients, the concentration C_s in any given gridcell c will be somewhat lower when it contains a parcel, then when it contains none. The artificial concentration gradients near parcels will hence result in temporal concentration fluctuations in each gridcell, which are easily quantified. Such variations are absent when the biomass phase is homogeneously distributed. To quantify these fluctuations we consider the concentration C_s in every gridcell c as a function time. The Coefficient-of-variation (CoV_c) of concentration variations in cell c is defined as the ratio of the temporal standard deviation $\sigma_{s,c}$ over the temporal mean $\langle C_{s,c}\rangle$. Subsequently, CoV_c is volume-averaged to yield a single number quantifying the fluctuations in the simulation, shown in equation 4.5.

$$\chi = \langle CoV_c\rangle \equiv \langle\frac{\sigma_{s,c}}{\overline{\overline{C_{s,c}}}}\rangle \tag{4.5}$$

With χ describing artificial gradients in simulations, we pose the proportionality $\chi \propto \langle\beta_{m,c}\sigma_{p,c}\rangle$ with a yet to be determined proportionality constant α_g. $\langle\beta_{m,c}\sigma_{p,c}\rangle$ is determined by solving eq. 4.3 and 4.4 for each gridcell, and volume-averaging their product over all cells. The constant α_g describes all effects that have not been accounted for in $\langle\beta_{m,c}\sigma_{p,c}\rangle$, including the fact that all above computations assumed the artificial gradient around the parcel was completely developed, while in reality it will be very dynamic. Now combining $\chi = \alpha_g\langle\beta_{m,c}\sigma_{p,c}\rangle$ with equations 4.1 - 4.4, we can solve for N_p, yielding equation 4.6. For convenience, the numerical constant $4\pi^2/3$ is absorbed in α_g in this equation and the rest of this work; accordingly, β_m is scaled to

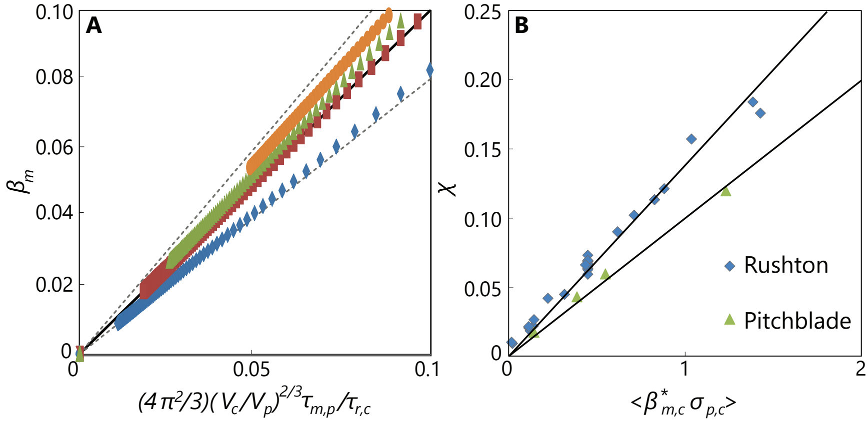

Figure 4.3: **A:** Calculated β_m versus predicting equation for a variety of settings. The different symbols indicate numerical resolution: $n_g = 3$ (blue diamonds), 5 (red squares), 9 (green triangles), 13 (orange circles). Black line: $X = Y$. Dashed lines: 20% deviation from the proposed relation. **B:** Observed fluctuations versus predicted value for the Rushton geometry and PBT geometry. The black lines show the obtained fits used for determining α_g.

$\beta^*_m = \beta_m/(4\pi^2/3)$. In eq. 4.6, the allowable artificial gradient magnitude is specified via χ (we use $\chi = 0.05$ as a default), and constant α_g has yet to be determined.

$$N_p = \alpha_g^2 \left[\frac{q_{s,max} C_x}{K_s \chi \sqrt{V_T}} \sum \left(\frac{V_c^{7/6}}{\mathcal{D}_{t,c}} \left(1 - \left(\frac{V_c}{V_T} \right) \right)^{1/2} \right) \right]^2 \tag{4.6}$$

4.3. CFD implementation

Simulations were performed in the commercial software package ANSYS FLUENT 15.07, which includes Euler-Lagrange modeling as the DPM model. FLUENT is equipped with a parcel-reaction model, but this model is not compatible with the massless tracking formulation. Hence, reaction routines were added as User-Defined Functions (UDFs). To allow direct comparison with Eulerian simulations for validation of the Euler-Lagrange implementation, the reaction rate used in this work is a function of a single external scalar only: $r_{s,p} = f(C_{s,c})$. Two different schemes for inter-phase reaction coupling were tested. In Approach I, the source term $S_{s,c}(t + \Delta t_c) = \Sigma N_{p,c} r_{s,p}(t)\Delta t_p$ with $\Sigma(\Delta t_p) = \Delta t_c$ and Δt_p a flexible timestep size determined by FLUENT. The value of the $S_{s,c}$ is determined at the beginning of each timestep, and is not updated in subsequent iterations of the Eulerian field. In essence, this makes approach I non-iterative. In Approach II, $S_{s,c}(t + \Delta t_c) = \Sigma N_{p,c} r_{s,p}(t + \Delta t_c)\Delta t_c$ where $S_{s,c}$ is recalculated every iteration, possibly increasing accuracy but also calculation time.

4.3.1. Computational setup

A RANS simulation approach was selected to keep the computational demands low; its accuracy is sufficient for providing insight in reactor-scale substrate concentration gradients [16]. The standard $k-\epsilon$ model was used in all simulations. Although this model is fundamentally weak for strongly rotating flows [58], it has been well established that the $k-\epsilon$ model can reasonably capture the fluid flow [138], turbulence quantities [59] and mixing time [62] in a stirred vessel. Our own simulations yield comparable results, further specifics have been discussed in the previous chapter. While performance of the $k-\epsilon$ is sufficient for our goals, the guidelines presented in this paper are by no means limited to this turbulence model; they are compatible with any eddy viscosity model.

The steady state Multiple Reference Frame (MRF) model for impeller simulation is favored over the inherently transient Sliding Mesh (SM) approach. In many stirred tank applications, the periodic velocity component arising from rotor-stator interaction is small and the MRF method can be applied [59]. As the MRF method calculates a steady state flowfield, there is no need to recalculate the flow every timestep saving an order of magnitude in computation time. Discretization was 2^{nd} order upwind in space [59] and 2^{nd} order implicit in time. The SIMPLE algorithm was used for pressure-velocity coupling. Convergence was assumed if all residuals were below 10^{-5} and oscillations in the mean velocity magnitude were below 1%.

Reaction and parcel tracking Species tracking was initially enabled including a volumetric (Eulerian) reaction term $r_{s,c} = q_{s,max} C_x \cdot (\frac{C_{s,c}}{K_s + C_{s,c}})$. The turbulent Schmidt number was kept at the default value of 0.7. After the concentration field converged to a steady state, the solver was switched to transient and massless parcels were added via the DPM model. The effect of turbulence was included using the *discrete random walk* model (DRW), where $\sqrt{\overline{u'^2}} = \sqrt{2k_t/3}$ and isotropic turbulence is assumed. During parcel tracking, the baffles and impeller boundary conditions were switched from wall to interface. As k_t vanishes at these walls, parcels tend to get stuck when the wall boundary condition is retained. Parcels were first distributed for 30 impeller revolutions without particle-coupled reactions. After this time, the volumetric reaction model was switched off, and the particle-coupled reaction model was enabled.

Physical conditions Water ($\rho = 1000$ kg/m^3, $\mu_l = 0.001$ Pa s) was used as a working fluid in all simulations. Glucose ($MW = 180$ g/mol) was the substrate. It was assumed that the dissolution of glucose did not influence μ_l and ρ of the continuous phase. The molecular diffusion coefficient $\mathcal{D}_m$ was arbitrarily set to 10^{-9}; the exact value is not of significant influence in turbulent simulations. Glucose uptake by the filamentous fungus *P. chrysogenum* was selected as a model reaction, described by Monod kinetics. De Jonge et al. determined the model parameters to be $q_{s,max} = 1600$ μmol/(g$_{dw}$ h) and $K_s = 7.8$ μmol/kg [44]. In our simulations the biomass concentration is set to $C_x = 10$ g/kg. Since we assume a continuous fluid with the properties of water for model-development purposes here, mass transfer limitations towards the microorganism will play a negligible role [278] and are not included in the simulations.

Table 4.1: An overview of all conducted simulations. Several cases were conducted in duplo. Case names are based on mesh (xxxkc) and parameter variation (I = coupling approach I, II = coupling approach II, LP = Low Power input, TET = tetrahedral, PBT = Pitch Blade Turbine).

Case	s^{-1}	No. Parcels	Δt_c (s)	coupling
51kcI	1.026	$5k$ - $2000k$	0.001 - 5	I
51kcII	1.026	$10k$, $500k$	0.01 - 3	II
51kcLP	0.750	$10k$ - $100k$	0.01	I
166kcI	1.026	$10k$, $500k$	0.01	I
341kcI	1.026	$10k$, $500k$	0.01	I
341kcII	1.026	$10k$, $500k$	0.01	II
TET	1.026	$10k$, $500k$	0.01	I
PBT	1.033	$10k$ - $500k$	0.01	I

As a hypothetical reactor, a flat bottomed tank with $H = T = 5$m agitated by a 6-blade Rushton turbine (RT) with a clearance $\Delta C = T/4$, diameter $D = T/3$ and baffle width was $T/10$ was used. To reduce computational effort $1/6^{th}$ of the tank was modeled, containing a single blade and baffle. The additional baffling was shown to be of negligible influence [59]. Three hexahedral grids with respectively $51k$, $166k$ and $341k$ gridcells, and one tetrahedral grid with $147k$ cells were used. All internals were modeled as thin surfaces. Substrate was fed to the domain via a source term in a region near the impeller top. In all simulations, the conditions were such that $\langle C_s \rangle << K_s$. Additional simulations were performed in a pitch blade tank (PBT), to test if the proportionality constant α_g is influenced by the geometry. The used dimensions are $\Delta C = T/2$, $D = 0.35T$ and $T = 5$ m; the impeller contained 4 blades with an angle of $45°$. For further geometric details, we refer to Bakker et al. [279]. The mesh was fully hexahedral with $99k$ grid cells and covered $1/4^{th}$ of the domain.

Monitoring Each timestep, the mean concentration $\overline{C_s}$, total uptake rate $\Sigma r_{s,p} V_p$, concentration and parcels per gridcell ($C_{s,c},\ N_{p,c}$) and concentration observed by each parcel ($C_{s,p}$) were monitored. To account for transients, the first 15 impeller revolutions with Lagrangian reaction were discarded - in all cases the concentration field was statistically steady after this time. All properties were monitored for $60 - 300$ impeller rotations to derive the reported statistics.

Cases Most simulations were conducted at an agitation speed of $N_s = 1.026$ s^{-1}; one series of simulations was executed with $N_s = 0.75$ s^{-1} to test the influence of power input. The typical timestep was set to $\Delta t_c = 0.01$ s, but other values have been applied to test the influence of Δt_c. An overview of cases is shown in table 4.1.

4.4. Results and discussion

We focus on four aspects of the simulations: 1) we compare χ against $\langle \beta^*_{m,c} \sigma_{p,c} \rangle$ to study the value of α_g under different conditions, 2) we compare mean concentration

$\langle\overline{C_s}\rangle$ between Eulerian and Lagrangian simulations to validate the Lagrangian reaction approach, 3) we study the effect of Δt and 4) we check whether the inter-phase mass balance is closed.

4.4.1. Artificial gradients in FLUENT

Artificial gradients were quantified by monitoring $\sigma_{s,c}/\overline{C_{s,c}}$ in each grid cell, and averaging them to yield χ. Data was stored every timestep and post-processing was performed in MATLAB 8.6.0. In figure 4.3 **B** χ is plotted against $\langle\beta^*_{m,c}\sigma_{p,c}\rangle$. We observe a linear relation between $\langle\beta^*_{m,c}\sigma_{p,c}\rangle$ and χ, in line with our expectations. The proportionality constant α_g is found to be 0.27 for the RT geometry and 0.19 for the PBT. This indicates α_g is dependent on the fermentor geometry. This is attributed to the difference in global flow pattern and thereby global parcel motion. In the RT case, runs with different meshes (hexa- and tetrahedral), different power input and different Δt all collapse on the same line. Also, we see no influence of the coupling mechanism on χ and thereby α_g. Additional runs were conducted in a tank stirred by 2 Rushton turbines, using the geometry of [65]. Here, α_g is also found to be 0.27, which is not surprising as the geometry can be seen as 2 single-RT tanks stacked together. Finally, sliding mesh simulations too yield $\alpha_g = 0.27$ for a Rushton turbine. For brevity, a detailed discussion of the sliding mesh results is omitted.

4.4.2. Mean concentration

A second prerequisite for the successful application of parcel-based reactions, is that the time-average substrate concentration field agrees with the steady state substrate concentration field found in a fully Eulerian simulation, for the simple kinetics applied here. To establish this, we compare the volumetric mean substrate concentration for the Lagrangian and Eulerian reaction implementation. First we consider how $\langle\overline{C_{s,c}}\rangle$ (the Eulerian mean in EL simulations in both space and time) develops with N_p, by comparing $\langle\overline{C_{s,c}}\rangle$ with $\langle\beta^*_{m,c}\sigma_{p,c}\rangle$ (figure 4.4 **A**). As can be expected, $\langle\overline{C_{s,c}}\rangle$ converges to a steady value for $\langle\beta^*_{m,c}\sigma_{p,c}\rangle \rightarrow 0$, with $\langle\overline{C_{s,c}}\rangle$ nearly independent of N_p for $\langle\beta^*_{m,c}\sigma_{p,c}\rangle$ below 0.5.

In table 4.2 we compare $\langle C_{s,c}\rangle$, the volume average in a steady state Eulerian simulation (first column), with the Lagrangian ensemble-and-time average $\overline{C_{s,p}}$ and $\langle\overline{C_{s,c}}\rangle$ for the same mesh. The agreement between $\langle C_{s,c}\rangle$ and $\overline{C_{s,p}}$ is expected; with the essentially 1^{st} order kinetics, there is a unique $\langle C_{s,c}\rangle$ at which substrate uptake and feed balance. This is the average concentration in an Eulerian simulation, and must also be the average concentration observed by the parcels in a Lagrangian simulation, regardless of N_p. The small difference between the meshes shows the Eulerian solution is not yet mesh independent for the $51k$ grid. More striking is the significant mesh dependency of $\langle\overline{C_{s,c}}\rangle$. We attribute this effect to the *DRW* model for turbulent parcel motion.

As noted before, the turbulent kinetic energy k_t vanishes near walls, and the convective velocity is low. Consequently parcels tend to have an unrealistically long residence time in these zones [21]. The effect is most pronounced in the crudest mesh,

Table 4.2: Mean concentration in the volumetric reaction case versus Lagrangian reaction case for selected cases. For the Lagrangian case, both the field mean, and mean observed by parcels is shown. For all cases, $\Delta t_c = 0.01$. Concentrations are given in mol/kg

Case	$\langle C_{s,c} \rangle$	$\langle \overline{C_{s,c}} \rangle$	$\overline{C_{s,p}}$
51kcE-100kp	7.28	2.90	7.06
166kcE-500kp	6.83	6.33	6.83
341kcE-500kp	6.83	7.28	6.83

which has a relatively large ratio of boundary gridcells over bulk gridcells. The result is a somewhat elevated average biomass concentration in some wall regions, most notably the vessel top - near the substrate feed. This leads to a comparatively large uptake in this region and thereby lower $\overline{C_s}$ in the bulk of the vessel. Higher mesh densities result in fewer wall cells compared to bulk gridcells and the offset decreases with increasing mesh resolution. Improvements over the DRW have been suggested, such as anisotropic-DRW or continuous random walk (CRW) [219] and probabilistic methods such as explored by Lapin et al. [21]. We consider the implementation of such methods outside the scope of this work. The main message is that the agreement between $\langle \overline{C_{s,c}} \rangle$ and $\langle C_{s,c} \rangle$ should be checked, as an offset is not fixed by simply increasing N_p. If an offset is detected, it should be checked whether parcels accumulate in certain regions, and measures (either mesh refinement or alternative tracking models) should be implemented.

Turning back to figure 4.4 **A**, the increase in $\langle \overline{C_{s,c}} \rangle$ at high $\langle \beta^*_{m,c} \sigma_{p,c} \rangle$, can be explained by the N_p-independent value of $\overline{C_{s,p}}$. Looking back at figure 4.2 **B** and **C**, the concentration in the parcel-containing grid cell is lower than in the surrounding cells as a result of uptake, an effect that becomes more pronounced with decreasing N_p; hence upon decreasing N_p, $\langle \overline{C_{s,c}} \rangle$ will increase. This notion still holds for the $51k$ grid.

4.4.3. Inter-phase mass balance

Having established the value of α_g, dependence of $\langle \overline{C_{s,c}} \rangle$ on N_p we have established the minimum required N_p for an accurate Euler-Lagrange bioreactor simulation. A final important aspect is the closure of the inter-phase mass balance. The substrate uptake from the field $\Sigma S_{s,c} V_c$, must be balanced by an equal accumulation term ($\Sigma r_p V_p$) in the Lagrangian phase in order to properly study intra-cellular reaction dynamics when more complex models are used. In practice, some imbalance will occur, due to numerical errors in the iterative solution of the scalar field, and due to uptake clipping. The latter occurs when the uptake from a gridcell, $S_{s,c} V_c \Delta t_c$, exceeds the availability in that cell, $C_{s,c} V_c$.

We quantify the instantaneous uptake imbalance as $\lambda(\%) = 100 \cdot \frac{r_{p,c} \Delta V_p \Delta t - S_{s,c} \Delta V_c}{r_{p,c} \Delta V_p \Delta t}$. A typical λ versus time plot is shown in figure 4.4 **B**. Both positive and negative imbalances are observed, the average $\overline{\lambda}$ is slightly positive. This is attributed to the two types of error mentioned above; the iteration error is distributed around 0, clipping

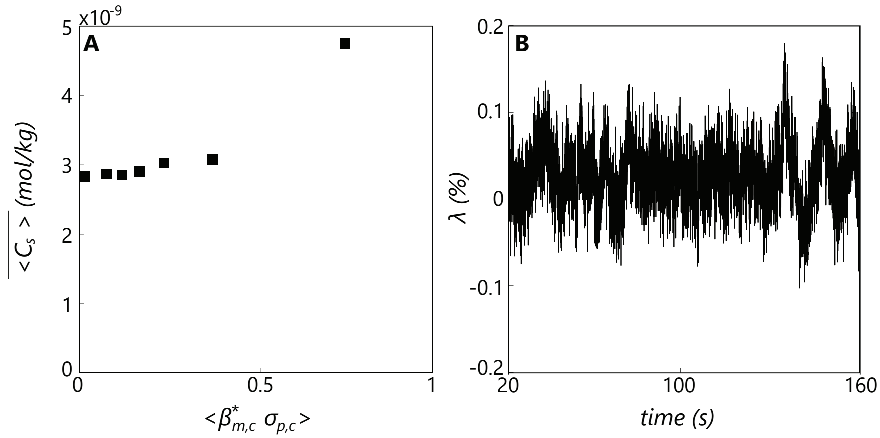

Figure 4.4: **A:** Mean concentration as a function of $\langle\beta^*_{m,c}\sigma_{p,c}\rangle$ showing the convergence of the $\langle\overline{C_s}\rangle$ as a function of N_p, for the $51kcE$ cases. The concentration is nearly independent of N_p for $\langle\beta^*_{m,c}\sigma_{p,c}\rangle$ below 0.5. For all cases, $\Delta t_c = 0.01$. **B:** Signed inter-phase mass imbalance λ versus time for case $166kcI{-}500kp$. The variations between timesteps are mainly due to numerical errors in the iterative solution procedure. Overall, λ is slightly positive with mean offset is $2.8 \cdot 10^{-2}$%. This offset occurs when in some gridcells, substrate uptake exceeds availability and the uptake must be clipped. The low offset magnitude indicates this effect is of negligible.

errors lead to a positive λ. In all cases where $\chi < 0.05$, the absolute time average mass imbalance $|\overline{\lambda}|$ was well below 1%, indicating the inter-phase mass balance is sufficiently closed.

4.4.4. Time step size

As noted in the introduction, the time resolution Δt_c will significantly affect the computation time, given a certain flowtime; a higher Δt_c simply means less timesteps are required for the same simulation. The influence of timestep size Δt_c has been studied in the $51kc$ Rushton grid. First, the effect of Δt_c on the mass imbalance $|\overline{\lambda}|$ is briefly considered. We scale Δt with the reaction timescale, $\Theta = \frac{\Delta t_c q_{s,max} C_x}{K_s}$; for $\Theta > 1$ significant clipping is expected since the uptake per timestep is bigger than the substrate availability. The effect of clipping is clearly visible in figure 4.5 (top). The value of $|\overline{\lambda}|$ is sufficiently small (consistently $< 1\%$) for $\Theta < 0.1$. It is noteworthy that coupling approach I (non-iterative) and II (iterative) yield no significant difference in error, meaning the additional computational burden of recalculating uptake each field iteration is not justified.

To conclude, the effect of timestep size on the χ is checked. The data in figure 4.5 (top) clearly shows that for $\Theta < 1$ there is no effect of Δt on χ. This is in line with our expectations; the parcel timestep Δt_p (controlling uptake and motion) is determined independent of the field timestep Δt_c; as long as there is no significant change in the external scalar field during Δt_c, no effect on χ is expected. Still, for a too large Δt_c parcel trajectories could not be computed successfully - this occurred when $\Delta t_c \approx N_s^{-1}$.

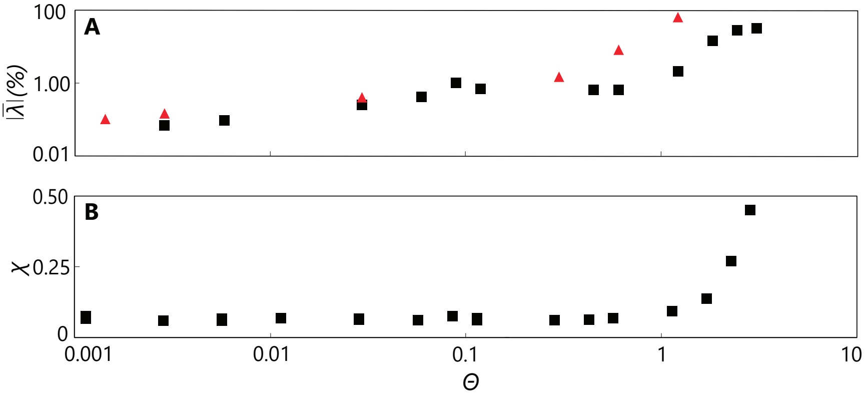

Figure 4.5: Uptake mass imbalance $|\overline{\lambda}|$ (top) and artificial gradients χ (bottom) as a function of time. Both parameters are shown to be independent of Δt_c for $\Theta < 1$. All shown data points are for the $51kc$ mesh. Black squares: Coupling approach I. Red triangles: Coupling approach II.

Hence, we advise a maximum timestep size $\Delta t_c < \frac{1}{10 N_s}$ and $\frac{\Delta t_c q_{s,max} C_x}{K_s} < 0.1$ to ensure successful trajectory calculation, time-independent χ and an acceptably low imbalance in the inter-phase mass balance.

4.5. Conclusion

Due to the large number of timesteps required when running an Euler-Lagrange simulation of a fermentation process Lagrangian reaction coupling, computational efficiency is essential. When the uptake of substrates from the broth (the Eulerian phase) by the organisms (the Lagrangian phase) is a function of intra-cellular parameters, the uptake rate q_s needs to be modeled as an inter-phase exchange term which is determined from the Lagrangian perspective. This means that locally q_s is a function of the local particle coverage, and a sufficient number of particles N_p is required to achieve accurate results. Inherently, the clustering of biomass in Lagrangian parcels leads to artificial substrate concentration fluctuations in the substrate concentration field. A sufficient number of parcels N_p must be used to minimize these effects, with higher N_p inherently leading to a longer computation time. In this work, we set out to predict the minimum value of N_p, as well as the maximum allowable timestep size Δt_c, necessary to acquire accurate simulation results at minimal computational cost.

Artificial substrate concentration fluctuations, caused by non-homogeneous distribution of the biomass phase in Euler-Lagrange (EL) simulations, scale linearly with $\langle \beta^*_{m,c} \sigma_{p,c} \rangle$. Here, $\beta^*_{m,c}$ is derived from the substrate gradient around a single, stationary parcel and $\sigma_{p,c}$ is the standard deviation of the binomial distribution, describing the random distribution of parcels. The proportionality constant α_g is found to depend solely on the geometry of the system; no effect of mesh, power input or timestep size was observed, provided the timestep size was below $K_s/q_{s,max} C_x$. Knowing α_g, the number of parcels N_p required to keep the artificial substrate fluctuations below a certain threshold can be calculated from equation 4.6, where N_p typically is of $O(10^5)$

for a threshold $\chi = 0.05$. Because of the iterative nature of the method, there is a mass-imbalance $|\bar{\lambda}|$ between the Eulerian and Lagrangian uptake. This imbalance was found to be $< 1\%$ when $\alpha_g \langle \beta^*_{m,c} \sigma_{p,c} \rangle < 0.05$ and $\Delta t < 0.1 K_s / q_{s,max} C_x$, for all cases. Both explicit and implicit uptake coupling were tested. No consistent improvement in performance was found regarding error or fluctuations for the implicit method, while a significant increase in calculation time was observed. Hence, we provide the following primary guidelines for setting up Euler-Lagrange fermentation simulations:

1. Calculate the minimum number of required parcels using equation 4.6.
2. A timestep size $\Delta t < \min\left(\frac{0.1 K_s}{q_{s,max} C_x}, \frac{1}{10 N_s}\right)$ is recommended.
3. Calculation inter-phase exchange terms only during the first iteration of a timestep is recommended to reduce computation time.

The size of microorganisms allows massless parcel tracking to be used, with reaction models supplied via user-defined functions, resulting in significant savings in computation time. Furthermore, computation time can be reduced by using the Multiple Reference Frame method for impeller simulation; the impeller and baffles have to be switched from ’wall’ to ’interface’ boundary condition to prevent parcels from getting stuck. It is advised to consider alternatives for the discrete random walk model for turbulent particle dispersion. Although its drawbacks can be diminished by increasing mesh density, a more systematic solution is preferred.

5

Analysis of organism life-lines

The trajectories, referred to as lifelines, of individual micro-organisms in an industrial scale fermentor under substrate limiting conditions were studied using an Euler-Lagrange computational fluid dynamics (CFD) approach. The metabolic response to substrate concentration variations along these lifelines provides insight in the dynamic environment inside a large scale fermentor, from the point of view of the micro-organisms themselves. We explore two methodologies to analyze the variations experienced along these lifelines; the first methodology is based on variations compared to a reference point (arc analysis) and the second based on transitions between metabolic 'regimes' (regime analysis). Both methodologies have the potential to provide comprehensive statistical insight in the environmental fluctuations experienced by micro-organisms inside an industrial bioreactor. These statistics provide the groundwork for the design of representative scale-down simulators, mimicking substrate variations experimentally. Two case studies are explored. First, the aerated fermentation of S. cerevisiae in a 22 m^3 *fermentor, as conduct in Stavanger, Norway [8, 16, 40, 277, 280]. Second, we study a simplified representation of an industrial fermentation of P. chrysogenum, dealing only with glucose gradients and ignoring aeration and rheology. Available experimental data shows the relevant hydrodynamic timescales are nevertheless reasonably captured. Together, these cases provide insight in how moderate- to extreme substrate gradients inside bio-reactors are experienced by micro-organisms. The competition between the timescale of reaction and timescale of circulation is highlighted, leading to different spatial layouts of the gradients between the cases. Micro-organisms experience significant substrate concentration fluctuations at timescales of seconds while traveling through these gradients, on average in the order of magnitude of the global circulation time. Such rapid fluctuations should be replicated in truly industrially representative scale-down simulators.*

5.1. Introduction

Non-ideal mixing in industrial bioreactors may lead to several large-scale gradients, for example in substrate concentration, in dissolved oxygen concentration and in pH. From the point of view of the organisms, these spatial gradients in the reactor translate to temporal variations in their observed environment to which they are continuously subjected [8], and which will influence their metabolism. In order to properly assess

---

Parts of this chapter have been published as: C. Haringa, W. Tang, A.T. Deshmukh, J. Xia, M. Reuss, J.J. Heijnen, R.F. Mudde and H.J. Noorman. Euler-Lagrange computational fluid dynamics for (bio)reactor scale-down: an analysis of organism life-lines, *Engineering in Life Sciences*, 16:652-663, 2016 and C. Haringa, A.T. Deshmukh, R.F. Mudde and H.J. Noorman, Euler-Lagrange analysis towards representative down-scaling of a 22 m^3 aerobic *S. cerevisiae* fermentation, *Chemical Engineering Science*, 170:653-669, 2017 the performance and feasibility of industrial bioprocesses upfront, the influence of these variations must be taken into account. This can be done via the use of so-called 'scale-down (SD) simulators' [43, 78]. The design parameters and operating conditions of these simulators are currently often chosen on the basis of intuition or engineering correlations, related to the vessel mixing time [44, 50, 54, 55], or chosen as a variable [49, 52, 53]. Whether the magnitude and frequency of fluctuations observed by organisms based on this assumption are representative is, however, questionable.

A more rational design of scale-down simulators requires deeper insight in the large-scale conditions to which organisms are exposed. Unfortunately, industrial vessels are typically poorly accessible for detailed measurements. With state of the art CFD, it is possible to obtain detailed insight in the environment inside the fermentor [19, 21, 23, 26, 212]. Of course, such methods involve several assumptions in the modeling of turbulent and multi-phase flows and are not perfect in their accuracy, but they provide a significant step forward compared to the information that is currently available experimentally.

Several authors have suggested the use of CFD to tune scale-down simulators [21, 23, 30, 56, 281], in particular the use of Euler-Lagrange CFD. In the Euler-Lagrange method the biomass phase is represented by a set of individual parcels, which provides the most straightforward way to study the environmental variations from the perspective of the micro-organisms. For each parcel, a 'condition versus time' series describing the observations of a single micro-organism is recorded, referred to as a lifeline, a term coined by Lapin et al. [23]. Although the focus here is on the extra-cellular environment, lifelines for intra-cellular conditions can similarly be obtained [21, 23].

Since the pioneering work of Lapin, who first presented the Euler-Lagrange methodology, only few authors have applied this method, and little attention has been devoted to analyzing fermentation simulations from the unique microbial perspective offered by the approach. Lapin et al. and Delvigne et al. [281] showed lifeline plots, but did not quantify fluctuation frequencies. Some initial quantification of substrate concentration variations, considering both frequency and magnitude, has been conducted by McClure et al. [282]. A more extensive statistical analysis of CFD-based lifelines is considered of great value for the design of representative scale-down simulators as they provide deeper insight in what conditions organisms experience in industrial scale fermentors and can therefore provide a basis of design for industrially representative scale-down simulations. The major challenge in this respect is to transform the large amount of simulation data to a manageable set of statistics. This chapter aims at developing a methodology to address this issue: we present methods to collect statistical insight in the environmental (substrate) variations observed by micro-organisms, that may serve as a basis of design of scale-down simulators.

5.2. Materials and Methods

We applied an Euler-Lagrange CFD approach to study the extra-cellular environment in industrial scale fermentors from the microbial viewpoint, focusing on the extra-cellular glucose concentration C_S (mol/kg). Extra-cellular variations in C_S lead to variations in the biomass specific substrate uptake rate q_s ($\text{mol}_s/\text{g}_{dw}/\text{h}$) for each individual organism. Since we are primarily interested in the response of the micro-organism, the lifelines are expressed in terms of q_s versus t.

In our study we consider 2 industrial fermentations. First, the aerobic fermentation of *Saccharomyces cerevisiae* strain CBS 8066 in a 22 m^3 reactor. This process has been studied extensively within the scope of the Nordic fermentation program between 1990 and 2000, which provides validation data for gas hold-up α, mass transfer rate $k_l a$, gassed power number Po_g and mixing time τ_{95} [40, 277]. Most important, the substrate concentration C_s has been measured at three axial positions in the fermentor [16], providing clear experimental evidence of a concentration gradient as well as a model validation opportunity. The second case focuses on the production of penicillin-G by *Penicillium chrysogenum* strain $DS17690$ in a 54m^3 reactor, formerly operated by DSM. In this chapter, we focus solely on extra-cellular variations; the impact of these on the intra-cellular response is treated in chapter 7.

5.2.1. Biomass specific kinetics

In both cases, hyperbolic Monod kinetics (eq. 5.1) are applied to compute the specific substrate uptake rate q_s based on the local substrate concentration C_s:

$$q_s = q_{s,max} \cdot \left(\frac{C_s}{K_s + C_s} \right) \ \text{mol}_s/\text{g}_{dw}/\text{h} \tag{5.1}$$

The kinetic parameters for both cases are reported in table 5.1. As discussed in chapter 2, variations in both $q_{s,max}$ and K_s may occur at long timescales due to adaptations in the glucose transporters. In this work, the simulated timeframe is $30-60$ min as we are interested in metabolic variations, which typically occur on the second - minute scale; $q_{s,max}$, K_s can be assumed constant. The used Monod parameters have been determined in experimental setups that do not reflect the highly dynamic reality of a large scale fermentor, which does mean that the pseudo-steady value of $q_{s,max}$ and K_s under reaction conditions may differ; this was currently not accounted for, values for $q_{s,max}$ and K_s were based on available literature. The simulated growth rate $\mu < 0.05$ h^{-1}, which means changes in C_x within the simulated timeframe can be ignored.

Under steady state conditions, Growth, production and maintenance (m_s) can be linked to q_s via the Herbert-Pirt equation, equation 5.2:

$$q_s = \frac{\mu}{Y_{sx}} + \frac{q_p}{Y_{sp}} + m_s \tag{5.2}$$

While we focus on q_s variations in this work, the Herbert-Pirt equation is used to comment on the state of being of organisms in certain zones of the reactor, for the *P. chrysogenum* case. The term q_p/Y_{sp} is small and can be safely neglected to make μ an function of C_s only.

Table 5.1: Monod parameters for case 1 (*S. cerevisiae CBS8066*) and case 2 (*P. chrysogenum DS17690*)

Parameter	Case 1	Case 2
$q_{s,max}$ (mol/g/h)	0.00944	0.0016
K_s (mol/kg)	0.001	$7.8 \cdot 10^{-6}$

Oxygen dynamics

Under oxygen limiting conditions, *S. cerevisiae* may ferment sugar to ethanol. Larsson et al. [16] report a dissolved oxygen tension $DO > 30\%$ and oxygen limitations were not observed in this case. In the very viscous penicillin fermentation, sufficient oxygen transfer may be a challenge. We currently do not consider dissolved oxygen (DO) gradients and assume sufficient oxygen is supplied. It is known for several *P. chrysogenum* strains that q_p is affected below $DO \approx 0.08$ mol/m^3, and may vanish at 0.026 mol/m^3. The reversibility of this loss is disputed [54, 240, 242]. The effect of low DO on q_s is not well known; Henriksen et al. [242] observed no change in μ and the residual glucose concentration $\overline{C_s}$ while McIntyre et al. [241] did observe a reduction in C_x under complete oxygen starvation (C_s was not reported). Industrial data for a 150 m^3 fermentor with 2 DO probes indicated an oxygen gradient of $0.05 - 0.1$ mol/m^3 (top-bottom). This indicates some effect on q_p could occur, but very serious limitations are not expected. Based on the 150 m^3 measurements, no serious limitations are expected to occur in the 54 m^3 vessel either.

5.2.2. Fermentation details

Case 1: S. cerevisiae

Geometrical details for the simulated *S. cerevisiae* fermentor can be found in figure 5.1 **A**. The liquid filled height was $H = 6.55$ m, or 22 m^3 filled volume, the total domain height was set to 11 m to allow for broth expansion during gassing. The reactor contained 4 Rushton impellers. In practice, the reactor had 4 baffles; in the simulation 6 baffles were used due to facilitate periodicity: a $60°$ section of the tank with 1 blade and 1 baffle was modeled. This did not significantly affect the overall flow [59]. The periodicity introduces additional feed points (6 instead of 1) at equal angular spacing. This has no strong influence on the substrate distribution, as the gradient is mostly axial [16, 21, 84, 160]. Furthermore, the tank was modeled with the shaft and baffles extending over the full height, and a flat bottom to facilitate meshing [84]. In reality, the bottom was slightly convex, and the shaft ended below the bottom impeller. The agitation rate was set to $N_s = 2.22$ s^{-1}. Gas was fed via a ring sparger located with a flow rate $Q_g = 0.182\ N$m^3/s, resulting in a gas-flow number $Gs = Q_g/N_s D^3 = 0.24$ and Froude number $N_s^2 D/g = 0.35$. Under these conditions the bottom impeller is expected to be in the loading regime [283], while the other impellers operate under dispersion conditions. The rheology of the broth was assumed to be equal to water ($\rho = 1000$kg/m^3, $\mu_l = 0.001$Pa s), the air-water surface tension $\gamma = 0.072$N/m. A fixed biomass concentration $C_x = 10$ g/kg (dry weight) was used, with a constant glucose feed rate $F = 52$ kg/h (as a $50\%\ wt.$ solution) and constant liquid-filled height.

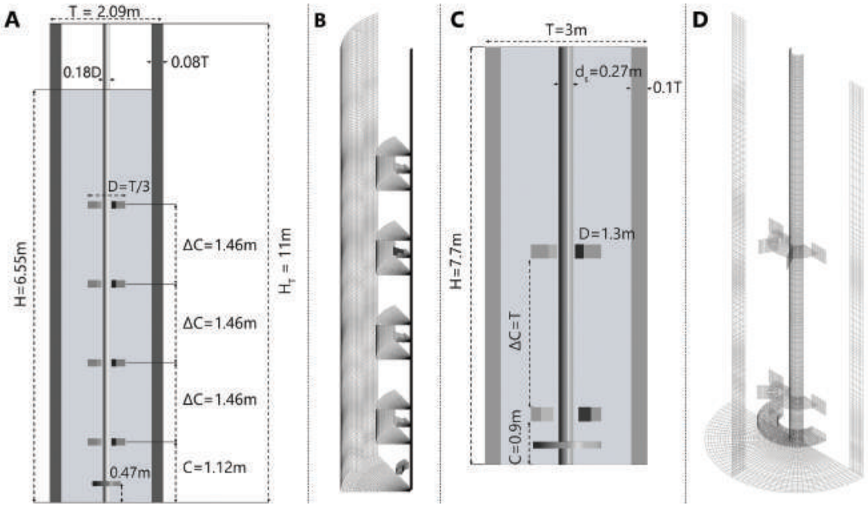

Figure 5.1: The reactors modeled in this study with listed dimensions and associated meshes. **A, B:** 22m^3 (liquid filled volume) *S. cerevisiae* fermentor, mesh containing 611.000 elements (MRF-interface shown). **C, D:** 54m^3 (liquid filled volume) *P. chrysogenum* fermentor, mesh containing 235.000 elements (MRF-interface not shown).

Case 2: P. chrysogenum

Geometrical details for the simulated *P. chrysogenum* fermentor can be found in figure 5.1 **C**. The filled volume was 54 m^3, with two Rushton turbines (8-blade bottom, 6-blade top, diameter $D = 1.3$ m) operating at $N_s = 1.63$ s^{-1} and four baffles of width $T/10$. The shaft is extended through the entire tank. Substrate solution was fed at the fermentor top with a rate of $F = 0.37$mol$_s$/s, the broth density was $\rho_{broth} = 1000$ kg/m^3 with biomass concentration $C_x = 1.96$ Cmol$_x$/kg (55 g/kg dry matter). In the industrial study of Goldrick et al. [254] the broth weight and F were constant after 80 h with C_x approximately constant after h. The process at hand had a shorter filling stage (≈ 1 day) and higher C_x, but qualitatively similar dynamics apply. As such, our simulation choices (constant $H,\ F,\ C_x$) represent the mid/late fermentation stage. Half of the tank was modeled by imposing periodic boundary conditions, similar comments apply as for the periodicity imposed in case 1. A cooling coil in the original geometry was omitted for simplicity. The feed point was mimicked by defining substrate source terms in a 0.034 m^3 box, 0.80 m off-center and at a height of 7.35 m. This is a simplification; the real feed tube is too small to resolve. Preliminary work showed that the size of the feed region, provided it is much smaller than the tank volume, has little effect on the metabolic regime distribution due to rapid dilution.

5.2.3. Hydrodynamic setup

We applied the well-validated RANS approach used by several earlier studies: The $k-\epsilon$ model for turbulence modeling in combination with the multiple-reference frame

(MRF) for impeller rotation [59, 62]. Substrate transport is included via equation 5.3:

$$\frac{\partial C_s}{\partial t} + \nabla \cdot (\mathbf{u}C_s) = -\nabla \cdot \left(\mathcal{D}_m + \frac{\nu_t}{Sc_t}\right)\nabla C_s + S_s \tag{5.3}$$

The internals of the reactor were modeled as sheet bodies, as this was observed to give better results in terms of the turbulent energy dissipation rate ϵ [59, 60, 62]. Standard wall functions [284] were used to avoid the need for excessive mesh resolution near the wall. Second order upwind discretization was used for all equations, with second order implicit time discretization during the transient stages. All simulations were conducted in ANSYS FLUENT 15.7, data analysis was conducted using MATLAB R2015b (v8.6.0).

Parcel tracking and reaction modeling Lapin et al. [21, 23] employed complex reaction models, coupled to the individual parcels (computational particles) in their work. Since we apply simple Monod kinetics, q_s instantaneously adapts to the local C_s and the reaction kinetics can be coupled to the liquid phase rather than parcel phase (see Chapter 4). Combined with the steady-state MRF impeller this yields steady state C_s-, q_s- and flowfields, which do not require updating during the parcel tracking simulation: with the reaction coupled to the liquid phase, the parcels do not influence the flow- or C_s fields. The influence of subgrid variations of C_s are assumed to be small based on the work of Linkés et al. [278], and reaction rates were based on the mean cell substrate concentration $\overline{C_{s,c}}$, rather than taking the subgrid distribution into account. External mass transfer limitations from bulk to organism were also omitted. If desired, such effects can be accounted for straightforwardly via common closure relations.

In contrast to the parcel-coupled reactions reported in the previous chapter, there is no lower limit on N_p since the reactions are fully Eulerian, and N_p is chosen such that reasonably converged fluctuation statistics are obtained without requiring excessive simulation times. With an organism size of $5-10$ μm, the parcel Stokes number $St <<1$ and parcels are treated as massless tracers. Turbulent motions were superimposed via the discrete random walk (DRW) model, which computes the motion timescale as the minimum of the eddy lifetime and particle-eddy crossing time, eq. 5.4:

$$\tau = \min\left(-C_L(k_t/\epsilon)\ log(r), -\tau_r \ln\left[1 - \frac{L_e}{\tau_r|u_f - u_p|}]\right]\right) \tag{5.4}$$

here, τ_r is the particle relaxation time, L_e the eddy length-scale and r a random number between 0 and 1. The constant C_L is linked to Sc_t, and has a default value of 0.15. The turbulent velocity magnitude is calculated as $u_p' = \chi\sqrt{2k_t/3}$, assuming isotropic turbulence, with χ a normally distributed random number. A known problem with the DRW model is the tendency of parcels to accumulate in regions where the convective velocity of the parcel and random velocity are near zero (i.e. near walls) [21, 219]. Improved treatments of parcel turbulence are described in literature, but have not been implemented in ANSYS FLUENT. The local accumulation of parcels was observed to be minor here, hence, no efforts were undertaken to include alternative methods of parcel turbulence treatment. A trapezoidal tracking scheme with an automatically adapting parcel timestep $\Delta t_p < \Delta t_c$ was applied.

Case-specific settings: S. cerevisiae

Aeration was included using the Euler-Euler approach. Gunyol et al. [84] showed that assuming a single bubble size in the range of $3-5$ mm (based on [37–39]) gave poor results for the gas hold-up α, which was strongly improved by using a population balance. We used the discrete population balance model, with 16 diameter classes ranging between 0.5 and 16 mm, with a ratio-exponent of 1. Our results are in good agreement with Gunyol et al. who used only 6 bubble classes, indicating sufficient size resolution. The break-up and coalescence kernels of Luo et al. [77] were employed. Bubble drag was modeled using Fluent's Universal drag model, based on the drag model of Ishii and Zuber [73]. Dispersed phase turbulence was included using the mixture model which shares k_t and ϵ equations between the phases. The mixing behavior was reasonable captured with $Sc_t = 0.7$.

The structured hexahedral mesh, shown in figure 5.1 **B**, had 611000 elements. All walls were no-slip boundaries for liquid, the impellers were no-slip for gas to account for cavity formation, all other walls had a free-slip boundary condition for gas. A gas-backflow pressure outlet was used as the top boundary condition, in combination with an extended headspace, to account for expansion of the liquid by gassing. During parcel tracking, the headspace was removed to prevent parcels from getting stuck, and a degassing condition was imposed at the top. $N_p = 12500$ parcels were added after flow convergence, they were tracked for 1190 s with a simulation timestep size $t_c = 0.005$ s during parcel tracking; larger timesteps led to parcel accumulation in the impeller gas cavities. The data writing interval should be sufficiently small to resolve the smallest global flow features. Here, 8 flow compartments are expected to form, due to the action of 4 Rushton impellers. The estimated inter-compartment circulation time is $\approx \tau_{circ}/8 \approx 5$ s. $\Delta t_{storage} = 0.03$ s, providing more than sufficient resolution here, and easily meeting the criteria of chapter 4.

Case-specific settings: P. chrysogenum

Simplified hydrodynamics were used in this case; the simulation routines used for the previous case were unable to capture the flow when aeration and the shear-thinning rheology of *P. chrysogenum* were included. Previous studies that did attempt to include the effect of shear-thinning rheology, with or without aeration, had limited success [160, 212, 285]. Moilanen et al. [212] strongly over-predicted τ_{mix} due to excessive formation of stagnant caverns, for example, and population balance models are poorly validated in non-Newtonian fluids. Further developments regarding the simulation of transitional, aerated, non-Newtonian flows are required for the reliable simulation of viscous fermentations. To focus on lifeline analysis rather than detailed bioreactor physics here, we opted to model a single-phase water situation. This assumption is further justified by considering that the τ_{circ} under fermentation conditions is reasonably close to that in non-aerated water (table 5.2). Aeration influences the spatial

Table 5.2: Experimental values for the circulation time under different flow conditions in industrial *P. chrysogenum* fermentations. $U_{sup,g}$ is the superficial gas velocity. Numerically, $\tau_{circ} = 18.2$ was found for the single phase water case used in parcel tracking.

Fluid	$U_{sup,g}$ (m/s)	τ_{circ} (s)
Water	0	19.3
Water	0.05	42.8
Broth	0	77
Broth	0.05	25.6

mixing behavior due to a change in the dominant transport mechanism [15, 286] and alteration of flow patterns, but at similar τ_{circ}/τ_{rxn}, the observations are expected to hold at least qualitatively. The applied simplifications do not compromise our current goal of lifeline analysis. Gassed simulations were successfully conducted in a later project stage, these are reported in chapter 7; simulations with non-Newtonian rheology proved highly sensitive to the exact rheological parameters when applied for single-phase flow, and diverged for multi-phase flow due to an indefinite increase in the gas hold-up. Hence, these simulations are not further addressed in this thesis.

The turbulent Schmidt number Sc_t was set to 0.2, based on the considerations reported in chapter 3 [84, 112, 160]. Accordingly, $C_L = 0.45$ in the DRW model. $N_p = 175000$ parcels were tracked for 1700 s of flow time ($\Delta t_c = 0.015$), q_s was stored every $\Delta t = 0.03$ s (approx. $\tau_{rxn,min}/10$), yielding the organism lifelines. All walls of the vessel had a no-slip boundary condition, the top was modeled as a no-shear surface. Meshes with $235000 - 809000$ elements were tested, the difference in $Po_\tau < 2.5$ % between the finest and crudest mesh, the difference in $\tau_{95} < 1$ %. Hence, parcel tracking simulations were conducted in the 235000 cell mesh, which is shown in figure 5.1, **D**.

Simulation strategy

The single phase hydrodynamics were first solved, convergence was declared when $\langle|U|\rangle$ was stable within 0.01% and the residuals were below 10^{-5}. For case 1, the 2−phase simulation (steady state) was started afterwards; some mass balance instabilities observed, we refer to the supplementary information of [20] for further discussion. The simulation was declared converged when the residuals $\approx 10^{-4}$ and $\langle U_{liq}\rangle$, $\langle d_b\rangle$ were stable within 2.5%. Deeper convergence could not be achieved due to the highly non-linear nature of the setup. After convergence, the headspace was removed, and a degassing boundary condition was set at the top surface. An additional 4000 iterations were executed, yielding a similar degree of convergence as when the headspace was included. Gas backflow over the degassing boundary was responsible for the formation of a small gas cavity around the shaft (visible in figure 5.5), this could not be avoided in the current setup.

After convergence the flow equations (turbulence, momentum, α, d_b) were frozen, fixing their respective fields. Monod kinetics were included via a user-defined function (UDF) and substrate feed was enabled. Once the steady-state concentration gradient was resolved, the simulation was switched to transient mode and parcels were added for lifeline registration. The parcels were first distributed for 1 mixing time before lifeline registration was enabled via user defined functions.

5.2.4. Validation parameters

For the gassed *S. cerevisiae* case, data on the overall gas holdup $\langle \alpha \rangle$ [40, 277], gassed impeller power numbers Po_g, overall $k_L a$ [16] and the mixing time τ_{95} [40, 277] was available. For *P. chrysogenum*, only τ_{95} was directly available from previously unpublished plant data, the ungassed impeller power number was available from literature [287] . Below, the calculation procedure of validation parameters is outlined.

The gas holdup was determined by volume-averaging the local gas holdup α_c according to eq. 5.5:

$$\langle \alpha \rangle = \frac{\Sigma V_c \alpha_c}{\Sigma V_c} \tag{5.5}$$

using the cell volume V_c as a weight. Similarly, the global mean bubble diameter was determined by volume-averaging the local Sauter mean diameter, weighted by the gas volume rather than the total cell volume (eq. 5.6):

$$\langle d_b \rangle = \frac{\Sigma V_c \alpha_c d_{b,c}}{\Sigma V_c \alpha_c} \tag{5.6}$$

The power number was calculated from the torque exerted on the individual impellers (eq 5.7):

$$Po = \frac{2\pi M}{\rho N_s^2 D^5} \tag{5.7}$$

with M the rotational moment for a full $360°$ domain. To calculate the inter-phase mass transfer coefficient k_l (in s^{-1}), we used the eddy cell model of Lamont and Scott [188], eq. 5.8, which was shown by Gimbun et al. [61] to yield good results.

$$k_l = 0.4 \cdot \mathcal{D}_m{}^{0.5} \left(\frac{\epsilon}{\nu_l} \right)^{0.25} \tag{5.8}$$

Following Gimbun et al., the interfacial area of the bubbles a was calculated taking into account bubble deformation via eq. 5.9, which estimates the ratio between the major and minor ellipsoid axes of a deformed bubble:

$$R = 1 + 0.163 Eo^{0.757} \tag{5.9}$$

With $Eo = g\Delta\rho d_b/\gamma$ being the Eötvös number. Using the local Sauter mean diameter d_b to determine the bubble volume, the ellipsoidal bubble's surface area can be calculated straightforwardly; the overall k_La is calculated by volume averaging, similar to α. The Eulerian mixing time τ_{95} was determined by placing a virtual probes inside the reactor vessel. In the *S. cerevisiae* case these were placed at $r = 0.3$ m, at three different heights: $Y = 1.12,\ 4.04,\ 6.56$ m, as done experimentally. For *P. chrysogenum*, a single monitor was used at coordinates 0.7 meter off-center, 0.25 meter from the bottom. Mixing was declared complete when $0.95 < C_s/\langle C_s\rangle < 1.05$ at all probed locations, yielding τ_{95}. Additionally, a Lagrangian mixing experiment was conducted for case 1, using $5.75 \cdot 10^6$ parcels, registering when $0.95 < C_p/\overline{C_p} < 1.05$ at each probe location. Here C_p is the local parcel concentration.

5.3. Lifeline analysis

The lifelines, exemplified in figure 5.2, **A** contain detailed information on how individual organisms experience the simulated fermentation environment, but in themselves they can not be straightforwardly translated to scale-down design criteria. Our analysis aims to translate the information from a large collection of lifelines to a small set of lifeline statistics, consisting of duration and magnitude distributions, that can serve as a basis for SD-simulator design. Regardless of the method, some reference point for fluctuations needs to be chosen. As micro-organisms have no notion of their spatial location, we do not use a spatial reference point to determine (circulation) time distributions [30, 288]. Rather, reference points are chosen within the limiting parameter space, q_s in this case. We currently focus on q_s parameters, which quantify the direct response to the extra-cellular environment and thereby aim to directly quantify the environment as experienced by organisms. In principle, *any* lifeline, based on the extra-cellular observations or intra-cellular state can be analyzed with the methods outlined here. We explore three methods for lifeline analysis in this work:

- Regime analysis: Divide the domain in several regimes based on critical values in q_s, register the exposure time each individual visit of a parcel to each regime, and how parcels transit between regimes.
- Arc (baseline) analysis: Select a reference value q_{ref}, monitor the time consecutive crossings of q_{ref} (arc duration, τ_{arc}) and the registered extreme value in q_s (arc magnitude $\Omega_{s,max}$).
- Fourier analysis: use the Fourier transformation to translate the lifeline time-series to frequency space, in order to study if any dominant fluctuation frequencies are present in the signal.

5.3.1. Regime analysis

During regime analysis, q_s-space is divided in several regimes, the boundaries between which can be based on metabolic considerations (excess/starvation effects, metabolic overflow), or on reactor compartmentalization (the formation of several well-mixed zones within the reactor). The continuous organism lifeline (fig. 5.2, **A**) is reduced to a discrete regime lifeline (fig. 5.2, **B**), which is used in the subsequent analysis. The

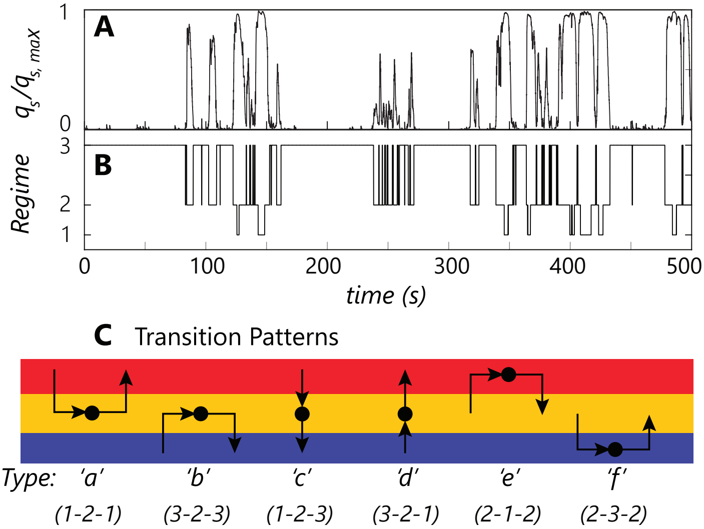

Figure 5.2: Steps in the regime-based analysis method. **A:** continuous lifeline in $q_s/q_{s,max}$ $vs.\ t$ as retrieved from CFD simulation. **B:** discretized lifeline based on regime methodology. **C:** Different possible transition patterns for a domain discretized in 3 regimes. The type convention for the different patterns will be used throughout this study.

regime residence time τ_{reg} is defined as the time that a micro-organism is exposed to a certain regime, between two consecutive crossings of the regime boundaries. By analyzing a large number of such events, per-regime residence time distributions can be determined.

A central concept in our analysis are transition patterns: these are determined by the nature of the 2 consecutive crossings. Transition patterns determine how organisms move between the different metabolic regimes (fig. 5.2, **C**), in essence providing the fluctuation magnitude. The regime analysis provides direct insight in whether or not overflow regions are expected to be present in the reactor, and how long organisms are exposed to them. Whether overflow actually occurs depends on the adaptation time of the metabolism, which can be elucidated with proper metabolic models, or by conducting a representative scale-down experiment.

Regime examples: excess/starvation kinetics As an example, consider a large vessel where $\tau_{rxn} << \tau_{circ}$ (a high Damköhler number, $Da = \tau_{circ}/\tau_{rxn}$) such that a very strong C_s gradient is present, with an organism lacking metabolic overflow mechanisms. Using Monod kinetics, q_s saturates for $C_s \rightarrow \infty$. For $C_s > 19K_s$, $q_s > 0.95q_{s,max}$ and q_s iters largely insensitive to further increases in C_s. We refer to the domain where $q_s > 0.95q_{s,max}$ as the (substrate) excess regime. In the domain where $C_s < K_s/19$, $q_s < 0.05q_{s,max}$. In this range q_s and C_s are linearly related, but in absolute terms strong variations in C_s result in minor variations in q_s. This domain is regarded as the (substrate) starvation regime, with negligible q_s (see the supplementary material of

[10] for discussion of this assumption). The range $K_s/19 < C_s < 19K_s$ is classified as the limitation regime, where C_s-fluctuations lead to non-negligible q_s variations. The above considerations lead to the following distinction:

- Excess regime ($q_s > 0.95q_{s,max}$)
- Limitation regime ($0.05q_{s,max} < q_s < 0.95q_{s,max}$)
- Starvation regime ($q_s < 0.05q_{s,max}$)

One of the benefits of the regime analysis for this case is clear: grouping all instances where $q_s > 0.95q_{s,max}$ into a single regime hardly reduces the amount of information in the lifelines, as q_s fluctuations *within* this regime are negligible; the same applies to the starvation regime. For the limitation regime, where q_s variations are strong, grouping all q_s instances to a single value leads to a considerable loss of information. Depending on their impact on the metabolism, quantification of fluctuations *within* the limitation regime may be required. This can be done, for example, by combining the regime method with the arc-method to examine intra-regime dynamics.

Regime transitions After pre-processing with turbulence filters (discussed below), the $q_s/q_{s,max}$ and conversion to the regime series, the regime residence time and the transition pattern are determined: the nature of the two successive crossings. For the above example, we distinguish between 6 of such transition patterns:

- a: From regime 1, in 2, back to 1
- b: From regime 1, in 2, to 3
- c: From regime 3, in 2, back to 3.
- d: From regime 3, in 2, to 1.
- e: From regime 2, in 1, back to 2.
- f: From regime 2, in 3, back to 2.

The trajectories are shown graphically in 5.2, **C**. A 6 second ‘a’ event means that a particle originates from regime 1, spends 6 seconds in regime 2, and then returns to regime 1. Due to the physical distance, no direct crossings between regime 1 and 3 occur in the reported cases. Discriminating between the different transition patterns provides insight in how micro-organisms move between regimes and how the regime-residence time is linked to their trajectory.

Turbulence filtering Prior to the analysis, the trajectories are smoothed and filtered to remove rapid turbulent fluctuations that would skew fluctuation statistics towards short timescales. These rapid variations are low in magnitude, and likely have little effect on the organism [278]. Smoothing is performed using a moving-average filter, with a filter window equal to the Lagrangian timescale $\tau_L = C_L k_t/\epsilon$ that is representative for turbulent motions imposed by the DRW model. This filtering step removes most of the rapid turbulent fluctuations. A dispersed rather than sharp regime boundary is applied to remove rapid consecutive regime-crossings of low magnitude. Using a fuzzy boundary, the regime boundary is set to $q_s/q_{s,max} = X \pm Y$, where Y is the filter strength. An example of smoothing + fuzzy boundary filtering is provided in figure 5.3; a regime boundary $q_s/q_{s,max} = 0.05 \pm 0.01$ is used in this example. Regime transitions from the upper to the lower regime are only registered if the lower filter boundary is crossed, and conversely, transitions from the lower to the upper regime are only counted when the upper boundary is crossed. In addition, extreme jumps in q_s may be registered if a particle moves close to a gas-filled trailing vortex in multi-phase simulations, due to the finite accuracy of the numerical particle trajectory integration. Such outliers are filtered out by a rate-of-change filter, meaning that $\Delta q_s/\Delta t$ may not exceed a certain threshold (which is crossed in case a parcels jumps into a trailing vortex, but not during regular motion).

To summarize, our regime analysis consists of four steps:

- Non-dimensionalize q_s with $q_{s,max}$
- Turbulence filtering: smoothing/amplitude/rate-of-change filter
- Conversion to regime vector
- Determination of transitions and residence times

5.3.2. Arc analysis

Arc analysis is a more straightforward manner of interpreting the particle trajectories. A reference value q_{ref} in q_s-space is chosen. This may be based on metabolic significance (the onset of metabolic overflow, for example), physical significance (based on a concentration jump between two compartments), or of statistical significance (the vessel mean or median $q_s/q_{s,max}$). The 'arc' refers to the section of the lifeline in between two crossings of q_{ref}, which is assumed to have an arc-shape, with the arc-time (τ_{arc}) being defined as the time between two consecutive crossings of q_{ref}, and the arc magnitude $\Omega_{s,max}$ defined as the extreme value in q_s encountered over the (smoothed) arc-trajectory (see figure 5.4). The shape of the arcs can simply be assumed symmetric as a first approximation; the arc symmetry $\Lambda_{arc} = t_\Omega/\tau_{arc}$ can be determined as a measure of skewness, where t_Ω is the time at which $\Omega_{s,max}$ is registered (shown in figure 5.4). The arc time distribution represents the duration distribution of global-vessel fluctuations with respect to q_{ref} and the values of $\Omega_{s,max}$ give the distribution of fluctuation magnitudes; correlating $\Omega_{s,max}$ and τ_{arc} completely quantifies the fluctuations and provides a basis for scale-down design. Since both τ_{arc} (especially for

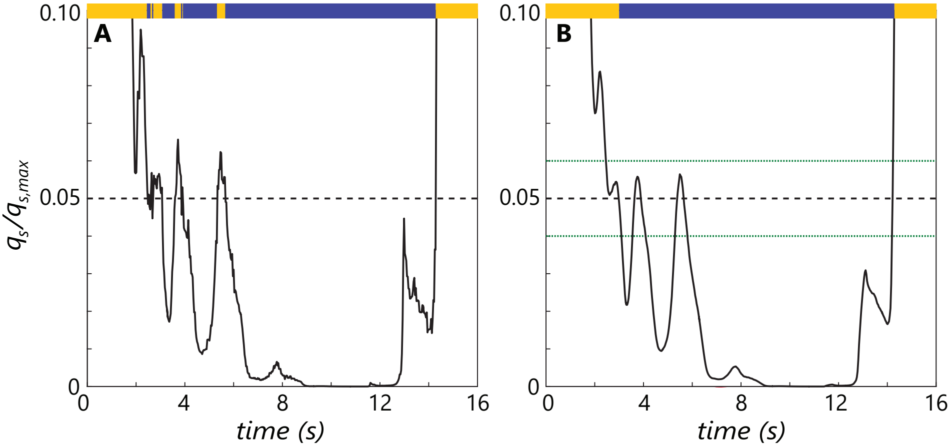

Figure 5.3: Example of the filtering procedure. **A:** Raw $q_s/q_{s,max}$ versus time signal, with the regime boundary at $q_s/q_{s,max} = 0.05$, indicated by the dashed line. The colored bar on top shows the registered regime; yellow means the particle is in regime 2, blue in regime 3. **B:** the same signal after smoothing, and with a 'Fuzzy boundary filter' of ± 0.01 indicated by the dotted lines. Now, a regime transition from 2 to 3 is only registered if the lower boundary is crossed, and a transition from 3 to 2 only if the upper boundary is crossed. The resulting regimes are again indicated by the colored bar on top. The rate of change filter is not shown in this example.

rapid variations) and $\Omega_{s,max}$ are sensitive to noise, the lifelines are smoothed based on the Lagrangian timescale before conducting the analysis.

The arc-analysis method can be superimposed on the regime analysis when fluctuations *within* one or more regimes are deemed important. In this case, q_{ref} should be chosen within the bounds of the relevant regime (for example the regime mean q_s), and care must be taken that only re-circulation trajectories completely enclosed within the regime are counted; those leaving the regime are already accounted for within the per-regime residence time distribution.

5.3.3. Fourier Analysis

The suggestion to decompose organism lifelines using Fourier analysis has been made in several unpublished talks by Reuss. There are reasons to be skeptical towards the applicability of Fourier analysis towards stirred tank analysis, as the circulation times of parcels are widely distributed [30, 162, 198, 288] and no dominant circulation frequencies are expected. We took the Fourier transform of each individual q_s-series, after subtracting the series mean q_s (which acts as a reference value in this method), and multiplication of the series with a Blackman window function [289]. The per-track frequency spectra were subsequently summed to form a composite spectrum.

5.3.4. Lifeline analysis: method selection

The preferred analysis method depends both on the system analyzed, and the available scale-down method. Using solely the arc method works best for comparatively simple

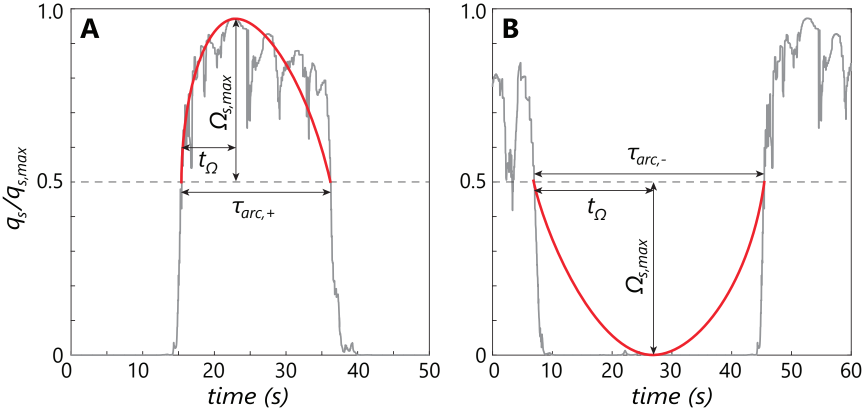

Figure 5.4: Outline of the arc method. A baseline of $q_s/q_{s,max} = 0.5$ is used for illustration. The solid gray line shows an excerpt of a lifeline, the red line shows the arc approximation for the shown sections. The arc time τ_{arc} is the time between the baseline crossings, the arc magnitude $\Omega_{s,arc}$ is the extreme value compared to the baseline. The arc symmetry is defined as $\Lambda_{arc} = t_\Omega/\tau_{arc}$ where t_Ω is the time at which $\Omega_{s,max}$ is registered. **A** shows a positive track compared to the baseline, **B** a negative track.

circulation systems, such as a single impeller tank, where the assumption of an arc-shape trajectory holds reasonably. The advantage of the arc-method in such cases is that it does not require discretization of the amplitudes, whereas the regime analysis method does require this. In strongly compartmentalized flows with many possible local trajectories, the assumption of simple arc-shaped trajectories fails, and may lead to a misjudgment of the exposure time to extreme conditions.

The discretization of the fluctuation amplitude to a few discrete levels (the regimes) means detailed information on the amplitude is lost in regime analysis. By construction, the regime analysis method does accurately capture the duration of individual exposures to a certain range of conditions, regardless of the complexity of the underlying flow patterns. This makes regime analysis preferred for complex flows with many possible (re-)circulation trajectories, where the assumption of arc-shaped fluctuations compared to q_{ref} obviously fails, or for situations where the exposure duration to (for example) overflow or starvation conditions must be properly captured. In case information regarding the q_s distribution within a certain regime has to be retained, superimposing arc-analysis in the relevant regimes is an option. The selection of the preferred analysis method may be influenced by the selected scale-down methodology; this is further treated in chapter 6.

5.4. Validation

Before moving to the Lagrangian viewpoint, the simulations are validated against available data.

Table 5.3: Global validation parameters for the simulation. $k_L a$ is retrieved from [16]. Experimental gas holdup is reported for water [40]. Mixing times differ between sources, the lower value is retrieved from [15], the higher value was reported by [40]. Power numbers are retrieved from previously unpublished data of the Stavanger experiments.

Parameter	Simulation	Experimental	Exp. Method
$\langle \alpha \rangle$	17.6	17.1	Height increase
Po_g	9.6	9.2	Torque
$k_L a$	144 h^{-1}	180 h^{-1}	O_2 balance
τ_{95}	183 s	147 – 166 s	Probe (bottom)
$\langle d_b \rangle$	8.9 mm	n/m	n/a

n/m = not measured, n/a = not applicable.

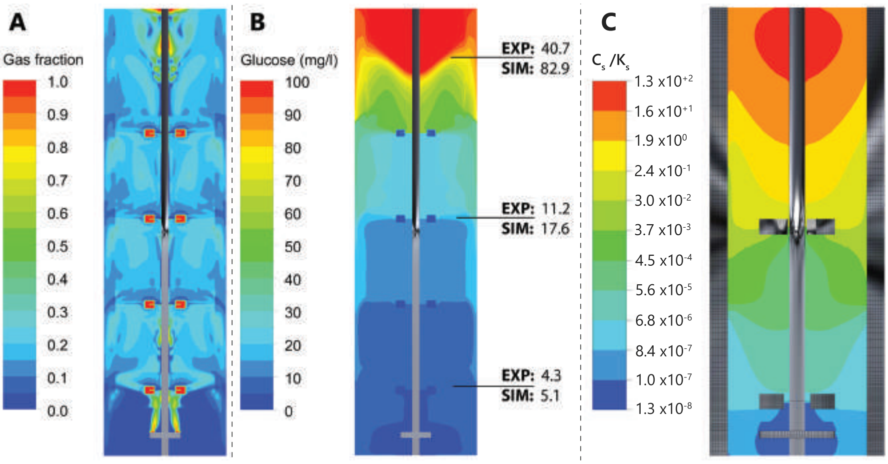

Figure 5.5: **A:** Gas holdup in *S. cerevisiae* fermentation. Close to the top there are some artifacts of the degassing method. **B:** Glucose concentration profile for the *S. cerevisiae* case (top feed). Experimental values (mg/L) are retrieved from [16]. **C:** Glucose concentration profile in the *P. chrysogenum* fermentation, scaled by K_s to emphasize the many orders of magnitude.

5.4.1. Case 1: S. cerevisiae

Table 5.3 reports all validation parameters; Po_g and $\langle \alpha \rangle$ are in good agreement with experimental data. The overall $k_L a$ is somewhat underestimated, which could be due to an overestimation of the bubble size; at $\langle d_b \rangle = 8.9$ mm the mean size is high compared to lab/pilot-scale studies [37–39]. Unfortunately, we lack experimental data on d_b for the current fermentation. Still, the agreement in $k_L a$ is very decent considering that broth is a complex, surfactant-laden substance. As α is properly predicted, and d_b does not directly impact our work, we did not attempt the use of other kernels. The volumetric gas distribution, figure 5.5 **A**, shows that the expected loading flow regime is indeed retrieved for the bottom impeller.

Mixing behavior

The Lagrangian mixing data gives $\tau_{95} = 183$ s, a $10 - 25\%$ overestimation compared to the experimental data, acceptable considering the complexity of the simulation and typical variation in experimental mixing studies. Eulerian mixing (pressure outlet boundary) yielded $\tau_{95} \approx 169$ s, but temporal variations in the total tracer mass were observed [84]. This limits the accuracy of the method, opposed to the Lagrangian simulations where parcel number is conserved. The tracer response dynamics deviate from the experimental curve reported by Noorman [15] for both approaches (figure 5.6). A feasible explanation is a difference in the dominant transport mechanism [15]; in dense bubbly flows bubble wake-induced convective mixing dominates over the turbulent mixing that dominates single-phase flow [286]. The employed mixture turbulence model and absence of a turbulence interaction force mean liquid phase mixing acts as in a single phase liquid, aside from stronger axial motion caused by the effects of buoyancy and drag. A consequence of the latter is that tuning Sc_t not lead to a consistent improvement in the Eulerian τ_{95}, in contrast to single phase simulations (see chapter 3 and *appendix C*).

Substrate concentration gradient

Figure 5.5 **B** shows the simulated concentration gradient (degassing boundary condition, $Sc_t = 0.7$). In agreement with previous simulations [16, 84], the weak axial mixing of Rushton turbines leads to strong axial heterogeneity. The flow remains impeller-dominated leading to clear compartment formation within the gradient, although the compartment boundaries are somewhat blurred due to improved axial mixing induced by gassing. The mass-based glucose concentration c_s is in fair agreement with experimental values [16], considering the inherent approximations made both in the CFD and metabolic models. At the top probe c_s is over-predicted by a factor 2, but it is very sensitive to axial position: a few cm down, $c_s = 50 - 60$ mg/L. Aside from the value at the top probe, changing the top boundary condition and Sc_t had little effect on the concentration gradient; this is further discussed in *appendix C*.

5.4.2. Case 2: P. chrysogenum

Experimental circulation time values have been reported in table 5.2. The CFD result, $\tau_{circ} = 18.2$ s, is close to the experimental value in water (19.3 s) and, despite the considerable difference in hydrodynamics, reasonably close to the aerated broth value of 25.6 s. Hence, the simplified simulation reflects the industrial case at least in an order of magnitude sense. The experimental values of the power number Po for 6— and 8— blade Rushton impellers is reported to be 5.6 and 6.6 for 6 and 8 blades respectively [287]; the CFD is in good agreement with values of 5.2 and 6.3. Profiles for k_t and ϵ in impeller discharge stream of the 6— bladed impeller were in good agreement with the profiles reported in chapter 3, and are not shown here for brevity.

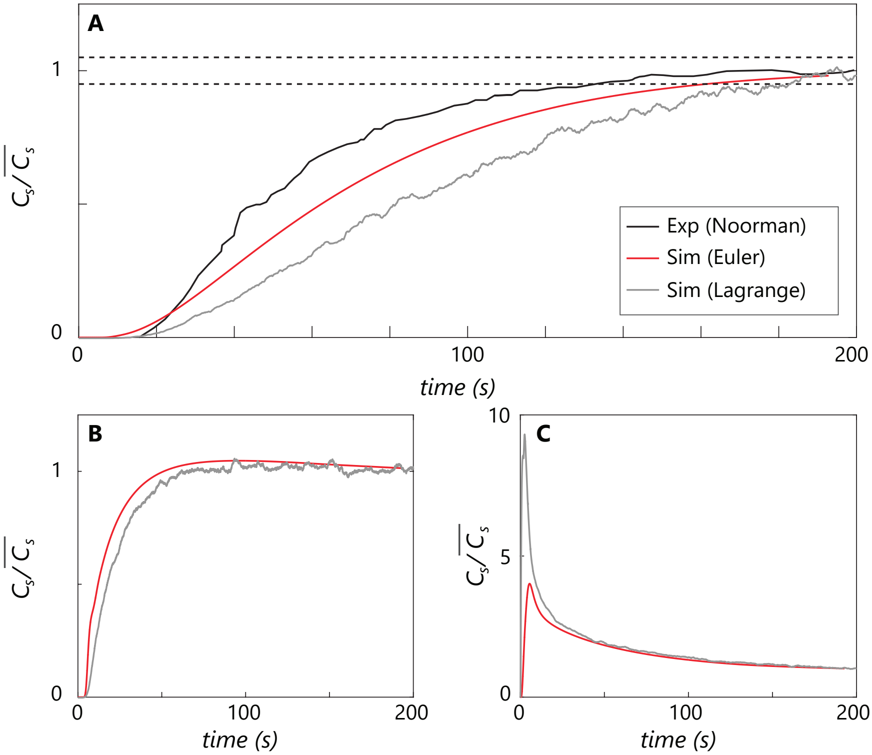

Figure 5.6: Mixing curves for $N_s = 2.22$ s^{-1} and $Q_g = 0.182$ m^3/s The experimental data was retrieved from Noorman [15] which yields a lower mixing time than [40]. Red curves show Eulerian tracer data (pressure outlet, $Sc_t = 0.7$.), gray curves show Lagrangian particle data (smoothed over a period of 4 s for noise removal, degassing b.c., $Sc_t = 0.7$) **A:** bottom probe. **B:** middle probe. **C:** top probe.

5.5. Results and discussion

5.5.1. Glucose concentration gradients: comparing cases

The reported q_s-gradient compartmentalization for *S. cerevisiae* contrasts the smooth gradient observed for *P. chrysogenum* . This difference in behavior arises from the Damköhler number $Da = \tau_{circ}/\tau_{rxn}$, with $\tau_{circ} \approx \tau_{95}/4$ [15] and $\tau_{rxn} = C_s/(q_s C_x)$. Under substrate limited conditions τ_{rxn} can be estimated by assuming the limit $C_s \rightarrow 0$ for Monod kinetics, yielding $\tau_{rxn} = K_s/(C_x q_{s,max})$. For *S. cerevisiae*, $\tau_{circ} = 46.5$ s and $\tau_{rxn,\ C_s \rightarrow 0} = 38$ s, yielding $Da \approx 1$. While yielding a significant substrate gradient overall, the broth *within* individual circulation loops is well mixed; estimating the per-loop circulation time as τ_{circ}/N_{loops} gives $46.5/8 = 5.8$ s; this means the Damköhler number for *intra-loop* mixing is $<< 1$, supporting the observation of intra-loop homogeneity. In the *P. chrysogenum* case, $\tau_{circ} = 18.2$ s and $\tau_{rxn,\ C_s \rightarrow 0} = 0.32$ s, hence $Da >> 1$. As a result, the *P. chrysogenum* case is characterized by a strong substrate gradient manifesting *within* the circulation loop of the top impeller. The difference in

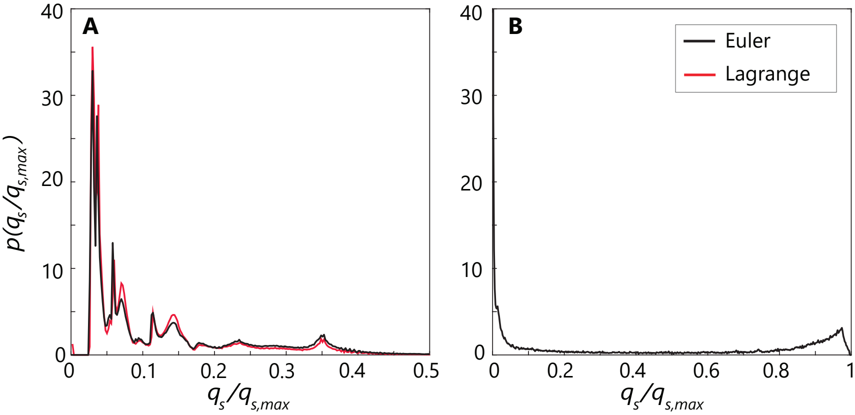

Figure 5.7: Normalized volumetric distribution function of $q_s/q_{s,max}$ in the tank domain; the y-axis is scaled such that the area under each curve is 1. **A:** Distribution for the *S. cerevisiae* simulation, both from the Eulerian and Lagrangian viewpoint. The effect of compartment formation is clearly visible. The Eulerian distribution results from the steady-state q_s field; in case an unsteady method is used, the field should be time-averaged. The Lagrangian distribution represents the overall distribution registered by parcels, taken over all lifelines and timesteps. **B:** Distribution for the *P. chrysogenum* fermentation. Both extremes are strongly represented within the volume, with a gradual gradient in between. Lagrangian results overlap with the Eulerian results and are not shown.

compartmentalization behavior is clearly visible in the volumetric substrate distribution, figure 5.7. In the *S. cerevisiae* case, several sharp peaks are observed, associated with the individual, well-mixed compartments. In the *P. chrysogenum* case, a large section of the domain is completely devoid of substrate and a small section has sugar in excess, with a gradual change in between.

5.5.2. Regime analysis: Case 1

At a high glucose concentration, *S. cerevisiae* CBS 8066 exhibits the *Crabtree-effect*: the aerobic production of ethanol resulting from saturation of the pyruvate to acetyl-CoA processing pathways [42, 227, 228, 256, 258, 259, 290]. The onset of the effect occurs around $C_s = 0.22$ mmol/kg [228], which equals $q_s/q_{s,max} \approx 0.2$ with the applied kinetics. We use this value as a basis for the first regime. In the bulk of the vessel, sufficient glucose is available. Near the bottom co-consumption of ethanol is reported to occur [15]; the exact onset of ethanol consumption is, however, unknown making it an unsuitable regime basis. In figure 5.7 **A** two closely spaced, sharp peaks are visible for $q_s/q_{s,max} < 0.05$, indicating that a large fraction of the liquid volume is in a state of low glucose availability, with a nearly constant q_s. When designing a laboratory scale representation of this industrial fermentor, this low-uptake regime can be approximated by a single $q_s/q_{s,max}$ value, yielding a convenient regime boundary and illustrating how regime boundaries may be based on different strategies. These considerations give the following regimes, ± the fuzzy boundary filter value:

- Regime 1: $q_s/q_{s,max} > 0.2 \pm 0.003$, Ethanol production.

- Regime 2: $0.05 \pm 0.01 < q_s/q_{s,max} < 0.2 \pm 0.003$, Glucose limitation.
- Regime 3: $q_s/q_{s,max} < 0.05 \pm 0.01$, Low glucose availability

Spatially, the interfaces between regime 1 and 2 and regime 2 and 3 coincide with the first (top) impeller and third impeller, respectively. Due to the steady-state background fields in this work, these interfaces are fixed both in space and time from the Eulerian perspective. This notion facilitates the subsequent analysis, as specific features observed in the Lagrangian residence time distributions (RTDs) can be linked to the location of regime interfaces and circulation loops directly. Since the regime division is based on the instantaneous q_s, this link is more difficult to establish when the Eulerian phase is unsteady, which leads to spatially dynamic regime distribution and interface location. Of course, the Lagrangian lifeline methodology and the regime-analysis in themselves are compatible with unsteady simulations; regime transitions and RTDs can be determined, regardless of whether the background fields are steady or unsteady.

From the Eulerian perspective, regimes 1, 2 and 3 cover $23/41/36\%$ of the total liquid volume, respectively. Taking the Lagrangian perspective, the regime division is determined by registering the average time spent by parcels inside each regime, yielding $18/42/40\%$, respectively. This is a notable difference, contrasting the *P. chrysogenum* case discussed later. It is difficult to pinpoint the exact reason of this difference, considering the good agreement between the observed regime distributions from the two perspectives (figure 5.7 **A**); it may simply be a statistical fluke originating from the slow convergence of the regime statistics.

The RTD for each regime, constructed by recording the duration of individual regime exposures, is reported figure 5.8. To facilitate the comparison of their magnitude, the curves are not normalized. A *log-lin* scale is used to highlight certain features of the RTDs: a constant slope on this plot signifies an exponential decay in probability, a manifestation of typical circulation behavior. Changes in slope hint at the existence of different circulation patterns with different associated time constants. For each RTD the mean residence time is calculated as $\overline{\tau_x} = \Sigma(\#_{t,x} t_{res,x})/\Sigma(\#_{t,x})$, $\#_{t,x}$ being the number of counts for a given residence time t_{res} in distribution x. To study the regime follow-up behavior, the four trajectories through limitation are registered separately, following the transition patterns $a - d$ outlined in section 5.3.1.

Of all trajectories entering regime 2 from 1, only 8.7% are of type b, all others being type a (in the converse direction, 18.7% are type d). As the regime $1 - 2$ interface coincides with the top impeller, by far most registered interface crossings concern parcels completing a single circulation in one of the loops originating from the top impeller. This trajectory lasts < 6 s, yielding the RTD peak clearly visible in the inset of 5.8 **A**. Similar single-circulation trajectories are found in distributions c, e, f.

Since all regimes enclose multiple circulation loops, multiple slopes are distinguished in each RTD. The mid-range ($6 - 40$ s for regime 2, and $6 - 20/6 - 30$ s for regimes 1 and 3, respectively) is a complex combination of several circulation loops through a regime-space. For $t > 40$ s all type $a - d$ trajectories have similar RTDs; these parcels have circulated within the region of space enclosed by regime 2 for a

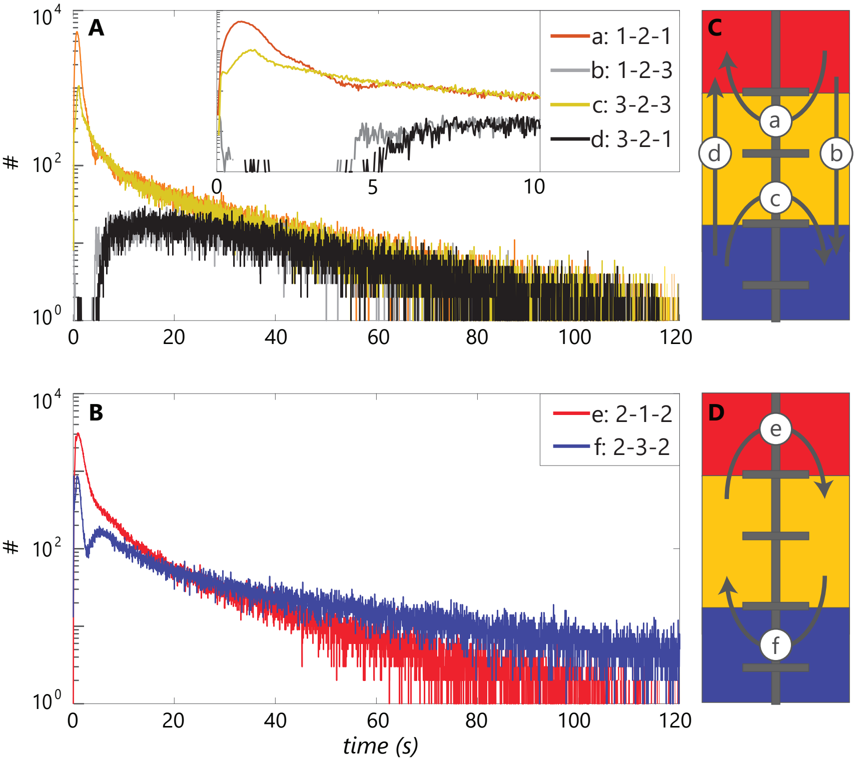

Figure 5.8: Lin-log plot of the residence time distributions for the 6 different trajectories. **A:** Trajectories through regime 2 for *S. cerevisiae*, discriminated by follow-up behavior (as indicated in **C**). **B:** Trajectories through regime 1 and 3 (directions indicated in **D**). # represents the number of counts for a given residence time. Mean residence times: $\overline{\tau_a}$: 6.96 s, $\overline{\tau_b}$: 38.37 s, $\overline{\tau_c}$: 14.03 s, $\overline{\tau_d}$: 39.41 s, $\overline{\tau_e}$: 8.03 s, $\overline{\tau_f}$: 34.19 s.

long time, and their behavior is no longer influenced by their regime of origin or destination. As trajectories b and d have to fully cross the regime 2 region a lag-time of 6 s is registered (figure 5.8 **A**, inset). The symmetry of the b and d RTD is noteworthy, consistent with the notion that the flow is still dominated by stirring despite the high Q_g and the minor influence of gassing does not lead to strong flow asymmetry.

5.5.3. Regime analysis: Case 2

The mean substrate concentration observed from population point of view, $\overline{C_{s,P}} = 32.9 \cdot 10^{-6}$ mol/kg agrees well with the Eulerian mean $\langle C_{s,c} \rangle = 34.4 \cdot 10^{-6}$mol/kg, indicating that the parcels are on average homogeneously distributed, which is also reflected by good agreement in the overlapping distributions in figure 5.7. Filtering of the lifelines to remove the most rapid turbulent fluctuations alters the overall regime distribution by $< 5\%$, an acceptable margin.

Excess substrate is not excreted as an overflow product by *P. chrysogenum* but

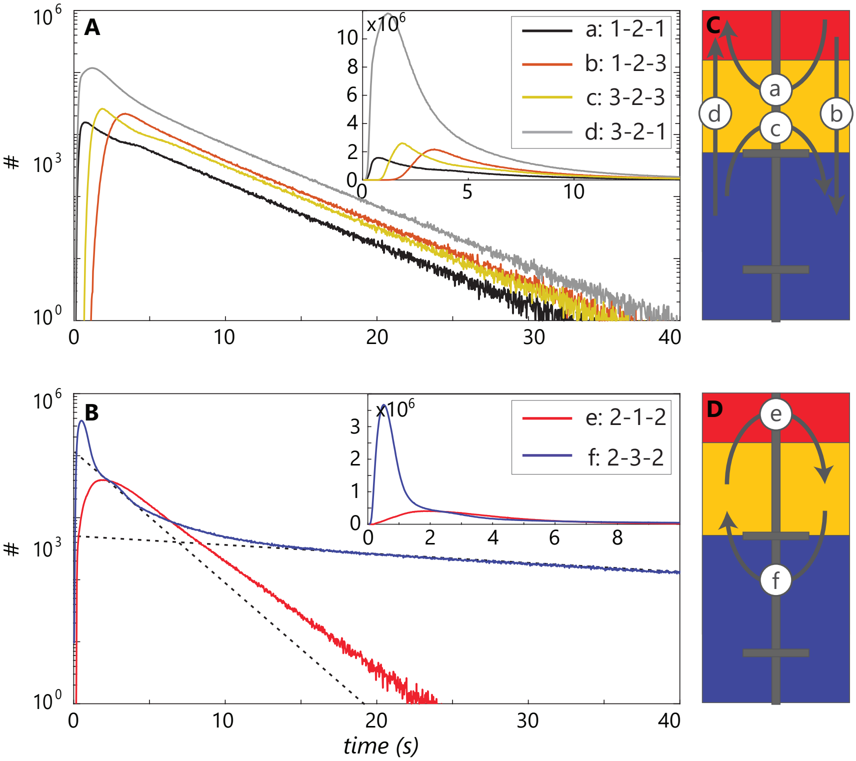

Figure 5.9: **A**: Residence time distributions (lin-log) for trajectories through the limitation regime (regime 2), *P. chrysogenum* (directions indicated in **C**). The inset shows short-timescale peaks (lin-lin plot). **B:** Residence time distributions (log-lin) for trajectories through the starvation and excess regime (regimes 1 and 3, directions indicated in **D**). The inset shows short-timescale peaks (lin-lin plot). # represents the number of counts for a given residence time. The mean trajectory residence times are: $\overline{\tau_{res,a}} = 4.67$ s, $\overline{\tau_{res,b}} = 3.77$ s, $\overline{\tau_{res,c}} = 6.45$ s, $\overline{\tau_{res,d}} = 5.39$ s, $\overline{\tau_{res,e}} = 3.65$ s, $\overline{\tau_{res,f}} = 9.37$ s.

stored internally. Combining the lack of overflow with the strong gradient, the regime division outlined in section 5.3.1 is applied here: $q_s/q_{s,max} > 0.95 \pm 0.01$ for excess, $q_s/q_{s,max} < 0.05 \pm 0.01$ for starvation, and limitation in-between. The Herbert-Pirt equation (eq. 5.2) with $m_s = 0.0015$ $\text{mol}_s/C\text{mol}_x/\text{h}$ shows that for $q_s/q_{s,max} < 0.05$ the energy supply from extra-cellular substrate is insufficient to fulfill maintenance requirements, which may strongly affect the cellular metabolism by requiring the consumption of intra-cellular storage polymer, and possible suppression of energy consuming processes such as penicillin production.

Figure 5.9 shows the excess and starvation residence time distributions (figures 5.9 A and B) and distribution for the four different limitation transitions (figures C and D). The RTD for the excess regime is straightforward: initially there is a gradual increase in counts, associated with short trajectories directly crossing the regimes enclosed space, of varying duration. The constant slope in the log-lin plot (figure 5.9 B)) is

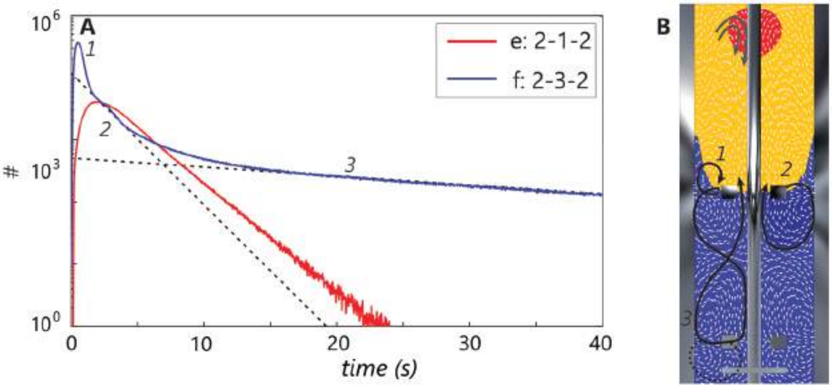

Figure 5.10: **A:** Residence time distributions for trajectories e and f (fig. 5.9). Several circulation modes are observed for trajectory f, due to the inclusion of multiple circulation loops in the regime space. The numbers indicate the trajectory variations outlined in figure B, the dashed lines emphasize different modes. Figure **B:** graphical outline off different trajectory variations. Gray arrows: trajectory e, with a single circulation mode. Black arrows: trajectory f, showing three distinct modes. Mode 1 is associated with the sharp peak at $t \approx 0.7$ s, mode 2 with the domain $5 < t < 10$ s, mode 3 with $t > 20$ s. # represents the number of counts for a given residence time.

indicative of an exponential decay for $t_{res} > 5$ s, representing trajectories with one or more circulations inside the excess region. The long-time behavior of the starvation distribution is particularly interesting, displaying 3 distinct circulation modes; these are illustrated in figure 5.10. A sharp peak at $t \approx 0.7$ s represents parcels coming from limitation, following the upward circulation in the direct vicinity of the top impeller, which quickly mixes them back with the substrate rich broth coming from above; this trajectory is denoted 1 in fig. 5.10. Although short, the low τ_{rxn} does cause a non-negligible q_s change along the trajectory; it is unknown if high-amplitude events with such brief duration will significantly affect the metabolism, however.

For $t_{res} \approx 10$ s, a milder slope represents downward re-circulation at the top impeller, this is emphasized with a dashed line in fig. 5.10, **A** and denoted as trajectory 2. For $t_{res} > 20$ s a very mild slope is observed (trajectory 3, fig. 5.10, emphasized with a dashed line), representing parcels that move all the way to the bottom of the tank; these can spend tens up to several hundred seconds circulating around the bottom impeller, leading to the long tail of the distribution. Type c trajectories may very briefly pass through limitation before moving back to starvation, result in a peak at $t_{res} \approx 1$ s (figure 5.9). It could again be argued that these very brief exposures have little influence on the metabolism; they may be removed by some form of low-pass filter, but more insight on their metabolic action is required to set a representative filter frequency. Details similar to the $t_{res} \approx 1$ s peak in the type c trajectory can also be found in a, b and d type trajectories, but the four distributions show an equal-sloped decay after approximately 5 s. This is again consistent with the notion that parcels end up in origin-independent re-circulation behavior if not crossing the limitation zone directly.

In total, 39% of the trajectories starting in excess are of type a, and 80% of the trajectories starting in starvation are type c. Clearly, on many occasions organisms will repeatedly oscillate between limitation and starvation conditions before being exposed to excess conditions, while prolonged oscillation between excess and limitation is less likely. Evidently, such sequential transitions should be reflected in a representative experimental SD-setup.

5.5.4. Arc analysis

For both organisms, C_s variations in the central regime result in significant intra-regime q_s variations. For *S. cerevisiae*, this is true for the overflow regime as well, as the onset of the Crabtree effect is well below the onset of saturation of the Monod kinetics. In this chapter, only the regime 2 variations are explored in depth, in view of brevity. For both cases, the arc-analysis is conducted *within* the central regime, meaning that only trajectories which do not cross the regime boundaries between two consecutive crossings of the reference value q_{ref} are registered.

Arc magnitude

We set q_{ref} to $q_s/q_{s,max} = 0.1$ for *S. cerevisiae*; this value is close to the regime median and is registered around the 2^{nd} impeller from the top. For *P. chrysogenum* we set $q_{ref}/q_{s,max} = 0.5$ in this example. Similar to the residence time analysis, a smoothed trajectory was used to decrease the sensitivity of arc magnitude $\Omega_{s,max}$ to turbulent noise. $\Omega_{s,max}$ is plotted as a function of arc duration τ_{arc} in figure 5.11, showing markedly different behavior between the cases. The aforementioned compartmentalization (section 5.4) is clearly observed for *S. cerevisiae* in figure 5.11 **A**. Since C_s within any given circulation loop is reasonably homogeneous in this case, the duration of a trajectory within a single loop has no effect on $\Omega_{s,max}$, while crossing over to a different loop leads to an instant jump in $\Omega_{s,max}$ (figure 5.11 **C**). In contrast, the intra-loop heterogeneity observed in the *P. chrysogenum* simulation means that longer trajectories (a higher τ_{arc}) lead to more extreme $\Omega_{s,max}$, even though all arc trajectories in the *P. chrysogenum* case are confined to a single circulation loop. This behavior is sketched in the right of figure 5.11 **D**. While there is significant spread around the mean, there is a clear, smooth correlation between τ_{arc} and $\overline{\Omega_{s,max}}$

We now focus on the *S. cerevisiae* case. Regime 2 encloses multiple circulation loops; the concentration jumps in figure 5.11 **A** show that virtually all trajectories that return to q_{ref} in less than 5 s follow the upward loop of the impeller (type I trajectories in figure 5.11 **C**), and register $\Omega_{s,max} \approx 0.115$. No events with $\Omega_{s,max} \approx 0.115$ are observed for $\tau_{arc} > 5$ s, which implies that there are no type I trajectories that do not return to the impeller (the 2^{nd} impeller from the top) within this timespan: either the parcel has returned already, or it jumped to a type III trajectory, through the lower-loop of the next impeller, before being transported down to q_{ref} again. This loop is again well mixed, meaning all parcels on a type III trajectory register the same extreme, $\Omega_{s,max} \approx 0.17$. A parcel may complete several circulations in this loop, or exhibit some complex back-and-forth jumping between trajectory I and III, before returning to q_{ref}, but the same $\Omega_{s,max}$ is recorded regardless of this behavior (provided the parcel does not cross the regime boundary, $q_s = 0.2 q_{s,max}$). This illustrates the

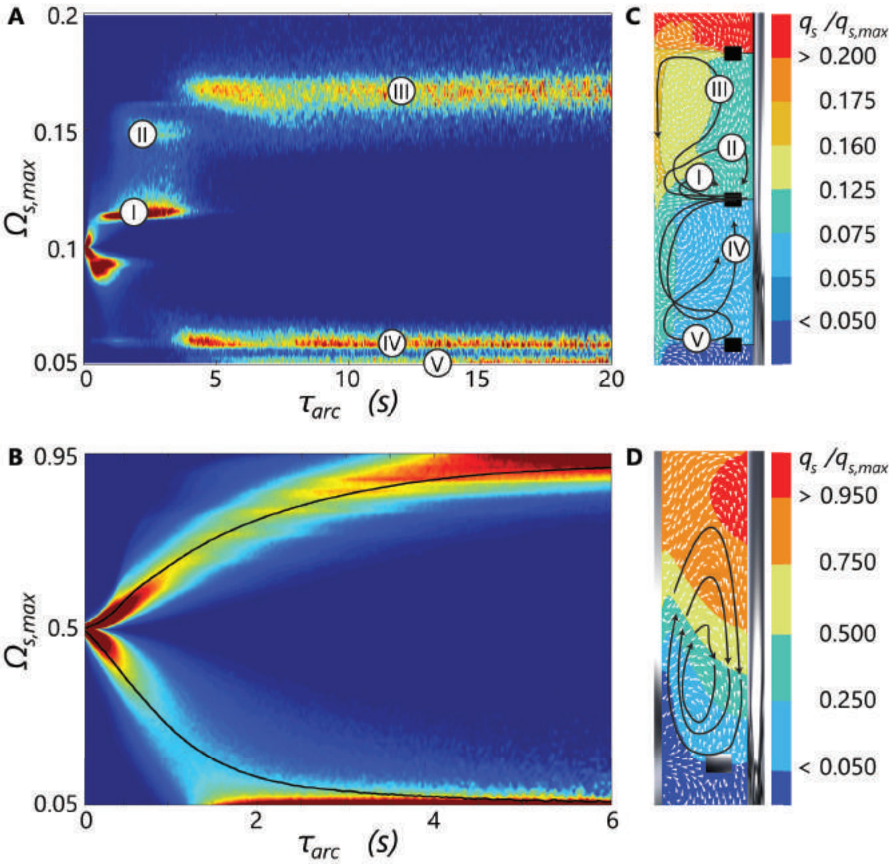

Figure 5.11: Results of the arc-magnitude analysis. $\Omega_{s,max}$ is the extreme value in $q_s/q_{s,max}$ encountered over an arc trajectory. **A:** *S. cerevisiae* results, arc magnitude versus τ_{arc} for regime 2. Each discrete level in **A** is associated with a certain circulation trajectories, marked by roman numerals, displayed in **C**. **B:** *P. chrysogenum* results, showing a smooth relation between arc magnitude $\overline{\Omega_{s,max}}$ and τ_{arc}, explained by the trajectories shown in **D**.

weakness of the arc-method for more complex flow profiles, which worsens as more flow-loops are enclosed in the regime space.

For parcels moving in the downward direction, the most frequently observed behavior is that they get drawn close to the lower impeller, before being transported back up via trajectories IV and V. The physical length of these trajectories mean very few events with a duration $\tau_{arc} < 5$ s are registered. The notion that jumps are typically observed after a duration of 5 s is in good agreement with the per-loop circulation time estimated in section 5.4. An oddity in this analysis are the type II trajectories which originate from the superimposed motion by gassing and the consequent asymmetry between the top- and bottom circulation loop around from the 2^{nd} impeller from the top.

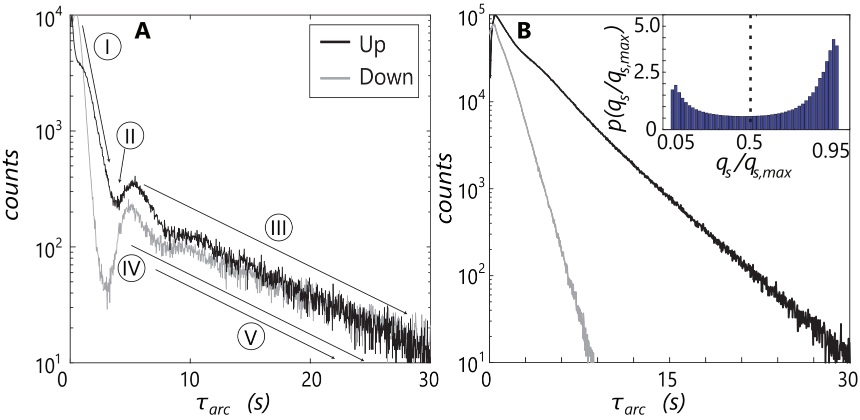

Figure 5.12: **A:** Distribution of τ_{arc} for regime 2, *S. cerevisiae*, with baseline $q_s/q_{s,max} = 0.1$. The different peaks are associated with the circulation trajectories of figure 5.11 and indicated with the same roman numerals. **B:** Distribution of τ_{arc} for regime 2, *P. chrysogenum*, with baseline $q_s/q_{s,max} = 0.5$. Inset: volumetric $q_s/q_{s,max}$ distribution within regime 2, showing values of $q_s/q_{s,max} > 0.5$ are dominant in this regime.

Arc duration

Similar to the regime RTD, a distribution for τ_{arc} can be constructed (figure 5.12). For *P. chrysogenum* (fig 5.12, **B**), the presence of a single circulation loop makes the distribution quite simple: a uni-model decay is observed both for upward and downward trajectories, with only a mild disturbance around $\tau_{arc} = 0$ due to remaining turbulent fluctuations. There is a clearly visible difference between upward- and downward trajectories. Due to the non-linear kinetics, the a larger fraction of the volume enclosed by regime 2 has $q_s > q_{ref}$ (shown in (fig 5.12 **B**, inset) , leading to a higher mean arc-time for upward trajectories: $\overline{\tau_{arc,+}} = 3.14$ s, $\overline{\tau_{arc,-}} = 1.11$ s. Furthermore, there are fewer closed downward trajectories: downward moving parcels reach the top impeller, where most are exposed to starvation conditions, and are not counted towards arc-analysis. Much fewer upward moving trajectories pass trough the excess zone.

The *S. cerevisiae* case (fig 5.12, **A**) shows a multi-modal exponential decay for both up- and downward trajectories, following from the much more complex behavior. The strong initial slope is associated with circulations in the direct vicinity of the impeller, the dip around $t = 4$ s results from the lag-time associated with parcels crossing over to different loops. Parcels completing a single circulation in a second loop lead to a peak at $t = 6$ s. For $t > 10$ s there are many possible combinations of circulation trajectories, making it impossible to discriminate distinct modes and lag-times; their overall combination leads to a constant slope. The total number of upward and downward trajectories is roughly the same; the median concentration in the regime was chosen as a reference point, such that for 50% of the regime $q_s > q_{ref}$.

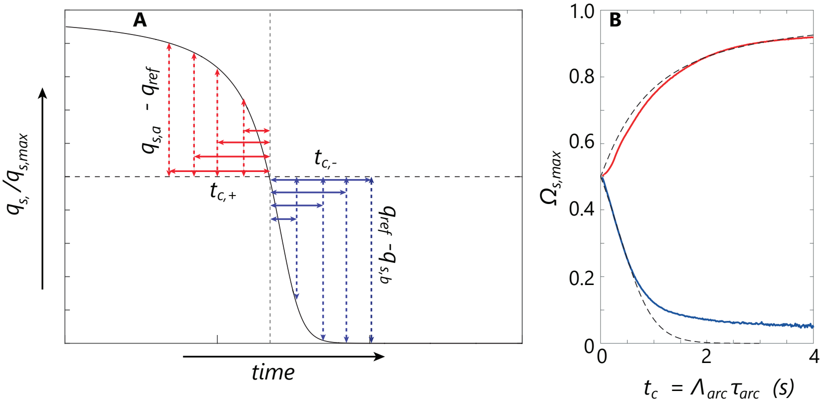

Figure 5.13: **A:** construction of the magnitude versus consumption time t_c distributions for an organism traveling inside a fluid element in an ideal plug flow reactor. For $q_s/q_{s,max} > q_{ref}$, $t_{c,+}$ is the time required to change from $q_{s,a}$ to q_{ref}, for $q_s/q_{s,max} < q_{ref}$, $t_{c,-}$ is the time required to change from q_{ref} to $q_{s,ab}$. **B:** Comparison of $\Omega_{s,max}$ vs. $t_{c,+}$ (red) and $t_{c,-}$ (blue) from the CFD simulations, compared to the PFR-relation $\Omega_{s,PFR}$ vs. $t_{c,+}$ and $t_{c,-}$ (dashed lines), showing good agreement between the observations of organisms in the limitation regime and organisms residing in a plug flow reactor.

Arc behavior

Above, it was established that the environment *within* the upward circulation loop of the top impeller is highly heterogeneous for the *P.chrysogenum* case. Further analysis of the relation $\overline{\Omega_{s,max}} = f(\tau_{arc})$ sheds additional light on this non-ideal behavior. The arc magnitude $\Omega_{s,max}$ is registered at time $\Lambda_{arc} \cdot \tau_{arc}$, as was illustrated in figure 5.4. For an upward arc, the average symmetry $\overline{\Lambda_{arc}} = 0.4$, which means that q_s increases over a period of $0.4\tau_{arc,+}$ and decreases over $0.6\tau_{arc,+}$. For the downward arc trajectories, $\overline{\Lambda_{arc}} = 0.5$, which means such trajectories can be regarded as symmetric

Due to the very high Da, the poorly mixed reactor may exhibit behavior close to that in a plug flow reactor (PFR), when evaluated from the microbial point of view. During the consumption period within an arc, the substrate concentration observed by an organism residing inside a fluid plug will change as eq. 5.10:

$$\frac{dC_s}{dt} = q_s C_x + M \tag{5.10}$$

Here, M is a mixing term representing exchange with neighboring fluid elements. We can compare this with the consumption profile inside a perfect PFR, where $M = 0$ and C_s/q_s decrease solely due to consumption. For upward arcs, this amounts to comparing the time required to change the concentration in a fluid element from some $q_{s,a}$ to q_{ref} with the time of q_s-decrease in an upward arc, $0.6\tau_{arc,+}$. For downward arcs, the time required to change from q_{ref} to $q_{s,b}$ is compared to $0.5\tau_{arc,-}$. A graphical outline of the $\Omega_s - \tau$ relation in a plug flow reactor is presented in fig. 5.13, **A**.

In 5.13 **B**, the $\Omega_s - \tau$ relation for a PFR operating at $C_x = 55$ g/kg (dashed lines) is compared with $\Omega_{s,max}$ vs. the consumption interval $\Lambda_{arc} \cdot \tau_{arc}$ from the CFD simula-

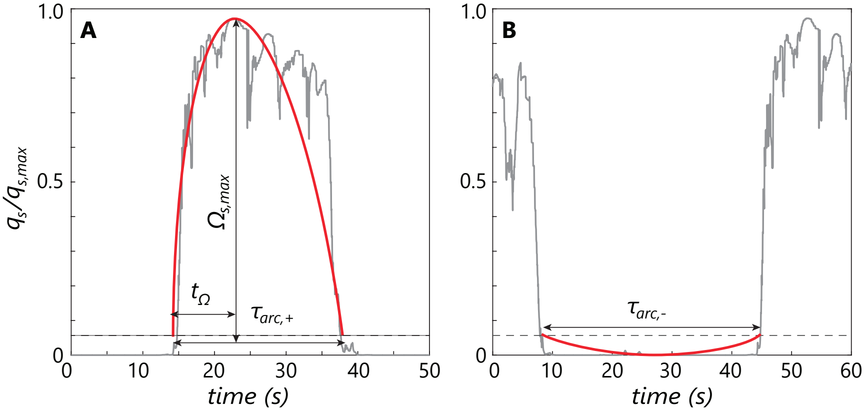

Figure 5.14: Outline arc analysis with alternative $q_{ref} = 0.05$ for *P. chrysogenum*. The solid gray line shows an excerpt of a lifeline, the red line shows the arc approximation for the shown sections. The arc time τ_{arc} is the time between the baseline crossings, the arc magnitude $\Omega_{s,arc}$ is the extreme value compared to the baseline. The arc symmetry is defined as $\Lambda = t_\Omega/\tau_{arc}$ where t_Ω is the time at which $\Omega_{s,max}$ is registered. **A:** A positive track compared q_{ref}. **B:** A negative track compared to q_{ref}, for which the magnitude can be neglected.

tions (solid lines). The agreement is striking; on average, the flow environment inside the limitation regime acts very close to a PFR, which means the exchange term M in eq. 5.10 is negligible. These notions have a profound impact on scale-down reactor design, which is discussed in the next chapter of this thesis. Naturally, the agreement breaks down near the regime boundaries, as all arc-trajectories crossing the regime boundary were discarded in this analysis.

Arc-analysis for *P. chrysogenum* with a different reference value

In the previous arc analysis for *P. chrysogenum*, $q_{ref} = 0.5$ was selected, being the value centered between the regime boundaries for the limitation regime. As was mentioned in the methodology section, the reference value for arc analysis can be chosen on multiple grounds, and arc-analysis can be conducted without an underlying regime analysis, too. We show such an approach here. In this approach, $q_{ref} = 0.05$, which is considered a relevant value for 2 reasons. First, on metabolic grounds, for $q_s < 0.05 q_{s,max}$ the organism takes up too little substrate to satisfy its maintenance demands. Second, on physical grounds, virtually the entire region of the broth with $q_s > 0.05 q_{s,max}$ is enclosed in the top circulation loop of the top impeller, which means the arc-shape assumption is reasonably satisfied. An added benefit is that the arc magnitude is negligible for downward arcs $q_s > 0.05 q_{s,max}$, and hence $\Omega_{s,max}$ only needs to be recorded for upward motions. Graphically, the alternative arc boundaries are presented in figure 5.14.

The arc magnitude, duration and symmetry plots resulting from this analysis are shown in figure 5.15. Again, the highly non-ideal mixing leads to a clear relation between $\Omega_{s,max}$ and τ_{arc} for positive fluctuations. However, the here-chosen q_{ref}

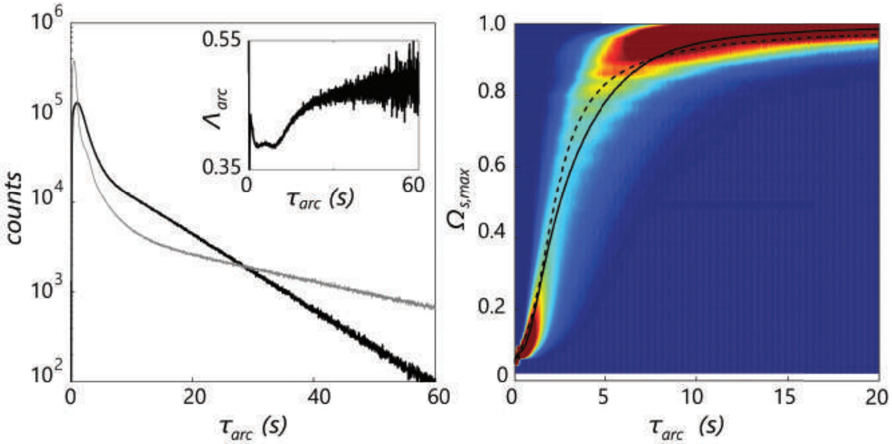

Figure 5.15: **A:** Arc-time distributions for arcs with $q_s/q_{s,max} < 0.05$ (gray) and $q_s/q_{s,max} > 0.05$ (black). The inset displays the arc symmetry t/τ_{arc}. **B:** Arc magnitude as a function of arc time. Colors indicate bin fraction (normalized per timestep). Solid line: $\overline{\Omega_{s,max}}$ $vs.$ τ_{arc} from CFD simulation. Dashed line: $\overline{\Omega_{s,max}}$ $vs.$ τ_{arc} for an ideal batch reactor; τ_{arc} is corrected for the arc-symmetry.

allows for a much simpler scale-down strategy than the earlier chosen baseline of $q_{ref} = 0.5$. This scale-down methodology is discussed in the next chapter.

5.5.5. Fourier analysis

A Fourier analysis was conducted on the q_s tracks in the *P. chrysogenum* reactor. The per-track frequency spectra were gathered according to the method outlined in section 5.3.3, yielding figure 5.16. As expected, no frequencies stand out due to the wide circulation time distribution, and no more direct insight in the fluctuations by moving to the frequency domain. We hence have chosen to discard the Fourier analysis in favor of a time-domain approach for stirred tanks. This does not mean that Fourier analysis could not be used in other situations; in *appendix E*, Fourier analysis of an airlift loop reactor is briefly discussed; due to the more structured flow pattern, distinct features in the spectrum are observed in that case, and Fourier analysis has the benefit of being more straightforward and faster than arc-analysis for such a case.

5.6. Concluding remarks

We have outlined a novel approach to analyze the data acquired by Euler-Lagrange CFD simulations of bioreactors. The Euler-Lagrange approach offers the possibility to analyze substrate concentration variations from the microbial point of view. The obtained $q_s(t)$ series, referred to as lifelines, are analyzed using three different methods. First, regime analysis, where the the lifeline is divided into metabolic regimes each representing a certain consistent response in an organism's metabolism to the extra-cellular substrate concentration. We record the residence time distribution within each regime as well as how organisms transit between regimes. Second, we use arc analysis, where the magnitude and duration of fluctuations with respect to a certain baseline q_{ref} are

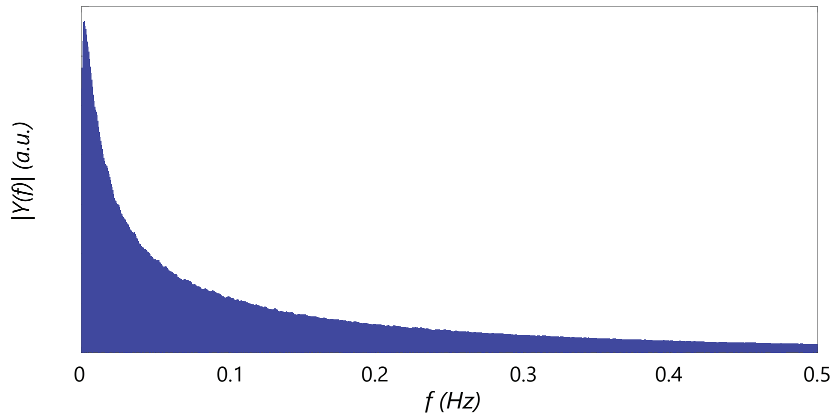

Figure 5.16: Fourier spectrum for 175.000 parcels in the *P. chrysogenum* process; the broad distribution of frequencies is a clear sign of the circulation behavior inside the domain.

analyzed in the time domain. Third, we use Fourier analysis, where the magnitude and duration of fluctuations with are analyzed in the frequency domain. For the widely distributed circulation time in a stirred tank, the first and second method provide most direct insight in the fluctuations that organisms are exposed to.

We provide a comprehensive statistical assessment of the substrate fluctuations experienced by organisms in an industrial scale fermentation. This information can a basis for the design of scale down simulators: lab-scale studies aimed at mimicking industrial scale conditions. In this work we studied the fermentation of *S. cerevisiae* in an aerated 22 m^3 reactor, and *P. chrysogenum* in a 54 m^3 stirred vessel with simplified hydrodynamics, neglecting aeration and non-Newtonian rheology. No oxygen limitation were assumed in either case, both cases were experimentally validated. In the *S. cerevisiae* case the circulation timescale and reaction timescale were in the same order of magnitude leading to a Damköhler number of $Da \approx 1$, leading to a significant substrate gradient over the entire reactor, with local well-mixed compartments around the individual impellers; in 24% of the reactor, ethanol formation by the Crabtree effect was predicted to occur. In contrast, in the *P. chrysogenum* case $Da >> 1$, resulting in a very strong gradient over the entire vessel and 57% of the vessel being effectively depleted of substrate. This different compartmentalization behavior was clearly reflected in the subsequent regime and arc analysis. The strong heterogeneity in the *P. chrysogenum* case means that organisms may observe an environment very much alike an ideal plug flow reactor; comparing the rate-of-change in the environment along an average arc-trajectory with the rate-of-change in a PFR yields very good agreement.

The regime analysis shows that the residence time in the prescribed regimes is follows an exponential distribution, in line with the circulation behavior inside the tank. In cases where multiple circulation compartments, which form around Rushton impellers, are enclosed inside a regime region, different circulation modes may occur.

These result in multi-modal exponential decay distributions, each slope in the distribution being associated with a certain circulation mode. The mean residence time in each regime is in the order of $3 - 30$ s, typically. This hints that the mean residence time inside different compartments of a representative scale-down simulator must be similarly short, much shorter than the timescales typically applied in the current generation of scale-down simulators. Similar observations are made in the arc-time analysis. The short timescales of concentration fluctuations, and high rates of change in the substrate concentration that organisms are predicted to observe, will lead to practical challenges in reactor scale-down. The next step towards rational design of scale down simulators is to use this CFD data as a basis of design. This issue, together with a discussion of the challenges that may be encountered in scale-down design, forms the subject of the next chapter.

6

Rational scale-down of industrial fermentors

The influence of extra-cellular variations on the organism can be probed using so-called scale-down simulators, laboratory scale setups where deliberate, controlled fluctuations are imposed in the extra-cellular environment. The major challenge associated with this scale-down philosophy is to design a scale-down simulator that resembles the extra-cellular environment of the industrial process. In the previous chapter, Euler-Lagrange CFD was explored to investigate the large scale environment from the microbial point of view, collecting statistics of the frequency and magnitude of environmental fluctuations that can serve as a basis for scale-down design. In this work, we discuss the scale down of the aerated fermentation of S. cerevisiae and a simplified representation of a P. chrysogenum fermentation, devising possible scale-down strategies based on this CFD data, both with fluctuating feed profiles and multiple compartments. All designs are deemed feasible within the limitations of current scale-down equipment. Additionally, several challenges of CFD-based scale down are discussed.

6.1. Introduction

Since large-scale gradients in industrial bioreactors can have a critical influence on the overall process performance, they should be accounted for during process development. To this end scale-down simulators (SD-simulators) have been developed; laboratory scale systems in which micro-organisms are subjected to temporal variations in a given process parameter [43, 48]. These may be well defined variations (e.g. [41, 44, 291]), typically imposed by a fluctuating feed in a single vessel, in order to study the direct impact of variations on the metabolism. Alternatively, fluctuations with a distributed duration can be imposed, being more representative of an actual industrial situation (e.g. [49, 50, 52, 55]). This is often done by placing multiple reactors, operating under different conditions, in a flow loop.

In order to obtain directly applicable insight into the effect of environmental variations in industrial scale reactors, the duration and magnitude of environmental variations imposed in SD-simulators should reflect the variations encountered at the large

---

Parts of this chapter have been published as: C. Haringa, W. Tang, A.T. Deshmukh, J. Xia, M. Reuss, J.J. Heijnen, R.F. Mudde and H.J. Noorman. Euler-Lagrange computational fluid dynamics for (bio)reactor scale-down: an analysis of organism life-lines, *Engineering in Life Sciences*, 16:652-663, 2016 and C. Haringa, A.T. Deshmukh, R.F. Mudde and H.J. Noorman, Euler-Lagrange analysis towards representative down-scaling of a 22 m^3 aerobic *S. cerevisiae* fermentation, *Chemical Engineering Science*, 170:653-669, 2017

scale. Statistics considering the distribution of the parameters of interest are, however, rarely available for industrial scale reactors. To approximate the industrial environment, current SD-simulators are often set to achieve a fluctuation duration in the order of the industrial 95% mixing time (τ_{95}), typically between $60-600$ s. In the previous chapter, we employed Computational Fluid Dynamics (CFD) simulations to show that this is too long; global concentration variations occurred on average in the order of the circulation time τ_{circ}, with local variations occurring at shorter timescales. Furthermore, low biomass concentrations (around $C_x = 5$ g/kg) are typically employed; a factor 10 lower than may be the case for a considerable portion of the industrial fermentation. As the rate of change in, for example, substrate concentration depends directly on C_x, the amplitude of extra-cellular variations that can be attained is typically constrained. While the currently generation of SD-simulators certainly has its merits for metabolic model development, they seem to poorly mirror industrial conditions.

The fluctuation statistics acquired from lifelines that were resolved with Euler-Lagrange CFD can serve as a basis of design for representative SD-simulators, which is explored in this chapter. The here-conducted analysis is based on the q_s-lifelines studied in the previous chapter. Using fluctuation statistics from q_s lifelines as a basis aims at replicating the large-scale extra-cellular environment, as experienced by micro-organisms, which should therefore induce the same metabolic response. The philosophy behind representative scale-down can be summarized as:

A representative scale-down simulator is to replicate those fluctuations in the extra-cellular environment to which the relevant metabolism of the micro-organism is sensitive, as observed by micro-organisms themselves, to the highest possible degree of accuracy.

It is possible to conduct a different scale-down strategy based on replication of the *intra-cellular* lifelines, if a metabolic model is available to simulate these lifelines. We briefly delve into this in *appendix B*. This scale-down philosophy is, however, more applicable for model verification, as intra-cellular scale-down may result in relevant extra-cellular variations being omitted, introducing unforeseen metabolic responses. This makes scale-down based on extra-cellular lifelines the preferred choice, especially when the goal is to study yield changes resulting from environmental variations.

Noorman previously concluded that there are 5 degrees of freedom in scale-down simulations. We explore how these degrees of freedom can be fixed based on the available statistics both for a single-vessel and multi-vessel scale down simulator. Several designs are compared in their agreement with the full CFD data. Finally, some previously operated scale-down simulators are discussed in terms of their agreement with industrial scale, and challenges associated with representative scale-down are identified.

6.2. Materials and Methods

Euler-Lagrange CFD simulations of an aerated 22 m^3 *S. cerevisiae* and a simplified representation of a 54 m^3 *P. chrysogenum* fermentation are studied for scale-down purposes in this study. The CFD setup, CFD validation and data processing routine have been discussed in the previous chapter. It is assumed that the lab-scale reactors used in this analysis are ideally mixed ($\tau_{95} << \tau_{rxn}$). This assumption is reasonable in all but the most extreme cases. A second effect that may introduce potentially unwanted transients in lab-scale fermentors is feed dripping; the feed rate F is often insufficient to maintain a steady flow. In case the dripping frequency $f_{drip} >> 1/\tau_{rxn}$ and $f_{drip} >> 1/\tau_{mix}$, no strong impact on the extra-cellular environment is to be expected. For a 3 L lab fermentor, both τ_{mix} and $1/f_{drip}$ are ≈ 2 s. This may introduce some transients, which are currently neglected. Of course, in case τ_{rxn} is low, the transient effects of dripping and the gradient resulting from insufficiently fast mixing can be used to impose deliberate heterogeneity; the resulting gradients are difficult to estimate, however, and they are currently not included in the analysis.

Scale down simulators may be operated in fed-batch mode (variable V_{tot}), or in chemostat mode (constant V_{tot}). Chemostat operation is often preferred for cell-analysis experiments, as the extra-cellular conditions are well-defined and constant in time. The growth rate μ in a chemostat is directly coupled to the dilution rate D_r, leading to a constant C_x, once the system reaches steady state. By construction, scale-down systems with feed variations will never be truly steady, but as the feed fluctuation timescale is far below μ^{-1} (with $\mu = 0.01 - 0.1$ h^{-1}), a statistically steady state is readily achieved. Chemostat operation is also preferred from the design point of view, as the CFD simulations used as a basis of design were similarly conducted with steady C_x, V_{tot} and a statistically steady extracellular environment. Because of this reason, chemostat scale-down is primarily explored in this chapter. Fed-batch operation, however, is more representative of the entire course typical industrial fermentations where C_x, V_{tot} and the extra-cellular conditions are a function of time. Computationally, these dynamics can be resolved by taking several snapshots at different stages of the fermentation, or simulating the entire fermentation with dynamic C_x; this is outside of the current scope, however.

6.2.1. Scale-down simulation

According to Noorman, any type of SD-simulator based on (ideal) lab reactors has a total of 5 degrees of freedom [15]:

- Number of compartments N_V
- Vessel volumes V_i or broth mass m_i
- Flow patterns (reactor types)
- Circulation rates ϕ_i
- Feed rates F_i (and locations)

The goal of CFD based scale-down analysis is to fix the values based on the fluctuation statistics acquired from CFD-generated organism lifelines.

Single-vessel scale down

Provided the ideal mixing assumption is met, all but one degree of freedom are fixed for a single-vessel approach: the feed rate of the limiting substrate $F_s = C_{s,f} \cdot F$ where $C_{s,f}$ is the substrate concentration in the feed, and F the total feed rate (if oxygen or CO_2 variations are imposed via gassing, $F = Q_g$). To impose extra-cellular variations, either F or $C_{s,f}$ can be varied in time. The desired q_s/C_s versus t profile, which can be seen as the lifeline of the scale-down simulator, is first determined. Then, F can be determined via the substrate balance, which for ideal mixing reads:

$$\frac{(FC_{s,f})}{m_{tot}} = q_s C_x + \frac{dC_s}{dt} \tag{6.1}$$

m_{tot} (the total mass) has been put on the left side of the equation to emphasize that the absolute size does not play a direct role in determining the feed fluctuations; m_{tot} can be freely chosen within practical limits. Single vessel scale-down is relatively straightforward in terms of operation: it does not require pumping of the broth between different compartments at high throughput rates, with possibly clogging pumps, shear damage to the cells, and several contamination-prone tubing sections. A drawback is that all organisms in the reactor experience the same extra-cellular conditions at the same instance of time, which may poorly reflect upon the population heterogeneity in industrial fermentors. Delvigne et al. [13] have shown that population divergence is to be expected even under well mixed conditions, but it may well be that the driving force of spatial heterogeneity in a large scale fermentor leads to a different rate of divergence within the population, or with different emergent phenotypes. Related to this (as further discussed in chapter 7) is the capturing of extreme events, such as lengthy starvation exposures. In real reactors, a small fraction of the population may be exposed to such events at any given time - but in a well-mixed single vessel scale down simulator, either none of the organisms are exposed to extremes, or all are.

Fourier analysis When there is a dominant circulation path in the reactor, extra-cellular fluctuations may have reasonably well-defined frequencies, in which case Fourier analysis provides useful insight and the scale-down procedure is comparatively simple. Sinusoidal variations in q_s can be imposed with the dominant fluctuation frequency from the Fourier spectrum; the associated amplitude can often simply be estimated directly from the lifelines. Once the scale-down lifeline is designed, the mass balance (eq. 6.1) can again be used to determine a feed profile. This method was not found to be applicable for stirred tanks due to the widely distributed circulation time, but it has merits for more defined flows, for example in airlift loop reactors. This is discussed in *appendix E*.

Arc analysis When the arc-time methodology is employed, q_s fluctuations compared to some baseline q_{ref} are to be imposed; this q_{ref} should be equal to the reference value chosen during the CFD analysis. The simplest approach is to impose cycles with a fixed period, alternating between upward and downward trajectories with the respective duration $\overline{\tau_{arc,+}}$ and $\overline{\tau_{arc,-}}$. The correlation between $\overline{\Omega_{s,max}}$ and τ_{arc} is used to set the associated magnitude. Using fixed-duration cycles has its merits for analysis: any effects on the metabolism can be linked to the well defined periodic fluctuations. However, this approach does not induce the most extreme events - both in duration and amplitude. The feed can be applied gradually, to impose smooth (sinusoidal) arcs, or instantaneously (at the start of an upward/end of a downward arc), to impose a saw-tooth shape. The first option is more realistic, as it is a better reflection of the rate-of-change in the environment that organisms experience. The instantaneous-pulse option is operationally simpler, however, but the metabolic shock induced by this method could lead to a different metabolic response than a more gradual feed. In case a metabolic model is available for the studied strain, this may be used to comment whether gradual and instantaneous feeding induce different metabolic responses.

The current generation of scale-down simulators typically applies fixed pulse intervals. Based on the CFD results, variable intervals are more realistic. These can be included based on the distribution in τ_{arc}, where the individual arc-duration is determined via inverse transform sampling. In this method, the cumulative distribution function (CDF) is used to transform a uniformly distributed random number into a random number distributed according to the corresponding probability distribution function (PDF). Once τ_{arc} is determined for a given cycle, the correlation between τ_{arc} and $\Omega_{s,max}$ can be used to match the correct amplitude with the sampled duration, and if desired, to match the arc-skewness Λ_{arc}.

Regime analysis The goal of regime-based scale down is to replicate the correct exposure duration to certain ranges of conditions, rather than mimicking the exact fluctuation amplitude. For each exposure, the extracellular substrate concentration should maintain between the regime boundaries. The simplest option is to impose variations of a fixed period, such as the feast-famine cycles used in prior scale-down experiments [44, 45]. The overall cycle time τ_{cycle} can be based on the vessel circulation time, which is representative of organism motion through the vessel, or on the summation of the mean regime residence times $\sum_{i=1}^{n} \overline{\tau_{res,i}}$ of all relevant transition patterns. The downside of using regular feast famine cycles is that, while the regime distribution is captured on average, the distribution in individual exposures may be poorly captured, and the correct regime transition behavior is not accounted for.

Regime transitions can be included if the trajectories are segregated based on their regime of origin and destination, as was done in the previous chapter. The regime-follow up probabilities can straightforwardly be introduced Using a random number generator, and if every individual regime exposure has a duration equal to the mean regime residence time $\overline{\tau_{res}}$, the per-exposure duration as well as the overall exposure to a certain regime are correctly captured. As for the arc-distribution, the residence time distribution per regime can be introduced via inverse transform sampling if desired. The advantage of arc-analysis is that the exposure duration to critical conditions, such as overflow conditions, can be properly captured. However, the method is less accurate in capturing exact fluctuation amplitudes, as the full lifeline is essentially reduced to a number of q_s-discrete levels. As a result, the method may perform poorly for gradual fluctuations without clear metabolic thresholds. Arc-analysis can be used to introduce super-imposed intra-regime fluctuations, if required.

Multi-vessel scale down

Multi-vessel scale-down is best based on the regime analysis method; it may be possible to conduct an arc-analysis based scale-down, but this is significantly less intuitive. All degrees of freedom have to be treated in this method.

Number of compartments The number of compartments is most straightforwardly based on the number of regimes. It is possible to impose multiple regimes in one (or more) compartments by adding feed variations, to reduce the set-up complexity. In the case of a complex regime residence time distribution, multiple physical compartments may be used to capture a single regime; this is further discussed under *flow patterns*.

Vessel volumes/broth mass The absolute vessel size is not relevant provided the ideal mixing assumption is satisfied, and the feed rate is sufficiently high to prevent excessive dripping intervals. The relative vessel broth mass m_i/M_T (or volume V_i/V_T) is to be matched with the relative mass enclosed by a given regime in the CFD data. If the full industrial fermentation is simulated, including long term dynamics in C_x and τ_{rxn}/τ_{circ}, the mass-per-compartment may change in time. This should be reflected in the filling level of the individual compartments.

Flow patterns The flow pattern of each compartment depends on the shape of the residence time distribution. A log-normal or exponential decay distribution hints at circulation behavior, best mimicked by a stirred tank. A narrow distribution hints at using an axially-dispersed PFR, where the variance of the distribution determines how much dispersion should be imposed. Fitting known RTD functions for particular lab-scale reactors to the regime RTDs can be used to find the best matching reactor type. RTDs enclosing multiple circulation loops may show complex RTDs with multiple time constants, as is the case for the starvation regime in the *P. chrysogenum* case. Such multi-modal distributions may be accurately reproduced with a combination of 2 or even 3 vessels, although this quickly leads to cumbersome designs.

Circulation rates Circulation rates (mass-based) are straightforwardly computed from the vessel mass m_i and mean residence time τ_i as $\phi_i = m_i/\tau_i$. However, the overall circulation of the system has to abide $\Sigma\phi_i = F - D_r$, which is 0 in chemostat operation while for a fed batch $D_r = 0$. Calculating ϕ_i from τ_i does not satisfy this constraint, due tot the influence of filtering and the complex shape of the distributions. A constrained fitting routine is used to find the best-fitting residence time distributions, by minimizing the sum-of-square difference between the CFD-based RTDs, and the idealized RTDs of the simulated compartments:

$$cost = \sum_{i=1}^{N_v} \left(\sum_{j=1}^{N_t} (RTD(j) - f(j))^2 \right)_i \tag{6.2}$$

Here, $f(j)$ is the RTD of the lab-scale vessel, and N_t the number of timeslots. Nearly all CFD RTDs discussed in the previous chapter exhibited a peak at $t \approx 1$s, which has a strong effect on τ_{res} and the fitted profiles. These short fluctuations are low in amplitude, and may be ignored by specifying a certain time-range for the cost function, rather than taking all data points.

Feed/drain selection The feed rate F and drain rate D require the circulation rates to be established, as their calculation is based on the per-vessel mass-balance. The feed and drain rate for each individual vessel can be calculated by solving equations 6.3 - 6.5, the given example being for a generic 3-vessel scale-down simulator, which is outlined in figure 6.1.

$$0 = \frac{F_1(C_{F,1} - C_{s,1})}{m_1} + \frac{\phi_1(C_{s,2} - C_{s,1})}{m_1} - q_{s,max}C_x\frac{C_{s,1}}{K_s + C_{s,1}} \tag{6.3}$$

$$\begin{aligned} 0 = \frac{F_2 C_{F,2}}{m_2} + \frac{(\phi_1 + F_1 - D_1)C_{s,1}}{m_2} + \frac{(\phi_2 + F_3 - D_3)C_{s,3}}{m_2} \\ - \frac{(\phi_1 + \phi_2 + D_2)C_{s,2}}{m_2} - q_{s,max}C_x\frac{C_{s,2}}{K_s + C_{s,2}} \end{aligned} \tag{6.4}$$

$$0 = \frac{F_3(C_{F,3} - C_{s,3})}{m_3} + \frac{\phi_2(C_{s,2} - C_{s,3})}{m_3} - q_{s,max}C_x\frac{C_{s,3}}{K_s + C_{s,3}} \tag{6.5}$$

For each vessel, a target C_s representative of the average extra-cellular conditions, or the average metabolic response within a certain regime should be specified. In most cases, the regime-mean q_s is the obvious choice, but there may be exceptions, for example in cases with strongly non-linear overflow conditions. There, a better choice may be the value of C_s that captures the mean production rate of the overflow metabolite, q_{ov}. Since the vessels are linked and substrate is carried over, it may not be possible to meet the target concentration for each individual vessel. A cost function minimization routine may be used to find the closest match in C_s values within the posed constraints, and to find the most suitable feed and drain layout. Again, when a metabolic model is available, the cost function may consider the best replication of the metabolic response observed in the CFD simulations, rather than solely fitting to the C_s values.

In principle, a feed and drain can be added in each compartment, but the most common solution is to feed only the compartment with the highest target q_s, and to

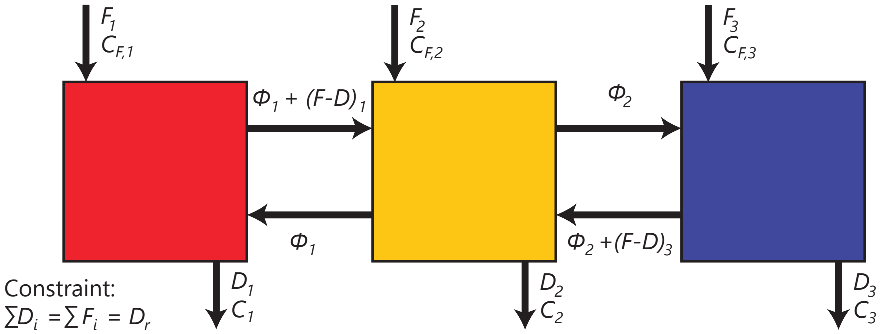

Figure 6.1: Example of a generic 3-vessel scale down reactor system. Solving the mass balances for the shown system determines the agreement in per-regime residence times. The substrate component balances can be used to determine required feed rates.

drain from the low-q_s compartment. In case a chemostat operation is decided upon, the growth rate μ equals dilution rate D_r, which means that the total feed rate ΣF_i has to equal $m_{tot} \cdot D_r$ on average. If it is desired to superimpose temporal variations in the feed, this can only be done by varying $C_{s,f}$, in this case.

6.3. Scale-down challenges

To fully replicate the q_s-fluctuations seen by organisms on the industrial scale, an SD simulator has to replicate the rate of change in the environment, dC_s/dt, as seen by organisms. In ideal scale-down simulators based on a PFR or (fed-)batch reactor (during a phase where $F_s = 0$), $dC_s/dt = -q_s C_x$ in the organism's frame of reference. In the industrial vessel, the rate of change in the organism's reference frame is:

$$\frac{dC_s}{dt} = q_s C_x + M \tag{6.6}$$

Here, M is a mixing term represents the exchange of substrate between the fluid package surrounding the organism, and neighboring fluid. For strongly non-ideal systems where $\tau_{rxn} << \tau_{circ}$, such as the studied *P. chrysogenum* fermentation, $M \approx 0$, which means an equal-rate of change dictates $(q_s C_x)_{industry} = (q_s C_x)_{SD}$, and since q_s are the intrinsic kinetics, $C_{x,ind.} = C_{x,SD}$. This notion was clearly illustrated in figure 5.13, where the plug-flow solution using $C_{x,ind.}$ perfectly collapsed on the $\overline{\Omega_{s,max}}$ $vs.$ t plot. Current lab-scale chemostat reactors are typically operated with $C_x = 5 - 10$ g/kg. This already indicates that such simulators at best represent industrial fermentations operating within this low range of C_x, and poorly reflect the conditions in high cell density fermentations.

In case of moderate heterogeneity ($\tau_{rxn} \approx \tau_{circ}$), M is non-negligible, and can be both positive and negative. Consider an organism carried by a down-flowing, glucose-rich broth stream. This stream interacts with an upward flow of glucose-depleted broth; if mixing between the two streams is significant, this enhances the rate of change observed by an organism in the downward flowing fluid element due to dilution with depleted broth, whereas organisms in the upward moving plug see some supply of substrate. Critically, the rate of change observed by organisms in the downward flowing fluid element is *higher* than the rate of change induced by their own consumption. A scale-down simulator with instantaneous mixing or pure plug flow can, by construction, not capture such effects unless $C_{x,lab} > C_{x,ind}$. This basically provides two options if such events are to be captured explicitly: operating at $C_{x,lab} > C_{x,ind}$, or deliberately introducing non-ideal behavior (axial dispersion, poor mixing) at the lab scale. In this chapter, we solely consider the first option; the more complex second options is out of our current scope.

We practically observe this in the *S. cerevisiae* case study, where the mean RTD of the *type b* trajectory $\overline{\tau_b} = 40$ s (see fig. 5.8). This *type b* trajectory amounts to a reduction in q_s from $q_s > 0.2 q_{s,max}$ to $q_s < 0.05 q_{s,max}$. In a plug flow reactor the same change requires 67 s, for the given kinetics and industrial biomass concentration $C_x = 10$ g/kg. The observed transition is 1.67 times faster in the CFD simulation than can be realized in an ideal scale-down simulator, unless C_x in the simulator is increased accordingly.

The arc analysis conducted for *S. cerevisiae* in the previous chapter shows that the organisms do not experience a gradual change in their environment in this case, but rather discrete jumps associated with changes in circulation loop. Such instantaneous jumps cannot be captured in fluctuating-feed single-vessel setups by construction, but they may be approximated in multi-compartment scale-down simulators. In such situations, the jump is still dictated by the overall rate of consumption. Assuming first order kinetics ($q_s = q_{s,max} C_s$) for simplicity, the concentration jump between two compartments reads $C_2 = C_1/(1 + q_{s,max} \cdot C_x \cdot \tau_2)$.

From the above, we conclude that any scale-down reactor, based on ideal unit operations (well-mixed or plug flow), needs to operate at equal or higher C_x as its industrial counterpart in order to capture the *rate-of-change* experienced by microorganisms. There may be possibilities to relax this requirement in certain cases, but this requires the metabolic response of the organism to be evaluated, and hence requires a metabolic model to be available. This is considered in the next chapter. Still, even if there is some room to relax C_x based on metabolic model predictions, we still deem operating at industrial C_x to be the preferred option, to avoid possible responses that are not accounted for by the model; representing the extra-cellular environment as truthfully is considered the best practice in any case. This requirement may impose operational challenges: primarily, high C_x may induce unfavorable rheological properties (especially for mycelial broths), which can lead to issues with pumping (in multi-vessel systems), inter-phase mass transfer and mixing. In this work, we do not take these limitations into account explicitly in the proposed conceptual scale-down simulator designs, but we do reckon they should be considered in the detailed design phase.

Table 6.1: Design aims for the 3-compartment scale-down approach. m is fixed, $q_s/q_{s,max}$ is based on the per-regime mean uptake rate.

Vessel	m_i/m_{tot} (kg/kg)	$q_s/q_{s,max}$
T1	0.24	0.309
T2	0.41	0.105
T3	0.35	0.034

6.4. Scale-down: examples

In this section, several conceptual scale-down strategies are presented, based on both case-studies outlined in the previous chapter. The main goal of these examples is to outline how CFD simulations can be used to guide scale-down design, not to yield detailed designs for actual scale-down simulators.

- 3 Regime based 3-vessel scale down, *S. cerevisiae*
- 3 Regime-based 1-vessel scale down, *S. cerevisiae*
- Arc-based 1-vessel scale down, *P. chrysogenum*

An additional Fourier-based 1-vessel scale-down methodology is presented in *Appendix E*.

6.4.1. Regime based 3-vessel design, *S. cerevisiae*

We fixed $N_V = 3$, each compartment representing one of the regimes discussed in section 5.5.2: an overflow compartment, a limitation compartment and a low-q_s compartment. The broad, exponentially decaying regime RTDs (fig. 5.8) clearly show that each regime is best represented by a stirred tank, which under ideal assumptions has the residence time distribution of eq. 6.7:

$$f(t) = \frac{1}{\tau_i} \exp\left(-t/\tau_i\right) \tag{6.7}$$

with $\tau_i = m_i/\phi_i$ where ϕ_i is the mass-based compartment flowrate. The relative compartment mass m_i, based on the volumetric regime distribution, is reported in table 6.1, column 2. The circulation rates ϕ_i have to be determined by fitting the per-regime RTD, constrained by $\phi_1 + \phi_3 = \phi_2$, as reported in section 6.2.1. Here, ϕ_2 is the overall residence time distribution for the limitation compartment, regardless of the parcel trajectories through the regime. The best fit, design M1, is summarized in table 6.2. A low τ_i is found for each compartment due to the short-timescale variations dominating the fit; the frequency of the more relevant longer exposures is strongly underestimated, and practically the very short residence times mean $\overline{q_s/q_{s,max}}$ cannot be met due to excessive substrate carry-over. An improved design (M2 in table 6.2) was constructed by evaluating the cost function 6.2 only for the interval $20 \text{ s} < t < 60 \text{ s}$.

Table 6.2: Tank specifications for design M1 (top three rows) and design M2 (bottom three rows).

Vessel	ϕ_i (kg/kg/s)	τ_i	R^2
T1-M1	0.0663	3.62	0.80
T2-M1	0.097	4.23	0.68
T3-M1	0.0307	11.41	0.67
T1-M2	0.0093	25.8	0.31
T2-M2	0.0193	21.2	0.29
T3-M2	0.0100	34.9	0.54

The overall R^2 of this fit is logically lower, as the short-time events remain unaccounted. However, this fit shows a more satisfactory reproduction of long-term behavior (figure 6.2 **A**) as the design filters out brief, low amplitude substrate fluctuations while retaining the desired long-term behavior.

The operating condition for each vessel is set to the regime mean $\overline{q_s/q_{s,max}}$, reported in table 6.1, which was determined from figure 5.7. In order to meet these conditions, we operate the reactor at $C_x = 20$ g/kg. We do not consider superimposed variations in $q_s/q_{s,max}$ in this example. We propose to operate the SD-simulator as a chemostat (reflecting the simulated snapshot). This means μ must be estimated under the simulated conditions, and D_r has to be set accordingly. Assuming that variations in μ are slow compared to imposed extra-cellular variations, we assume $\overline{\mu} = f(\overline{q_s})$. This assumption is supported by the work of Suarez-Mendez et al. [45], who showed that variations in metabolites such as amino-acids and TCA intermediates are strongly dampened when 400 s feast-famine cycles are imposed. It is likely variations in a derivative process such as growth are consequently dampened as well. This does not imply that $\overline{\mu}$ under dynamic conditions equals $\overline{\mu}$ under steady conditions with the same $\overline{q_s}$, but lacking data on the effect of q_s-dynamics on $\overline{\mu}$, we here do assume that $\overline{\mu}$ can be estimated by solving the Herbert-Pirt equation, eq. 6.8:

$$\overline{\mu} = (\overline{q_s} - m_s) \cdot Y_{sx} \tag{6.8}$$

where the maintenance coefficient $m_s = 0.01$ g$_s$/g$_{dw}$/h and $Y_{sx} = 0.5$ [42, 228]. The CFD simulations give $\overline{q_s} = 0.129 q_{s,max}$, yielding $\overline{\mu} = 0.10$ h^{-1}, or $D_r = 2.8 \cdot 10^{-5}$ kg/kg/s. If an instantaneous adaptation of μ to the conditions in each individual compartment is assumed instead, the result setup-average $\overline{\mu} = 0.11$ h^{-1} and $D_r = 3.1 \cdot 10^{-5}$ kg/kg/s, showing comparatively little difference.

The individual vessel feed rates are found by solving the coupled mass balances (see section 6.2.1) with the constraint $\Sigma^{i=3} F_i = D_r = 2.8 \cdot 10^{-5}$ kg/kg/s. Optimization was conducted using the genetic algorithm available in MATLAB, yielding the feed parameters reported in table 6.3 for design M2; the design is outlined graphically in 6.2 **B**. An organism lifeline is included in 6.2 **C** to sketch the qualitative behavior of an organism in the proposed simulator. The feed and concentration constraints could not be satisfied for design M1 with $C_x = 20$ g/kg.

Table 6.3: Design M2: Best fit for the feed conditions and estimated per-compartment glucose uptake rate.

Vessel	c_F (mol/kg)	F_i (s^{-1})	$q_{s,fit}/q_{s,max}$
T1-M2	0.25	$2.8 \cdot 10^{-5}$	0.309
T2-M2	0.041	$5.2 \cdot 10^{-8}$	0.107
T3-M2	0.021	$4.5 \cdot 10^{-8}$	0.042

When designing a fed batch system rather than a chemostat, a reasonable choice may be to regard the above conditions as a starting point, subsequently allowing C_x to develop freely while keeping F constant. Ideally, ϕ_i and m_i should change over time to reflect the changes in regime distribution inside the industrial reactor over time, which can be estimated by repeating the CFD analysis for different C_x.

6.4.2. Single vessel, Regime-based: *S. cerevisiae*

As noted in section 6.2.1, the simplest approach to an oscillating feed is to impose feed-famine cycles, imposing a regime $1-2-3$ pattern, or transition pattern $e-b-f$, based on the trajectory definitions of fig. 5.8. Taking the per-regime residence times as a basis of design would significantly under-represent the exposure to regime 1, the overflow regime, as the above methodology does not account for regime follow-up.

The first objective of this scale-down approach is to capture the overall regime exposure (24% overflow, 41% limitation and 35% starvation), the second objective is to do so at timescales reasonably reflecting the large-scale fluctuation time. Due to the reasons outlined in sec. 6.3, the *type b* trajectory is the most challenging to replicate. Its mean duration, $\tau_b = 38.4$ s, can be captured if we operate at $C_x = 16.7$ g/kg. Abiding the overall regime exposure distribution then gives a total cycle time of 93.7 s, about twice the vessel circulation time. This design, named $S1$, captures the duration of b trajectories by design, and reasonably captures the duration of the f trajectory, as is shown in table 6.4. The duration of the e trajectory is highly over-estimated: in the CFD simulation, parcels visit the overflow regime more frequently, but with much shorter average exposure times. The maximum $q_s/q_{s,max}$ obtained in the simulator, named QM, is 0.34. This is much lower than the value of 0.66 observed in the CFD simulations; the most extreme amplitude events will never be reproduced in a vessel with a fixed oscillation period. Whether this is a significant issue is open for debate, since a) the region in which such high concentrations occur is comparatively small and b) the CFD simulations assume a homogeneous biomass concentration in the tank, whereas in reality it will take some time to mix the biomass broth with the viscous glucose syrup fed into the reactor. This means that the fraction of organisms exposed to excessive substrate concentrations may be even smaller practically. A subgrid mixing model will need to be included in future CFD simulations to capture mixing between the broth and feed stream.

Randomized cycle design The above design has its merits in studying how organisms respond to repetitive, well-defined variations, with a duration of the correct order-of-magnitude. Yet, they do not include several aspects of the CFD results and an alterna-

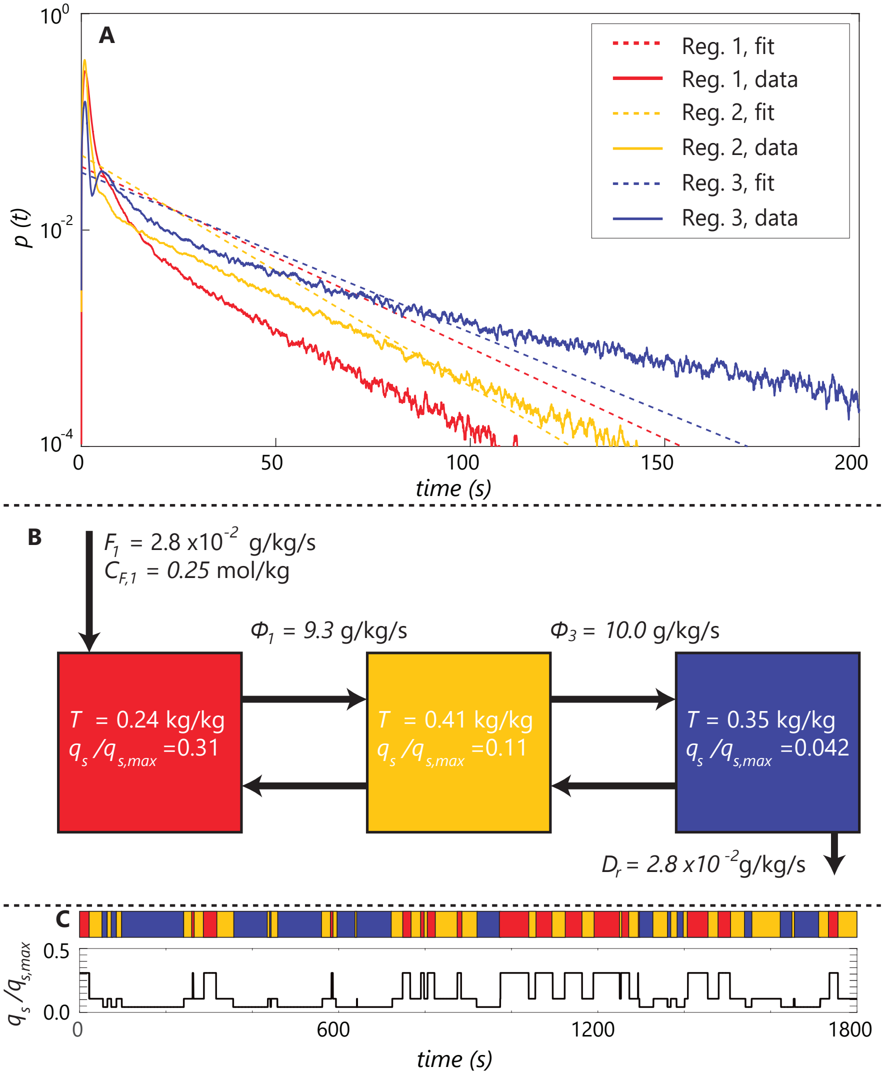

Figure 6.2: **A, B:** Specifications design M2 **A:** Comparison between the normalized RTDs from CFD (solid) and fitted RTDs (dashed). **B:** Schematic design of the proposed simulator. Volumes and flow rates are given per liter of total setup volume; the absolute vessel size is a free parameter. **C:** Example of an Oscillation profile experienced by a single organism circulating through the system.

Table 6.4: Simple single vessel design strategies, based on the global regime distribution, compared to the Eulerian and Lagrangian simulation perspective (row EUL and LAG, respectively). Design S1 considers fixed cycle pulsing, S2 a more complex oscillation strategy. R1, R2, R3 are the regime fractions.

Case	τ_a (s)	τ_b (s)	τ_c (s)	τ_d (s)	τ_e (s)	τ_f (s)	R1 (%)	R2 (%)	R3 (%)	QM –	$\overline{q_s/q_{s,max}}$ –
EUL	–	–	–	–	–	–	24	41	35	0.66	0.129
LAG	7.0	38.4	14.0	39.4	8.0	34.2	18	42	40	0.66	0.11
S1	–	38.4	–	–	22.50	32.8	24	41	35	0.34	0.123
S2	7.0	38.4	14.0	39.4	8.0	34.2	19	43	38	0.26	0.11

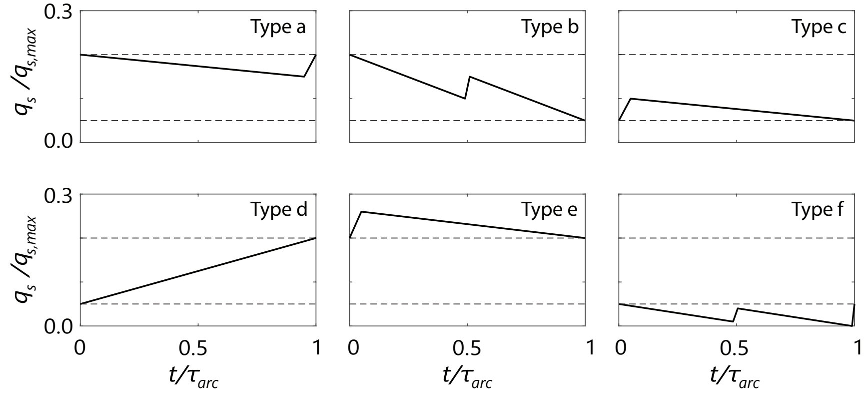

Figure 6.3: Simplified graphical representation of the 6 building blocks used to construct the fluctuating feed signal. Dashed lines represent the regime boundaries. At the end of an e-type block, a random number determines if an a or b block follows. After an f block, a random number determines whether a c or d block follows. a and d are always followed by e, b and c always by f.

tive design including regime follow-up and properly capturing residence time distribution in each regime must be considered. Here, we propose a regime-based randomized cycle design which captures the regime follow-up behavior and mean residence time $\overline{\tau_i}$ for each of the six trajectories; capturing the full distribution in residence times is problematic due to the consumption limitation in instantaneously mixed vessels, discussed in 6.3, and is considered to be out of the current scope.

To construct a scale-down lifeline that abides the regime follow-up registered in CFD simulation, we specify six building blocks, each representing one of transition trajectories reported in figure 5.2. The duration of each block is equal to $\overline{\tau_i}$. After each e- or f-type block, a random number generator is used to determine which block type follows based on the follow-up distribution. The blocks are graphically represented in figure 6.3. To allow for more complex feed profiles that better capture the q_s distribution within each regime, we set $C_x = 20$ g/kg, as was done for the multi-vessel simulator. This means an additional substrate pulse is injected halfway each $b-$ and $f-$ type block to achieve the proper block duration. In the type d-type block, the substrate concentration is gradually increased. Type e and c blocks both have a feed-spike at the start of the block, with consumption only during the remainder. An example of

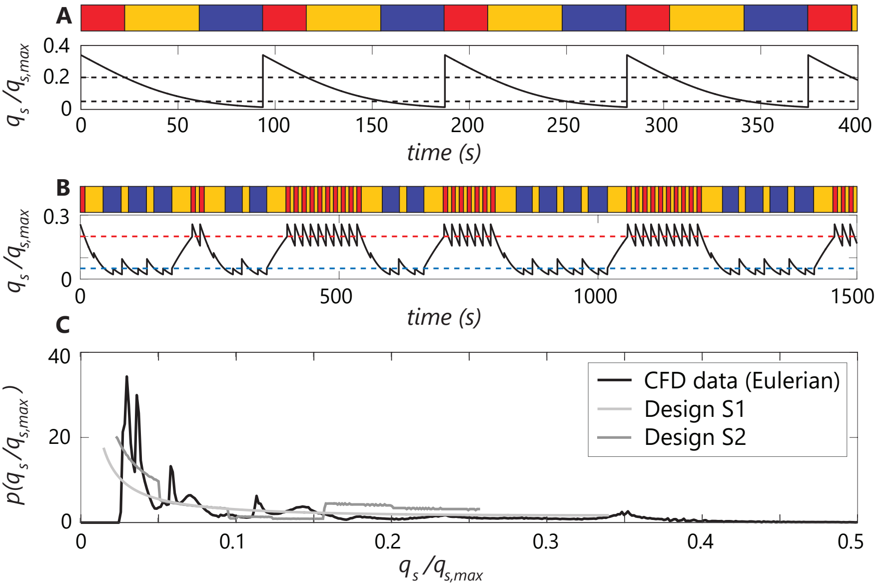

Figure 6.4: Design strategies for a single-vessel SD-simulator. **A:** $q_s/q_{s,max}$ oscillation profile (and associated regime profile) vs. t series for design S1, based on the per-regime exposure described in table 6.4. **B:** Randomized feed signal (design S2), based on $\overline{\tau}$ for each regime. **C:** Overlays the volumetric q_s-distribution for a 300 h stretch of such each signal, compared with the (Eulerian) q_s-distribution of the CFD data.

a sampled $q_s/q_{s,max}$-lifeline based on the approach outlined above is displayed in figure 6.4 **C**.

Running the proposed protocol for $t = 300$ h yields a regime division of 19 %, 43 %, 38 % for regimes $1,\ 2,\ 3$, respectively, which reflects upon the Lagrangian distribution reported in 5.5.2. The time-averaged uptake $\overline{q_s/q_{s,max}} = 0.110$, in excellent agreement with the Lagrangian and acceptable agreement with the Eulerian CFD results. A weak design aspect is the achieved $QM = 0.26$, a consequence of the short duration of the type-e block. This can be improved by further increasing C_x or by including the block RTD, allowing longer exposures. Considering the overall feed rate under chemostat conditions, the calculations are equal to the 3-vessel design.

Distributions of $q_s/q_{s,max}$ The time-averaged q_s-exposure distribution is captured in figure 6.4, **C** for each proposed feed cycle, and compared with the Eulerian distribution observed in the CFD simulation. Naturally, the compartment peaks are not resolved by any design, but the global trends are retrieved, most properly by S2. S1 only roughly captures the global distribution in comparison. The highest values of q_s are poorly captured by design S2, which is compensated in the range $q_s/q_{s,max} = 0.2 - 0.25$. A deficit in counts in the region of $q_s/q_{s,max} = 0.1 - 0.15$ is visible as this region lies outside of the current range for both the a and c-block; this can be fixed by either increasing C_x, or accounting for the RTDs.

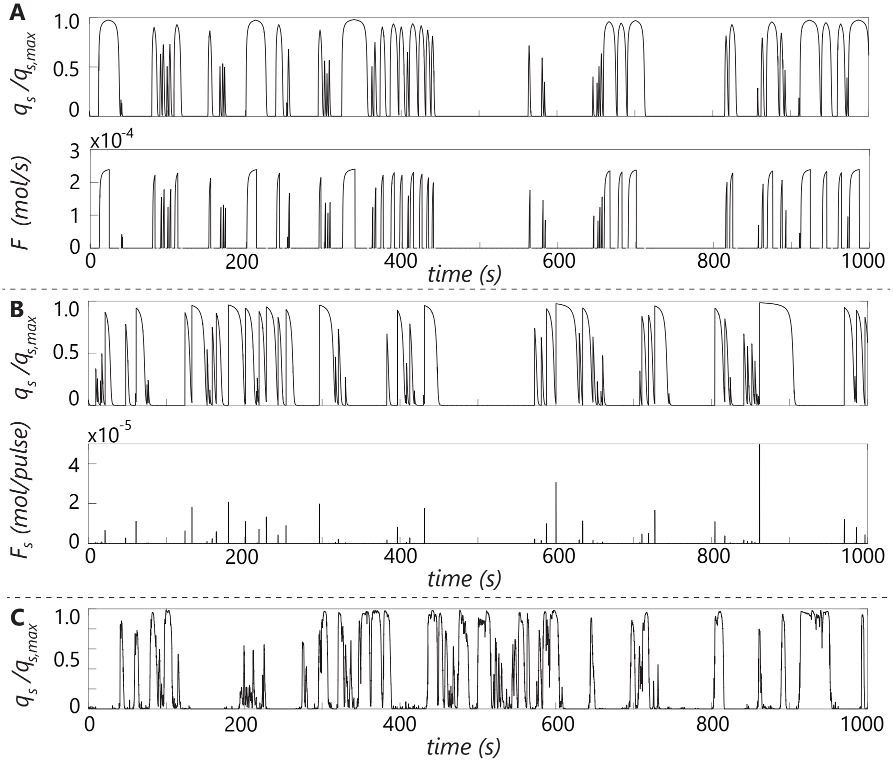

Figure 6.5: **A:** Randomly sampled oscillation profile, design PC.S1. The top figure shows the q_s-response of particles assuming ideal mixing conditions, the bottom figure the required feed profile. **B:** Similar to **A**, for design PC.S2. Instantaneous pulses are applied, hence the feed profile is now expressed in mol/$pulse$ rather than mol/s. **C:** Reference track from the CFD simulations of chapter 5.

6.4.3. Single vessel, arc-based: *P. chrysogenum*

A single-vessel scale-down protocol for *P. chrysogenum* is reported based on the arc-analysis method with $q_{ref} = 0.05q_{s,max}$, outlined in section 5.5.4, without requiring the specification of any further regimes. For famine arcs ($q_s < 0.05q_{s,max}$), we assume $q_s \approx 0$ regardless of duration. For feast arcs, the correlation between magnitude $\Omega_{s,max}$ and duration τ_{arc} can be used to quantifies the arc-magnitude, and together with statistics on the arc-time distribution, this follows a full set of statistics quantifying q_s fluctuations.

Representative profiles of alternating feast-famine intervals are generated from the τ_{arc} distributions by inverse transform sampling; for each feast interval, the maximum q_s is retrieved from the mean τ_{arc}-$\overline{\Omega_{s,max}}$ correlation, Determining the feed rate F_s is straightforward from the mass balance. Do note that we still work under the assumption of ideal mixing here, even though the substrate concentration varies in time. The notion of ideal mixing here means each feed pulse is instantaneously distributed within the volume, and the reactor is spatially homogeneous at all times, even though

Table 6.5: Regime distribution for single-vessel scale-down designs of the *P. chrysogenum* process. The values for the scale down simulators represent the mean ± 1 standard deviation over 5 runs of 100 h.

Regime	CFD	$PC.S1$	$PC.S2$
1 (excess)	6.8%	$9.6 \pm 0.3\%$	$8.0 \pm 0.2\%$
2 (limitation)	36.2%	$32.4 \pm 0.3\%$	$34.2 \pm 0.1\%$
3 (starvation)	57.0%	$56.8 \pm 0.6\%$	$57.8 \pm 0.3\%$

it is temporally heterogeneous. During famine intervals, $F_s = 0$ and $q_s \approx 0$ by construction. This approach provides a relatively truthful representation of feast-famine alternations in the industrial reactor. The most realistic approach is to feed gradually, such that the arc-shape is symmetric (fig. 6.5, **A**) and the rate-of-change observed by organisms in the large-scale reactor is adequately captured; this requires the lab-scale to operate at the industrial biomass concentration $C_x = 55$ g$_{dw}$/kg; this design is referred to as PC.S1.

If we compromise the agreement in rate-of-change by administering instantaneous feed pulses instead of gradual feeding, the required biomass concentration can be relaxed to $C_x = 27.5$ g$_{dw}$/kg: the instantaneous pulse administration means the total length of the feast arc is available decreasing q_s by consumption, whereas with gradual pulsing q_s decreases only during half of the arc duration. The instantaneous-pulse design is referred to as PC.S2, and a sample trajectory is given in fig. 6.5, **B**. In 6.5 **C** a CFD track is shown for reference. In both cases, a regime analysis, using the excess/limitation/starvation division used in chapter 5 shows that the q_s-lifelines for both PC.S1 and PC.S2 reflect the regime division observed in the CFD simulation. The question remains whether or not the compromise in the rate-of-change for design PC.S2 will influence the metabolic response; this is explored with metabolic modeling in chapter 7.

6.5. Analysis of prior scale-down designs

Previously, scale-down studies on *S. cerevisiae* have been performed replicating both oxygen [41, 53, 292] and glucose gradients [42, 45, 49, 51, 52, 293, 294]. Being the focus of the current work, we briefly discuss the glucose-variation experiments.

Multi-compartment George et al. [51, 293] based their scaledown study on a 215 m^3 industrial bubble column, with a PFR representing the 'crabtree compartment' ($C_s >$ 0.11 g/kg for the used strain), which contained 10% of the process volume. Despite replicating a different reactor, this volume was based on observations by Larsson et al. [16]. C_x was $10 - 50$ g/kg, in the industrial range. Both the SD-simulator and the well mixed benchmark of George et al. ran at high residual substrate (glucose + fructose) concentrations, between 100 and 150 mg/L most of the time. These levels roughly correspond to experimental samples taken at heights of 2.1 and 6.3 m in their fermentor. With a total filled $9.7 - 16.3$ m, the overall gradient was likely stronger. The average residence time in the stirred compartment was 9 min, the PFR residence time 1 min. The mixing time in a bubble column can be estimated using eq. 6.9 [169], yielding $\tau_{95} = 57$ s for the highest hold-up, with τ_{circ} around a factor 4 lower. This indicates that the SD-simulator design of George et al. strongly overestimated the fluctuation duration.

$$\tau_{95} = 1.6T^{2/3} \cdot (gU_g)^{-1/3}(H/T)^2 \tag{6.9}$$

Based on our CFD data, the inclusion of feed variations to create a hybrid multi-vessel fluctuating-feed setup would constitute an upgrade for the design of George et al. This would induce q_s-lifelines similar to those in figure 6.2 **C**, where the multi-vessel construction is responsible for the high-amplitude variation (between the border of the overflow regime and the border of the starvation regime), with the more rapid substrate variations around these borders being imposed by feed fluctuations. Such a hybrid between the varying feed and multiple vessel approach was not assessed in detail in our work, but may provide a method to reproduce rapid variations at the relevant timescales in multi-vessel setups, without requiring excessive pumping rates by keeping τ_{circ} for the individual vessels in the range utilized by George et al.

Sweere et al. [52] simulated glucose variations in a 2 STR system with τ_{circ} ranging between 0.6 and 20.5 min, using strain $CBS8066$. They observed a reduction in C_x and increase in ethanol production for increasing τ_{circ}. This is likely an effect caused by the increasing gap in residual C_s upon increasing τ_{circ}, which is reflected in the growing difference in the respiration quotient between the two compartments while increasing τ_{circ}. Overall, C_x varied between $6.5 - 25$ g/kg during the process. No information on C_s was provided, but an estimate could be made by assuming Monod kinetics. From the microbial point of view, this yields q_s profiles as given in figure 6.6, for $\tau_{circ} = 0.6$ min and $\tau_{circ} = 6.3$ min, respectively. For both cases, the profiles at $C_x = 10$ g/kg and $C_x = 20$ g/kg are shown (left and right of the dashed line respectively).

Figure 6.6 **A, B** shows that q_s oscillates between regimes 1 and 2, but the oscillation magnitude depends strongly on τ_{circ}; ranging from $0.13 - 0.21$ (with negligible ethanol production) for $C_x = 10$ g/kg and $\tau_{circ} = 0.6$ to $q_s/q_{s,max} = 0.06 - 0.48$ in case $\tau_{circ} = 6.3$ min and $C_x = 20$ g/kg. The latter conditions reflect the magnitude of industrial fluctuations better, while $\tau_{circ} = 0.6$ mimics their duration best. Overall, the work of Sweere et al. covers cases that provide a decent reflection of industrial frequencies (for low τ_{circ}) and amplitude (for high τ_{circ}), although both were not captured simultaneously.

The two-compartment chemostat of Heins et al. [49] operated at $C_x = 10 - 20$ g/kg, representing part of an industrial operation. The circulation time $\tau_{circ} = 1.17$ h at minimum, hence the exposure of organisms to extra-cellular variations is not considered to be truly industrially representative. One of the merits of this setup is the strong C_s gradient between the vessels ($C_s >> 1$ g/kg in compartment 1, and $C_s << 1$ g/kg in compartment 2), allowing to study the effect substrate concentration variations with an extreme magnitude on the population.

Single-compartment: Pham et al. [42] used a fluctuating feed experiment to validate their metabolic model for CBS8066, imposing oscillations of 15% around the mean

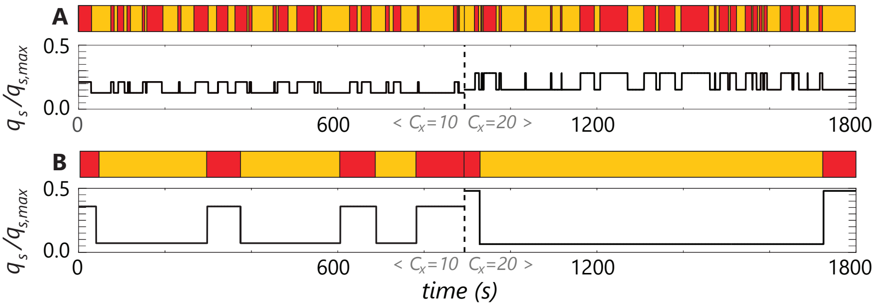

Figure 6.6: Reproduction of the oscillations experienced by organisms in the 2-vessel scale-down simulations conducted by Sweere et al. **A:** cycles with $\tau_{circ} = 0.6$ min, **B:** cycles with $\tau_{circ} = 6.3$ min. Sweere et al. operated the set-up as a fed-batch reactor, hence C_x varied in time. The left side of both figures shows the oscillation amplitude at $C_x = 10$ g/kg, the right side at $C_x = 20$ g/kg.

substrate feed rate of 21 g/h in a fed batch process. Both C_x and the filled reactor volume are dynamic; for comparison we constructed a snapshot where $C_x = 10$ g/kg and $V \approx 9$ L ($C_x = 20$ g/L was not reached experimentally). No ethanol production is predicted to occur under these conditions as $q_s/q_{s,max}$ oscillates between $0.12 - 0.158$ (figure 6.6). Their experimental data confirms the lack of ethanol production. Compared to our CFD benchmark, it is clear that the oscillations imposed by Pham et al. were too long in duration and too low in magnitude to be considered industrially representative.

Van Kleeff et al. [294] exposed strain $CBS8066$ to feast famine cycles. The cycle duration was 200 s or 400 s, with a feed period of 20 and 40 s, respectively. The dilution rate was approximately $D_r = 0.055$ h^{-1} and C_x was around 3.6 g/kg. Inspired by van Kleeff et al., Suarez-Mendez et al. [45] imposed 400 s cycles (40 s feed) to strain CEN PK 113-7D, with C_s oscillating between $0.46 - 0.094$ mmol/kg at $C_x = 3.46$g/kg. A 5% reduction in C_x was observed compared to their steady state reference, without ethanol production. For illustrative purposes, we assume the uptake kinetics of CBS8066 apply to CEN PK 113-7D, in which case q_s cycled between $0.048 - 0.082 q_{s,max}$. Both for van Kleeff et al. and Suarez-Mendez et al., the long cycle times and low fluctuation magnitude (due to the low C_x) indicate their setups are not industrially representative. Of course, they are suitable for revealing the effects of well-defined, repeatable fluctuations on micro-organisms.

6.6. Concluding remarks

Above, relatively simple SD-designs were discussed, which can all be realized within current scale-down practices. Our scale-down approach uses Euler-Lagrange CFD data to fix the five degrees of freedom for scale-down design that Noorman [15] reported. Both approaches with a single vessel and with multiple compartments are explored. The proposed designs aim to reproduce the amplitude and frequency of extra-cellular variations on an average scale; (explicitly) including the most extreme events is typically unworkable within the limitations of scale-down simulators using ideal reactors.

An important notion is that SD-simulators which seek to reproduce the rate-of-change in the environment experienced by organisms on the large scale, must at least operate at the industrial biomass concentration C_x. Since industrial processes are frequently operated at high biomass concentrations, and possibly include highly viscous, shear thinning broths, this notion may lead to operational complexities for some of the proposed scale-down simulations. Reducing C_x may relax some of these restrictions, but inherently this reduces the agreement with the rate-of-change observed by organisms in the industrial-scale fermentation. In many cases, this will in turn compromise the agreement in magnitude and/or duration of oscillations, although arc-based design for *P. chrysogenum* shows that it may be possible to reduce C_x in some cases, without compromising the overall fluctuation duration and magnitude. This will, however, compromise the achieved rate of change; a metabolic model study is required to comment on whether or not this changes the metabolic response, and hence whether or not lowering C_x is an allowed simplification. In any case, a practical scale-down simulator requires some trade-off between practical operation, simple design, and accuracy of reproduction. This trade-off should be based on the metabolic characteristics of the used organism. The influence of C_x on operational parameters will furthermore play a significant role in how much operational simplifications will be practically required. In the current chapter, the focus was fully on q_s-lifeline replication, which aims at mimicking the extra-cellular environment in large-scale fermentors. Alternative scale-down methodologies, with different operating windows and constraints, may be devised based on intra-cellular lifelines. Such an approach was not considered in this chapter.

Within the limitations of ideal scale-down simulators, the current CFD-based scale-down proposals are a reasonable reflection of the industrial scale conditions and are a step forward compared to the current generation of scale-down simulators which were typically designed based on a combination of global parameters such as τ_{95} and intuition, often leading to an overestimation of the fluctuation duration and/or an underestimation of the amplitude. We conducted an analysis of previously operated scale-down simulators for *S. cerevisiae* which shows that, with the hindsight offered by state-of-the-art CFD simulations, most indeed do not closely represent industrial conditions. With the availability of novel (CFD) methodologies, improvements to these designs that improve their agreement with industrial conditions can be proposed.

7

Coupled hydrodynamic-kinetic simulation

We assess the effect of substrate heterogeneity on the metabolic response of P. chrysogenum in industrial bioreactors via the coupling of a 9-pool metabolic model with Euler-Lagrange CFD simulations. In this work, we outline how this coupled hydrodynamic-metabolic modeling can be utilized in 4 *steps: 1) a model response study with a fixed spatial extra-cellular glucose concentration gradient, which reveals a drop in penicillin production rate* q_p *of* $18-50\%$ *for the simulated reactor, depending on model setup. 2) Scale-down verification, where we numerically compare the model response in a scale-down simulator (proposed in chapter 6) with the large-scale CFD response. 3) Reactor design optimization, reducing the drop in penicillin production by a change of feed location. 4) Long-term fed-batch simulation, where we verify model predictions against experimental data, and discuss population heterogeneity. Overall, these steps present a coupled hydrodynamic-metabolic approach towards bioreactor evaluation, scale-down and optimization.*

7.1. Introduction

Due to the presence of gradients in substrate concentration [8], dissolved oxygen concentration [9] and other process variables in industrial bio-reactors, organisms are subject to temporal variations in their environment. Such variations impose stresses on these organisms [12, 43, 56], which may in turn affect the process yield [44]. There are cases where extra-cellular variations appear to be advantageous [8], but typically the impact is negative as the process is driven away from the conditions set for yield optimization [44, 48]. Being related to mixing behavior, these gradients amplify upon scale-up, which may hence come with a yield loss that should be considered when judging scale-up economics. Furthermore, knowledge on the impact of bioreactor heterogeneity can be used to guide design changes to the reactor and, with genetic engineering, the micro-organism itself.

Previously, we used Euler-Lagrange CFD to study the environmental fluctuations experienced by micro-organisms (chapter 5) and showed how fluctuation statistics can be acquired from such simulations to guide SD-simulator design (chapter 6). These chapters focused on simulation and fluctuation quantification using the substrate uptake (q_s) lifeline, and did not quantitatively consider the metabolic response. When

---

Accepted for publication as: C. Haringa, W. Tang, G. Wang, A.T. Deshmukh, J. Xia, M. Reuss, J. Chu, W.M. van Gulik, J.J. Heijnen, R.F. Mudde, H.J. Noorman. Computational fluid dynamics simulation of an industrial P. chrysogenum fermentation with a coupled 9-pool metabolic model: towards rational scale-down and design optimization., *Chemical Engineering Science*.

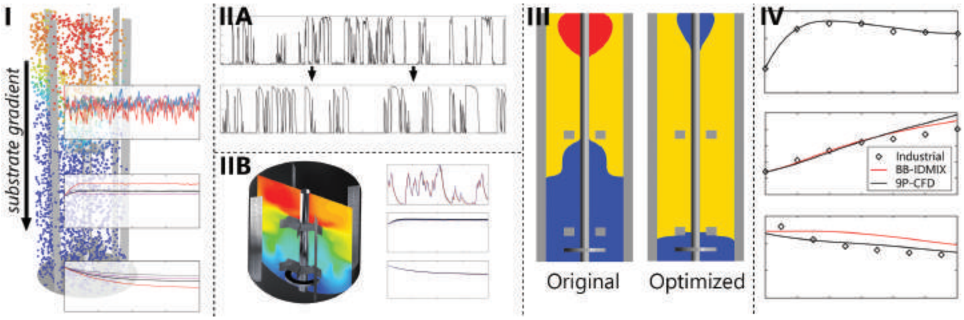

Figure 7.1: Graphical outline of the 4 subjects covered in this paper. **I:** Metabolic response simulation. **II:a** CFD-guided scale-down simulator design. **IIb:** Numerical verification of scale-down reactor performance. **III:** Numerical full-scale design optimization. **IV:** Industrial fed-batch simulation.

a dynamic metabolic model is available for the studied organism, coupled metabolic-hydrodynamic simulations can be used to evaluate the expected metabolic impact [21, 23]. Combined with experiments in representative scale-down simulators, such a coupled hydrodynamic-metabolic approach is applicable towards: 1) scale-down verification: does a scale-down simulator result in the same metabolic response as observed in the large-scale CFD simulation? and 2) design optimization: what is the expected impact of reactor design changes or metabolic modifications based on numerical assessment? The most promising changes can then be experimentally tested in representative scale-down simulations, offering a powerful approach to rational bioreactor design and scale-up [48, 56].

We discuss four topics in this chapter, outlined in figure 7.1, highlighting the different aspects of the CFD-based scale-down workflow. A penicillin production process is used as a case-study. *Part I* considers the coupled hydrodynamic-metabolic simulation of a 54 m^3 industrial *P. chrysogenum* fermentation [10], focusing on mixing dynamics and neglecting slow processes such as biomass growth. We study the impact of mixing on metabolic variations using a 9-pool metabolic model [226]. In *part II*, we numerically compare the metabolic response in the arc-analysis based SD-simulator proposed in sec. 6.4.3 to the CFD response, first assuming ideal mixing, and second by a CFD simulation of a 3 L reactor with dynamic feed. In *part III*, we discuss process optimization and propose a simple reactor alteration to improve the penicillin yield. To conclude, in *part IV* we simulate 60 h of a fed-batch fermentation for comparison with industrial data. With this, we explore various aspects of the use of coupled hydrodynamic-metabolic modeling for process evaluation and optimization.

7.2. Methodology

All CFD simulations were conducted in ANSYS FLUENT 15.7, MATLAB 8.6.0 was used for post-processing and ideal mixing simulations.

7.2.1. Metabolic model

The 9-pool metabolic model for *P. chrysogenum* developed by Tang et al. [226] contains 5 intra-cellular metabolite and 4 enzymatic pools, and couples to the extra-cellular substrate concentration C_s and phenylacetic acid (PAA) concentration C_{PAA}. The metabolite pools are: Glycolytic intermediates (X_{gly}), Amino acids (X_{AA}), Storage polymers (X_{sto}), ATP (X_{ATP}) and intra-cellular PAA (X_{PAA}), all reported in μmol/g$_{dw}$ with g$_{dw}$ being the dry biomass weight. Three dimensionless enzyme pools influence metabolic rates: $X_{E,11}$ (the substrate uptake capacity), $X_{E,32}$ (PAA export capacity) and $X_{E,4}$ (storage capacity). The 4^{th} enzyme pool controls the biomass specific penicillin production rate q_p [236] and is reported in mol$_p$/Cmol$_x$/h [44, 233, 236]. The effect of oxygen limitations has not been studied sufficiently to be included in the current model [10, 226], and will be considered in future extensions. For a model overview, we refer to Tang et al. [226].

Model simplifications Tang et al. developed and validated their model against a range of experimental data [44, 226, 233] including 360 s feast-famine cycles [44]. These results provide confidence that the model is able to capture the impact of circulation-timescale substrate variations. However, instabilities in X_{ATP} were encountered in our CFD simulations, which resulted from the sensitivity of the storage pool fluxes to turbulence-induced C_s fluctuations on the sub-second timescale, which were not accounted for in model development (for details see *appendix A*). A structural solution of this issue requires deeper analysis of the signaling mechanism behind storage dynamics. As we currently lack the information to develop such improvements, we instead opted for a patch solution by assuming the ATP pool is in quasi-steady state, meaning the fluxes in- and out of the ATP pool balance, giving $dX_{ATP}/dt \approx 0$ [255]. This converts the dynamic ATP-balance in an algebraic expression:

$$0 = \sum^{i} v_i(X_{gly}, X_{AA}, X_{ATP}, ...) \tag{7.1}$$

For the current non-linear kinetics, equation 7.1 was evaluated for 10^5 randomly generated sets of intra-cellular pools. Subsequent correlation showed X_{ATP} can be modeled as $X_{ATP} = 8.25 \cdot X_{gly}^3/(10.5^3 + X_{gly}^3)$. The model response was deemed satisfactory under all tested conditions. Further details on the approach and verification against experimental data are reported in *appendix A*.

7.2.2. CFD setup

54m^3 reactor setup

We use the 54 m^3 reactor simulation (chapter 5) with simplified single-phase hydrodynamics as the industrial base-case. We furthermore simulate the same case including aeration, which was in previous chapters for *P. chrysogenum*. The superficial gas velocity, measured at STP conditions, $U_g = 0.05$ m/s. The pressure in the reactor headspace was 1.85 bar, the air density was set to 2.4 kg/m^3 based on the mean pressure. The total domain height $H_t = 11$ m to account for broth expansion upon

Table 7.1: Validation parameters of 54 m^3 fermentor simulations. The holdup for air-water is averaged over 3 experiments, while a single experiment is reported for broth. The CFD circulation time is based on 5% saturation of the probe signal (mixing time τ_{95} is based on 95% saturation). For the experimental data, the half-circulation time was determined by recording the time lag between H_2SO_4 insertion at the top and probe response at the bottom.

Parameter	Exp. water	Exp. broth	Exp. air-water	Exp. air-broth	CFD water	CFD air-water
Gas hold-up	n/a	n/a	16.4 ± 0.8	12.6	n/a	20.4
d_b (mm)	n/a	n/a	n/m	n/m	n/a	7.1
τ_{circ} (s)	19.3	77.0	41.6	25.7	18.2	32.9

n/a = not applicable; n/m = not measured.

gassing, the gas-filled headspace is removed during parcel tracking [20]. The mesh (180° domain) contained $9.23 \cdot 10^5$ gridcells. A discrete population balance (8 bins, $0.5 - 12.7$mm) with the Luo and Svendsen [77] was employed to capture the bubble size distribution. Furthermore we used the standard $k - \epsilon$ model (dispersed turbulent formulation), multiple-reference frame impeller modeling, and the universal drag model for inter-phase momentum exchange. Other inter-phase forces were neglected [20, 84, 191]. The broth rheology was set equal to water; simulations using Casson rheology [243] diverged in volume fraction α, and the combination of single-phase and air-water hydrodynamics captures the range of mixing times measured industrially, which suffices for the current purpose. The air-water surface tension $\gamma = 0.072$ N/m, the turbulent Schmidt number was set to $Sc_t = 0.2$.

The gas flow number $Gs = Q_g/N_sD^3 = 0.1$ implies the fermentor operates at the boundary of the $3-3$ cavity regime and recirculation regime, where the mixing time τ_{95} is equal to and above that of single phase-flow, respectively [169]. Available industrial data on the circulation time [10] ($\tau_{circ} \approx \tau_{95}/4$, [15]) suggests the latter; the circulation time τ_{circ} is compared to simulation results in table 7.1. The single-phase and two-phase simulation under- and over-estimate τ_{circ} for aerated broth with 30 %, respectively. Note the experimental value is based on a single measurement and hence comes with a significant margin of uncertainty. We regard the single-phase and aerated simulation as a lower and upper bound mixing time scenario, with the true mixing behavior in the range. This level of accuracy suffices for our current demonstration purposes, but we stress the need for further investigation into modeling true aerated, non-Newtonian fermentation broths, and associated with that, a wider range of large-scale validation data (gas hold-up, local mixing curves and preferably local DO/substrate concentrations). The simulation is observed to over-estimate the hold-up by 25% in water, and by nearly 60% in broth. Currently we are not directly interested in gas-holdup, but in case oxygen dynamics are included, this aspect requires further study.

3-l laboratory reactor setup

A round-bottom vessel with a working volume of 3 L [226] is simulated for scale-down verification. Geometric parameters are reported in *appendix D*. The typical gas flowrate is 2 L/min, giving $Fl = 0.009$ with an agitation rate of $N_s = 10$ s^{-1} (600 RPM). This value is outside of the range probed in mixing experiments [169], but implies θ_{95} is similar to or slightly higher than for single-phase conditions. For simplicity, we hence ignore the effect of gas flow and model single-phase water. All walls were no-slip while the top surface had a no-shear free surface condition. Computational mixing simulations at $N_s = 10$ s^{-1} yield $\theta_{95} = 22$, in excellent agreement with experiments (*appendix D*); the dimensionless circulation time $\theta_{circ} \approx \theta_{95}/4$.

At high C_x, the high effective liquid viscosity μ_l may practically lead to transitional flow, possibly increasing θ_{95} significantly. Previous non-Newtonian simulations of aerated lab-scale reactors did not produce realistic mixing results due to stagnant zones [212], and preliminary work using a low$-Re\ k-\epsilon$ model with $\mu_l = 0.15$ Pa s led to parcel tracking issues, with parcels sticking in the impingement point of the impeller discharge stream. We hence opted to decrease the agitation rate N_s to 1.67 s^{-1} (100 RPM) to assess the effect of mixing time on the performance of a lab-scale scale-down simulator. At 600 and 100 RPM, $\tau_{circ} = 0.55$ and 3.3 s, respectively. Experimental evaluation of mixing behavior in real fermentation broths is required to comment on whether this range of τ_{circ} represents lab-scale practice.

Metabolic model coupling

In the 9-pool model the glucose uptake rate q_s is subject to transporter control, where the availability of transporter ($X_{E,11}$) is controlled by growth rate μ (h^{-1}). This means that strictly speaking 2-way coupling is required to resolve the substrate environment, which requires simulating long timespans (O(h)) due to the long transporter adaptation time, and is therefore computationally expensive.

The long adaptation time allows for the assumption that the average transport capacity $\overline{X_{E,11}}$ is homogeneous in the fermentor. As $\overline{X_{E,11}} = f(\mu)$, its value can be estimated based on growth rate under ideally mixing conditions, μ_{id}. For the applied model, the average growth rate under dynamic conditions $\overline{\mu}$ was typically close to μ_{id}, and the estimated $\overline{X_{E,11}}$ was similarly close. A-priori estimation of $\overline{X_{E,11}}$ allows to use 1-way coupling, as in our earlier work [10, 20], which means the number of tracked parcels N_p does not influence the substrate gradient and can be freely chosen. This simplification does not hold when circulation timescale-intracellular dynamics affect q_s [21, 23, 31], or when $\overline{X_{E,11}}$ under dynamic conditions differs strongly from the ideal-mixing assessment.

The above $1-$way coupled approach was used to study mixing-timescale dynamics, assuming constant C_x, $\overline{X_{E,11}}$, feed rate F and liquid-filled height H. This practically represents a chemostat cultivation, where the dilution rate D_r is equal to the mean growth rate $\overline{\mu}$. $1-$way coupling is conducted as a post-processing step; the (statistical) steady state allows to simulate $O(10)$ mixing times to acquire fluctuation statistics; lifelines of 80 h are subsequently generated to study the adaptation of q_p to mixing-time dynamics (with constant C_x, $\overline{X_{E,11}}$ by construction) by joining together individual lifelines, exploiting the statistically-steady extra-cellular nature.

For the fed-batch simulation we use $2-$way coupling to include temporal changes in C_x and $X_{E,11}$. The long variation time of both parameters allows the assumption

Table 7.2: Comparison of the assumptions between 1-way and 2-way coupling method used in this work. 1-way coupling is here used for chemostat cultivation, and 2-way coupling for fed-batch cultivation.

Method	1-way coupling	2-way coupling
Software	MATLAB 8.6.0 (post-process)	FLUENT 15.7 (in-process)
C_x	Fixed	Variable
X_{E11}	Fixed	Variable
μ	Variable, stat. steady	Variable
D_r	stat. steady, $D_r = \overline{\mu}$	$D_r \approx 0$ (fed-batch)

that C_x and $\overline{X_{E,11}}$ are spatially homogeneous ($X_{E,11}$ may be heterogeneous within the population, but to a same degree at every spatial location). This means that each timestep $\overline{C_x}$ and $\overline{X_{E,11}}$ can be calculated as the parcel population ensemble average, and the local uptake rate can be computed from the Eulerian framework as eq. 7.2:

$$r_{s,c} = \overline{C_x} \cdot k_{11} \cdot \overline{X_{E,11}} \cdot \frac{C_s}{K_s + C_s} \tag{7.2}$$

This simplified 2-way coupling requires the parcel number to be sufficient to capture overall heterogeneity, for which $N_p = O(10^3)$ typically suffices; full 2−way coupling would require $N_p = O(10^5) - O(10^6)$ [31]. 1− and 2− way coupling require similar computation time per hour flow-time, but 2− way coupling does require the full fermentation time to be simulated to account for changes in C_x and $X_{E,11}$. A comparison of the assumptions between 1 and 2-way coupling is given in table 7.2.

7.2.3. Overview of cases

Here, we provide an overview of all simulations (table 7.3), both conducted with CFD (FLUENT) and with the ideal or instantaneous mixing assumption (MATLAB), including the assumptions made and sections where these simulations are described. There is some variability in the applied timestep size Δt in FLUENT; in all cases it was ensured the particle trajectories were completed within the default accuracy settings. In all cases, glucose concentration C_s was variable, and the PAA concentration was fixed at $C_{PAA} = 3$ mmol/kg.

As noted in section 7.2.2, the uptake capacity $q_{s,max} = k_{11} \cdot X_{E,11}$ in the 9−pool model depends on the growth rate μ. In the chemostat simulations, we aimed at $\mu \approx 0.03$ h^{-1} to maximize q_p; at this value of μ, the 9−pool model predicts $q_{s,max} \approx 1.13$ mmol/g$_{dw}$/h under well mixed conditions, which is markedly lower than the $q_{s,max} = 1.6$ mmol/g$_{dw}$/h reported by de Jonge et al. [44], measured for $\mu = 0.05$ h^{-1}. The large scale simulations $TU - A,\ TG - A,\ MU - A$ were conducted with $q_{s,max} = k_{11} \cdot X_{E,11} = 1.13$ mmol/g$_{dw}$/h and $K_s = 9.8$ μmol/kg.

The lab-scale CFD simulations (part *II*) were conducted before the 9−pool model was available, which meant we had to rely on the kinetic parameters of De Jonge et al. [44], as in our previous work where we solely considered glucose uptake [10]. For consistency, we hence report a set of CFD simulations ($TU - B,\ TG - B,\ MU - B$) which use the 9−pool model, but with the uptake kinetics as published by De Jonge et

Table 7.3: Overview of all the simulations, both CFD and ideal/instantaneous-mixing based (IDM), conducted in this work. All cases were conducted as chemostats, except for $TU/ID - FB$, which is a fed-batch simulation. Naming convention: T = top feed. M = mid feed (impeller discharge stream). U = ungassed. G = gassed. FB = fed-batch (2-way coupled). ID = instantaneously mixed. SD = scale-down. $9 - P$ indicates the 9−pool model of Tang et al. [226] is used for metabolic coupling, $1 - P$ indicates the Dynamic Gene Regulation model of Douma et al. is used [236]. A and B indicate which kinetic parameter values are used. Part indicates the section of the chapter where the simulation is discussed.

Name	CFD/IDM	Model	Part	Gassing	Coupling	Feed	$q_{s,max}$ (mmol/g_{dw}/h)	K_s (μmol/kg)	C_x (g_{dw}/kg)	N_p	Δt (s)
TU-A	CFD	$9 - P$	I	no	1-way	top	1.13	9.8	55	4000	0.1
TG-A	CFD	$9 - P$	I	yes	1-way	top	1.13	9.8	55	4000	0.2
MU-A	CFD	$9 - P$	III	no	1-way	imp.	1.13	9.8	55	4000	0.3
TU-B	CFD	$9 - P$	I	no	1-way	top	1.6	7.8	55	4000	0.03
TG-B	CFD	$9 - P$	I	yes	1-way	top	1.6	7.8	55	4000	0.2
MU-B	CFD	$9 - P$	III	no	1-way	imp.	1.6	7.8	55	4000	0.3
TU-1P	CFD	$1 - P$	I	no	1-way	top	1.6	7.8	55	n/a	st. st.
ID-1P	IDM	$1 - P$	I	n/a	n/a	n/a	1.6	7.8	55	n/a	st. st.
ID-9P	IDM	$9 - P$	I	n/a	n/a	n/a	1.6	7.8	55	n/a	st. st.
ID-SD-27	IDM	$9 - P$	II	n/a	n/a	n/a	1.6	7.8	27	n/a	0.03
ID-SD-55	IDM	$9 - P$	II	n/a	n/a	n/a	1.6	7.8	55	n/a	0.03
CFD-SD-100	CFD	$9 - P$	II	no	1-way	top	1.6	7.8	27	5000	0.01
CFD-SD-600	CFD	$9 - P$	II	no	1-way	top	1.6	7.8	27	5000	0.002
ID-1P-FB	IDM	$9 - P$	IV	n/a	n/a	n/a	var.	9.8	var.	n/a	1
TU-FB	CFD	$9 - P$	IV	no	2-way	top	var.	9.8	var.	2000	0.2

n/a = not applicable; var. = variable; st. st. = simulation conducted in steady state.

al., $K_s = 7.8$ μmol/kg and $q_{s,max} = 1.6$ mmol/g$_{dw}$/h. We note that the fluctuations in q_s and the intra-cellular pools are too strong in these cases. The purpose of these simulations is to show that the intra-cellular response predicted between the industrial and lab-scale simulations matches; not to predict the metabolic response in the absolute sense.

Part I: Model response study Part I focuses on *TU-A* (non-aerated, top feed) and *TG-A* (aerated, top feed), to study the metabolic response to extra-cellular variations in an industrial-scale reactor with a statistically steady extra-cellular environment. As in our earlier work, a late fermentation stage was modeled, with $C_x = 55$ g/kg and substrate feed rate $F_s/V = 1.23$ g/m^{3}s [10]. The $1-$way coupling approach means $X_{E,11}$ remains unchanged in time. All other pools were variable, and initialized based on ideal mixing results. For consistency with *part II*, *TU-B* and *TU-B* are also reported here. The results are compared with a CFD simulation coupled with the dynamic gene regulation model of Douma et al. (non-aerated, top feed, case *TU-1P*), and ideal-mixing simulations with both the dynamic gene regulation (*ID-1P*) and $9-$pool (*ID-9P*) model.

Part II: Scale-down verification First the performance of the scale-down protocols from section 6.4.3 are assessed assuming ideal mixing (cases *ID-SD-27* and *ID-SD-55*). Next, CFD simulations of the 3 L lab scale reactor were conducted with the $C_x = 27.5$ g$_{dw}$/kg scale-down protocol, to study the effect of non-ideal mixing on SD performance. Instantaneous feed pulse injection was assumed in a small volume near the top surface. The hydrodynamics were frozen, but the substrate field was updated every timestep. The feed pulse scheme was supplied to FLUENT via a user defined function coupled to a lookup table. The fast mixing required time resolutions of $\Delta t = 0.002$ s for 600 RPM (case *CFD-SD-600*), $\Delta t = 0.01$ s for 100 RPM (case *CFD-SD-100*); this limited the resolved flow-time to 650 s, in which 42 feed pulses were applied. This number is too small for a proper replication of the industrial-scale fluctuation statistics; therefore, scale-down performance was judged by comparing the model performance with the ideal-mixing response for the same 42 pulses.

Part III: Design optimization Industrial-scale CFD simulations were conducted with the substrate feed directly in the top impeller discharge stream (non-aerated hydrodynamics), referred to as *MU-A* and *MU-B*.

Part IV: Full-scale fed-batch Verification We simulated a 60 h timespan of a fed-batch fermentation (top feed, non-aerated) which was conducted in the current 54 m^3 geometry, named *TU-B*, to verify model performance with industrial data which was kindly provided by the DSM biotechnology center. The simulation was started at $t = 10$ h after the batch start $C_x = 14$ g/L. All model parameters are initialized based on the ideally-mixed $9-$pool model outcome for the given starting conditions. In the industrial fermentation the total broth mass increased from 36 to $46 \cdot 10^3$ kg over the simulated timespan. However, explicitly modeling the volume change is computationally costly. As an approximation, we kept the volume constant at 54 m^3, with

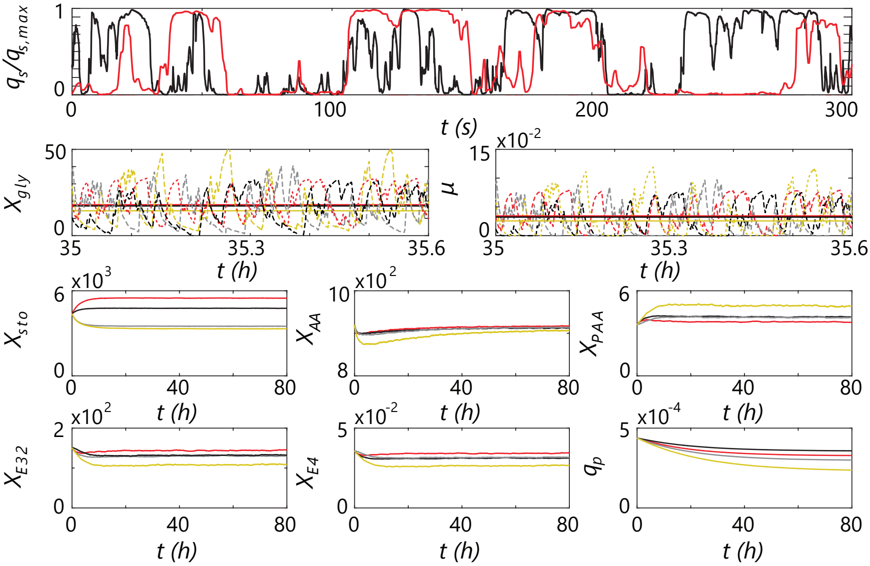

Figure 7.2: Long-term 9-pool model response for *TU-A* (black), *TG-A* (red), *TU-B* (gray), *TU-B* (yellow). The top panel shows examples of extra-cellular variations experienced by a single parcel in *TU-A*, *TG-A*. For X_{gly} and μ, the solid lines represent the mean, the dashed lines represent single parcel tracks to indicate the variations. All other lines represent are averages of 100 parcels. Intracellular pools X_{gly}, X_{AA}, X_{sto} and X_{PAA} have units μmol/g$_{dw}$. μ has units h^{-1}. q_p has units mol/Cmol$_x$/h. All other pools are dimensionless.

the hydrodynamics of *TU-A*; as both impellers are submerged at all times, the change in τ_{circ} over the course of the fermentation is assumed to be minor. To compensate for the higher volume, the provided feed profile (reported in fig. 7.10) was adjusted to ensure an equal feed in g/kg/s between the simulation and industrial fermentation at all times. Experimental data for q_p and μ were used to evaluate model performance for *TU-B*, as well as an ideal-mixed simulation with the model of Douma et al., case *ID-1P-FB*.

7.3. Results and discussion

7.3.1. Part I: Model response study

CFD simulations

We study the long-term adaptation of *P. chrysogenum* exposed to a strong substrate gradient. The most notable difference between *TU-A/B* and *TG-A/B* is the higher τ_{circ} for the latter, as discussed in sec. 7.2.2, yielding q_s fluctuations of longer duration. As q_s is locally saturated in all cases, the fluctuation amplitude hardly differs. Examples of single lifelines for *TU-A* and *TG-A* are shown in the figure 7.2, *top panel*.

Figure 7.2 shows the pool dynamics over an 80 h period for *TU-A*, *TG-A*, *TU-B*, *TU-B*. All cases show qualitatively similar behavior, but the higher $X_{E,11}$ for *TU/TG-B* has a clear negative impact on q_p. This illustrates the error introduced by taking kinetic

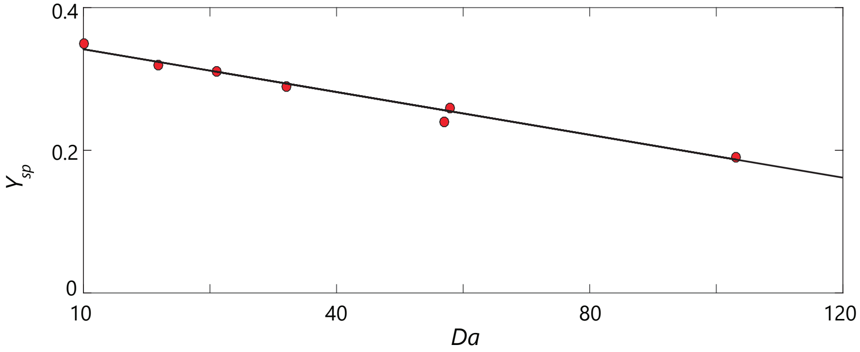

Figure 7.3: Relation between the Damköhler number $Da = \tau_{circ}/\tau_{rxn}$ and the penicillin yield on substrate Y_{sp}. Dots: simulation data (industrial-scale). Line: $Y_{sp} = 0.3417 - 0.0015Da$.

parameters directly from literature, without accounting for the adaptation of $q_{s,max}$ to μ.

Practically, q_p is controlled by X_{gly}: high X_{gly} inhibits synthesis of penicillin producing enzyme, but it increases growth rate μ which enhances enzyme synthesis. The first effect scales with X_{gly}^6 [226], meaning that high values of X_{gly} are highly repressive, but below-average values of X_{gly} are hardly influential. This explains the large difference in q_p between the cases, even though all cases have a nearly equal average $\overline{X_{gly}}$. The cases with the highest X_{gly} buildup show the biggest q_p loss. As τ_{circ} is higher for aerated cases, the parcels experience prolonged exposures to excess conditions, resulting in strong X_{gly} accumulation. Similarly, the higher transport capacity for *TU/TG-B* causes increased glycolytic accumulation. The effect of both kinetics and τ_{circ} is summarized in the Damköhler number $Da = \tau_{circ}/\tau_{rxn}$, where we take $\tau_{rxn} = K_s/(q_{s,max}C_x)$, the limit for $C_s \to 0$. This definition for τ_{rxn} does not require a value of C_s, which makes it straightforward to evaluate for both experimental and CFD cases. Including the impeller-fed cases *MU-A/B* (*part III*), a linear trend between the penicillin yield Y_{sp} (table 7.4) and Da is observed: $Y_{sp} = 0.3417 - 0.0015Da$ ($R^2 = 0.97$), graphically shown in figure 7.3.

q_p is linearly dependent on μ, and μ depends on $X_{gly}^2/(K_{gly}^2 + X_{gly}^2)$ [226]; the effect of high and low X_{gly} values on μ nearly averages out: $\mu(\overline{X_{gly}}) \approx \overline{\mu(X_{gly})}$. Only the most extreme case (*TU-B*) deviates from this; the very lengthy exposures to starvation conditions leads to a lower $\overline{\mu}$. The data clearly shows that the duration of exposures to excess- and starvation conditions strongly impacts the metabolic response. Since these time periods are highly distributed, there is considerable heterogeneity in X_{gly} at any given location. This feature is inherently not captured by black-box models that instantaneous adaptation of the intra-cellular to the extra-cellular domain. $X_{E,32}$ and $X_{E,4}$ are hardly affected in case *TU/TG-A* where $X_{E,11}$ was preconditioned for $\mu = 0.03$ h^{-1}, whereas the higher uptake for *TU/TG-B* causes some changes in these pools. X_{AA} is hardly affected in all cases. The value the intra-cellular pools is homogeneous within the population, as is shown in figure 7.4 for case *TU-A*.

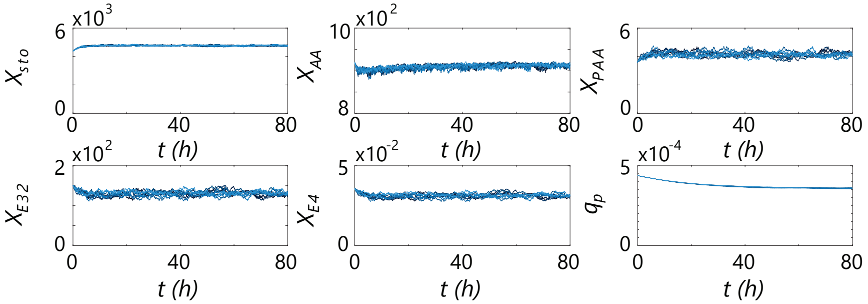

Figure 7.4: Pool response (*TU-A*) for 10 individual particles to indicate the observed degree of population heterogeneity in fixed-$X_{E,11}$ simulations. Intra-cellular pools X_{gly}, X_{AA}, X_{sto} and X_{PAA} have units μmol/g$_{dw}$. q_p has units mol/Cmol$_x$/h. All other pools are dimensionless.

Experimental data and yields

The CFD results are compared with experimental chemostat data [233] and ideal-mixing simulations using both the model of Douma et al. [236] (*ID-1P*) and the model of Tang et al. [226] (*ID-9P*). Both models are known to under-predict q_p around $\mu = 0.03$ h^{-1} compared to steady-state experiments. Compared to the 9−pool model with ideal mixing, the CFD simulations show a yield loss between 18% (*TU-A*) and 46% (*TU-B*). The real circulation time for the 54 m^3 reactor lies in between the extremes simulated here; based on the Da-correlation a yield loss of 22% is expected for $\tau_{circ} = 25.7$ s, using $X_{E,11}$ value for $\mu = 0.03$ h^{-1} .

For demonstration, we have also coupled the model of Douma directly to FLUENT (*TU-1P*). Coupling to CFD required some minor model alterations, these are elucidated in *appendix A*. This yields an extreme 85% decrease in Y_{sp} and strong increase in Y_{sx}, which are not deemed realistic. In *TU-1P* both dq_p/dt and μ adapt to the local C_s instantaneously; dq_p/dt is highly negative close to the feed (substrate inhibition) as well as in the starvation zone (zero growth); a positive dq_p/dt exists only in a very narrow band. The very high μ close to the feed leads to a high μ overall, despite the slightly negative $\mu \approx -m_s$ [10] in the starvation zone. This extreme result shows the merits of using a structured model in non-ideal reactors with strong substrate gradients. Although the chemostat assumption used here introduces some simplifications, we are confident the overall trends hold, making the outlined method suitable for a quick assessment of the impact of design changes on the fermentation process. The most promising cases can subsequently be studied in more detail with 2-way coupling and experimental scale-down assessment.

7.3.2. Part II: Scale-down verification

A scale-down design analysis was conducted for *TU-B* using the arc-analysis method reported in chapter 5, section 5.5.4, using a reference value $q_{ref} = 0.05 q_{s,max}$. This means the lifelines are divided in feast- ($q_s/q_{s,max} > 0.05$) and famine-arcs ($q_s/q_{s,max} < 0.05$). The rationale behind this reference value is that the amplitude in famine arcs can be neglected, and that for feast arcs the distribution for τ_{arc} is comparatively

Table 7.4: Comparing yields and productivity between experimental data of van Gulik et al. [233], the black box (BB) model of Douma et al. [236] and the 9-pool model [226] with ideal mixing assumption and the 9-pool (9P) of Tang et al. [226]. Feed $F_s = 0.0125$ mol$_s$/Cmol$_x$/h for all simulations and 0.0118 mol$_s$/Cmol$_x$/h for the experiment.

case	μ (h^{-1})	q_p (mol$_p$/Cmol$_x$/h)	Y_{sx} (Cmol$_x$/Cmol$_s$)	Y_{sp} (mol$_p$/mol$_s$)	Da
Exp.	0.029	$5.33 \cdot 10^{-4}$	0.41	0.045	n/a
ID-1P	0.032	$4.94 \cdot 10^{-4}$	0.43	0.040	0
ID-9P	0.033	$4.40 \cdot 10^{-4}$	0.44	0.035	0
TU-1P	0.043	$0.73 \cdot 10^{-4}$	0.57	0.006	n/a
TU-A	0.032	$3.57 \cdot 10^{-4}$	0.44	0.029	32.1
TG-A	0.035	$3.28 \cdot 10^{-4}$	0.47	0.026	58.0
TU-B	0.033	$2.99 \cdot 10^{-4}$	0.44	0.024	57.0
TG-B	0.027	$2.38 \cdot 10^{-4}$	0.36	0.019	103

n/a = not applicable.

simple, providing a clear correlation between $\Omega_{s,max}$ and τ_{arc}. These statistics quantify q_s-lifeline fluctuations and form a basis for representative scale-down simulation. This scale-down analysis was conducted in chapter 6, section 6.4.3, based on inverse transform sampling. Representative lifelines were shown for both $C_x = 55$ g$_{dw}$/kg and $C_x = 27.5$ g$_{dw}$/kg. The latter may be beneficial for operation of the scale-down simulator, but required a compromise in the rate-of-change experienced by the microorganisms. In this section, we use the 9—pool model to evaluate the effect of this compromise on the microbial metabolism, first assuming instantaneous mixing, and latter including non-instantaneous mixing in a CFD simulation of the lab-scale reactor. Note instantaneous mixing means pulses are instantaneously spread in space; concentration variations will still occur in time due to pulsed feeding.

Instantaneous mixing

Both for *ID-SD-55* and *ID-SD-27*, 5 statistically representative lifelines were generated and analyzed. Table 7.5 lists the metabolic response in q_p and μ compared to *TU-B*. Additionally, the exposure to excess (E), limitation (L) and starvation (S) conditions, based on the regime definitions of Haringa et al. [10], is reported. Case *ID-SD-55* slightly over-estimates exposure to excess conditions. This results in a higher $\overline{\mu}$, mildly lower q_p and minor offsets in the intra-cellular pool sizes (fig. 7.5), but overall we conclude that both cases excellently represent the large-scale simulation. The good performance of *ID-SD-27* follows from the notion that the total uptake within a pulse of duration τ_{arc}, $\int_0^{\tau,arc} q_s d\tau$, is equal between the two pulse administration methods, and the turnover time of X_{gly} is sufficiently low to yield similar responses in X_{gly}, as is visible in the instantaneous X_{gly} variations shown in fig. 7.5. If the turnover time of X_{gly} was well below τ_{arc}, the metabolic response is expected to differ between the cases, and lowering C_x might not be allowed. We hence regard the possible reduction in C_x as a case-dependent effect, and it should be evaluated as such. In case no predictions regarding the metabolic response are available, a scale-down simulator should in any case aim to produce the best possible replication of the extra-cellular

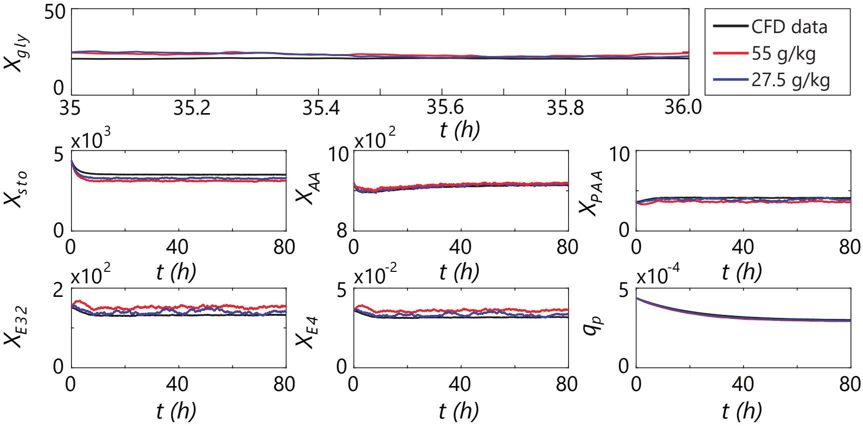

Figure 7.5: Model prediction for ideal-mixed scale-down simulators *ID-SD-55* and *ID-SD-27*. The CFD results (*TU-B*) are averaged over 100 tracks, the scale-down simulations averaged over 5 realizations. In both cases X_{gly} is smoothed with a moving average filter over 1800 s to remove rapid variations and yield average levels. The dashed lines represent instantaneous values in X_{gly} for a single realization. Intra-cellular pools X_{gly}, X_{AA}, X_{sto} and X_{PAA} have units µmol/g$_{dw}$. q_p has units mol/Cmol$_x$/h. All other pools are dimensionless.

Table 7.5: Comparison of the instantaneous mixing cases *ID-SD-27* and *ID-SD-55* with CFD simulation *TU-B*. Inst. = instantaneous feed, Grad. = gradual feed. Changes Δq_p are reported with respect to the ideal mixing benchmark *ID-9P*. Regimes definitions for E (excess), L (limitation) and S (starvation) are from [10].

Case	C_x (g/kg)	feed	$\overline{\mu}$ (h^{-1})	q_p (mol$_p$/Cmol$_x$/h)	Δq_p %	E %	L %	S %
TU-B	55.0	-	0.0330	$2.99 \cdot 10^{-4}$	-31.8%	6.8	36.2	57.0
ID-SD-55	55.0	grad.	0.0386	$2.90 \cdot 10^{-4}$	-33.7%	9.8	32.7	57.5
ID-SD-27	27.5	inst.	0.0340	$2.93 \cdot 10^{-4}$	-33.2%	8.0	34.2	57.8

environment (q_s-lifelines), and no compromises in C_x should be made.

The ability to use the metabolic model to investigate the predicted effect of compromises in the extra-cellular domain presents a first step towards an alternative scale-down philosophy, where the goal is to maintain the intra-cellular response despite (highly) simplified extra-cellular fluctuations. We explore this philosophy in *appendix B*, but do stress indulging in such simplifications makes the scale-down routines prone to unforeseen metabolic responses. We hence regard this possibility most suitable for metabolic model verification (is the metabolic response as predicted, or are there indeed unforeseen effects, which means the metabolic model is incomplete?) in the relevant range, and not for direct evaluation of the large-scale metabolic response.

CFD verification

CFD simulations of a SD-simulator were conducted with $C_x = 27.5$ g/kg to probe the possible impact of non-instantaneous mixing. Instantaneous spatial heterogeneity again depends on the Damköhler number. Here, $\tau_{circ} \approx 0.5 - 3.3$ s (for 600 and

100 RPM, respectively). As the concentration field is now dynamic, we employ a more general definition of the reaction time, $\overline{\tau_{rxn}} = \langle C_s \rangle / \langle R_s \rangle = (\langle C_s \rangle + K_s)/(q_{s,max} C_x)$ with $\langle C_s \rangle$ the volume average substrate concentration. Right after pulse administration, $\langle C_s \rangle >> K_s$ and $Da << 1$: this implies the pulse will be mixed before $\langle C_s \rangle$ is reached and thereby τ_{rxn} drops significantly, leading to a homogeneous broth and equal experiences by all micro-organisms in the domain.

This is reflected in the model response for both case *CFD-SD-600* and *CFD-SD-600*. The q_s lifelines in fig. 7.6 **B** (600 RPM) and **C** (100 RPM) show evidence of spatial heterogeneity directly following pulse administration, which for case *CFD-SD-600* rapidly wears off, meaning the lifeline under the instantaneous mixing assumption is retrieved (fig. 7.6 **A**). The heterogeneous period lasts longer for *CFD-SD-100*, but eventually the population synchronizes, and the metabolic response is hardly affected (fig. 7.6, **D**). To comment on the role of non-ideal mixing in (aerated) SD-simulators with a high liquid viscosity μ_l, experimental measurements are required, but the results for *CFD-SD-100* imply very poor mixing is required to yield significant heterogeneity in the population, and to yield a different metabolic response compared to the pulse-profile under the assumption of instantaneous mixing. This stems positive for practical application of fluctuating-feed SD-simulators.

7.3.3. Part III: Design optimization

Part I revealed that reducing the frequency of q_s variations reduces the amplitude of X_{gly} fluctuations, which reduces inhibition of q_p. Cronin et al. reduced τ_{95} by a factor $2 - 2.5$ by placing the feed point just below the top impeller [40, 169, 295]. We find $\tau_{95} = 23$ s (non-aerated, $MU - A/B$) when the feed is placed in the top-impeller discharge stream, a 2.7-fold reduction in τ_{95} compared to the top feed. This exceeds expectations and may be excessively low for a true penicillin fermentation when rheology and aeration are accounted for, but we accept this result for the sake of demonstration. The pool response for simulations *MU-A* and *MU-B* is reported in fig. 7.7.

Compared to *TU-A*, the q_s-lifelines for *MU-A* show a lower fluctuation amplitude, and strong reduction in fluctuation duration (fig. 7.7, top). This translates to much milder X_{gly} variations that directly relate to a higher q_p for *MU-A/B* cases (table 7.6). Again, $\overline{X_{gly}}$ and hence $\overline{\mu}$ remains virtually equal between the cases. With a q_p loss of 8.6% compared to *ID-9P*, where the top-feed case with equal τ_{circ}, *TU-A*, gave a loss of 17%. The reduced exposure to starvation conditions is furthermore observed to yield a higher X_{sto} for $MU - 1$ cases. An alternative process improvement may be to increase K_s by modifying the glucose transporter, thereby reducing sensitivity to C_s fluctuations. We attempted this by setting $K_s = 0.001$ mol/kg [16] based on yeast, but the sensitivity of the storage equations to C_s resulted in an uncontrolled increase of X_{sto}, quenching X_{gly}. A better understanding of storage dynamics is required to further assess this option.

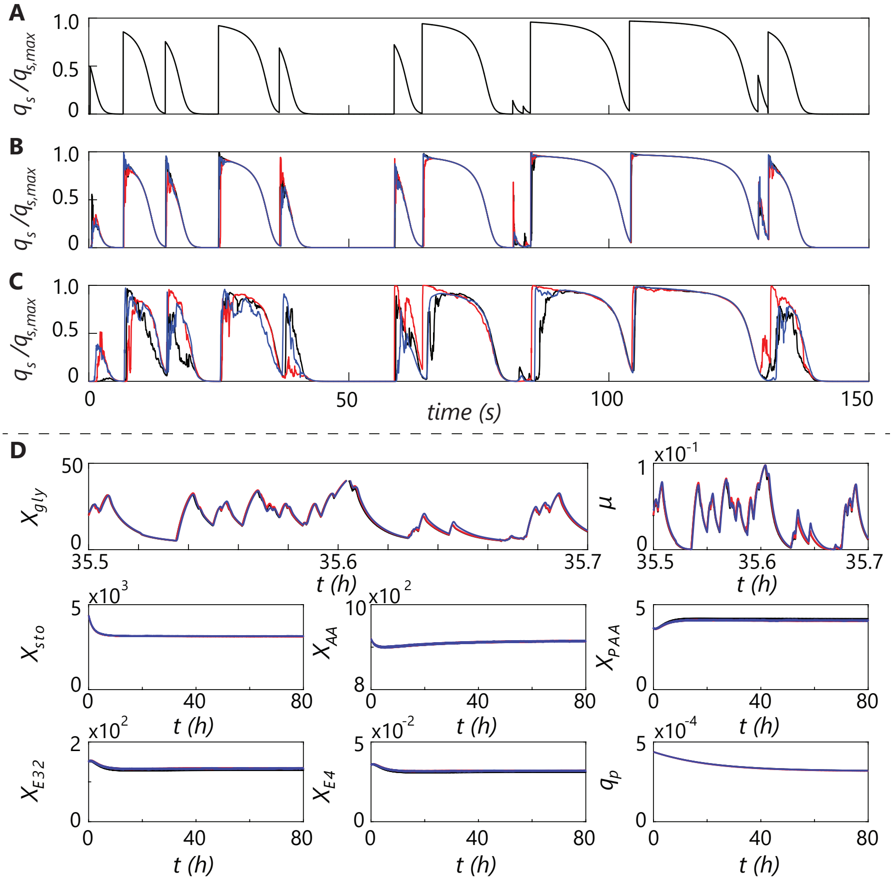

Figure 7.6: Particle tracks in scale-down simulation CFD. **A:** instantaneous mixing simulation. **B:** *CFD-SD-600*, 3 tracks. **C:** *CFD-SD-100*, 3 tracks. **D:** Response of intra-cellular pools in the 3 L lab-scale reactor simulations. Black line: instantaneous mixing results. Red line: *CFD-SD-600*, average over 5000 tracks. Blue line: *CFD-SD-100* simulation, average over 5000 tracks. Intra-cellular pools X_{gly}, X_{AA}, X_{sto} and X_{PAA} have units μmol/g$_{dw}$. μ has units h^{-1}. q_p has units mol/Cmol$_x$/h. All other pools are dimensionless.

7.3.4. Part IV: Industrial-scale Fed-batch Simulation

The long time metabolic response in an industrial fed-batch reactor is simulated; the feed profile is reported in fig. 7.10 **A**. C_x and μ are well captured ((fig. 7.10 **B** and **C**, resp.), although an ideal-mixed simulation with model of Douma et al. [236] ($ID-FB$) better captures the final 20 h. The 9-pool CFD simulation, however, performs superior in predicting the gradual reduction in q_p (fig. 7.10 **D**). The initial offset results from the lower peak q_p prediction by the 9-pool model around $\mu = 0.03$ h^{-1}.

The trends in intra-cellular pools (fig. 7.10, **E**) reveal major temporal changes in the pool averages (solid lines), as well as the emergence of significant heterogeneity within the population; the dashed lines in fig. 7.10, **E** represent the pool size standard deviation over 2500 tracks. The decreasing trend in all enzyme pools is a consequence

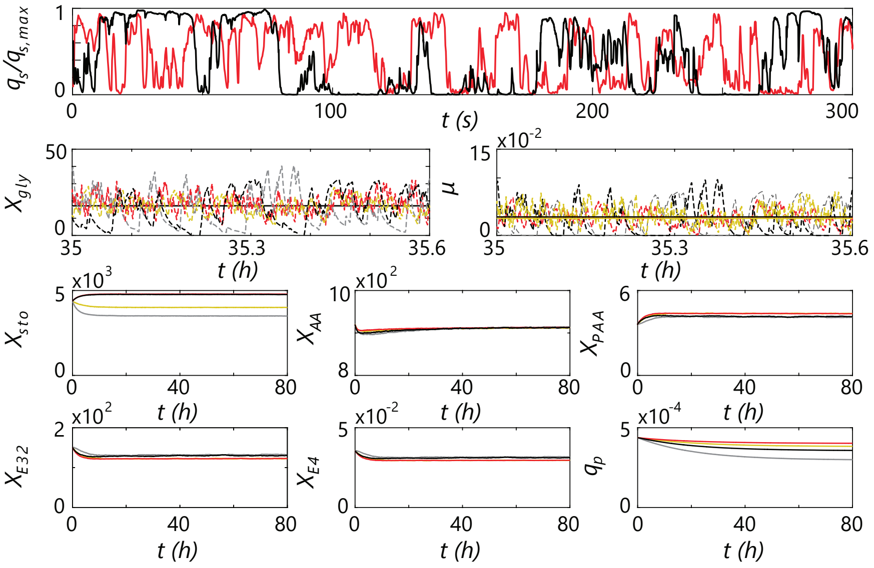

Figure 7.7: Long-term 9-pool model response large-scale simulations for *TU-A* (black), *MU-A* (red), *TU-B* (gray), *MU-B* (yellow). The top panel shows examples of q_s-lifelines for single parcels in *TU-A*, *MU-A*. For X_{gly} and μ, the solid lines represent the average, the dashed lines represent single parcel tracks to indicate the variations. All other solid lines represent are averages of 100 parcels. Intracellular pools X_{gly}, X_{AA}, X_{sto} and X_{PAA} have units µmol/g$_{dw}$. μ has units h^{-1}. q_p has units mol/Cmol$_x$/h. All other pools are dimensionless.

of the reduction in $\overline{\mu}$ to 0.01 h; the drop in X_{E32} reduces the PAA export capacity, giving rise to a strong PAA build-up. Similarly, a buildup in X_{sto} is observed. As before, the AA pool is least sensitive, although it undergoes some changes in later stages. The strong rise in population heterogeneity roughly coincides with the switch to a constant feed rate F_s (g/kg/h).

The high degree of heterogeneity in the enzyme pools may be surprising at first glance; their long adaptation timescale strongly exceeds τ_{circ}, meaning all parcels are expected to observe highly similar C_s fluctuations during the cultivation. The link between μ and $X_{E,11}$ plays a key role here; a parcel residing in a famine zone ($\mu \approx 0$) for a prolonged time undergoes a reduction in $X_{E,11}$. This means that this parcel's q_s is lower than the population average following this starvation exposure, due to the reduced uptake capacity. This lower q_s gives rise to a comparatively lower μ, which further lowers $X_{E,11}$ compared to the population mean: the initial disturbance is amplified.

This behavior is shown for 2 lifelines in figure 7.8; the black line is among the fastest growers, the red among the poorest. A prolonged exposure to starvation conditions in the period $t = 10.6 - 10.9$ h for the red parcel caused a period with $\mu = 0$, reducing $X_{E,11}$. In the subsequent period both parcels have roughly similar experiences, but the lower $X_{E,11}$ causes the red track to diverge. Once the feed is switched

Table 7.6: Comparing yields and productivity for the 9-pool model [226] between an ideal mixed situation, and several non-ideal CFD simulations coupled with the 9-pool model.

case	F (mol$_s$/Cmol$_x$/h)	μ (h^{-1})	q_p (mol$_p$/Cmol$_x$/h)	Y_{sx} (Cmol$_x$/Cmol$_s$)	Y_{sp} (mol$_p$/mol$_s$)
IDM	0.0125	0.033	$4.40 \cdot 10^{-4}$	0.44	0.035
TU-1A	0.0125	0.033	$2.99 \cdot 10^{-4}$	0.44	0.024
TU-1B	0.0125	0.032	$3.57 \cdot 10^{-4}$	0.43	0.029
MU-1A	0.0125	0.030	$3.83 \cdot 10^{-4}$	0.40	0.031
MU-1B	0.0125	0.030	$4.02 \cdot 10^{-4}$	0.40	0.032

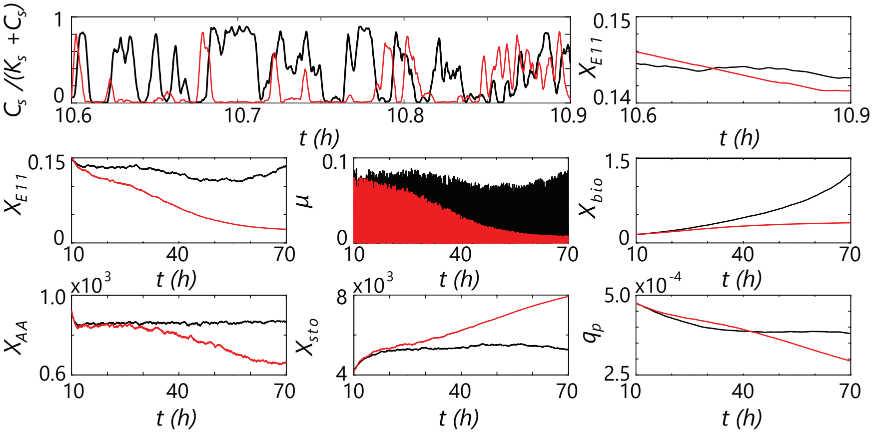

Figure 7.8: Heterogeneous lifelines for 2 parcels in the fed-batch simulation *TU-B*, conducted in *part IV*. Starting off at similar $X_{E,11}$, a prolonged starvation period (top left panel) for the red track causes a downward spiral in $X_{E,11}$ (top right panel for short timescale, mid-left panel for full simulation span), which causes divergence in all other pools compared to the fast-grower black lifeline. Intra-cellular pools X_{AA}, X_{sto} and X_{PAA} have units μmol/g$_{dw}$. μ has unit h^{-1}. q_p has units mol/Cmol$_x$/h. X_{bio} is the parcel biomass content in kg. All other pools are dimensionless.

from increasing to steady, the substrate availability per parcel starts dropping more rapidly, accelerating the divergence. The rapidly decreasing average $\overline{X_{E,11}}$ causes the mean substrate concentration C_s to stabilize, and even slightly increase after a while. The organisms that enter this stage with high $X_{E,11}$, such as the black parcel in fig. 7.8, now thrive: while the mean population experiences a decrease in substrate availability, they experience an increase. Not only $X_{E,11}$ is controlled by μ, but also the PAA exported $X_{E,32}$ and storage control enzyme $X_{E,4}$. Both enzymes are present in reduced levels for the poorly growing parcel, causing accumulation of PAA and storage material. The latter can physically be interpreted as preparing a buffer for true starvation, at the cost of growth and production.

A prolonged exposure to excess conditions after a starvation period may reverse the offset, but the further the parcel has deviated from the population average, the more unlikely this becomes. Figure 7.9, **C** shows that the parcels with $X_{E,11}$ slightly

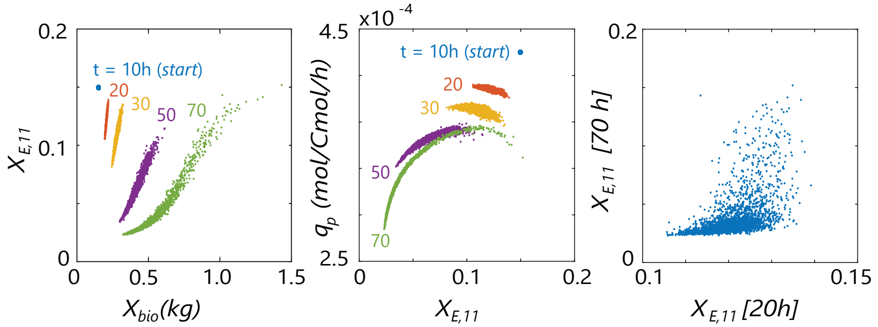

Figure 7.9: **Left:** correlation between $X_{E,11}$ and biomass content X_{bio} (g/$parcel$); the colored number with each associated scatter plot is the time of recording in h. **middle:** correlation between $X_{E,11}$ and the penicillin production rate q_p. **right:** correlation between $X_{E,11}$ after 20 h and $X_{E,11}$ after 70 h.

below average after 20 h exclusively end at the bottom of the $X_{E,11}$ distribution after 70 h. Having a high $X_{E,11}$ after 20 h appears to be a prerequisite for ending among the most rapid growers, but it by no means a guarantee: many parcels that did well after 20 h did end up with low $X_{E,11}$ eventually.

The parcels with high $X_{E,11}$ are the fastest growers (fig. 7.9 **A**); some acquire double the population average biomass over the cultivation time, whereas for the poorest growers $\mu \approx 0$ in the late process stage. As a low $\overline{\mu}$ has a negative effect on q_p, the fastest growers are also among the best penicillin producers (fig. 7.9 **B**), whereas the poor growers mostly accumulate storage material. Whether or not the predicted degree of heterogeneity is realistic requires an experimental scale-down study where population heterogeneity is probed on the single-cell level [13, 296]. The simulations predict notable heterogeneity enzyme levels, which may provide suitable targets for fluorescent marking for experimental quantification. Besides bench-scale scale-down, the use of microfluidic tools [297, 298] with highly controllable substrate feed rates may be a promising route towards studying the effects of substrate variations on enzyme expression and population heterogeneity.

7.4. Concluding remarks

We reported on the use of coupled hydrodynamic-metabolic simulations to assess large-scale fermentation processes in four parts: I) industrial-scale metabolic response analysis, II) scale-down design and verification, III) design optimization and IV) industrial-scale fed-batch analysis. Combined, these steps provide a methodology for the analysis, scale-down and optimization of large-scale fermentation processes.

We combined the $9-$pool metabolic model for *P. chrysogenum* of Tang et al. [226] with CFD simulations of a 54 m^3 fermentor [10]. In part I we studied the influence of non-ideal mixing in this reactor using a $1-$way coupled chemostat-simulation approach, which facilitates rapid assessment of the metabolism. Within the varied parameter space, the penicillin yield loss was $18-45\%$, which correlated linearly with

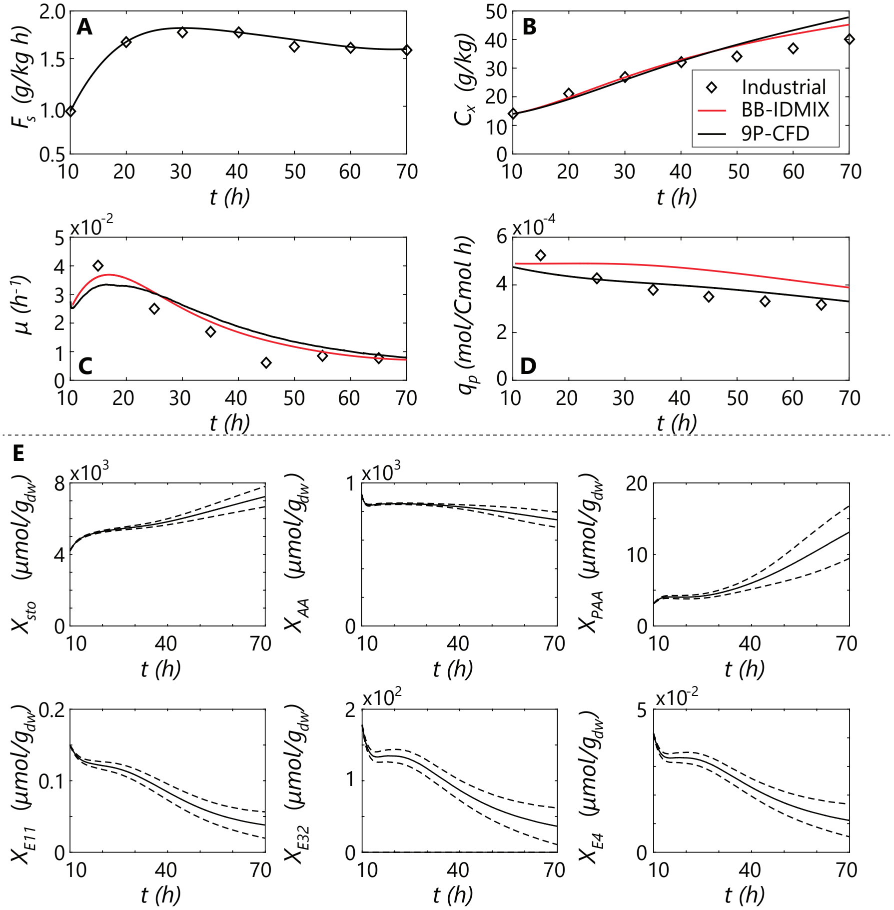

Figure 7.10: Response profiles of simulation *TU-FB*, comparing industrial data (diamonds), CFD response (black line) and an ideal-mixed black-box simulation (red line). **A:** Feed rate per unit reactor volume. **B:** Biomass concentration. **C:** Growth rate. **D:** Penicillin production. Panel **E** shows the response of 6 slow-responding intra-cellular pools, with the solid line the mean and dashed lines ±1 st. dev.

the Damköhler number. The yield loss was a result of high intra-cellular glycolytic levels, which relate to a higher circulation time (longer exposures to excess conditions) as well a higher substrate uptake capacity/substrate affinity. These observations provide targets for reactor- and metabolic optimization.

Numerical evaluation (*part II*) of the scale down simulator designs presented in section 6.4.3 showed the proposed scale-down design well captured the metabolic response observed in *part I*. Capturing the rate-of-change in the environment from the microbial point of view requires operating the scale-down simulator at the industrial biomass concentration $C_x = 55$ g/kg. Assessment of the scale-down simulator design with the 9−pool model predicted it is possible to compromise the rate of change without changing the metabolic response, provided the overall fluctuation duration and magnitude remain unchanged. This allows for a factor 2 reduction in C_x, which will benefit practical operation. We do emphasize this is a case-dependent prediction; the general best practice remains to match C_x between the scales for truthful replication of the q_s-lifelines, especially if no metabolic predictions considering the impact of operational compromises can be made.

CFD simulations of a 3 L lab scale-down simulator with pulsed feeding showed non-instantaneous mixing hardly effected the metabolic response; both at 600 and 100 RPM (circulation times of 0.55 and 3.3 s) the metabolic response was equal to that when instantaneous mixing was assumed. This gives a relatively wide operating window for the scale-down simulator, which provides confidence that the proposed lab-scale simulators are experimentally feasible; we do stress this window has to be evaluated case-by-case.

In part *III* change the substrate feed location in the industrial-scale fermentor from the vessel top to the top-impeller discharge stream to improve substrate distribution. The yield loss for the most favorable case was reduced from 18.4% to 8.6%. This shows the potential for coupled hydrodynamic-kinetic simulations for in-silico design optimization. To conclude, we present a 60 h fed-batch study in part *IV*, showing good agreement in μ and q_p compared to industrial data. Significant intra-cellular heterogeneity was observed, which was attributed to the interplay between μ and the glucose transport capacity $X_{E,11}$. The results illustrate the importance of simulating $2-$way coupled fed-batch dynamics to capture population heterogeneity. We do stress this does not mean the $1-$way coupled simulations are useless; $1-$way coupling is preferred for a quick assessment of the likely impact of design changes. We advise that the most promising cases observed with $1-$way coupling are simulated with $2-$way coupling (and/or experimentally assessed) to verify their performance when the effect of population heterogeneity is included.

Altogether, we outlined the different roles of coupled hydrodynamic-metabolic modeling in the assessment and improvement of large-scale fermentor designs. In future work, the proposed scale-down simulators are to be tested to verify model predictions; the predicted yield loss and population heterogeneity provide clear targets for assessment and model verification. There is room for improvement in both the CFD models and dynamic metabolic models, which would greatly benefit from a broader availability of industrial-scale data for verification. Such improvements act towards increasing the accuracy and reliability of the here-shown coupled CFD approach, but will not influence the methodology in itself. We believe the here-presented methodology, combined with practical scale-down simulation, opens up a new approach towards rational fermentor design and scale-up, accounting for the effect of large-scale reactor heterogeneity.

8

Conclusions and outlook

The growing market for biological platform chemicals, bulk pharmaceuticals and food additives raises interest in bioprocesses, and calls for ever larger fermentation capacities. Arthur Humphrey [1] called bioreactor scale-up ”more an art than a science”, due to the complex interplay of physical phenomena at different scales, often relating to transport issues: mixing, mass-transfer and/or cooling. Inadequate transport capacities manifest themselves in large scale gradients, in substrate, pH, dissolved oxygen/CO_2, shear rates, temperature, and so on. The complexities of bio-reactor scale-up arise from the interplay between these gradients and the metabolism of the organism. Metabolic responses to heterogeneous extracellular conditions may be reversible, such as substrate inhibition, or irreversible, or may come as irreversible viability losses. In some cases, the effect may be positive [8], but frequently, it is not [226]. It is this complexity that brings uncertainty in bioreactor scale-up.

Much has changed since the statement by Humphrey. Scale-down simulation became a much more prominent tool [43, 56], although the underlying concepts are older [41, 52, 53, 299]. Metabolic adaptation to extracellular variations is studied on long [49] and short [17, 44] timescales, as are population heterogeneity triggers [13], etcetera. Scale-down studies allow for understanding and quantification of the metabolic response to large-scale heterogeneities, thereby contributing to more rational and reliable scale-up procedures.

Compartment models [9] and later CFD simulations [16] allow reactor assessment beyond what can be measured experimentally, with ever-increasing resolution. Although requiring some approximations and simplifications, large-scale bio-processes can be simulated with reasonable accuracy [16, 30, 59, 61], allowing equipment-scale gradients to be captured [10, 16, 19, 20, 32], and population heterogeneity to be evaluated [19, 21, 23, 26–28, 281]. Lagrangian particle tracking methods allow to study how organisms experience their surroundings [10, 20, 21, 23, 31]. Simulation techniques allow to quantify large-scale conditions from the microbial point of view, and when metabolic models are available, to predict the metabolic impact of large-scale heterogeneity.

Combining these two fields offers an obvious perspective: CFD simulations can be used to design scale-down simulations representative of industrial conditions, whereas the metabolic insight from scale-down simulations can be used to develop metabolic models and predict the impact of metabolic responses in industrial scale-processes. This is the scope of the hé project.

8.1. Conclusions

8.1.1. CFD implementation

Guidelines and simplifications

Implementation and metabolic coupling We have successfully implemented the methodology to couple metabolic dynamics to a parcel (virtual particle) phase, as proposed by Lapin et al. [21, 23], in ANSYS FLUENT. For free-flowing microbes (low-Stokes number) massless parcels tracking is favored, which required implementation of a user-defined reaction model, as reported in chapter 4. The discrete, finite number of parcels leads to numerical gradients in biomass concentration and thereby (for example) substrate uptake, unless even the smallest grid-cells contain $O(10)$ parcels at all times, which is computationally infeasible. The effect of numerical biomass gradients can be mitigated by distributing the parcel-grid interaction of each individual over a larger volume. A cruder, simpler option is choosing the number of parcels sufficiently high so that biomass gradients do exist, but their effect on the other fields is small due to parcel motion and physical mixing.

The latter approach was chosen here. Based on the timescales of substrate uptake and turbulent distribution within the parcel swept volume (total reactor volume/number of parcels), we derived an expression to compute the minimum number of parcels required [31]. This number is in the same order of magnitude as the number of grid-cells typically, which is computationally feasible. We reported guidelines for the timestep size in coupled hydrodynamic-metabolic studies, and showed that use of the computationally cheaper multiple reference frame (MRF) impeller model instead of sliding mesh (SM) yielded a similar degree of accuracy in a simple 1-impeller tank.

Simplified uptake models Depending on the situation, the used uptake model may be simplified, graphically outlined in figure 8.1. When rapidly changing intra-cellular pools influenced uptake [21, 23], the local substrate uptake depends strongly on the local intra-cellular composition, which varies through the domain; accounting for this requires 2-way coupling and a large number of parcels [31]. In case uptake is solely controlled by the local extra-cellular environment (such as Monod kinetics), it can be fully coupled to the Eulerian phase with the Lagrangian phase merely ’reading’ the environment (1-way coupling). When uptake is controlled by enzymatic pools (on long timescales), the population will be heterogeneous, but to a similar degree everywhere in the domain. In that case, simpler averaged-2-way coupling can be used, where the average uptake capacity of the population is computed every timestep. which is then assumed homogeneous in the reactor. Whereas full 2-way coupling requires sufficient parcels to capture heterogeneity locally, the average-2-way coupling only needs to do so globally, requiring much lower N_p. With $O(10^3)$ parcels it is feasible to run such simulations near-real time on desktop computers: a flow-time resolution of $5-10$ h per day could be achieved near the end of this project. For comparison, using $O(10^5)$ parcels with sliding mesh impeller modeling allows for tens of seconds to be resolved in this timeframe. This does mean that situations with local heterogeneity, as those simulated by Lapin et al., are much more time-taking to simulate. Fed-batch simulations of such systems for full fermentation times are not yet feasible.

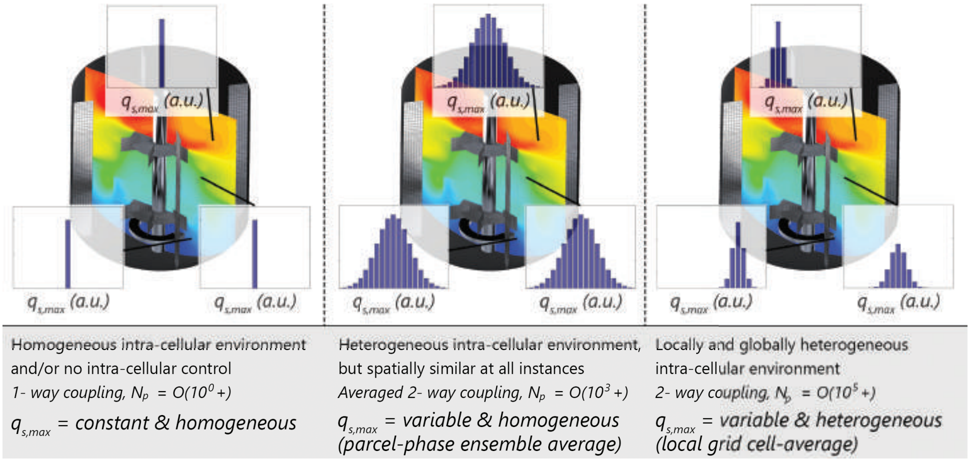

Figure 8.1: Illustration of coupling approaches used in this work. **Left:** if substrate uptake is only influenced instantaneously by the extra-cellular domain (the uptake capacity $q_{s,max}$ is constant and homogeneous), *1-way coupling* is used. **Middle:** If there is heterogeneity within the population, but the population is similar at each point in the tank, $q_{s,max}$ is assumed to depend on the average overall population composition, $\overline{X_{int}}$, and is regarded spatially homogeneous but temporally variable. N_p should suffice to capture the global population distribution. **Right:** In case the population is heterogeneous both locally and globally, $q_{s,max}$ may vary locally and should be based on the local composition X_{int}. N_p should suffice to capture the local population distribution, and can be calculated from eq. 4.6.

Bioreactor physics

Fermentor simulation requires the combination of models for many phenomena. Ideally, the following aspects ought to be accounted for:

- Macromixing (impeller interaction)
- Mesomixing (Feed mixing)
- Micromixing (Film diffusion, intra-pellet mass transfer,...)
- Rheology (typically shear thinning, turbulence/aeration interaction)
- Aeration (interaction with rheology, swarm effects, population dynamics)
- organism/pellet motion (turbulent behavior, settling, ...)
- Inter-phase mass transfer ($k_L a$ models)
- Heat transfer

All of these issues have been studied individually in many contexts. However, the interaction between different phenomena (turbulence, aeration, rheology in particular), and possibly empirical, case specific nature of models (for example the effect of surfactants on $k_L a$), mean that routine usage of CFD models for bioreactors with quantitative predictive purposes is not generally feasible currently. Developments in the above-mentioned aspects were considered out of scope in this work, the developed analysis methods work independent of the applied level of simulation detail.

One exception that was studied in detail is single-phase multi-impeller mixing. Mass transfer between the compartments around individual impellers is underestimated by RANS simulations of Rushton-stirred tanks (chapter 3). This stems from an under-estimation in turbulent kinetic energy between the compartments, for both sliding mesh and multiple-reference frame simulations, as well as the inability to capture macro-instabilities for the latter. As a consequence, the mixing time is overestimated by these models. Practically, this is often solved by reducing the turbulent Schmidt number, but this is a situation-dependent patch rather than a structural solution, thereby limiting predictive value of the simulations.

Aeration (air-water, Newtonian broth) with a high hold-up was reasonably captured by combining the universal drag law and the Luo/Svendsen [77] population balance model in FLUENT (chapter 5). Interphase mass transfer can be reasonably assessed for air-water cases [61], although the Luo-Svendsen population balance kernels predict high bubble sizes [77]. The applied drag modeling strategy works well for high gas fractions, but at lower gas fractions turbulence interaction and modulation plays a big role [191, 192, 195, 200]; this makes the modeling approach case dependent. Together with the required case-by-case Schmidt number tuning for the mixing time, this limits predictive value of the simulations. Attempts to include rheology were not satisfactory, especially when combined with aeration. We did not consider meso- or micro-mixing effects in this work.

Overall, the global features of large-scale fermentors with Newtonian characteristics (gas holdup, mixing time) can be captured within $\approx 25\%$ of their experimental value with the used RANS approach, and the substrate gradient is captured in the correct order of magnitude for the case where validation data was available. This is certainly a step ahead compared to ideal mixing assumptions, and suffices to comment on possible productivity loss in large-scale fermentors, although quantitative statements come with a margin of error. In terms of the underlying physics, and reducing this error margin, there is still room for improvement considering the physics of bioprocess simulation.

8.1.2. Lagrangian analysis

Compartment formation around the impellers strongly influences the substrate gradient. Unless the timescale of substrate uptake significantly exceeds the reactor circulation time, there will be a large-scale gradient. In tall multi-impeller bioreactors, flow compartments may form around each individual impeller; then mixing inside the compartment around a single impeller is fast compared to uptake, the (substrate) gradient manifests between the compartments. When uptake is faster than mixing inside these compartments, there may be a strong intra-compartment gradient. The former situation was observed in the *S. cerevisiae* simulations, the latter with *P. chrysogenum*. With a strong inter-compartment gradient, discrete jumps in the environment are experienced by micro-organisms, with a near-homogeneous environment between the jumps. A strong intra-compartment gradient results in continuous but smooth varia-

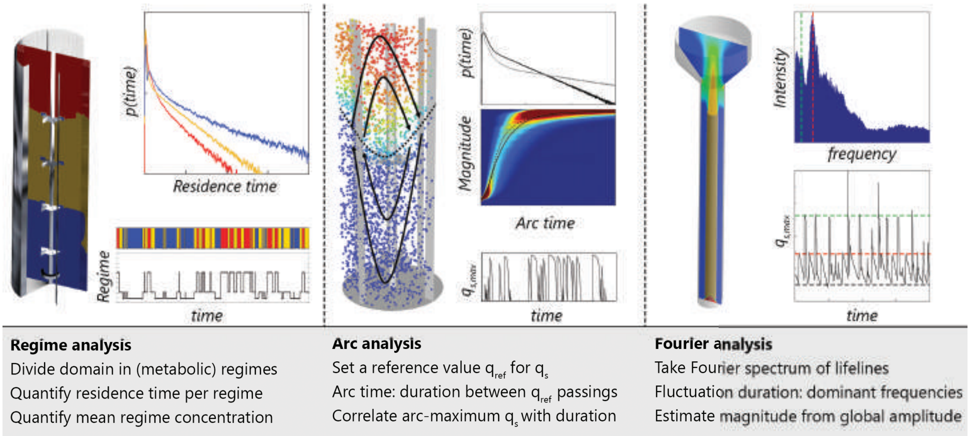

Figure 8.2: Lagrangian analysis methods used in this work. **Left:** Regime analysis, based on regions in q_s-space with a consistent metabolic response. **Middle:** Arc-analysis, based on the duration between subsequent crossings of a reference value in q_s. **Right:** Fourier analysis, seeking the dominant fluctuation frequencies when dominant circulation trajectories exist. In this work, methods were illustrated with q_s variations but they may similarly be applied to other parameters.

tions, as described in chapter 5.

The tank circulation time distribution provides the relevant timescales for fluctuations on the largest scale, the residence time distributions of the individual compartments for more rapid, lower amplitude variations. Each compartment acts as an individual stirred vessel, with a circulation time distribution $p(t) = \exp(-t/\tau_i)$, τ_i being the average compartment residence time. Variations at more rapid timescales are introduced by turbulence in case there are intra-compartment gradients.

From the practical perspective of scale-down, the whole tank or all individual compartments may not be the most suitable division for studying fluctuation behavior. We developed several analysis methods to quantify the magnitude and duration of fluctuations for more applicable statistics. An overview of methods is given in figure 8.2.

In the regime methodology the domain is divided into several virtual compartments, defined in uptake rate (q_s) space of the relevant metabolite, typically based on a consistent metabolic response such as overflow, starvation, substrate inhibition, etcetera. The regime residence time distribution describes the duration of exposure to each regime, the magnitude should be chosen as a representative value, such as the mean q_s or $q_s = 0$ for a starvation regime, which is evaluated per case. Alternatively, complementary arc-analysis can be used to quantify intra-regime fluctuations.

Arc analysis, used together with regime analysis or on its own, quantifies q_s fluctuations compared to a single reference value q_{ref} in the relevant parameter space. The duration between subsequent q_{ref} crossings quantifies the fluctuation time, the magnitude is given by the most extreme value in q_s along the (smoothed) arc trajectory. Correlating duration and magnitude provides information about compartmentalization of the gradient; inter-compartment gradients exhibit magnitude jumps at the intra-compartment circulation time. A smooth correlation hints at a strong intra-compartment gradient, and the duration between magnitude and time follows the relation between uptake and residence time in a plug-flow reactor, illustrating that poorly mixed tanks locally approach pipe-flow behavior, albeit with a distributed residence time.

The highly distributed circulation behavior in stirred tanks means that no dominant fluctuation frequencies exist within the domain, hence Fourier analysis provides no directly applicable information. Additional simulations of an airlift loop reactor (*appendix E*) demonstrated the applicability of Fourier analysis in situations with a narrower circulation distribution. As the above-mentioned analysis methods are typically conducted towards the design of scale-down simulators based on the fluctuation statistics, the type of scale-down reactor may also play a role in deciding the preferred analysis methodology. Based on the analysis conducted in this work, a selection diagram for the preferential (but not necessarily the only suitable) method is outlined in figure 8.3.

8.1.3. Scale-down design

The quantified fluctuation statistics provide a novel basis of design for scale-down simulators, that reflect the industrial-scale environment. Traditionally, scale-down simulators were often designed without reference to industrial mixing conditions [49], or based on estimations of the vessel mixing time [44]. Our analysis shows that fluctuations typically occur at the circulation timescale and below (chapter 5). Sweere et al. [41, 52, 53, 299], among the first to use scale-down simulators, got it right in this respect.

Based on Lagrangian CFD data, we can impose representative fluctuation time distributions rather than fixed-period fluctuations in single-vessel scale-down simulators, and determine the size and residence time of individual compartments in a multi-vessel scale-down simulator. Obtaining a perfect reflection of the large scale is unfeasible, but the design methods in chapter 6 capture the essential timescales of large-scale fluctuations in liter-scale reactors. The general approach is to systematically fix the five degrees of freedom for scale-down design reported by Noorman [15] using the available CFD data (chapter 5).

The rate-of-change in the (substrate) environment is essentially controlled by consumption/production by the micro-organisms. When the consumption timescale is much lower than that of circulation, the consumption rate of change is followed closely everywhere. With better mixing, the rate of change is close to 0 at many locations, but the concentration jump between two compartments may give a much higher local rate-of-change, the magnitude of which still depends on the rate of consumption. In order to capture the observed rate of change, the biomass concentration hence needs to be at least equal between the large and the small scale. Fed-batch experiments frequently use high biomass concentrations (C_x), but chemostat simulators typically operate at $C_x \approx 5$ g/kg, which gives a poor reflection of reality as reducing C_x inadvertently results in milder concentration variations.

High C_x may, due to unfavorable rheology and higher consumption rates, lead to

	Multi-vessel	**Single-vessel**
Grad.-induced population heterogeneity	*Yes*	*No*
Straightforward input-output relation:	*No*	*Yes (rapid sample)*
Operational challege (high viscosity) :	*Mixing* *Mass transfer* *Pumping*	*Mixing* *Mass transfer*

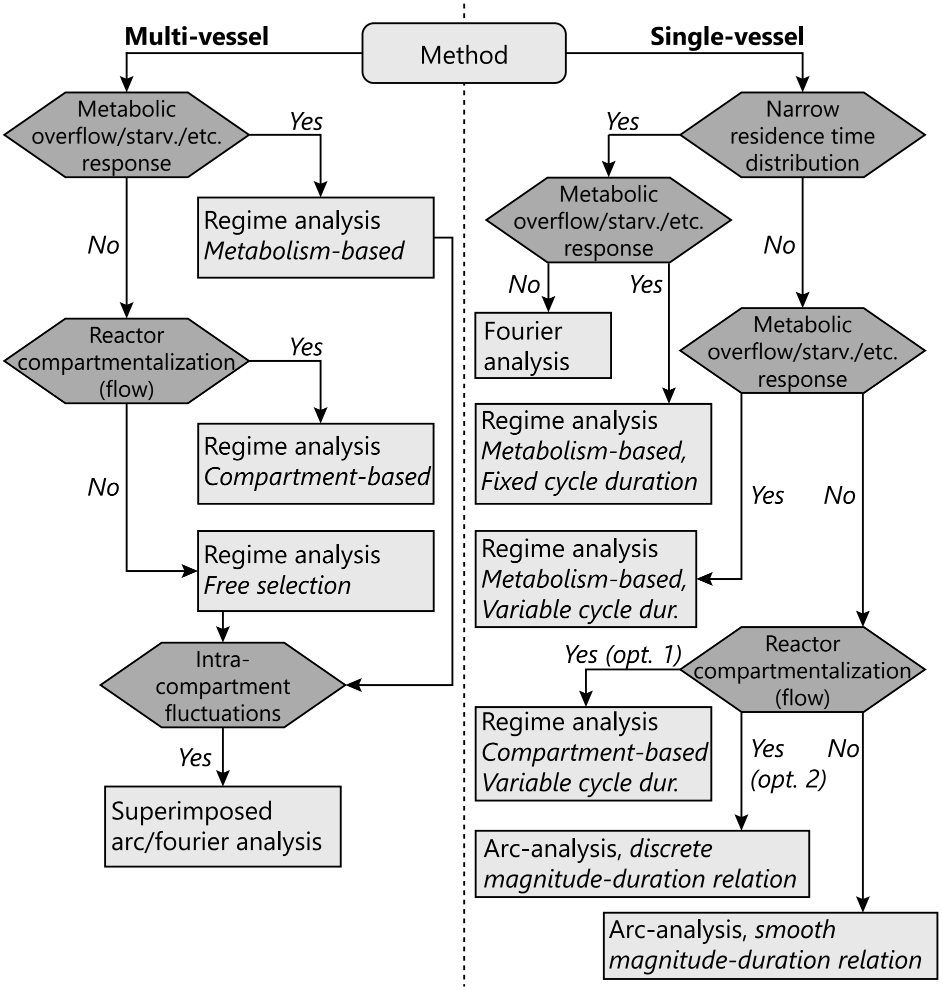

Figure 8.3: Selection diagram for lifeline analysis methods. Top shows some considerations for choosing a single or multi-vessel scale-down (list by no means complete). Gradient-induced population heterogeneity means heterogeneity induced by different individuals having different experiences in the reactor (not heterogeneity in general). Operational challenges will be most prominent with unfavorable rheology, although sufficiently fast pumping can always be a constraint with a multi-vessel approach. The bottom shows a selection chart for the *preferred* analysis method (this does not mean other methods are necessarily inapplicable for the described situations).

inadequate mixing and mass-transfer at the lab scale. Furthermore, pumping in multi-vessel geometries may become problematic. In some cases a reduction in C_x may be possible, even though this affects the agreement in rate of change. Using a coupled metabolic model, we showed that a factor 2 decrease in C_x (*P. chrysogenum*, single-vessel scale-down) did not lead to a different metabolic response by applying instantaneous rather than gradual pulse-feeding. This possibility is highly case-dependent, and should be evaluated as such. An alternative may be to match the intra-cellular lifelines instead of the extra-cellular environment on a scale-down simulator, an option that is explored in *appendix G*. Such an approach may come with a more favorable operating window, but we stress it is no full replacement of the q_s-lifeline based extra-cellular scale-down methodology; as scale-down based on intra-cellular lifelines may simplify some extra-cellular events, there is a risk of unforeseen responses.

8.1.4. Coupled metabolic-hydrodynamic simulations

Combined hydrodynamic-metabolic simulations for *P. chrysogenum* with the model of Tang et al. [226] showed that extremes in the glycolitic intermediate pool have a strong repression effect on the synthesis of penicillin-pathway enzymes, thereby affecting production. The mean growth rate could also affect production, but only in extreme situations. Depending on the lower/upper bound circulation time and kinetic assumptions, the predicted yield loss was $18 - 46\%$ compared to ideal mixing. By moving the feed to the top impeller discharge stream, this was reduced to 9% in the most favorable case. The structure of the metabolic model did not allow for evaluation of strong changes in uptake affinity, but in principle such changes can be similarly proposed. While further improvements in the simulation approach may change the numbers somewhat, the general observations are expected to hold, and the approach shows the promise of the coupled hydrodynamic-metabolic simulation approach (chapter7).

The approach was furthermore used to numerically evaluate scale-down designs, as partially discussed in the previous section. The single-vessel scale-down protocols proposed in chapter 7 exhibit good agreement in yield and growth rate compared to the large-scale CFD simulations. CFD simulations of the lab-scale showed mixing times of $2.2 - 13.2$ s on the lab-scale had no significant effect on the results, which shows mixing may not be a large issue for representative scale-down. To conclude, a 60 h flow-time simulation of a fed-batch process favorably compared with experimental data in terms of q_p over time. Significant heterogeneity was observed within the population with respect to the uptake capacity $q_{s,max}$, which was self-amplifying due to the relation between the uptake q_s, growth rate μ and transport enzyme capacity $X_{E,11}$. These results illustrate the prospects of coupled simulations.

8.2. Outlook

In this thesis, we have explored the use of Euler-Lagrange simulations for rational bioreactor scale-down and scale-up. In short, we have made progress considering the use of coupled hydrodynamic-metabolic simulations to evaluate the performance of large scale bioreactors, the use of representative scale-down simulators to verify these predictions, and the use of CFD and scale-down data to suggest scale-up improvements. And, we have shown how computational simplifications make it feasible to model long stretches of flowtime in certain situations, even using commercial CFD software not necessarily optimized for this type of application.

Overall, computational bioreactor engineering is very much an emerging field, with the proposed ideas being picked up in scale-down design [300–303], and several lines of development [19, 30, 282]. There are many more aspects to explore, both regarding improvements of the CFD methods and regarding experimental assessment of non-ideal bioprocesses.

8.2.1. Computational advances

Simulation and validation While somewhat tangential to the Lagrangian analysis discussed in this thesis, there is still ground to gain in the physical modeling of industrial bioreactors to improve overall accuracy. RANS-Turbulence models may not properly predict the interaction between impellers in multi-impeller tanks, as reported in chapter 3, and structural improvements are desired. For bubbly multiphase flows, there is a wide variety of interphase-force models and population balance kernels, which are selected on a case-by-case basis. Already a comprehensive study towards best practices for large-scale bioreactor modeling would be valuable. Turbulent drag modification, bubble induced turbulence and turbulence-bubble interaction are inadequately understood and captured [72]. Turbulent/aerated non-Newtonian flows remain troublesome, meso-mixing issues (i.e. blobs of unmixed feed) need to be included, and a whole range of micro-mixing phenomena (Kolmogorov-scale mixing, intra-pellet transport of substrate in pelleted biomass, etc.) has to be considered; the importance of such phenomena will be case-dependent. Coalescence and mass transfer in surfactant-laden flows is poorly captured by available models.

One particular issue is that CFD modeling advances mostly in the direction of high resolution LES and DNS approaches, whereas the field of bioreactor modeling calls for simulating long physical time-spans rather than high spatial resolution. For such applications, RANS approaches remain indispensable. The current state of affairs prohibits unverified predictive application of CFD models. However, keeping the limitations and margins of error into account, the current state of models can certainly provide insight beyond what is experimentally accessible, and far beyond the typical ideal mixing assumption. The need for further model development may appear pessimistic, but it certainly is not. It should be regarded as a warning against blind faith in simulations, but when properly applied, simulations are certainly valuable for rapid quantitative and qualitative evaluation of current fermentations, and future improvements.

The call for developments in CFD methods comes with a need for more large-scale validation data to be published in the public domain to encourage academic endeavors into large-scale fermentor modeling, instead of being forced to stick with lab-scale data. We do not expect detailed profiles; overall gas hold-up and $k_L a$ and rheological information, as well as the mixing profile, substrate/oxygen concentration at a couple of points, would already be highly valuable in verifying simulation performance.

Numerical challenges Gains in calculation speed are required for routine industrial application. This acts at two levels: highly simplified simulations of full fed-batch processes, and shorter time-spans with more physical details. We could currently achieve around $5 - 10$ h of flowtime per day of computation time with highly simplified simulations in ANSYS FLUENT on a desktop computer (XEON E5-2665, 2.4GHz), where the low gridcell count allows little speed-up with further parallelization. The most promising route to faster computations is likely the use of dedicated software, rather than general CFD packages which were currently chosen for their flexibility and to focus on application rather than software development. With a combination of optimized software, fast processors, and optimized simulation settings, it should be possible to run real-time simulations, and likely well beyond that, within the foreseeable future.

The second track considers introducing more physical realism within manageable solution times. Rapid inter-phase dynamics call for many computational parcels, and the steady-state MRF impeller model may not always be applicable. Oscillating bubble plumes in bubble columns may also call for transient flowfields, greatly increasing simulation time. Early simulations that we conducted, with sliding mesh and $2 \cdot 10^5$ parces, ran around tens of seconds of flow time per day on a desktop computer. Since these aspects are periodic, it may be possible to simulate a single (developed) period, and load the appropriate flowfield every timestep rather than solving it. In cases with high mesh resolution, parallelization can save significant time, although our experience was that parcel tracking slowed down in heavily parallelized cases (with FLUENT 14/15). Real-time simulations for these more complex cases are a long term perspective, but even resolving 1 h flowtime per day would bring routine-scanning of design optimizations based on the 1-way coupling method of chapter 7 within reach.

8.2.2. Scale-down simulation

The obvious first step is to build and operate CFD-based scale-down designs, explore their operational feasibility (at high C_x), and to verify model predictions made regarding the output of these simulators. The proposed designs include novel elements, such as the combination of three stirred tank reactors, and the use of randomized feed profiles, but these are all are practically realizable within the limits of current technology. The output of these scale-down simulators may of course differ from the model predictions, pushing further development of metabolic models; scale-down development and metabolic model development go hand in hand. We have provided several methodologies to extract fluctuation statistics from lifelines, and over the years of the project these methods continued to evolve. We hope they will keep doing so after; there may be other avenues towards acquiring fluctuation statistics, perhaps even more promising ones than those explored here. The translation of lifelines to scale-down simulators may also evolve. Compartmentalization leads to discrete levels in the signal, which may guide a 1-vessel design alternating between these levels as a more robust alternative to arc-analysis. We have also not delved into the design of hybrid multi-vessel fluctuating-feed scale-down simulators. In case new lifeline analysis method be proposed, they may come associated with new rational downscaling approaches.

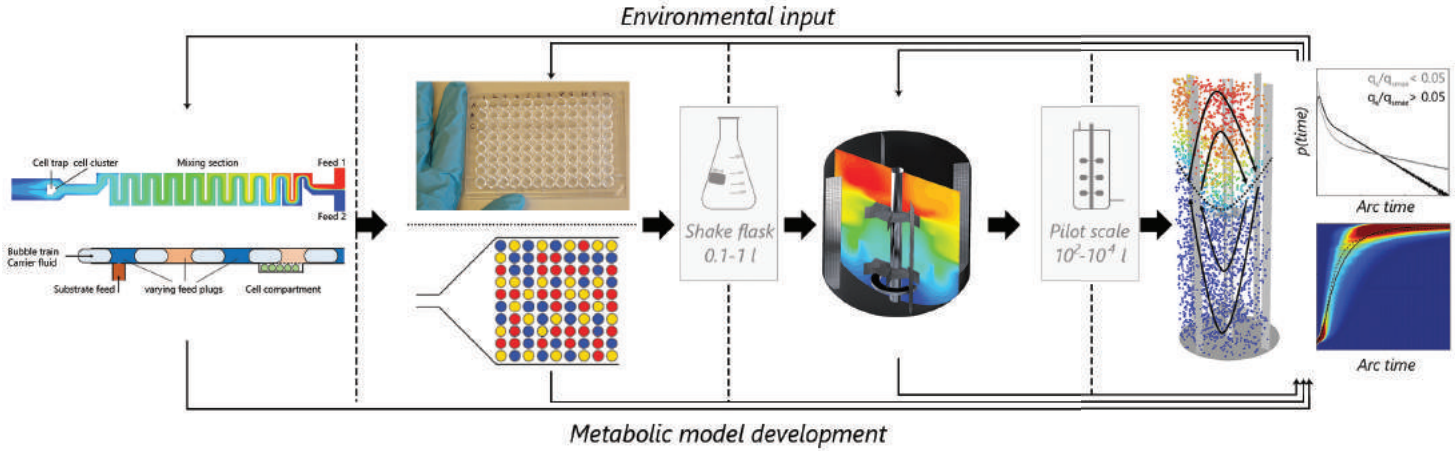

Microfluidics	**Parallel well-plate (now)**	**Lab-scale cultivation**	**Industrial-scale process**
Metabolic understanding:	**Massive Microfluidics (future)**	*Scale-down verification*	*(CFD based) environment*
modeling, metabolic triggers	*Strain selection*	*Heterogeneity study*	*quantification*
Single-cell response analysis	*Heterogeneity triggers*	*(population interaction)*	*Production optimization*
Direct lifeline screening	*Operation condition screening*	*Operational verification*	

Figure 8.4: Multi-scale bioreactor evaluation and design approach. Upcoming micro-fluidic approaches allow metabolic evaluation at single-cell level. Combined with omics-information from the other lab-scales, this feeds comprehensive metabolic model formulation. The microtiter-scale, augmented (and perhaps in time replaced) by massive parallel microfluidics, provides the environment for rapid parallel strain evaluation and selection, which may make the shake-flask obsolete. Massively parallel single-cell analysis allows to study heterogeneity triggers and effects. The regular bench-scale remains valuable for verification and population behavior. Large-scale (CFD) data feeds environmental information, and is the target for reactor optimization. For well-defined processes, the intermediate pilot scale may soon be omitted.

Liter-scale reactors are inherently limited by their reliance on consumption to induce extra-cellular changes, which caps the achievable rate-of-change by C_x. Preferably, a next generation of scale-down simulators decouples the achievable rate of change from C_x. This requires some form of substrate flushing, possibly using membrane reactors or biomass retention on the bench-scale, which likely come associated with fouling, clogging, etcetera. The use of micro-fluidic devices may be a more feasible route. Single cells or small clusters of cells can be trapped in these devices [297, 298, 304–308], which makes it possible to control the environment around the organism directly [309, 310]. Preliminary 2D simulation with a conceptual, non optimized design (*appendix F*) shows it should be possible to achieve environmental control on the second scale. Alternating between fluid streams saturated with oxygen and nitrogen can be used to simulate rapid oxygen variations. In principle, proper dosing of the streams could even be used to directly mimic particle tracks retrieved from CFD experimentally.

The microfluidic approach is most suitable to study the metabolic response in detail on the single cell level. The largest challenge therein is likely data collection: normally, the few mL of broth retrieved for analysis already contains an enormous amount ($\approx 10^{11}$ mL^{-1}) of cells. Single-cell analysis requires measuring minute quantities, intra- or extra-cellular. Luckily, these fields are subject to rapid developments [13, 296, 298, 311, 312]. Rapid-fluctuation studies based on single-cell responses in well controlled environments are becoming an established part of the biological analysis toolbox, and in the future may be used for representative design. Combined with advances in rapid strain screening using parallelized micro-titerplate applications, and with some projections for future developments (discussed in the next section), the bioprocess development platform landscape takes the outline presented in figure 8.4. The drive to smaller and smaller screening platforms makes one fear for the future of shake-flask fermentation.

8.2.3. And further...

Freely quoting the late professor Gert Frens, *The road [for an engineer] extends beyond the horizon*. What lies beyond? Many possibilities, to be sure. With proper microfluidic scale-down simulation and analysis protocols, the next step is to replace the microtiterplate with truly high-throughput screening. Massively parallel microfluidics allows to screen thousands of strains in parallel, under constant conditions to understand their metabolism, or under fluctuating conditions to screen their industrial applicability. Or, the same strain may be exposed to many feed protocols to optimize operating conditions. Thousands of individual cells exposed to equal conditions may be studied to reveal what gives rise to spontaneous heterogeneous conditions. Massive parallel single-cell studies promise a new era for understanding and selecting micro-organisms.

On the CFD-side, improvements in physical modeling will allow us to better capture the environment of large-scale reactors, with experimental flow-following probes possibly offering large-scale validation data from the microbial reference frame. Developments in computational speed will lead to more routine application of simulation approaches; the ability to run real-time hydrodynamic-metabolic simulations may open new avenues in process control. Running in parallel to the actual fermentation, and directly coupled to process inputs, processes could be followed beyond what the sensors measure. This can be used for on-the-go optimization, response to process perturbations, or early batch canceling if there are signs of an irreversible production loss. Combined with neural network models, pre-conditioned using both CFD and factory data, on-line simulations may help in rapid troubleshooting.

Imagine a situation where the broth oxygen level is measured to be insufficient. The hydrodynamic-metabolic model running in parallel starts showing signs of intra-cellular oxygen starvation, while the neural network correlates the sensory data with an elevation in broth viscosity due to higher hyphal length. It suggests increasing the agitation rate to shear off some hyphea, and increase oxygen transfer. At some point, however, the CFD model suggests that the intra-cellular impact of oxygen starvation is too severe to continue the process, and it may be better to dump the batch. A waste of material maybe, but at least valuable time is saved. Coupled with modern visualization technology, a process operator may stream real time data on the state of the process, extra- *and* intra-cellular, to their smartphone or augmented reality glasses. They can then evaluate a process while walking in the factory, and act whenever the system hints at possible process improvements to optimize batch quality.

”From shake flask to fermentor” became ”From cell to fermentor”, maybe even ”From gene to fermentor”; in the course we’ve learned a lot. Yet, the age of biology has only just begun, and all the best may still lie ahead.

Nomenclature

Abbreviations: general

CFD	Computational Fluid Dynamics
CoM	Coefficient of Mixing
CoV	Coefficient of Variation
DO	Dissolved Oxygen
DRW	Dynamic Random Walk
EL	Euler-Lagrange
LDA	Laser Doppler Anemometry
LES	Large Eddy Simulation
MI	Macro Instability
MRF	Multiple Reference Frames
PIV	Particle Image Velocimetry
(A)PFR	(Axially dispersed) Plug Flow Reactor
RANS	Reynolds Averaged Navier Stokes
RD	Reaction Dynamics
RKE	Realizable $k-\epsilon$ model
RTD	Residence Time Distribution
RSM	Reynolds Stress Model
SD	Scale-Down
SGDH	Simple Gradient Diffusion Hypothesis
SM	Sliding Mesh
STR	Stirred Tank Reactor

Abbreviations: species

6-APA	6-aminopenicillanic
AAA	α-aminoadipate
ACV	α-aminoadipyl-L-cysteinyl-D-valine
ACVS	ACV-synthase
CoA	coenzyme-A
CYS	L-cysteine
IPN	isopenicillin-N
IPNS	IPN synthase
PAA	phenylacetic acid
Pen-G	penicillin-G
VAL	L-valine

Roman (I)	**Units**	**Description**
a	m^2/m^3	Area concentration
A	m^2	Area (general)
c_i	–	Amplitude coefficient in autocorr. signal
C_S	–	Smagorinsky constant, LES model
C_s	mol/kg	Substrate concentration (mole based)
c_s	mg/L	Substrate concentration (mass based)
$C_{s,b}$	mol/kg	Substrate concentration at a boundary b
$C_{s,c}$	mol/kg	Substrate concentration in cell c
$C_{s,p}$	mol/kg	Substrate conc. observed by parcel p
C_x	g/kg	Biomass concentration
C_F	mol/kg	Feed concentration
C	–	Constant (general notation)
C	m	Off-bottom clearance impeller
C_D	–	Drag coefficient
D	m	Impeller diameter
D_r	h^{-1}	Dilution rate
d_b	mm	Sauter mean diameter
$\mathcal{D}_m$	m^2/s	Diffusion coefficient
$\mathcal{D}_t$	m^2/s	Turbulent diffusion coefficient
E_{per}	m^2/s^2	Energy per kg, periodic
E_{tot}	m^2/s^2	Energy per kg, total
$f_{i.j}$	Hz	j^{th} harmonic of i^{th} frequency comp.
F	kg/s	Feed rate (general)
F_i	kg/kg/s	Specific feed flowrate, vessel i
F_s	mol/s	Substrate feed rate (general)
$F_{s,i}$	mol/s	Substrate feed rate, vessel i
g	m/s^2	Gravitational acceleration
H	m	Tank height
H_L	m	Liquid height
k_t	m^2/s^2	Turbulent kinetic energy
k_{t*}	m^2/s^2	Total fluctuating kinetic energy
k_{MI}	m^2/s^2	Macro-instability kinetic energy
k_{sgs}	m^2/s^2	Subgrid turbulent kinetic energy
k_l	m/s	Local mass transfer coeff.
k_La	h^{-1}	Overall mass transfer coeff.
K_s	mol/kg	Affinity constant for substrate
L_{res}	m	Integral lengthscale
M	mol/kg/s	General mixing term
M_I	Nm	Impeller moment
m_s	mol$_s$/Cmol$_x$/h	Maintenance coefficient
n	–	Integer multiplier
N_s	s^{-1}	Impeller revolutions
N_c	–	Total number grid cells
N_p	–	Total number particles
$N_{p,c}$	–	Number particles in cell c

Roman (II)	**Units**	**Description**
p	Pa	Instantaneous pressure
P	Pa	Average pressure
P	W	Power input
q_p	mol$_p$/Cmol$_x$/h	Specific production rate of product
q_s	mol$_s$/Cmol$_x$/s	Specific uptake rate of substrate
$q_{s,max}$	mol$_s$/Cmol$_x$/s	Max. Specific uptake rate of substrate
q_{ref}	$-$	Reference $q_s/q_{s,max}$
Q_g	m^3/s	Gas flowrate
r_p	m	Particle radius
r_{tip}	m	Impeller radius
R	m	Tank radius
$R_{s,c}$	m	Reaction rate of s, cell-based
$R_{s,p}$	m	Reaction rate of s, parcel-based
$S_{s,c}$	mol/kg/s	Source term of s
S	s^{-1}	Strain rate magnitude
s_{ij}	s^{-1}	Rate-of-strain (component)
S_{ij}	s^{-1}	Average Rate-of-strain (component)
T	m	Tank diameter
T_i	kg/kg	Mass fraction compartment i, SDS
t	s	Time (general)
u_f	m/s	Fluid velocity
u_i	m/s	Instantaneous velocity (component)
u_p	m/s	Particle velocity
u'	m/s	Fluctuating velocity
u'_t	m/s	MI-free fluctuating velocity
U_i	m/s	Average velocity (component)
U_g	m/s	Superficial gas velocity
V	m^3	Tank volume
V_i	m^3	Vessel volume in SDS
V_p	m^3	Parcel associated volume (V_T/N_P)
V_T	m^3	Total volume (general)
V_{tot}	m^3	Total volume SDS
w	$-$	Tuckey-Hanning window function
x_i	m	Spatial coordinate (component)
X_i	µmol/g$_{dw}$	Intracellular metabolic pool
$X_{E,i}$	$-$	Intracellular enzyme pool
X_{bio}	g$_{dw}$	Biomass content per parcel
Y_{sx}	Cmol$_x$/mol$_s$	Max. biomass yield on substrate
Y_{sp}	mol$_p$/mol$_s$	Product yield on substrate

Greek	**Units**	**Description**
α	–	Gas fraction
α_0	–	Damping coefficient in autocorr. signal
α_a	–	Phase a fraction
α_g	–	Geometry constant for no. parcels
β	–	Heterogeneity ratio around parcel
β_m	–	Max. heterogeneity ratio around parcel
γ	N/m	Surface tension
δ_{ij}	–	Kronecker delta
Δ	m	filter size (LES)
Δt	s	Timestep size
Δt_c	s	Eulerian timestep size
Δt_p	s	Lagrangian timestep size ($t_p \leq t_c$)
ΔC	m	Mutual clearance impellers
ϵ	m^3/s^2	Turbulent energy dissipation rate
θ_{95}	–	Dimensionless mixing time
Θ	–	Timestep - uptake rate ratio
λ	%	Inter-phase mass imbalance (Euler-Lag.)
λ_k	m	Kolmogorov lengthscale
λ_i	nm	Wavelength
λ_I	m	Integral lengthscale
μ	h^{-1}	Specific growth rate
μ_l	Pa s	Viscosity, dynamic
μ_t	Pa s	Turbulent viscosity, dynamic
ν	m^2/s	Viscosity, kinematic
ν_t	m^2/s	Turbulent viscosity, kinematic
ρ	kg/m^3	Density
$\hat{\rho}$	–	(Auto-) correlation coefficient
$\sigma_{s,c}$	–	Standard deviation no. parcels in cell
τ_{95}	s	Mixing time
τ_{arc}	s	Arc-time
τ_{circ}	s	Circulation timescale
τ_i	s	Residence time, vessel i.
τ_{lag}	s	Autocorr. lag time
τ_m	s	Mixing in parcel-swept volume V_T/N_P
τ_{rxn}	s	Uptake timescale of substrate
τ_{ij}	Pa	Stress tensor components
ϕ_i	kg/s	Circulation flowrate
χ	–	Heterogeneity in domain
χ_a	–	Phase indicator function phase a
Ψ	–	Noise fraction, LDA signal
$\Omega_{s,max}$	–	Max. $q_s/q_{s,max}$ on arc trajectory
Ω_i	s^{-1}	Vorticity (component)

Tensors and vectors

Symbol	Units	Description
$\overline{\overline{\boldsymbol{\tau}}}$	Pa	Stress tensor
$\overline{\overline{\boldsymbol{\delta}_{\boldsymbol{ij}}}}$	–	Kronecker delta
ω	s^{-1}	Angular velocity (vector)
$\mathbf{u}$	m/s	Instantaneous velocity (vector)
$\mathbf{u}_a$	m/s	Instantaneous velocity phase a (vector)
ω	s^{-1}	Angular velocity (vector)
$\mathbf{x}$	m	Spatial coordinate (vector)

Operations

Operator	Description
$\overline{y}$	Time or ensemble average of y
$\langle y \rangle$	Volume average of y
$\widetilde{y}$	Spatially filtered y (in LES)
$\overline{\tau_i}$	Mean residence time, regime i.
y_i'	Fluctuating component of y
$p(y)$	Probability of y
$\sigma(y)$	Standard deviation of y

Population balance variables

Var.	Units	Description
$n(V,t)$	m^{-3}	Number density
$a(V_a,V_b)$	m^3/s	Aggregation kernel
f	–	Bin fraction (number)
$g(V_a)$	s^{-1}	Breakup frequency
$\beta(V_a \vert V_b)$	(–)	Breakage pdf
Ω_{br}	$\mathrm{m}^{-3}\mathrm{s}^{-1}$	Breakage rate Luo model ($\beta,\ g$ integrated)
ω_{ag}	s^{-1}	Collision frequency
P_{ag}	–	Collision probability

Dimensionless numbers

Number	Description
Da	Damköhler number
Eo	Eötvös number
Gs	Gas flow number
Po_ϵ	Power number (ungassed) based on energy dissipation
Po_τ	Power number (ungassed) based on torque
Po_g	Power number (gassed) based on torque
Re	Tank Reynolds number based on D
Re_p	Particle Reynolds number based on d_p
Sc_t	Schmidt number, turbulent
σ_i	Prandtl number for i (RANS models)
St	Stokes number
We	Weber number

References

[1] A. Humphrey, *Shake Flask to Fermentor: What Have We Learned?* Biotechnology Progress **14**, 3 (1998).

[2] R. Carlson, *Estimating the biotech sector's contribution to the US economy,* Nature Biotechnology **34**, 247 (2016).

[3] G. Reh, M. Standing, K. Asami, S. Jacobson, E. de Vettori, Y. Wu, Y. Jarlaud, G.-K. Elbel, C. Sehgal, T. Nagakawa, J. Cueto, O. Berezin, V. Adao, M. Grover, R. Reppas, and J. Haughey, *2016 Global life sciences outlook: Moving forward with cautious optimism,* (2015).

[4] H. J. Noorman and J. J. Heijnen, *Biochemical engineering's grand adventure,* Chemical Engineering Science (2017), 10.1016/j.ces.2016.12.065.

[5] A. Burgard, M. J. Burk, R. Osterhout, S. Van Dien, and H. Yim, *Development of a commercial scale process for production of 1,4-butanediol from sugar,* Current Opinion in Biotechnology **42**, 118 (2016).

[6] B. Cok, I. Tsiropoulos, A. L. Roes, and M. K. Patel, *Succinic acid production derived from carbohydrates: An energy and greenhouse gas assessment of a platform chemical toward a bio-based economy,* Biofuels, Bioproducts and Biorefining **8**, 16 (2014).

[7] M. L. Jansen and W. M. van Gulik, *Towards large scale fermentative production of succinic acid,* Current Opinion in Biotechnology **30**, 190 (2014).

[8] S.-O. Enfors, M. Jahic, A. Rozkov, B. Xu, M. Hecker, B. Jürgen, E. Krüger, T. Schweder, G. Hamer, D. O'Beirne, N. Noisommit-Rizzi, M. Reuss, L. Boone, C. Hewitt, C. McFarlane, A. Nienow, T. Kovacs, C. Trägårdh, L. Fuchs, J. Revstedt, P. Friberg, B. Hjertager, G. Blomsten, H. Skogman, S. Hjort, F. Hoeks, H.-Y. Lin, P. Neubauer, R. van der Lans, K. Luyben, P. Vrabel, and Å. Manelius, *Physiological responses to mixing in large scale bioreactors,* Journal of Biotechnology **85**, 175 (2001).

[9] N. M. Oosterhuis and N. W. Kossen, *Dissolved oxygen concentration profiles in a production-scale bioreactor,* Biotechnology and bioengineering **26**, 546 (1984).

[10] C. Haringa, W. Tang, A. T. Deshmukh, J. Xia, M. Reuss, J. J. Heijnen, R. F. Mudde, and H. J. Noorman, *Euler-Lagrange computational fluid dynamics for (bio)reactor scale down: An analysis of organism lifelines,* Engineering in Life Sciences **16**, 652 (2016).

[11] A. R. Lara, L. Leal, N. Flores, G. Gosset, F. Bolívar, and O. T. Ramírez, *Transcriptional and metabolic response of recombinant Escherichia coli to spatial dissolved oxygen tension gradients simulated in a scale-down system.* Biotechnology and bioengineering **93**, 372 (2006).

[12] A. R. Lara, E. Galindo, O. T. Ramírez, and L. A. Palomares, *Living With Heterogeneities in Bioreactors: Understanding the Effects of Environmental Gradients on Cells,* Molecular Biotechnology **34**, 355 (2006).

[13] F. Delvigne and P. Goffin, *Microbial heterogeneity affects bioprocess robustness: dynamic single-cell analysis contributes to understanding of microbial populations*. Biotechnology journal **9**, 61 (2014).

[14] F. R. Schmidt, *Optimization and scale up of industrial fermentation processes*. Applied microbiology and biotechnology **68**, 425 (2005).

[15] H. Noorman, *An industrial perspective on bioreactor scale-down: what we can learn from combined large-scale bioprocess and model fluid studies*. Biotechnology journal **6**, 934 (2011).

[16] G. Larsson, M. Törnkvist, E. S. Wernersson, C. Trägårdh, C., H. Noorman, and S. O. Enfors, *Substrate gradients in bioreactors: origin and consequences,* Bioprocess Engineering **14**, 281 (1996).

[17] B. Wu, *Large eddy simulation of mechanical mixing in anaerobic digesters,* Biotechnology and Bioengineering **109**, 804 (2012).

[18] J. Morchain, J.-C. Gabelle, and A. Cockx, *Coupling of biokinetic and population balance models to account for biological heterogeneity in bioreactors,* AIChE Journal **59**, 369 (2013).

[19] J. Morchain, J.-C. Gabelle, and A. Cockx, *A coupled population balance model and CFD approach for the simulation of mixing issues in lab-scale and industrial bioreactors,* AIChE Journal **60**, 27 (2014).

[20] C. Haringa, A. T. Deshmukh, R. F. Mudde, and H. J. Noorman, *Euler-Lagrange analysis towards representative down-scaling of a 22m3 aerobic S. cerevisiae fermentation,* Chemical Engineering Science **170**, 653 (2017).

[21] A. Lapin, J. Schmid, and M. Reuss, *Modeling the dynamics of E. coli populations in the three-dimensional turbulent field of a stirred-tank bioreactor—A structured–segregated approach,* Chemical Engineering Science **61**, 4783 (2006).

[22] R. Agren, L. Liu, S. Shoaie, W. Vongsangnak, I. Nookaew, and J. Nielsen, *The RAVEN Toolbox and Its Use for Generating a Genome-scale Metabolic Model for Penicillium chrysogenum,* PLoS Computational Biology **9**, e1002980 (2013).

[23] A. Lapin, D. Müller, and M. Reuss, *Dynamic Behavior of Microbial Populations in Stirred Bioreactors Simulated with Euler–Lagrange Methods: Traveling along the Lifelines of Single Cells,* Industrial & Engineering Chemistry Research **43**, 4647 (2004).

[24] X. Wang, J. Ding, W.-Q. Guo, and N.-Q. Ren, *A hydrodynamics–reaction kinetics coupled model for evaluating bioreactors derived from CFD simulation,* Bioresource Technology **101**, 9749 (2010).

[25] M. Laakkonen, P. Moilanen, V. Alopaeus, and J. Aittamaa, *Dynamic modeling of local reaction conditions in an agitated aerobic fermenter,* AIChE Journal **52**, 1673 (2006).

[26] M. Pigou and J. Morchain, *Investigating the interactions between physical and biological heterogeneities in bioreactors using compartment, population balance and metabolic models,* Chemical Engineering Science **126**, 267 (2014).

[27] J. Morchain, M. Pigou, and N. Lebaz, *A population balance model for bioreactors combining interdivision time distributions and micromixing concepts,* Biochemical Engineering Journal (2016), 10.1016/j.bej.2016.09.005.

[28] M. Pigou, J. Morchain, P. Fede, M.-I. Penet, and G. Laronze, *An assessment of methods of moments for the simulation of population dynamics in large-scale bioreactors,* Chemical Engineering Science **171**, 218 (2017).

[29] C. D. Rielly and A. J. Marquis, *A particle's eye view of crystallizer fluid mechanics,* Chemical Engineering Science **56**, 2475 (2001).

[30] A. Delafosse, S. Calvo, M.-L. Collignon, F. Delvigne, M. Crine, and D. Toye, *Euler–Lagrange approach to model heterogeneities in stirred tank bioreactors – Comparison to experimental flow characterization and particle tracking,* Chemical Engineering Science **134**, 457 (2015).

[31] C. Haringa, H. J. Noorman, and R. F. Mudde, *Lagrangian modeling of hydrodynamic–kinetic interactions in (bio)chemical reactors: Practical implementation and setup guidelines,* Chemical Engineering Science **157**, 159 (2017).

[32] Y. Liu, Z.-J. Wang, J.-y. Xia, C. Haringa, Y.-p. Liu, J. Chu, Y.-P. Zhuang, and S.-L. Zhang, *Application of Euler-Lagrange CFD for quantitative evaluating the effect of shear force on Carthamus tinctorius L. cell in a stirred tank bioreactor,* Biochemical Engineering Journal **114**, 209 (2016).

[33] M. Warmoeskerken and J. M. Smith, *Flooding of disc turbines in gas-liquid dispersions: A new description of the phenomenon,* Chemical Engineering Science **40**, 2063 (1985).

[34] H. Wu and G. Patterson, *Laser-Doppler measurements of turbulent-flow parameters in a stirred mixer,* Chemical Engineering Science **44**, 2207 (1989).

[35] A. Ducci and M. Yianneskis, *Direct determination of energy dissipation in stirred vessels with two-point LDA,* AIChE Journal **51**, 2133 (2005).

[36] N. G. Deen, T. Solberg, and B. H. Hjertager, *Flow Generated by an Aerated Rushton Impeller: Two-phase PIV Experiments and Numerical Simulations,* The Canadian Journal of Chemical Engineering **80**, 1 (2008).

[37] M. Laakkonen, P. Moilanen, T. Miettinen, K. Saari, M. Honkanen, P. Saarenrinne, and J. Aittamaa, *Local Bubble Size Distributions in Agitated Vessel,* Chemical Engineering Research and Design **83**, 50 (2005).

[38] M. Laakkonen, M. Honkanen, P. Saarenrinne, and J. Aittamaa, *Local bubble size distributions, gas–liquid interfacial areas and gas holdups in a stirred vessel with particle image velocimetry,* Chemical Engineering Journal **109**, 37 (2005).

[39] M. Barigou and M. Greaves, *Bubble-size distributions in a mechanically agitated gas—liquid contactor,* Chemical Engineering Science **47**, 2009 (1992).

[40] P. Vrábel, R. Van der Lans, Y. Cui, and K. Luyben, *Compartment Model Approach,* Chemical Engineering Research and Design **77**, 291 (1999).

[41] A. P. J. Sweere, J. R. Mesters, L. Janse, K. C. A. M. Luyben, and N. W. F. Kossen, *Experimental simulation of oxygen profiles and their influence on baker's yeast production: I. One-fermentor system,* Biotechnology and Bioengineering **31**, 567 (1988).

[42] H. T. B. Pham, G. Larsson, and S.-O. Enfors, *Growth and energy metabolism in aerobic fed-batch cultures ofSaccharomyces cerevisiae: Simulation and model verification,* Biotechnology and Bioengineering **60**, 474 (1998).

[43] P. Neubauer and S. Junne, *Scale-down simulators for metabolic analysis of large-scale bioprocesses.* Current opinion in biotechnology **21**, 114 (2010).

[44] L. P. de Jonge, N. A. A. Buijs, A. ten Pierick, A. Deshmukh, Z. Zhao, J. A. K. W. Kiel, J. J. Heijnen, and W. M. van Gulik, *Scale-down of penicillin production in Penicillium chrysogenum,* Biotechnology journal **6**, 944 (2011).

[45] C. Suarez-Mendez, A. Sousa, J. Heijnen, and A. Wahl, *Fast "Feast/Famine" Cycles for Studying Microbial Physiology Under Dynamic Conditions: A Case Study with Saccharomyces cerevisiae,* Metabolites **4**, 347 (2014).

[46] S. Reinecke, A. Deutschmann, K. Jobst, H. Kryk, E. Friedrich, and U. Hampel, *Flow following sensor particles—Validation and macro-mixing analysis in a stirred fermentation vessel with a highly viscous substrate,* Biochemical Engineering Journal **69**, 159 (2012).

[47] R. Takors, *Scale-up of microbial processes: impacts, tools and open questions.* Journal of biotechnology **160**, 3 (2012).

[48] G. Wang, W. Tang, J. Xia, J. Chu, H. J. Noorman, and W. M. van Gulik, *Integration of microbial kinetics and fluid dynamics toward model-driven scale-up of industrial bioprocesses,* Engineering in Life Sciences **15**, 20 (2015).

[49] A.-L. Heins, R. Lencastre Fernandes, K. V. Gernaey, and A. E. Lantz, *Experimental and in silico investigation of population heterogeneity in continuous Sachharomyces cerevisiae scale-down fermentation in a two-compartment setup,* Journal of Chemical Technology & Biotechnology **90**, 324 (2015).

[50] A. Lemoine, N. Maya Martinez-Iturralde, R. Spann, P. Neubauer, and S. Junne, *Response of Corynebacterium glutamicum exposed to oscillating cultivation conditions in a two- and a novel three-compartment scale-down bioreactor,,* Biotechnology and bioengineering **112**, 1220 (2015).

[51] S. George, G. Larsson, and S. O. Enfors, *A scale-down two-compartment reactor with controlled substrate oscillations: Metabolic response of Saccharomyces cerevisiae,* Bioprocess Engineering **9**, 249 (1993).

[52] A. P. J. Sweere, Y. A. Matla, J. Zandvliet, K. C. A. M. Luyben, and N. W. F. Kossen, *Experimental simulation of glucose fluctuations,* Applied Microbiology and Biotechnology **28**, 109 (1988).

[53] A. P. J. Sweere, L. Janse, K. C. A. M. Luyben, and N. W. F. Kossen, *Experimental simulation of oxygen profiles and their influence on baker's yeast production: II. Two-fermentor system,* Biotechnology and Bioengineering **31**, 579 (1988).

[54] F. Vardar and M. D. Lilly, *Effect of cycling dissolved oxygen concentrations on product formation in penicillin fermentations,* European Journal of Applied Microbiology and Biotechnology **14**, 203 (1982).

[55] M. H. Limberg, V. Pooth, W. Wiechert, and M. Oldiges, *Plug flow vs. stirred tank reactor flow characteristics in two compartment scale down bioreactor: Setup specific influence on the metabolic phenotype and bioprocess performance of Corynebacterium glutamicum,* Engineering in Life Sciences **16**, 610 (2016).

[56] G. Wang, J. Chu, H. J. Noorman, J. Xia, W. Tang, Y. Zhuang, and S. Zhang, *Prelude to rational scale-up of penicillin production: a scale-down study,* Applied microbiology and biotechnology **98**, 2359 (2014).

[57] S. B. Pope, *Turbulent Flows*, 11th ed. (Cambridge University Press, 2011).

[58] H. K. Versteeg and W. Malalasekera, *An introduction to Computational Fluid Dynamics - the finite volume method*, 2nd ed. (Longman Scientific and Technical, Essex, England, 2007).

[59] O. Gunyol and R. F. Mudde, *Computational Study of Hydrodynamics of a Standard Stirred Tank Reactor and a Large-Scale Multi-Impeller Fermenter,* International Journal for Multiscale Computational Engineering **7**, 559 (2009).

[60] H. Singh, D. F. Fletcher, and J. J. Nijdam, *An assessment of different turbulence models for predicting flow in a baffled tank stirred with a Rushton turbine,* Chemical Engineering Science **66**, 5976 (2011).

[61] J. Gimbun, C. Rielly, and Z. Nagy, *Modelling of mass transfer in gas–liquid stirred tanks agitated by Rushton turbine and CD-6 impeller: A scale-up study,* Chemical Engineering Research and Design **87**, 437 (2009).

[62] M. Coroneo, G. Montante, A. Paglianti, and F. Magelli, *CFD prediction of fluid flow and mixing in stirred tanks: Numerical issues about the RANS simulations,* Computers & Chemical Engineering **35**, 1959 (2011).

[63] *Turbulence,* in *ANSYS theory guide* (SAP IP, inc., Canonsburg, PA 15317, 2017) release 18 ed., Chap. 4.

[64] J. J. J. Gillissen and H. E. A. Van den Akker, *Direct numerical simulation of the turbulent flow in a baffled tank driven by a Rushton turbine,* AIChE Journal **58**, 3878 (2012).

[65] M. Jahoda, M. Moštěk, A. Kukuková, and V. Machoň, *CFD Modelling of Liquid Homogenization in Stirred Tanks with One and Two Impellers Using Large Eddy Simulation,* Chemical Engineering Research and Design **85**, 616 (2007).

[66] H. E. A. van den Akker, *Momentum equations in dispersed two-phase flows,* in *Encyclopedia of Fluid Mechanics* (Gulf publishing company, 1986).

[67] D. A. Drew, *Mathematical Modeling of Two-Phase Flow,* Annual Review of Fluid Mechanics **15**, 261 (1983).

[68] J. Wutz, A. Lapin, F. Siebler, J. E. Schäfer, T. Wucherpfennig, M. Berger, and R. Takors, *Predictability of $k_L a$ in stirred tank reactors under multiple operating conditions using an Euler-Lagrange approach,* Engineering in Life Sciences **16**, 633 (2016).

[69] C. Witz, D. Treffer, T. Hardiman, and J. Khinast, *Local gas holdup simulation and validation of industrial-scale aerated bioreactors,* Chemical Engineering Science **152**, 636 (2016).

[70] J. O. Hinze, *Fundamentals of the hydrodynamic mechanism of splitting in dispersion processes,* AIChE Journal **1**, 289 (1955).

[71] M. Sommerfeld, B. van Wachem, and R. Oliemans, *Best practice guidelines for multiphase flows*, 1st ed. (ERCOFTAC, 2008).

[72] H. Van den Akker, *Mesoscale Flow Structures and Fluid-Particle Interactions,* in *Mesoscale Modeling in Chemical Engineering Part I*, Advances in Chemical Engineering, Vol. 46, edited by G. B. Marin and J. Li (Elsevier Science, 2015) Chap. 6, pp. 281–354.

[73] M. Ishii and N. Zuber, *Drag coefficient and relative velocity in bubbly, droplet or particulate flows,* AIChE Journal **25**, 843 (1979).

[74] J. Richardson and W. Zaki, *The sedimentation of a suspension of uniform spheres under conditions of viscous flow,* Chemical Engineering Science **3**, 65 (1954).

[75] N. Kolev, *Multiphase flow dynamics, vol. 2 thermal and mechanical interactions* (Springer, Berlin, New York, Tokyo, 2007).

[76] V. P. Carey, *Liquid Vapor Phase Change Phenomena: An Introduction to the Thermophysics of Vaporization and Condensation Processes in Heat Transfer Equipment*, 2nd ed. (CRC Press, 2007).

[77] H. Luo and H. F. Svendsen, *Theoretical model for drop and bubble breakup in turbulent dispersions,* AIChE Journal **42**, 1225 (1996).

[78] T. Wang, J. Wang, and Y. Jin, *Population Balance Model for Gas–Liquid Flows: Influence of Bubble Coalescence and Breakup Models,* Industrial & Engineering Chemistry Research **44**, 7540 (2005).

[79] M. J. Prince and H. W. Blanch, *Bubble coalescence and break-up in air-sparged bubble columns,* AIChE Journal **36**, 1485 (1990).

[80] F. Lehr, M. Millies, and D. Mewes, *Bubble-Size distributions and flow fields in bubble columns,* AIChE Journal **48**, 2426 (2002).

[81] J. Sanyal, D. L. Marchisio, R. O. Fox, and K. Dhanasekharan, *On the Comparison between Population Balance Models for CFD Simulation of Bubble Columns,* Industrial & Engineering Chemistry Research **44**, 5063 (2005).

[82] A. Buffo, M. Vanni, and D. Marchisio, *Multidimensional population balance model for the simulation of turbulent gas–liquid systems in stirred tank reactors,* Chemical Engineering Science **70**, 31 (2012).

[83] A. Buffo and D. L. Marchisio, *Modeling and simulation of turbulent polydisperse gas-liquid systems via the generalized population balance equation,* Reviews in Chemical Engineering **30**, 73 (2014).

[84] O. Gunyol, H. J. Noorman, and R. F. Mudde, *CFD simulations of a large-scale fermenter with muliple impellers,* in *Proceedings of the 9th International Conference on Gas-Liquid Solid Reactor Engineering*, edited by P. Chaouki, J., Tanguy (Montreal, 2009) pp. 1–4.

[85] M. Petitti, A. Nasuti, D. L. Marchisio, M. Vanni, G. Baldi, N. Mancini, and F. Podenzani, *Bubble size distribution modeling in stirred gas-liquid reactors with QMOM augmented by a new correction algorithm,* AIChE Journal **56**, 36 (2010).

[86] P. Harvey and M. Greaves, *Turbulent flow in an agitated vessel,* Chemical Engineering Research and Design **60a**, 195 (1982).

[87] J. Middleton, F. Pierce, and P. Lynch, *Computations of flow fields and complex reaction yield in turbulent stirred reactors and comparison with experimental data,* Chemical Engineering Research and Design **64**, 18 (1986).

[88] A. Bakker and H. E. A. Van den Akker, *Single-phase flow in stirred reactors,* Chemical Engineering Research and Design **72**, 583 (1994).

[89] V. Ranade, J. Joshi, and A. Marathe, *flow generated by pitched blade turbines II: simulation using k-e model,* Chemical Engineering Communications **81**, 225 (1989).

[90] J. Luo and A. Gosman, *Prediction of impeller-induced flow in mixing vessels using multiple frames of reference,* Institute of chemical engineers, symposium series (1994).

[91] J. Murthy, S. Mathur, and D. Choudhury, *CFD simulation of flows in stirred tank reactors using a sliding mesh technique,* Institution of Chemical Engineers Symposium Series **136**, 341 (1994).

[92] A. Brucato, M. Ciofalo, F. Grisafi, and G. Micale, *Numerical prediction of flow fields in baffled stirred vessels: A comparison of alternative modelling approaches,* Chemical Engineering Science **53**, 3653 (1998).

[93] V. Ranade and H. Van den Akker, *A computational snapshot of gas—liquid flow in baffled stirred reactors,* Chemical Engineering Science **49**, 5175 (1994).

[94] P. R. Gogate, A. A. Beenackers, and A. B. Pandit, *Multiple-impeller systems with a special emphasis on bioreactors: a critical review,* Biochemical Engineering Journal **6**, 109 (2000).

[95] K. Ng, N. Fentiman, K. Lee, and M. Yianneskis, *Assessment of Sliding Mesh CFD Predictions and LDA Measurements of the Flow in a Tank Stirred by a Rushton Impeller,* Chemical Engineering Research and Design **76**, 737 (1998).

[96] K. Ng and M. Yianneskis, *Observations on the Distribution of Energy Dissipation in Stirred Vessels,* Chemical Engineering Research and Design **78**, 334 (2000).

[97] B. Murthy and J. Joshi, *Assessment of standard , RSM and LES turbulence models in a baffled stirred vessel agitated by various impeller designs,* Chemical Engineering Science **63**, 5468 (2008).

[98] M. Schäfer, M. Höfken, and F. Durst, *Detailed LDV Measurements for Visualization of the Flow Field Within a Stirred-Tank Reactor Equipped with a Rushton Turbine,* Chemical Engineering Research and Design **75**, 729 (1997).

[99] B. C. Venneker, J. J. Derksen, and H. E. Van den Akker, *Turbulent flow of shear-thinning liquids in stirred tanks—The effects of Reynolds number and flow index,* Chemical Engineering Research and Design **88**, 827 (2010).

[100] K. C. Lee and M. Yianneskis, *Turbulence properties of the impeller stream of a Rushton turbine,* AIChE Journal **44**, 13 (1998).

[101] J. Derksen *, M. Doelman, and H. Van den Akker, *Three-dimensional LDA measurements in the impeller region of a turbulently stirred tank,* Experiments in Fluids **27**, 522 (1999).

[102] A. Khopkar, J. Aubin, C. Rubio-Atoche, C. Xuereb, N. Le Sauze, J. Bertrand, and V. V. Ranade, *Flow Generated by Radial Flow Impellers: PIV Measurements and CFD Simulations,* International Journal of Chemical Reactor Engineering **2** (2004), 10.2202/1542-6580.1146.

[103] V. Ranade, M. Perrard, N. Le Sauze, C. Xuereb, and J. Bertrand, *Trailing Vortices of Rushton Turbine: PIV Measurements and CFD Simulations with Snapshot Approach,* Chemical Engineering Research and Design **79**, 3 (2001).

[104] R. Escudié and A. Liné, *Experimental analysis of hydrodynamics in a radially agitated tank,* AIChE Journal **49**, 585 (2003).

[105] R. Escudié, D. Bouyer, and A. Liné, *Characterization of trailing vortices generated by a Rushton turbine,* AIChE Journal **50**, 75 (2004).

[106] S. Baldi and M. Yianneskis, *On the quantification of energy dissipation in the impeller stream of a stirred vessel from fluctuating velocity gradient measurements,* Chemical Engineering Science **59**, 2659 (2004).

[107] S. Baldi, A. Ducci, and M. Yianneskis, *Determination of Dissipation Rate in Stirred Vessels Through Direct Measurement of Fluctuating Velocity Gradients,* Chemical Engineering & Technology **27**, 275 (2004).

[108] A. Liné, J.-C. Gabelle, J. Morchain, D. Anne-Archard, and F. Augier, *On POD analysis of PIV measurements applied to mixing in a stirred vessel with a shear thinning fluid,* Chemical Engineering Research and Design **91**, 2073 (2013).

[109] H. Hartmann, J. Derksen, C. Montavon, J. Pearson, I. Hamill, and H. van den Akker, *Assessment of large eddy and RANS stirred tank simulations by means of LDA,* Chemical Engineering Science **59**, 2419 (2004).

[110] K. Rutherford, K. C. Lee, S. M. S. Mahmoudi, and M. Yianneskis, *Hydrodynamic characteristics of dual Rushton impeller stirred vessels,* AIChE Journal **42**, 332 (1996).

[111] V. P. Mishra and J. B. Joshi, *Flow generated by a disc turbuine: Part IV: Multiple impellers,* Chemical Engineering Research and Design **72**, 657 (1994).

[112] A. Delafosse, M.-L. Collignon, S. Calvo, F. Delvigne, M. Crine, P. Thonart, and D. Toye, *CFD-based compartment model for description of mixing in bioreactors,* Chemical Engineering Science **106**, 76 (2014).

[113] G. Micale, A. Brucato, F. Grisafi, and M. Ciofalo, *Prediction of flow fields in a dual-impeller stirred vessel,* AIChE Journal **45**, 445 (1999).

[114] V. Roussinova, S. M. Kresta, and R. Weetman, *Low frequency macroinstabilities in a stirred tank: scale-up and prediction based on large eddy simulations,* Chemical Engineering Science **58**, 2297 (2003).

[115] L. Nikiforaki, J. Yu, S. Baldi, B. Genenger, K. Lee, F. Durst, and M. Yianneskis, *On the variation of precessional flow instabilities with operational parameters in stirred vessels,* Chemical Engineering Journal **102**, 217 (2004).

[116] L. Nikiforaki, G. Montante, K. Lee, and M. Yianneskis, *On the origin, frequency and magnitude of macro-instabilities of the flows in stirred vessels,* Chemical Engineering Science **58**, 2937 (2003).

[117] A. Paglianti, G. Montante, and F. Magelli, *Novel experiments and a mechanistic model for macroinstabilities in stirred tanks,* AIChE Journal **52**, 426 (2006).

[118] A. Paglianti, Z. Liu, G. Montante, and F. Magelli, *Effect of Macroinstabilities in Single- and Multiple-Impeller Stirred Tanks,* Industrial & Engineering Chemistry Research **47**, 4944 (2008).

[119] F. Guillard, C. Trägårdh, and L. Fuchs, *A study of turbulent mixing in a turbine-agitated tank using a fluorescence technique,* Experiments in Fluids **28**, 225 (2000).

[120] F. Guillard, C. Trägårdh, and L. Fuchs, *New image analysis methods for the study of mixing patterns in stirred tanks,* The Canadian Journal of Chemical Engineering **78**, 273 (2000).

[121] B. Zakrzewska and Z. Jaworski, *CFD Modeling of Turbulent Jacket Heat Transfer in a Rushton Turbine Stirred Vessel,* Chemical Engineering & Technology **27**, 237 (2004).

[122] M. Ammar, W. Chtourou, Z. Driss, and M. Abid, *Numerical investigation of turbulent flow generated in baffled stirred vessels equipped with three different turbines in one and two-stage system,* Energy **36**, 5081 (2011).

[123] G. L. Lane, M. P. Schwarz, and G. M. Evans, *Comparison of CFD methods for modeling stirred tanks,* in *Proc. 10th European conference on mixing (Delft))*, Vol. 5805 (Elsevier, 2000).

[124] M. Jenne and M. Reuss, *A critical assessment on the use of $k-\epsilon$ turbulence models for simulation of the turbulent liquid flow induced by a Rushton-turbine in baffled stirred-tank reactors,* Chemical Engineering Science **54**, 3921 (1999).

[125] J. Revstedt, L. Fuchs, and C. Trägårdh, *Large eddy simulations of the turbulent flow in a stirred reactor,* Chemical Engineering Science **53**, 4041 (1998).

[126] S. Yeoh, G. Papadakis, and M. Yianneskis, *Numerical Simulation of Turbulent Flow Characteristics in a Stirred Vessel Using the LES and RANS Approaches with the Sliding/Deforming Mesh Methodology,* Chemical Engineering Research and Design **82**, 834 (2004).

[127] S. Yeoh, G. Papadakis, and M. Yianneskis, *Determination of mixing time and degree of homogeneity in stirred vessels with large eddy simulation,* Chemical Engineering Science **60**, 2293 (2005).

[128] Y. ZHANG, C. YANG, and Z. MAO, *Large Eddy Simulation of Liquid Flow in a Stirred Tank with Improved Inner-Outer Iterative Algorithm,* Chinese Journal of Chemical Engineering **14**, 321 (2006).

[129] J. G. M. Eggels, *Direct and large-eddy simulation of turbulent fluid flow using the lattice-Boltzmann scheme,* International Journal of Heat and Fluid Flow **17**, 307 (1996).

[130] J. Derksen and H. E. A. Van den Akker, *Large eddy simulations on the flow driven by a Rushton turbine,* AIChE Journal **45**, 209 (1999).

[131] M. Micheletti, S. Baldi, S. Yeoh, A. Ducci, G. Papadakis, K. Lee, and M. Yianneskis, *On Spatial and Temporal Variations and Estimates of Energy Dissipation in Stirred Reactors,* Chemical Engineering Research and Design **82**, 1188 (2004).

[132] A. Delafosse, A. Liné, J. Morchain, and P. Guiraud, *LES and URANS simulations of hydrodynamics in mixing tank: Comparison to PIV experiments,* Chemical Engineering Research and Design **86**, 1322 (2008).

[133] A. Delafosse, J. Morchain, P. Guiraud, and A. Liné, *Trailing vortices generated by a Rushton turbine: Assessment of URANS and large Eddy simulations,* Chemical Engineering Research and Design **87**, 401 (2009).

[134] M. Soos, R. Kaufmann, R. Winteler, M. Kroupa, and B. Lüthi, *Determination of maximum turbulent energy dissipation rate generated by a rushton impeller through large eddy simulation,* AIChE Journal **59**, 3642 (2013).

[135] J. Gimbun, C. D. Rielly, Z. K. Nagy, and J. J. Derksen, *Detached eddy simulation on the turbulent flow in a stirred tank,* AIChE Journal **58**, 3224 (2012).

[136] Z. Chara, B. Kysela, J. Konfrst, and I. Fort, *Study of fluid flow in baffled vessels stirred by a Rushton standard impeller,* Applied Mathematics and Computation **272**, 614 (2016).

[137] G. Lane, *Predicting the energy dissipation rate in a mechanically stirred tank,* in *Eleventh International Conference on CFD in the Minerals and Process Industries* (CSIRO Australia, Melbourne, Australia, 2015).

[138] A. Kukuková, M. Moštěk, M. Jahoda, and V. Machoň, *CFD Prediction of Flow and Homogenization in a Stirred Vessel: Part I Vessel with One and Two Impellers,* Chemical Engineering & Technology **28**, 1125 (2005).

[139] W. Bujalski, Z. Jaworski, and A. Nienow, *CFD Study of Homogenization with Dual Rushton Turbines—Comparison with Experimental Results,* Chemical Engineering Research and Design **80**, 97 (2002).

[140] J. Bujalski, Z. Jaworski, W. Bujalski, and A. Nienow, *The Influence of the Addition Position of a Tracer on CFD Simulated Mixing Times in a Vessel Agitated by a Rushton Turbine,* Chemical Engineering Research and Design **80**, 824 (2002).

[141] W. Bujalski, Z. Jaworski, and A. Nienow, *CFD Study of Homogenization with Dual Rushton Turbines—Comparison with Experimental Results: Part II: The Multiple Reference Frame,* Chemical Engineering Research and Design **80**, 97 (2002).

[142] Z. Jaworski, W. Bujalski, N. Otomo, and A. Nienow, *CFD Study of Homogenization with Dual Rushton Turbines—Comparison with Experimental Results,* Chemical Engineering Research and Design **78**, 327 (2000).

[143] Z. Jaworski, W. Bujalski, N. Otomo, and A. Nienow, *CFD Study of Homogenization with Dual Rushton Turbines—Comparison with Experimental Results: Part I: Initial Studies,* Chemical Engineering Research and Design **78**, 327 (2000).

[144] F. Magelli, G. Montante, D. Pinelli, and A. Paglianti, *Mixing time in high aspect ratio vessels stirred with multiple impellers,* Chemical Engineering Science **101**, 712 (2013).

[145] K. Javed, T. Mahmud, and J. Zhu, *Numerical simulation of turbulent batch mixing in a vessel agitated by a Rushton turbine,* Chemical Engineering and Processing: Process Intensification **45**, 99 (2006).

[146] M. F. W. Distelhoff, A. J. Marquis, J. M. Nouri, and J. H. Whitelaw, *Scalar mixing measurements in batch operated stirred tanks,* The Canadian Journal of Chemical Engineering **75**, 641 (1997).

[147] A. Kukuková, B. Noël, S. M. Kresta, and J. Aubin, *Impact of sampling method and scale on the measurement of mixing and the coefficient of variance,* AIChE Journal **54**, 3068 (2008).

[148] A. Kukuková, J. Aubin, and S. M. Kresta, *A new definition of mixing and segregation: Three dimensions of a key process variable,* Chemical Engineering Research and Design **87**, 633 (2009).

[149] H. Hartmann, J. J. Derksen, and H. E. A. van den Akker, *Mixing times in a turbulent stirred tank by means of LES,* AIChE Journal **52**, 3696 (2006).

[150] M. Moo-Young, K. Tichar, and F. A. L. Dullien, *The blending efficiencies of some impellers in batch mixing,* AIChE Journal **18**, 178 (1972).

[151] K. Lee and M. Yianneskis, *A Liquid Crystal Thermographic Technique for the Measurement of Mixing Characteristics in Stirred Vessels,* Chemical Engineering Research and Design **75**, 746 (1997).

[152] A. Nienow, *On impeller circulation and mixing effectiveness in the turbulent flow regime,* Chemical Engineering Science **52**, 2557 (1997).

[153] K. S. M. S. Raghav Rao and J. B. Joshi, *liquid phase mixing in mechanically agitated vessels,* Chemical Engineering Communications **74**, 1 (1988).

[154] V. Rewatkar and J. B. Joshi, *Effect of impeller design on liquid phase mixing in mechanically agitated reactors,* Chemical Engineering Communications **102**, 1 (1991).

[155] N. K. Nere, A. W. Patwardhan, and J. B. Joshi, *Liquid-Phase Mixing in Stirred Vessels: Turbulent Flow Regime,* Industrial & Engineering Chemistry Research **42**, 2261 (2003).

[156] R. Zadghaffari, J. Moghaddas, and J. Revstedt, *Large-eddy simulation of turbulent flow in a stirred tank driven by a Rushton turbine,* Computers & Fluids **39**, 1183 (2010).

[157] R. Zadghaffari, J. Moghaddas, and J. Revstedt, *A mixing study in a double-Rushton stirred tank,* Computers & Chemical Engineering **33**, 1240 (2009).

[158] M. Jahoda and V. Machoň, *Homogenization of liquids in tanks stirred by multiple impellers,* Chemical Engineering & Technology **17**, 95 (1994).

[159] M. Moštěk, A. Kukuková, M. Jahoda, and V. Machoň, *CFD Prediction of Flow and Homogenization in a Stirred Vessel: Part II Vessel with Three and Four Impellers,* Chemical Engineering & Technology **28**, 1134 (2005).

[160] G. Montante, M. Moštěk, M. Jahoda, and F. Magelli, *CFD simulations and experimental validation of homogenisation curves and mixing time in stirred Newtonian and pseudoplastic liquids,* Chemical Engineering Science **60**, 2427 (2005).

[161] Y. Tominaga and T. Stathopoulos, *Turbulent Schmidt numbers for CFD analysis with various types of flowfield,* Atmospheric Environment **41**, 8091 (2007).

[162] A. R. Khopkar and V. V. Ranade, *CFD simulation of gas–liquid stirred vessel: VC, S33, and L33 flow regimes,* AIChE Journal **52**, 1654 (2006).

[163] A. W. Nienow and M. D. Lilly, *Power drawn by multiple impellers in sparged agitated vessels,* Biotechnology and Bioengineering **21**, 2341 (1979).

[164] F. Saito, A. W. Nienow, S. Chatwin, and I. P. T. Moore, *Power, gas dispersion and homogenisation characteristics of Scaba SRGT and rushton turbine impellers*. Journal of chemical engineering of Japan **25**, 281 (1992).

[165] D. Hari-Prajitno, V. P. Mishra, K. Takenaka, W. Bujalski, A. W. Nienow, and J. Mckemmie, *Gas-liquid mixing studies with multiple up- and down-pumping hydrofoil impellers: Power characteristics and mixing time,* The Canadian Journal of Chemical Engineering **76**, 1056 (1998).

[166] B. H. Junker, M. Stanik, C. Barna, P. Salmon, E. Paul, and B. C. Buckland, *Influence of impeller type on power input in fermentation vessels,* Bioprocess Engineering **18**, 401 (1998).

[167] A. Bakker, J. M. Smith, and K. J. Myers, *How to disperse gases in liquids,* Chemical engineering **101**, 98 (1994).

[168] N. Otomo, W. Bujalski, A. W. Nienow, and K. Takahashi, *Gas Dispersion Characteristics of Newly Developed Impellers in a Stirred Vessel.* Journal of chemical engineering of Japan **36**, 166 (2003).

[169] R. G. van der Lans and K. van 't Riet, *Mixing in bioreactor vessels,* in *Comprehensive Biotechnology Volume 2: Engineering Fundamentals of Biotechnology*, edited by M. Moo-Young (Elsevier, Amsterdam, 2011) 2nd ed., Chap. 2.07, pp. 63–80.

[170] M. Jafari and J. Soltan Mohammadzadeh, *Mixing Time, Homogenization Energy and Residence Time Distribution in a Gas-Induced Contactor,* Chemical Engineering Research and Design **83**, 452 (2005).

[171] M. Wang, A. Dorward, D. Vlaev, and R. Mann, *Measurements of gas–liquid mixing in a stirred vessel using electrical resistance tomography (ERT),* Chemical Engineering Journal **77**, 93 (2000).

[172] V. Machon and M. Jahoda, *Liquid Homogenization in Aerated Multi-Impeller Stirred Vessel,* Chemical Engineering & Technology **23**, 869 (2000).

[173] G. Montante and A. Paglianti, *Gas hold-up distribution and mixing time in gas–liquid stirred tanks,* Chemical Engineering Journal **279**, 648 (2015).

[174] N. Otomo, W. Bujalski, A. W. Nienow, and K. Takahashi, *A Novel Measurement Technique for Mixing Time in an Aerated Stirred Vessel,* Journal of chemical engineering of Japan **36**, 66 (2003).

[175] D. Hadjiev, N. E. Sabiri, and A. Zanati, *Mixing time in bioreactors under aerated conditions,* Biochemical Engineering Journal **27**, 323 (2006).

[176] F. Guillard and C. Trägårdh, *Mixing in industrial Rushton turbine-agitated reactors under aerated conditions,* Chemical Engineering and Processing: Process Intensification **42**, 373 (2003).

[177] M. Bouaifi and M. Roustan, *Bubble size and mass transfer coefficients in dual-impeller agitated reactors,* The Canadian Journal of Chemical Engineering **76**, 390 (1998).

[178] M. Bouaifi, G. Hebrard, D. Bastoul, and M. Roustan, *A comparative study of gas hold-up, bubble size, interfacial area and mass transfer coefficients in stirred gas–liquid reactors and bubble columns,* Chemical Engineering and Processing: Process Intensification **40**, 97 (2001).

[179] F. Garcia-Ochoa and E. Gomez, *Theoretical prediction of gas–liquid mass transfer coefficient, specific area and hold-up in sparged stirred tanks,* Chemical Engineering Science **59**, 2489 (2004).

[180] F. Garcia-Ochoa and E. Gomez, *Prediction of gas-liquid mass transfer coefficient in sparged stirred tank bioreactors.* Biotechnology and bioengineering **92**, 761 (2005).

[181] F. Garcia-Ochoa and E. Gomez, *Bioreactor scale-up and oxygen transfer rate in microbial processes: an overview.* Biotechnology advances **27**, 153 (2009).

[182] M. Martín, F. J. Montes, and M. A. Galán, *Mass transfer rates from bubbles in stirred tanks operating with viscous fluids,* Chemical Engineering Science **65**, 3814 (2010).

[183] M. Martín, F. J. Montes, and M. A. Galán, *Bubbling process in stirred tank reactors II: Agitator effect on the mass transfer rates,* Chemical Engineering Science **63**, 3223 (2008).

[184] V. Linek, M. Kordač, and T. Moucha, *Mechanism of mass transfer from bubbles in dispersions: Part II: Mass transfer coefficients in stirred gas–liquid reactor and bubble column,* Chemical Engineering and Processing: Process Intensification **44**, 121 (2005).

[185] S. S. Alves, J. M. Vasconcelos, and S. P. Orvalho, *Mass transfer to clean bubbles at low turbulent energy dissipation,* (2006).

[186] R. Higbie, *The rate of absorption of a pure gas into still liquid during short periods of exposure,* (1935).

[187] P. V. Danckwerts, *Significance of Liquid-Film Coefficients in Gas Absorption,* Industrial & Engineering Chemistry **43**, 1460 (1951).

[188] J. C. Lamont and D. S. Scott, *An eddy cell model of mass transfer into the surface of a turbulent liquid,* AIChE Journal **16**, 513 (1970).

[189] S. Alves, C. Maia, J. Vasconcelos, and A. Serralheiro, *Bubble size in aerated stirred tanks,* Chemical Engineering Journal **89**, 109 (2002).

[190] D. Qian, J. B. Mclaughlin, K. Sankaranarayanan, S. Sundaresan, and K. Kontomaris, *Simulation of Bubble Breakup Dynamics in Homogeneous Turbulence,* Chem. Eng. Comm. **193**, 1038 (2006).

[191] A. R. Khopkar, J. Aubin, C. Xuereb, N. Le Sauze, J. Bertrand, and V. V. Ranade, *Gas - Liquid Flow Generated by a Pitched-Blade Turbine: Particle Image Velocimetry Measurements and Computational Fluid Dynamics Simulations,* Industrial & Engineering Chemistry Research **42**, 5318 (2003).

[192] F. Scargiali, A. D'Orazio, F. Grisafi, and A. Brucato, *Modelling and Simulation of Gas–Liquid Hydrodynamics in Mechanically Stirred Tanks,* Chemical Engineering Research and Design **85**, 637 (2007).

[193] L. Schiller and Z. Naumann, *A drag coefficient correlation,* Z. Ver. Deutsch. Ing **77**, 318 (1935).

[194] S. Balachandar and J. K. Eaton, *Turbulent Dispersed Multiphase Flow,* Annual Review of Fluid Mechanics **42**, 111 (2010).

[195] A. Brucato, F. Grisafi, and G. Montante, *Particle drag coefficients in turbulent fluids,* Chemical Engineering Science **53**, 3295 (1998).

[196] A. Bakker and H. E. A. Van den Akker, *A computational model for the gas-liquid flow in stirred reactors,* Chemical Engineering Research and Design **72**, 573 (1994).

[197] G. Lane, M. Schwarz, and G. Evans, *Numerical modelling of gas–liquid flow in stirred tanks,* Chemical Engineering Science **60**, 2203 (2005).

[198] A. Khopkar, A. Rammohan, V. Ranade, and M. Dudukovic, *Gas–liquid flow generated by a Rushton turbine in stirred vessel: CARPT/CT measurements and CFD simulations,* Chemical Engineering Science **60**, 2215 (2005).

[199] Y. Sato and K. Sekoguchi, *Liquid velocity distribution in two-phase bubble flow,* International Journal of Multiphase Flow **2**, 79 (1975).

[200] M. Karimi, G. Akdogan, K. H. Dellimore, and S. M. Bradshaw, *Comparison of different drag coefficient correlations in the CFD modeling of a laboratory-scale rushton-turbine flotation tank,* in *Ninth International Conference on CFD in the Minerals and Process Industries* (CSIRO Australia, Melbourne, Australia, 2012).

[201] R. Newell and S. Grano, *Hydrodynamics and scale up in Rushton turbine flotation cells: Part 2. Flotation scale-up for laboratory and pilot cells,* International Journal of Mineral Processing **81**, 65 (2006).

[202] R. Newell and S. Grano, *Hydrodynamics and scale up in Rushton turbine flotation cells: Part 1 — Cell hydrodynamics,* International Journal of Mineral Processing **81**, 224 (2007).

[203] G. Montante, A. Paglianti, and F. Magelli, *Experimental Analysis and Computational Modelling of Gas–Liquid Stirred Vessels,* Chemical Engineering Research and Design **85**, 647 (2007).

[204] M. Petitti, D. L. Marchisio, M. Vanni, G. Baldi, N. Mancini, and F. Podenzani, *Effect of drag modeling on the prediction of critical regime transitions in agitated gas-liquid reactors with bubble size distribution modeling,* Multiphase Science and Technology **21**, 95 (2009).

[205] B. C. H. Venneker, J. J. Derksen, and H. E. A. Van den Akker, *Population balance modeling of aerated stirred vessels based on CFD,* AIChE Journal **48**, 673 (2002).

[206] P. Chen, J. Sanyal, and M. Dudukovic, *CFD modeling of bubble columns flows: implementation of population balance,* Chemical Engineering Science **59**, 5201 (2004).

[207] T. Wang, J. Wang, and Y. Jin, *A novel theoretical breakup kernel function for bubbles/droplets in a turbulent flow,* Chemical Engineering Science **58**, 4629 (2003).

[208] T. Wang, J. Wang, and Y. Jin, *A CFD-PBM coupled model for gas-liquid flows,* AIChE Journal **52**, 125 (2006).

[209] T. Wang, J. Wang, and Y. Jin, *Theoretical prediction of flow regime transition in bubble columns by the population balance model,* Chemical Engineering Science **60**, 6199 (2005).

[210] M. Laakkonen, V. Alopaeus, and J. Aittamaa, *Validation of bubble breakage, coalescence and mass transfer models for gas–liquid dispersion in agitated vessel,* Chemical Engineering Science **61**, 218 (2006).

[211] M. Laakkonen, P. Moilanen, V. Alopaeus, and J. Aittamaa, *Modelling local bubble size distributions in agitated vessels,* Chemical Engineering Science **62**, 721 (2007).

[212] P. Moilanen, M. Laakkonen, O. Visuri, and J. Aittamaa, *Modeling Local Gas - Liquid Mass Transfer in Agitated Viscous Shear-Thinning Dispersions with CFD,* Industrial & Engineering Chemistry Research **46**, 7289 (2007).

[213] A. Tzounakos, D. G. Karamanev, A. Margaritis, and M. A. Bergougnou, *Effect of the Surfactant Concentration on the Rise of Gas Bubbles in Power-Law Non-Newtonian Liquids,* Industrial & Engineering Chemistry Research **43**, 5790 (2004).

[214] Z. Kálal, M. Jahoda, and I. Fořt, *CFD Prediction of Gas-Liquid Flow in an Aerated Stirred Vessel Using the Population Balance Model,* Chemical and Process Engineering **35**, 55 (2014).

[215] G. Montante, D. Horn, and A. Paglianti, *Gas–liquid flow and bubble size distribution in stirred tanks,* Chemical Engineering Science **63**, 2107 (2008).

[216] Y.-J. Liu, W. Li, L.-C. Han, Y. Cao, H.-a. Luo, M. Al-Dahhan, and M. Dudukovic, *γ-CT measurement and CFD simulation of cross section gas holdup distribution in a gas–liquid stirred standard Rushton tank,* Chemical Engineering Science **66**, 3721 (2011).

[217] J. Sarkar, L. K. Shekhawat, V. Loomba, and A. S. Rathore, *CFD of mixing of multi-phase flow in a bioreactor using population balance model,* Biotechnology Progress **32**, 613 (2016).

[218] Y. Zhang, C. Yang, and Z.-S. Mao, *Large eddy simulation of the gas–liquid flow in a stirred tank,* AIChE Journal **54**, 1963 (2008).

[219] A. Dehbi, *A CFD model for particle dispersion in turbulent boundary layer flows,* Nuclear Engineering and Design **238**, 707 (2008).

[220] A. Dehbi, *Turbulent particle dispersion in arbitrary wall-bounded geometries: A coupled CFD-Langevin-equation based approach,* International Journal of Multiphase Flow **34**, 819 (2008).

[221] M. Jahoda, L. Tomášková, and M. Moštěk, *CFD prediction of liquid homogenisation in a gas–liquid stirred tank,* Chemical Engineering Research and Design **87**, 460 (2009).

[222] J. Monod, *The growth of bacterial cultures,* Ann. Rev. Microbiol **3**, 371 (1949).

[223] J. J. Heijnen and B. Romein, *Derivation of kinetic equations for growth on single substrates based on general properties of a simple metabolic network,* Biotechnology Progress **11**, 712 (1995).

[224] H. Van Urk, E. Postma, W. A. Scheffers, and J. P. Van Dijken, *Glucose Transport in Crabtree-positive and Crabtree-negative Yeasts,* Microbiology **135**, 2399 (1989).

[225] J. C. du Preez, S. H. de Kock, S. G. Kilian, and D. Litthauer, *The relationship between transport kinetics and glucose uptake by Saccharomyces cerevisiae in aerobic chemostat cultures,* Antonie van Leeuwenhoek **77**, 379 (2000).

[226] W. Tang, A. T. Deshmukh, C. Haringa, G. Wang, W. van Gulik, W. van Winden, M. Reuss, J. J. Heijnen, J. Xia, J. Chu, and H. J. Noorman, *A 9-pool metabolic structured kinetic model describing days to seconds dynamics of growth and product formation by Penicillium chrysogenum,* Biotechnology and Bioengineering **114**, 1733 (2017).

[227] E. Postma, W. Alexander Scheffers, and J. P. Van Dijken, *Kinetics of growth and glucose transport in glucose-limited chemostat cultures ofSaccharomyces cerevisiae CBS 8066,* Yeast **5**, 159 (1989).

[228] E. Postma, C. Verduyn, W. A. Scheffers, and J. P. Van Dijken, *Enzymic analysis of the crabtree effect in glucose-limited chemostat cultures of Saccharomyces cerevisiae.* Applied and environmental microbiology **55**, 468 (1989).

[229] A. T. Deshmukh, *Elucidation and modeling of the in-vivo kinetics of enzymes and membrane transporters associated with beta-lactam and non-ribosomal peptide production in P. Chrysogenum*, Phd thesis, Delft university of Technology (2013).

[230] A. T. Deshmukh, P. J. Verheijen, R. Maleki Seifar, J. J. Heijnen, and W. M. van Gulik, *In vivo kinetic analysis of the penicillin biosynthesis pathway using PAA stimulus response experiments,* Metabolic Engineering **32**, 155 (2015).

[231] R. D. Douma, A. T. Deshmukh, L. P. de Jonge, B. W. de Jong, R. M. Seifar, J. J. Heijnen, and W. M. van Gulik, *Novel insights in transport mechanisms and kinetics of phenylacetic acid and penicillin-G in Penicillium chrysogenum.* Biotechnology progress **28**, 337 (2011).

[232] W. M. van Gulik, M. R. Antoniewicz, W. T. A. M. DeLaat, J. L. Vinke, and J. J. Heijnen, *Energetics of growth and penicillin production in a high-producing strain ofPenicillium chrysogenum,* Biotechnology & Bioengineering **72**, 185 (2001).

[233] W. M. van Gulik, W. T. A. M. de Laat, J. L. Vinke, and J. J. Heijnen, *Application of metabolic flux analysis for the identification of metabolic bottlenecks in the biosynthesis of penicillin-G,* Biotechnology and Bioengineering **68**, 602 (2000).

[234] U. Nasution, W. M. van Gulik, C. Ras, A. Proell, and J. J. Heijnen, *A metabolome study of the steady-state relation between central metabolism, amino acid biosynthesis and penicillin production in Penicillium chrysogenum,* Metabolic Engineering **10**, 10 (2008).

[235] R. J. Kleijn, F. Liu, W. A. van Winden, W. M. van Gulik, C. Ras, and J. J. Heijnen, *Cytosolic NADPH metabolism in penicillin-G producing and non-producing chemostat cultures of Penicillium chrysogenum,* Metabolic Engineering **9**, 112 (2007).

[236] R. D. Douma, P. J. T. Verheijen, W. T. A. M. de Laat, J. J. Heijnen, and W. M. van Gulik, *Dynamic gene expression regulation model for growth and penicillin production in Penicillium chrysogenum.* Biotechnology and bioengineering **106**, 608 (2010).

[237] P. de Noronha Pissara, J. Nielsen, and M. J. Bazin, *Pathway kinetics and metabolic control analysis of a high-yielding strain of Penicillium chrysogenum during fed batch cultivations,* Biotechnology and Bioengineering **51**, 168 (1996).

[238] Z. A. Bainbridge, R. I. Scott, and D. Perry, *Oxygen utilisation by isopenicillin n synthase from penicillium chrysogenum,* Journal of Chemical Technology & Biotechnology **55**, 233 (2007).

[239] G. Larsson and S.-O. Enfors, *Influence of oxygen starvation on the respiratory capacity of Penicillium chrysogenum,* Appl . Microbiol . Biotectnol. **21**, 228 (1985).

[240] G. Larsson and S. O. Enfors, *Studies of insufficient mixing in bioreactors: Effects of limiting oxygen concentrations and short term oxygen starvation on Penicillium chrysogenum,* Bioprocess Engineering **3**, 123 (1988).

[241] M. McIntyre, D. R. Berry, and B. McNeil, *Response of Penicillium chrysogenum to oxygen starvation in glucose- and nitrogen-limited chemostat cultures,* Enzyme and Microbial Technology **25**, 447 (1999).

[242] C. Henriksen, J. Nielsen, and J. Villadsen, *Influence of the Dissolved Oxygen Concentration on the Penicillin Biosynthetic Pathway in Steady-State Cultures of Penicillium chrysogenum,* Biotechnology Progress **13**, 776 (1997).

[243] J. A. Roels, J. Van Den Berg, and R. M. Voncken, *The rheology of mycelial broths,* Biotechnology and Bioengineering **16**, 181 (1974).

[244] B. Metz, N. W. F. Kossen, and J. C. Suijdam, *The rheology of mould suspensions,* in *Advances in biochemical engineering vol. 11*, edited by T. K. Ghose, A. Fiechter, and N. Blakebrough (Springer Berlin Heidelberg, 1979) pp. 103–156.

[245] D. Grant Allen and C. W. Robinson, *Measurement of rheological properties of filamentous fermentation broths,* Chemical Engineering Science **45**, 37 (1990).

[246] G. L. Riley, K. G. Tucker, G. C. Paul, and C. R. Thomas, *Effect of biomass concentration and mycelial morphology on fermentation broth rheology,* Biotechnology and Bioengineering **68**, 160 (2000).

[247] R. Wittier, H. Baumgartl, D. W. Lübbers, and K. Schügerl, *Investigations of oxygen transfer into Penicillium chrysogenum pellets by microprobe measurements,* Biotechnology and Bioengineering **28**, 1024 (1986).

[248] A. Amanullah, P. Jüsten, A. Davies, G. Paul, A. Nienow, and C. Thomas, *Agitation induced mycelial fragmentation of Aspergillus oryzae and Penicillium chrysogenum,* Biochemical Engineering Journal **5**, 109 (2000).

[249] J. J. Smith, M. D. Lilly, and R. I. Fox, *The effect of agitation on the morphology and penicillin production ofPenicillium chrysogenum,* Biotechnology and Bioengineering **35**, 1011 (1990).

[250] P. Jüsten, G. C. Paul, A. W. Nienow, and C. R. Thomas, *A mathematical model for agitation-induced fragmentation of Penicillium chrysogenum,* Bioprocess Engineering **18**, 7 (1997).

[251] P. Jüsten, G. C. Paul, A. W. Nienow, and C. R. Thomas, *Dependence ofPenicillium chrysogenum growth, morphology, vacuolation, and productivity in fed-batch fermentations on impeller type and agitation intensity,* Biotechnology and Bioengineering **59**, 762 (1998).

[252] R. K. Bajpai and M. Reuß, *A mechanistic model for penicillin production,* Journal of Chemical Technology and Biotechnology **30**, 332 (1980).

[253] G. Birol, C. Ündey, and A. Çinar, *A modular simulation package for fed-batch fermentation: penicillin production,* Computers & Chemical Engineering **26**, 1553 (2002).

[254] S. Goldrick, A. Ştefan, D. Lovett, G. Montague, and B. Lennox, *The development of an industrial-scale fed-batch fermentation simulation.* Journal of biotechnology **193**, 70 (2015).

[255] I. E. Nikerel, P. J. T. Verheijen, W. M. van Gulik, and J. J. Heijnen, *Model-Based Design of Superior Cell Factory: An Illustrative Example of Penicillium chrysogenum,* in *Systems Metabolic Engineering* (Springer Netherlands, Dordrecht, 2012) pp. 221–270.

[256] C. Verduyn, E. Postma, W. A. Scheffers, and J. P. van Dijken, *Physiology of Saccharomyces Cerevisiae in Anaerobic Glucose-Limited Chemostat Cultures,* Journal of General Microbiology **136**, 395 (1990).

[257] J. P. van Dijken, R. A. Weusthuis, and J. T. Pronk, *Kinetics of growth and sugar consumption in yeasts,* Antonie van Leeuwenhoek **63**, 343 (1993).

[258] H. Van Urk, P. R. Mark, W. A. Scheffers, and J. P. Van Dijken, *Metabolic responses of Saccharomyces cerevisiae CBS 8066 and Candida utilis CBS 621 upon transition from glucose limitation to glucose excess,* Yeast **4**, 283 (1988).

[259] C. Verduyn, E. Postma, W. A. Scheffers, and J. P. Van Dijken, *Effect of benzoic acid on metabolic fluxes in yeasts: A continuous-culture study on the regulation of respiration and alcoholic fermentation,* Yeast **8**, 501 (1992).

[260] H. Van Urk, W. S. Voll, W. A. Scheffers, and J. P. Van Dijken, *Transient-state analysis of metabolic fluxes in crabtree-positive and crabtree-negative yeasts.* Applied and environmental microbiology **56**, 281 (1990).

[261] M. Petrik, O. Kappeli, and A. Fiechter, *An Expanded Concept for the Glucose Effect in the Yeast Saccharomyces uvarum: Involvement of Short- and Long-term Regulation,* Microbiology **129**, 43 (1983).

[262] J. T. Pronk, H. Y. Steensma, and J. P. van Dijken, *Pyruvate Metabolism in Saccharomyces cerevisiae,* Yeast **12**, 1607 (1996).

[263] F. Lei, M. Rotbøll, and S. B. Jørgensen, *A biochemically structured model for Saccharomyces cerevisiae,* Journal of Biotechnology **88**, 205 (2001).

[264] C. Verduyn, T. P. L. Zomerdijk, J. P. van Dijken, and W. A. Scheffers, *Continuous measurement of ethanol production by aerobic yeast suspensions with an enzyme electrode,* Applied Microbiology and Biotechnology **19**, 181 (1984).

[265] M. Kresnowati, C. Suarez-Mendez, W. van Winden, W. van Gulik, and J. Heijnen, *Quantitative physiological study of the fast dynamics in the intracellular pH of Saccharomyces cerevisiae in response to glucose and ethanol pulses,* Metabolic Engineering **10**, 39 (2008).

[266] L. Wu, J. van Dam, D. Schipper, M. T. A. P. Kresnowati, A. M. Proell, C. Ras, W. A. van Winden, W. M. van Gulik, and J. J. Heijnen, *Short-term metabolome dynamics and carbon, electron, and ATP balances in chemostat-grown Saccharomyces cerevisiae CEN.PK 113-7D following a glucose pulse.* Applied and environmental microbiology **72**, 3566 (2006).

[267] M. T. A. P. Kresnowati, W. A. van Winden, M. J. H. Almering, A. ten Pierick, C. Ras, T. A. Knijnenburg, P. Daran-Lapujade, J. T. Pronk, J. J. Heijnen, and J. M. Daran, *When transcriptome meets metabolome: fast cellular responses of yeast to sudden relief of glucose limitation.* Molecular systems biology **2**, 49 (2006).

[268] B. Sonnleitner and O. Käppeli, *Growth ofSaccharomyces cerevisiae is controlled by its limited respiratory capacity: Formulation and verification of a hypothesis,* Biotechnology and Bioengineering **28**, 927 (1986).

[269] M. Rizzi, M. Baltes, U. Theobald, and M. Reuss, *In vivo analysis of metabolic dynamics in Saccharomyces cerevisiae: II. Mathematical model.* Biotechnology and bioengineering **55**, 592 (1997).

[270] M. J. Tummers and D. M. Passchier, *Spectral estimation using a variable window and the slotting technique with local normalization,* Measurement Science and Technology **7**, 1541 (1996).

[271] M. J. Tummers and D. M. Passchier, *Spectral analysis of biased LDA data,* Measurement Science and Technology **12**, 1641 (2001).

[272] H. R. E. van Maanen, H. Nobach, and L. H. Benedict, *Improved estimator for the slotted autocorrelation function of randomly sampled LDA data,* Measurement Science and Technology **10**, L4 (1999).

[273] H. R. E. van Maanen, *Retrieval of Turbulence and Turbulence Properties from Randomly Sampled Laser-Doppler Anemometry Data with Noise*, Phd thesis, Delft university of Technology (1999).

[274] V. V. Ranade and J. B. Joshi, *Flow generated by a disc turbine. II: Mathematical modelling and comparison with experimental data,* Chemical engineering research & design **68**, 34 (1990).

[275] A. Paglianti, K. Takenaka, and W. Bujalski, *Simple model for power consumption in aerated vessels stirred by Rushton disc turbines,* AIChE Journal **47**, 2673 (2001).

[276] J. J. Heijnen, *Impact of Thermodynamic Principles in Systems Biology,* (2010), 10.1007/10.

[277] P. Vrábel, R. G. van der Lans, K. C. Luyben, L. Boon, and A. W. Nienow, *Mixing in large-scale vessels stirred with multiple radial or radial and axial up-pumping impellers: modelling and measurements,* Chemical Engineering Science **55**, 5881 (2000).

[278] M. Linkès, P. Fede, J. Morchain, and P. Schmitz, *Numerical investigation of subgrid mixing effects on the calculation of biological reaction rates,* Chemical Engineering Science **116**, 473 (2014).

[279] A. Bakker, K. J. Myers, R. W. Ward, and C. K. Lee, *The laminar and turbulent flow pattern of a pitched blade turbine,* Chemical Engineering Research and Design **74**, 485 (1996).

[280] P. Vrábel, R. G. van der Lans, F. N. van der Schot, K. C. Luyben, B. Xu, and S.-O. Enfors, *CMA: integration of fluid dynamics and microbial kinetics in modelling of large-scale fermentations,* Chemical Engineering Journal **84**, 463 (2001).

[281] F. Delvigne, J. Destain, and P. Thonart, *A methodology for the design of scale-down bioreactors by the use of mixing and circulation stochastic models,* Biochemical Engineering Journal **28**, 256 (2006).

[282] D. D. McClure, J. M. Kavanagh, D. F. Fletcher, and G. W. Barton, *Characterizing bubble column bioreactor performance using computational fluid dynamics,* Chemical Engineering Science **144**, 58 (2016).

[283] B. W. Lee and M. P. Dudukovic, *Determination of flow regime and gas holdup in gas–liquid stirred tanks,* Chemical Engineering Science **109**, 264 (2014).

[284] T. von Karman, *Mechanical similitude and turbulence,* achrichten von der Gesellschaft der Wissenschaften zu Göttingen **5**, 58 (1939).

[285] R. Sungkorn, J. Derksen, and J. Khinast, *Modeling of aerated stirred tanks with shear-thinning power law liquids,* International Journal of Heat and Fluid Flow **36**, 153 (2012).

[286] A. Lübbert and B. Larson, *Detailed investigations of the multiphase flow in airlift tower loop reactors,* Chemical Engineering Science **45**, 3047 (1990).

[287] J. Wu, Y. Zhu, and L. Pullum, *Impeller Geometry Effect on Velocity and Solids Suspension,* Chemical Engineering Research and Design **79**, 989 (2001).

[288] B. S. Choi, B. Wan, S. Philyaw, K. Dhanasekharan, and T. A. Ring, *Residence Time Distributions in a Stirred Tank: Comparison of CFD Predictions with Experiment,* Industrial & Engineering Chemistry Research **43**, 6548 (2004).

[289] S. Smith, *Digital Signal Processing: A Practical Guide for Engineers and Scientists: A Practical Guide for Engineers and Scientists*, 1st ed. (Elsevier Science, 2013) p. 672.

[290] H. van Urk, D. Schipper, G. J. Breedveld, P. R. Mak, W. Alexander Scheffers, and J. P. van Dijken, *Localization and kinetics of pyruvate-metabolizing enzymes in relation to aerobic alcoholic fermentation in Saccharomyces cerevisiae CBS 8066 and Candida utilis CBS 621,* Biochimica et Biophysica Acta (BBA) - General Subjects **992**, 78 (1989).

[291] H. Ying Lin and P. Neubauer, *Influence of controlled glucose oscillations on a fed-batch process of recombinant Escherichia coli,* Journal of Biotechnology **79**, 27 (2000).

[292] C. Abel, U. Hübner, and K. Schügerl, *Transient behaviour of Baker's yeast during enforced periodical variation of dissolved oxygen concentration,* Journal of Biotechnology **32**, 45 (1994).

[293] S. George, G. Larsson, K. Olsson, and S.-O. Enfors, *Comparison of the Baker's yeast process performance in laboratory and production scale,* Bioprocess Engineering **18**, 135 (1998).

[294] B. van Kleeff, J. Kuenen, and J. Heijnen, *Heat Flux Measurements for the Fast Monitoring of Dynamic Responses to Glucose Additions by Yeasts That Were Subjected To Different Feeding Regimes in Continuous Culture,* Biotechnology Progress **12**, 510 (1996).

[295] D. Cronin, A. W. Nienow, and G. Moody, *An experimental study of mixing in a proto-fermenter agitated by dual Rushton turbines,* Food and Bioproducts Processing **72c**, 35 (1994).

[296] R. Zenobi, *Single-Cell Metabolomics: Analytical and Biological Perspectives,* Science **342** (2013).

[297] A. Grünberger, W. Wiechert, and D. Kohlheyer, *Single-cell microfluidics: opportunity for bioprocess development,* Current Opinion in Biotechnology **29**, 15 (2014).

[298] C. Dusny and A. Schmid, *Microfluidic single-cell analysis links boundary environments and individual microbial phenotypes,* Environmental Microbiology **17**, 1839 (2015).

[299] A. Sweere, K. Luyben, and N. Kossen, *Regime analysis and scale-down: Tools to investigate the performance of bioreactors,* Enzyme and Microbial Technology **9**, 386 (1987).

[300] G. Salierno, M. Maestri, S. Piovano, M. Cassanello, M. A. Cardona, D. Hojman, and H. Somacal, *Calcium alginate beads motion in a foaming three-phase bubble column,* Chemical Engineering Journal **324**, 358 (2017).

[301] J. D. Simen, M. Löffler, G. Jäger, K. Schäferhoff, A. Freund, J. Matthes, J. Müller, and R. Takors, *Transcriptional response of Escherichia coli to ammonia and glucose fluctuations,* Microbial Biotechnology **10**, 858 (2017).

[302] M. Kuschel, F. Siebler, and R. Takors, *Lagrangian Trajectories to Predict the Formation of Population Heterogeneity in Large-Scale Bioreactors,* Bioengineering **4**, 27 (2017).

[303] A. Lemoine, F. Delvigne, A. Bockisch, P. Neubauer, and S. Junne, *Tools for the determination of population heterogeneity caused by inhomogeneous cultivation conditions,* Journal of Biotechnology **251**, 84 (2017).

[304] M. R. Bennett and J. Hasty, *Microfluidic devices for measuring gene network dynamics in single cells,* Nature Reviews Genetics **10**, 628 (2009).

[305] F. S. Fritzsch, C. Dusny, O. Frick, and A. Schmid, *Single-Cell Analysis in Biotechnology, Systems Biology, and Biocatalysis,* Annual Review of Chemical and Biomolecular Engineering **3**, 129 (2012).

[306] G. Lambert, E. Kussell, J. Heuveling, V. Wendisch, and R. Hengge, *Memory and Fitness Optimization of Bacteria under Fluctuating Environments,* PLoS Genetics **10**, e1004556 (2014).

[307] A. Grünberger, C. Probst, S. Helfrich, A. Nanda, B. Stute, W. Wiechert, E. von Lieres, K. Nöh, J. Frunzke, and D. Kohlheyer, *Spatiotemporal microbial single-cell analysis using a high-throughput microfluidics cultivation platform,* Cytometry Part A **87**, 1101 (2015).

[308] G. Amselem, C. Guermonprez, B. Drogue, S. Michelin, C. N. Baroud, C. N. Baroud, A. Milarcik, L. Clapp, R. Schwartz, N. P. Keller, and D. J. Beebe, *Universal microfluidic platform for bioassays in anchored droplets,* Lab Chip **16**, 4200 (2016).

[309] S. Kim, H. J. Kim, and N. L. Jeon, *Biological applications of microfluidic gradient devices,* Integrative Biology **2**, 584 (2010).

[310] A. F. Oliveira, A. C. S. N. Pessoa, R. G. Bastos, and L. G. de la Torre, *Microfluidic tools toward industrial biotechnology,* Biotechnology Progress **32**, 1372 (2016).

[311] A. Amantonico, P. L. Urban, S. R. Fagerer, R. M. Balabin, and R. Zenobi, *Single-Cell MALDI-MS as an Analytical Tool for Studying Intrapopulation Metabolic Heterogeneity of Unicellular Organisms,* Analytical Chemistry **82**, 7394 (2010).

[312] Y. Ding, J. Choo, and A. J. DeMello, *From single-molecule detection to next-generation sequencing: microfluidic droplets for high-throughput nucleic acid analysis,* Microfluidics and Nanofluidics **21**, 58 (2017).

[313] D. J. Pollard, A. P. Ison, P. A. Shamlou, and M. D. Lilly, *The Examination of Bioreactor Heterogeneity with Rheological Different Fermentation Broths,* in *Advances in Bioprocess Engineering* (Springer Netherlands, Dordrecht, 1994) pp. 163–170.

[314] P. Ayazi Shamlou, D. Pollard, A. Ison, and M. Lilly, *Gas holdup and liquid circulation rate in concentric-tube airlift bioreactors,* Chemical Engineering Science **49**, 303 (1994).

[315] P. Ayazi Shamlou, D. Pollard, and A. Ison, *Volumetric mass transfer coefficient in concentric-tube airlift bioreactors,* Chemical Engineering Science **50**, 1579 (1995).

[316] D. J. Pollard, P. A. Shamlou, M. D. Lilly, and A. P. Ison, *Saccharomyces cerevisiae fermentations in a pilot scale airlift bioreactor: Comparison of air sparger configurations,* Bioprocess Engineering **15**, 279 (1996).

[317] M. Šimčík, A. Mota, M. Ruzicka, A. Vicente, and J. Teixeira, *CFD simulation and experimental measurement of gas holdup and liquid interstitial velocity in internal loop airlift reactor,* Chemical Engineering Science **66**, 3268 (2011).

[318] O. Simonin and P. Viollet, *Modeling of Turbulent Two-Phase Jets Loaded with Discrete Particles,* Phenomena in Multiphase Flows , 259 (1990).

[319] A. Grünberger, K. Schöler, C. Probst, G. Kornfeld, T. Hardiman, W. Wiechert, D. Kohlheyer, and S. Noack, *Real-time monitoring of fungal growth and morphogenesis at single-cell resolution,* Engineering in Life Sciences **17**, 86 (2017).

[320] C. Probst, A. Grünberger, W. Wiechert, and D. Kohlheyer, *Polydimethylsiloxane (PDMS) Sub-Micron Traps for Single-Cell Analysis of Bacteria,* Micromachines **4**, 357 (2013).

[321] C. Westerwalbesloh, A. Grünberger, B. Stute, S. Weber, W. Wiechert, D. Kohlheyer, and E. von Lieres, *Modeling and CFD simulation of nutrient distribution in picoliter bioreactors for bacterial growth studies on single-cell level,* Lab Chip **15**, 4177 (2015).

Appendix A: The $9 - pool$ model

Model formulation The $9 - pool$ model proposed by Tang et al. [226] was used to study the metabolic response of micro-organisms in large scale fermentors. The model structure is reported in figure A1. The following intra-cellular pools are included:

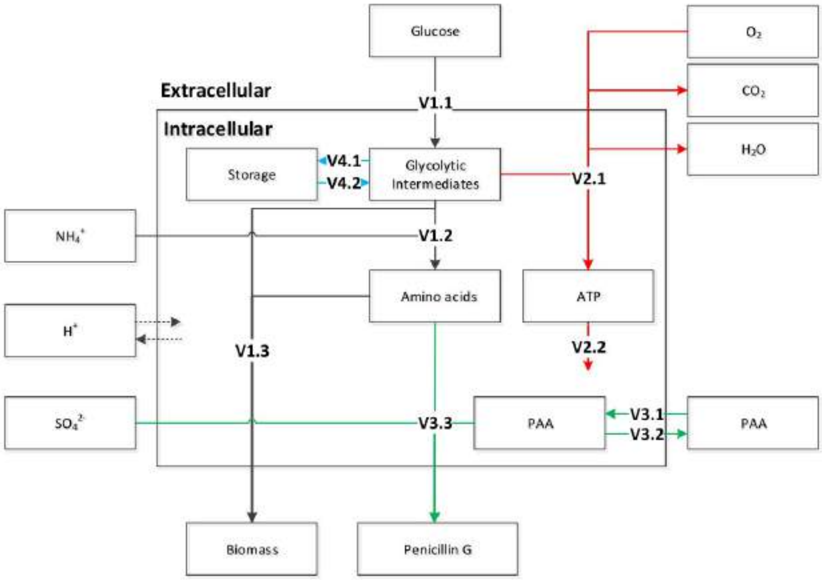

Figure A1: Overview of the $9 - pool$ metabolic model developed by Tang et al. [226] for *P. chrysogenum* DS17690. [reprinted from [226] with permission].

- **Glycolytic intermediates:** Lumped pool representing glycolytic (GLY) intermediates (G6P to pyruvate). Consumed glucose (consumption rate v_{11}) is converted to GLY at cost of 2 mol/mol of ATP by substrate uptake and phosphorylation. Responds rapidly ($O(10)$ s), acts as a gateway to the rest of the metabolism. During substrate starvation, GLY is generated from stored carbon. This rate v_{42} is controlled by C_s. Storage release requires ATP; v_{42} is quenched at low ATP levels.

- **Amino acids:** Lumped amino acid (AA) pool, building block for biomass synthesis (v_{13}, controlled by GLY, ATP and AA, requires ATP) and penicillin production (v_{33}). AA supply is governed by v_{12} expending 0.65mol ATP per mol AA, and is controlled by GLY, AA and ATP. Slow response ($O(1)$ h).

Table A1: Stoichiometric matrix of the metabolically structured kinetic model (in mol/mol, from: Tang et al. [226]). X_{bio} is the biomass pool, $gluc$ the extra-cellular glucose pool.

Pool	v_{11}	v_{12}	v_{13}	v_{21}	v_{22}	v_{31}	v_{32}	v_{33}	v_{41}	v_{42}	v_d
Glyc.	6	-1	-0.578	-1	0	0	0	-4.81	-1.07	1	0
AA.	0	1	-0.5	0	0	0	0	-6.25	0	0	0
Sto.	0	0	0	0	0	0	0	0	1	-1	
ATP	-2	-0.65	-1.037	4.43	-1	0	-2	-8	-0.167	-0.167	0
PAA	0	0	0	0	0	1	-1	-1	0	0	0
Gluc.	-1	0	0	0	0	0	0	0	0	0	0
X_{bio}	0	0	1	0	0	0	0	0	0	0	-1

- **Storage carbon:** Polymeric carbon (STO) stored during excess, released during starvation. The storage rate is v_{41} and release rate is v_{42}. Both require 0.1667 mol ATP per mol stored/released. Slow response ($O(10)$ h).
- **ATP:** Energy carrier, generated in v_{21} (controlled by GLY and ATP) and consumed in most other reactions. Very fast response ($O(1)$ s).
- **PAA:** Penicillin precursor. Diffuses into the cell (v_{31}, controlled by pH and C_{PAA}), while being actively transported out (v_{32}, controlled by X_{E32} and X_{PAA}, at cost of 2 mol ATP per mol PAA). This passive import and active export leads to a futile ATP consuming cycle.
- **Enzyme pools:** X_{E11}: Controls the substrate import capacity. X_{E32}: Controls the PAA export capacity. X_{E4}: Controls storage/release capacity. Enzyme synthesis is controlled by the growth rate, v_{13}.
- **V_{33}/q_p**: Production rate of penicillin (q_p), governed by enzymatic control. Enzyme synthesis/breakdown is controlled by the growth rate v_{13} (also called μ) as described by Douma et al. [236]. Enzyme synthesis is suppressed by high GLY levels.

All metabolic pools are reported in X_i μmol/g$_{dw}$. The explicitly defined extracellular pools are: C_x, the biomass concentration in g$_{dw}$/kg (alternatively referred to as X_{bio} g/$parcel$ in lagrangian tracking), C_s, the glucose concentration in mol/kg and C_{PAA}, the PAA concentration in mol/kg. Rate v_{22} represents maintenance, consuming a constant ATP amount. Death rate $v_d = 0.005$ h^{-1} represents a lump-sum parameter including all cell deterioration effects. Excretion/uptake rates related to O_2, CO_2, H_2O, NH_4^+, H^+, SO_4^{2-} can be computed with the model based on stoichiometry, but none of these components currently influences the metabolism itself.

Model equations The model stoichiometry is given in table A1, the kinetic equations in table A2, and model parameters in A3.

Model instabilities and modification Instabilities in X_{ATP} were noted in coupled simulations with the 9-pool model. We conducted turbulent plug-flow simulations to replicate the 360 s feast-famine cycles of De Jonge et al. [44] in a flow reactor.

Table A2: Kinetic equations of the $9 - pool$ model.

Reaction	Kinetics	Eq.
Transporter capacity	$\frac{dX_{E,11}}{dt} = q_{E,11,max} \cdot \frac{((\mu+\mu_0)/k_{11})^5}{1+((\mu+\mu_0)/k_{11})^5} - (\mu + k_{dE,11})X_{E,11}$	$dv_{X,11}$
Carbon uptake	$v_{11} = k_{E,11} X_{E,11} \frac{C_s}{C_s+K_{s,11}}$	v_{11}
Amino Acid synthesis	$v_{12} = v_{12,max} \cdot \frac{X_{gly}^2}{K_{gly,12}^2+X_{gly}^2} \cdot \frac{K_{AA,12}^2}{K_{AA,12}^2+X_{AA}^2} \cdot \frac{X_{ATP}^3}{K_{ATP,12}^3+X_{ATP}^3}$	v_{12}
Growth	$v_{13} = v_{13,max} \cdot \frac{X_{gly}^2}{K_{gly,13}^2+X_{gly}^2} \cdot \frac{X_{AA}^2}{K_{AA,13}^2+X_{AA}^2} \cdot \frac{X_{ATP}^3}{K_{ATP,13}^3+X_{ATP}^3}$	v_{13}/μ
ATP production	$v_{21} = v_{21,max} \cdot \frac{X_{gly}^3}{K_{gly,21}^3+X_{gly}^3} \cdot \frac{K_{ATP,21}^4}{K_{ATP,21}^4+X_{ATP}^4}$	v_{21}
Maintenance	$v_{22} = m_{ATP,22}$	v_{22}
PAA import	$v_{31} = k_{perm,31} \cdot a_{cell} \cdot \left(\frac{X_{PAA}/2.5}{1+10^{pH,ext-pK}} - \frac{C_{PAA} \cdot \rho_{broth}}{1+10^{pH,int-pK}} \right)$	v_{31}
PAA export capacity	$\frac{dX_{E,32}}{dt} = \alpha_{32} + \beta_{32} \cdot \mu - k_{dE,32} \cdot X_{E,32} - \mu \cdot X_{E,32}$	$dv_{X,32}$
PAA export	$v_{32} = X_{E,32} \cdot X_{PAA} \cdot M_X \cdot 10^{-6}$	v_{32}
Pen-G production capacity	$\frac{dv_{33}}{dt} = \frac{\beta_{33} \cdot \mu}{1+(X_{gly}/K_{gly,33})^{m33}} - \left(k_{dE,33} + \mu\right) \cdot v_3 3$	v_{33}/q_p
Storage capacity	$\frac{dX_{E,4}}{dt} = \alpha_4 + \beta_4 \cdot \mu - k_{dE,4} \cdot X_{E,4} - \mu \cdot X_{E,4}$	$dv_{X,4}$
Carbon storage	$k_{41} \cdot X_{E,4} \cdot \frac{C_s}{C_s+K_{s,41}} \cdot \left(1 + 2 \cdot \frac{C_s}{C_s+K_{s,42}}\right) \cdot \frac{K_{sto,41}}{X_{sto}+K_{sto,41}}$	v_{41}
Storage release	$k_{42} \cdot X_{E,4} \cdot \frac{K_{s,42}}{C_s+K_{s,42}} \cdot \left(1 + 2 \cdot \frac{C_s}{C_s+K_{s,41}}\right) \cdot \frac{X_{sto}^2}{X_{sto}^2+K_{sto,42}^2} \cdot \frac{X_{ATP}^2}{X_{ATP}^2+K_{ATP,42}^2}$	v_{42}
Death rate	$v_{d,m}$	v_d

Herein, X_{ATP} was observed to become negative for the majority of parcels directly after the feast-famine transition. Further investigation revealed the extra-cellular signaling terms in storage equations v_{41} and v_{42} were very sensitive to small variations in C_s in the range $10^{-8} < C_s < 10^{-4}$: turbulent fluctuations in the parcel trajectory imposed rapid C_s oscillations within this amplitude range around the feast-famine transition. We illustrate this by comparing the model response of the 9—pool model in a feast famine cycle, with the same cycle where some C_s-noise was added as $C_s(t) = C_s(t) \pm 0.5 \cdot 10^{-7} \cdot rand()$ mol/kg, with $rand()$ an random number between 0 and 1 (fig. A2). Even though the overall q_s is slightly higher with noise (since C_s is always positive), the X_{ATP} pool collapses only when noise is imposed. These fluctuations caused rapid switching between storage and liberation, resulting in an insufficient overall flux from X_{sto} to X_{gly} to maintain the required level of ATP synthesis. Low ATP levels in turn quench storage release (v_{42}) inevitably leading to a collapse of X_{ATP} that does not reflect upon experimental observations [44].

In case storage/release is indeed directly regulated by the extra-cellular glucose concentration C_s, a timescale of activation/deactivation of the signal cascade should be introduced to dampen the effect of turbulent oscillations. Alternatively, storage/release may be triggered by an intra-cellular signal molecule; for example, ATP or

Table A3: Parameters of the $9 - pool$ model.

Param.	Value	St. Err.	Unit
$q_{E,11,max}$	$6.5 \cdot 10^{-2}$	$4.41 \cdot 10^{-3}$	U/Cmol$_x$/h
μ_0	$5.5 \cdot 10^{-2}$	$1.03 \cdot 10^{-3}$	h^{-1}
k_{11}	0.10	$1.16 \cdot 10^{-3}$	h^{-1}
$k_{dE,11}$	$1.46 \cdot 10^{-2}$	$6.55 \cdot 10^{-3}$	h^{-1}
$k_{E,11}$	0.26	$1.54 \cdot 10^{-2}$	mol$_s$/U
$k_{s,11}$	$9.8 \cdot 10^{-6}$	$1.54 \cdot 10^{-2}$	mol/kg
$v_{12,max}$	0.18	$7.74 \cdot 10^{-2}$	mol/Cmol$_x$/h
$K_{gly,12}$	31.38	4.91	μmol/g$_{dw}$
$K_{AA,12}$	870.23	69.6	μmol/g$_{dw}$
$K_{ATP,12}$	2.01	0.26	μmol/g$_{dw}$
$v_{13,max}$	0.32	$9.92 \cdot 10^{-2}$	mol/Cmol$_x$/h
$K_{gly,13}$	38.54	9.25	μmol/g$_{dw}$
$K_{AA,13}$	757.81	128.83	μmol/g$_{dw}$
$K_{ATP,13}$	1.95	0.24	μmol/g$_{dw}$
$v_{21,max}$	0.35	$9.45 \cdot 10^{-2}$	mol/Cmol$_x$/h
$K_{gly,21}$	25.64	5.58	μmol/g$_{dw}$
$K_{ATP,21}$	6.01	0.66	μmol/g$_{dw}$
$m_{ATP,22}$	$3.3 \cdot 10^{-2}$	$1.2 \cdot 10^{-2}$	mol/Cmol$_x$/h
$k_{perm,31}$	$1.62 \cdot 10^{-2}$	$3.74 \cdot 10^{-3}$	m/h
a_{cell}	56.00	$-$	m^2/Cmol$_x$
α_{32}	0	0	h^{-2}
β_{32}	$1.56 \cdot 10^{3}$	218.4	h^{-1}
$k_{dE,32}$	0.35	$4.90 \cdot 10^{-2}$	h^{-1}
β_{33}	$6.5 \cdot 10^{-4}$	$-$	mol/Cmol$_x$/h
$k_{dE,33}$	$1.47 \cdot 10^{-2}$	$1.2 \cdot 10^{-3}$	h^{-1}
$K_{33,gly}$	30.76	1.58	μmol/g$_{dw}$
m_{33}	6.00	$-$	$-$
α_4	$8.01 \cdot 10^{-4}$	$1.68 \cdot 10^{-4}$	mol/Cmol$_x$/h^2
β_4	0.289	$1.49 \cdot 10^{-2}$	mol/Cmol$_x$/h
$k_{dE,4}$	0.29	$1.23 \cdot 10^{-2}$	h^{-1}
k_{41}	1.01	0.1	mol/mol
$K_{s,41}$	10^{-8}	$1.33 \cdot 10^{-8}$	mol/kg
$K_{sto,41}$	$4.25 \cdot 10^{3}$	$9.32 \cdot 10^{2}$	μmol/g$_{dw}$
k_{42}	3.99	0.48	mol/mol
$K_{s,42}$	10^{-4}	$1.37 \cdot 10^{-4}$	mol/kg
$K_{sto,42}$	$7.99 \cdot 10^{3}$	$1.07 \cdot 10^{3}$	μmol/g$_{dw}$
$K_{ATP,42}$	6.48	0.9	μmol/g$_{dw}$
pH_{int}	2.20	$-$	$-$
pH_{ext}	6.50	$-$	$-$
pK_{PAA}	4.31	$-$	$-$
$v_{d,m}$	$5 \cdot 10^{-3}$	$-$	h^{-1}
$M_{w,bio}$	28.05	$-$	g$_{dw}$/Cmol

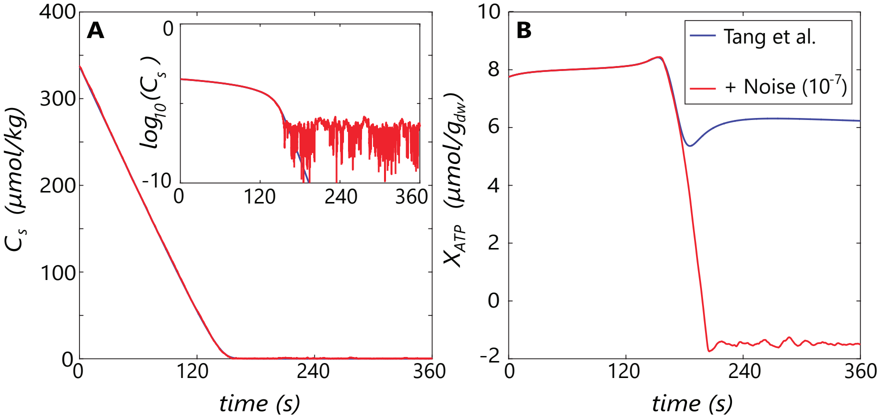

Figure A2: **A:** Concentration profiles in a perfect plug flow reactor ($\tau_{res} = 360$ s), without superimposed noise (blue) and with superimposed noise (red). Inset shows the same curve with a logarithmic y-axis. **B:** ATP pool response to both profiles, generated with the 9−pool model [226].

the glycolytic intermediates may trigger the release of stored carbon when the cell energy charge becomes critical. Lacking the required information to propose a structural model improvement at this time, we opted for a patch solution based on the quasi-steady state assumption. Since X_{ATP} changes at shorter timescales than the other pools, it is valid to assume that X_{ATP} the fluxes in and out of X_{ATP} instantaneously balance, which means we can set $dX_{ATP}/dt = 0$, yieldin $X_{ATP} = f[X_{gly}, X_{sto}, ..., X_{E4}]$, which replaces the dynamic balance by an algebraic equation, eq. 1, with all X except X_{ATP} fixed [255].

$$0 = \sum^{n_i=1} \left(v_n[X_{ATP}, X_{gly}, X_{sto}, ..., X_{E4}]\right) \tag{1}$$

With the current non-linear kinetic model, a numerical procedure is required to find X_{ATP} for a given set of conditions. To study the dependency of X_{ATP} on the other pools, we generated 100.000 sets of values for the other pool sizes, assuming a) the pool sizes are statistically independent and b) each pool can vary within a certain range 0...Z with Z being a pool-dependent estimation based on experimental observations. For each set eq. 1 was solved to find X_{ATP}. A strong relation between X_{ATP} and X_{gly} could be observed (fig. A3), while the other pools were non-influential. This is understood as 1) ATP generation and consumption depend strongly on the availability of glycolytic intermediates and 2) the timescale of variations in X_{gly} lies between that of X_{ATP} and the other pools.

Using non-linear regression, a function of the form $X_{ATP} = A \cdot X_{gly}^3/(X_{gly}^3 + B^3)$ is fitted to the data. A bi-square weighting routine is used to reduce outlier influence, which is most notable around $X_{gly} = 0$ where the initial guess of X_{ATP} may satisfy the tolerance of the *fsolve* solution algorithm of MATLAB, as the fluxes here are

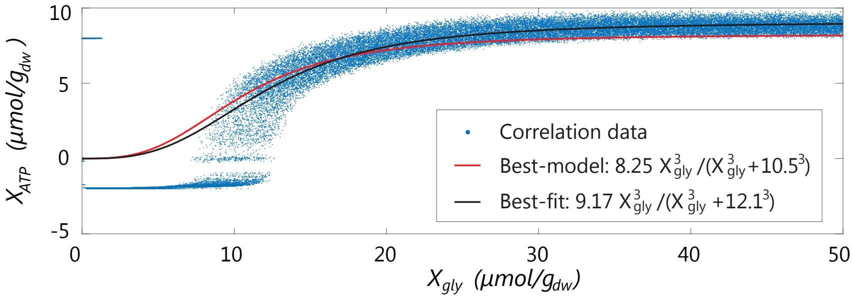

Figure A3: Correlation between X_{ATP} and X_{gly} observed from 100.000 randomly generated pool datasets. Non-linear regression was used to find a best-fit function (black line), manual finetuning was used to optimize the model response to experimental conditions (red line).

(close to) 0. The best-fit parameters are $A = 9.07$ μmol/g$_{dw}$, $B = 12.1$ μmol/g$_{dw}$ with $R^2 = 0.96$. Use of the best-fit parameters did result in some offsets compared to available experimental data. This is deemed a consequence of the assumptions: the range of allowed pool values may be unrealistically large, and pools may not be fully statistically independent. Manual fine-tuning of the parameters gave $A = 8.5$ μmol/g$_{dw}$ and $B = 10.5$ μmol/g$_{dw}$, which was used in our simulations. The data clearly shows that for $X_{gly} < 10$ μmol/g$_{dw}$ there is no positive solution for X_{ATP} in the current pool formulation. With the patch solution, X_{ATP} will approach 0 at low X_{gly}, reducing μ and other intra-cellular responses, no negative X_{ATP} is allowed.

The response of the pools under A-stat conditions is shown in figure A4 **A**, for steady state conditions in A4 **B**. The patched model with $A = 8.5$ μmol/g$_{dw}$ and $B = 10.5$ μmol/g$_{dw}$ is in perfect agreement with the full model of Tang et al. under the assessed conditions. Deviations between the original model and patched model were observed for feast-famine conditions (fig. A5), notably in X_{sto}, and X_{ATP} during famine cycles. The predicted ATP value under-estimates the experimental values reported by de Jonge et al. [44], but the value is more stable than in the original model of Tang et al. [226].

Experimental data considering longer starvation periods is required to comment on whether or not the ATP pool indeed settles at a pseudo-steady value, what this value is, and how the rest of the cell metabolism is affected during starvation periods. As such we stress that the current model revision considers a quick patch, and a more structural model improvement and model validation under a broader range of fluctuation conditions is desired.

The dynamic gene regulation model

Model modifications Douma et al. [236] based kinetic parameters related to substrate uptake on work by Gulik et al. [232, 233]. Updates parameters were acquired by De Jonge et al. [44], with improved methods to determine the residual substrate concentration (see table A4). These parameters were used in our Monod model, requiring

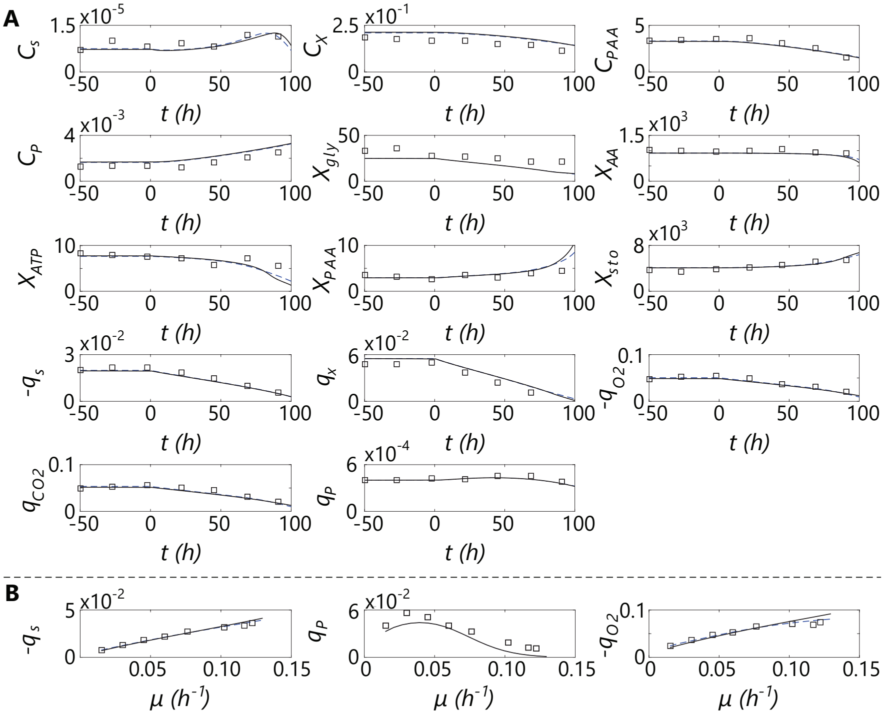

Figure A4: **A:** Validation of the modified metabolic model vs. A-stat data (Tang et al., [226]). Solid black line: original model. Dashed blue line: algebraic ATP formulation. **B:** Validation of the modified metabolic model vs. steady state chemostat data (van Gulik et al, [233]). Solid black line: original model. Dashed blue line: algebraic ATP formulation. All intracellular fractions X are in (C)mol/g$_{dw}$, extra-cellular concentrations C in mol/kg and all q-rates in (C)mol/Cmol$_x$/h.

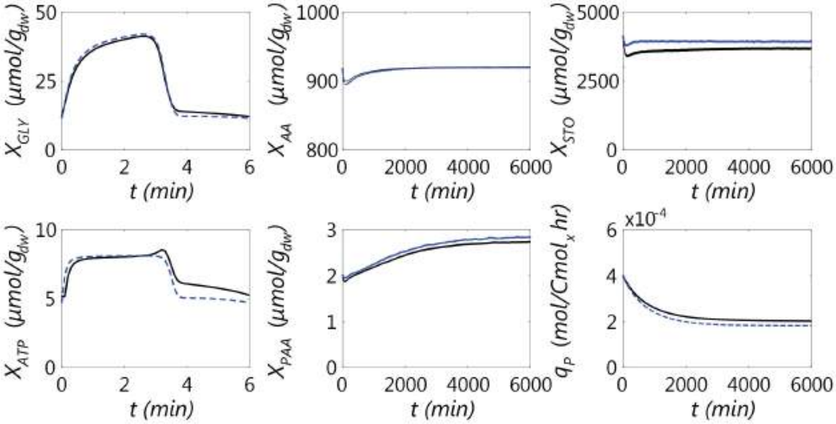

Figure A5: **A:** Validation of the modified metabolic model vs. feast-famine data (De Jonge et al., [44]. Solid black line: original model. Dashed blue line: algebraic ATP formulation. A single feast-famine cycle is displayed for rapid pools GLY and ATP, whereas the long-term trends are displayed for the other pools.

Table A4: Parameters for the *P. chrysogenum* gene regulation model of Douma et al., modified for use in this work.

Parameter	Value	Unit
$q_{s,max}$	$12.47 \cdot 10^{-6}$	$\text{mol}_s/C\text{mol}_x/\text{s}$
K_s	$7.8 \cdot 10^{-6}$	mol_s/kg
K_p	$8.36 \cdot 10^{-6}$	mol_s/kg
k_{dE}	0.0147	h^{-1}
β	$8 \cdot 10^{-4}$	$\text{mol}_p/C\text{mol}_x/\text{s}$
Y_{sx}^{max}	3.96	$C\text{mol}_x/\text{mol}_s$
Y_{sp}^{max}	0.174	$\text{mol}_p/\text{mol}_s$
m_s	$0.41 \cdot 10^{-6}$	$\text{mol}_s/C\text{mol}_x/\text{s}$
m_x	28.05	g/mol

K_p in eq. 2 to be re-evaluated, yielding $K_p = 8.36 \cdot 10^{-6}\text{mol}_s/\text{kg}$. An overview of all model parameters used is given in table A4.

$$\frac{dq_p}{dt} = \frac{\beta \cdot \max(0, \mu)}{1 + \left(\frac{C_s}{K_p}\right)^m} - (k_{dE} + |\mu|)q_p \tag{2}$$

In the original model, the terms $\max(0, \mu)$ and $|\mu|$ simply read $|\mu|$. However, the heterogeneous environment in the large scale reactor contains substantial regions where $q_s < q_p \ / \ Y_{sp} + m_s$, leading to negative values for μ, and erroneous behavior of eq. 2. The first term on the right hand side of eq. 2 represents enzyme synthesis, hence the modification prescribes no enzyme is produced under starvation conditions. The modification of term 2 proposes enzyme destruction under starvation conditions to mitigate energy shortages in the metabolism. We stress there is no experimental backing for these choices, but we deem them defendable for the goal of our investigation. We further emphasize that the dynamic gene model is not developed for rapid fluctuations in extra-cellular conditions, and the instantaneous response of μ to rapid variations is unlikely to hold in reality. The above model is purely used to illustrate how a black-box model would predict q_p to change under highly dynamic conditions.

Appendix B: Scale-down based on intra-cellular lifelines

Extra-cellular scale-down In this thesis, we focused on scale-down using the q_s-lifelines extracted from CFD simulations. This amounts to scale-down based on a replication of the extra-cellular environment, as experienced by micro-organisms in the fermentor. We see accurate replication of the extra-cellular environment as the preferential scale-down methodology; if the extra-cellular environment is fully replicated between the scales (q_s, but also q_{O2}, T, shear rates...), then so is the metabolic response. Practically, several of these rates/phenomena will be non-influential, or can be considered constant. This means that the primary goal of a scale-down simulator is to *accurately replicate those lifeline variations to which the relevant metabolic response of the micro-organism is sensitive.* Any simplification (omitting certain lifelines which do turn out to be influential, simplifications of the fluctuation distributions by using a single frequency or amplitude, changing the rate-of-change, ...) has the potential to change the metabolic response between the scales, and introduce unforeseen effects. Any practical scale-down protocol will require some simplifications and compromises, but their effects must be well considered, in order to design a set-up that replicates the environmental environment at the highest accuracy. If a metabolic model is available for the tested strain, this model can be used to probe the impact of simplifications on the metabolic response (as was done in *chapter 7*), although we again emphasize that such simplifications should only be made if required from an operational point of view: there is still the chance that these induce unforeseen responses, not currently captured in the metabolic model. To summarize, the core philosophy of extra-cellular scale-down reads:

To replicate those fluctuations in the extra-cellular environment to which the relevant metabolism of the micro-organism is sensitive, as observed by micro-organisms themselves, to the highest possible degree of accuracy.

Intra-cellular scale-down If some information about the metabolic response is already available in the form of a metabolic model, there is an alternative scale-down philosophy that can be considered: intra-cellular scale down. We do stress this is *not* a replacement for extra-cellular scale-down, as it has a higher chance of introducing unforeseen effects; it should be regarded as an addition to the overall toolbox, that should be used predominantly for metabolic verification. The philosophy behind intra-cellular scale-down is summarized in the following statement:

To replicate the fluctuations in those parts of the metabolism of the micro-organisms, to which the overall process performance is sensitive, to the highest possible degree of accuracy.

This may regard oscillations in metabolic pools that control the relevant rates, or capturing the correct level of the relevant enzyme levels. The advantage of intra-cellular scale-down is that it leads to different operational considerations. Replication of the relevant intra-cellular response may not require operating the lab-scale at equal C_x as the industrial scale, it may allow for the use of fixed-frequency feed intervals, etcetera. The downside is that information about the metabolic response needs to be priorly available in order to assess which intra-cellular pools influence overall process performance, and that there is no guarantee that the designed scale-down protocol induces the expected metabolic response. The disregard of mimicking extra-cellular conditions means the response in parts of the metabolism not included in the metabolic model could be altered, which could subsequently interfere with the relevant part of the metabolism. While this is a clear disadvantage when the goal of the scale-down experiment is to replicate an industrial environment and probe the expected process yield loss, it can be considered an advantage when the goal of the scale-down study is to improve metabolic understanding: if the metabolic response differs from the model prediction, clearly the model omits parts of the relevant metabolism, which provides targets for future study.

As an example for intra-cellular scale-down, we study the *P. chrysogenum* case. The relevant pools for process performance in this case are q_p and C_x (although X_{gly} is influential, it does not directly control the process, and hence we do not consider it a target). The results in chapter 7 do clearly show q_p is sensitive to extra-cellular fluctuations, its level under fluctuating conditions with a statistical steady state differing from that under true steady-state conditions, due to the effect of oscillations in X_{gly}. The long turn-over time in the penicillin-producing enzyme level means q_p itself does not significantly change at short (circulation) timescale, which implies that it is not relevant to capture the *distribution* in fluctuation frequency accurately; it is sufficient to capture fluctuations in X_{gly} in an average sense to induce a change in q_p, without capturing the distributions of the frequency and amplitude of X_{gly}-fluctuations. The other relevant process variable, C_x, is directly controlled by μ. While μ is predicted by the 9−pool model to vary at short timescales, the turnover time of C_x itself implies that it suffices to capture growth only in the time-average sense, $\overline{\mu}$. The goal of the scale-down protocol in this example is to capture the q_p-lifeline and $\overline{\mu} >$-lifeline.

Because q_p and $\overline{\mu}$ vary only at long timescales and it is not required to exactly replicate environmental fluctuations at the circulation timescale, the requirement of equal C_x can be relaxed. The desired response in q_p and $\overline{\mu}$ can be captured with any practical value of C_x, due to the non-linear model formulation. Previous chemostat-based steady-state and scale-down experiments conduced with *P. chrysogenum* operated at $C_x = 6$ g/kg [44, 226], hence we selected this value for consistency. The dilution rate is set to $D_r = 0.033$ h^{-1}, equal to $\overline{\mu}$ for case $TU - B$ (chapter 7). Imposing feed cycles at a fixed frequency, there are three free parameters: feed time τ_f, cycle time τ_c and feed concentration $C_{s,f}$. The value of these parameters must be chosen such that the response in q_p is equal to the response observed in $TU - B$, which served as a basis here. Using MATLAB's genetic algorithm, the three parameters are varied while evaluating a 20 h model response to the cost function in eq. 3:

$$\begin{aligned} Cost = 10^{10} \cdot ((q_{p,SD}[10\text{ h}] - q_{p,CFD}[10\text{ h}])^2 \\ + (q_{p,SD}[20\text{ h}] - q_{p,CFD}[20\text{ h}])^2) + (6- < C_x >)^2 \end{aligned} \quad (3)$$

Here, $\overline{C_x}$ is averaged between $10-20$ h. The optimal parameter set to replicate the q_p-lifeline of $TU-B$ was found to be $\tau_c = 113.1$ s, $\tau_f = 37.4$ s, $C_{s,f} = 0.0895$ mol/kg. Imposing this feed-famine regime yields the model response shown in fig. B1, which shows q_p to be in excellent agreement despite the highly different lifelines in q_s and X_{gly}.

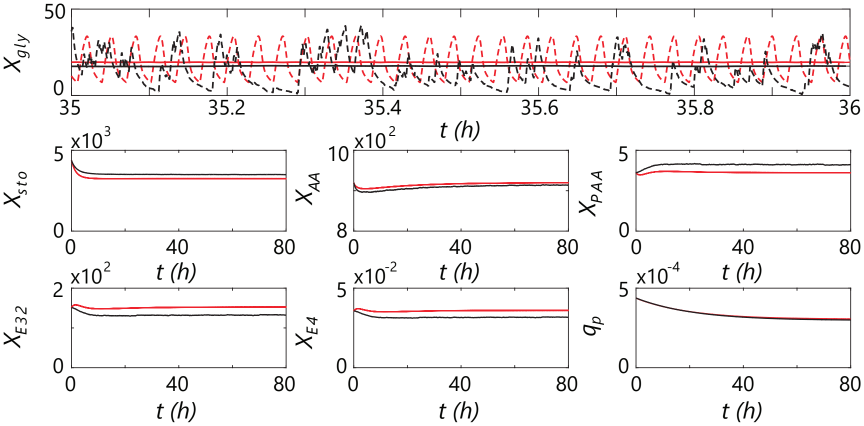

Figure B1: Pool response for a scale-down design protocol design for a fixed biomass concentration of 6 g/kg, with fixed feed intervals. Black lines: CFD data. Red lines: SD simulator response. Intracellular pools X_{gly}, X_{AA}, X_{sto} and X_{PAA} have units µmol/g$_{dw}$. μ has units h^{-1}. q_p has units mol/Cmol$_x$/h. All other pools are dimensionless.

Of course, it is not necessary to impose a q_p-lifeline equal to the large-scale response; the performance of a metabolic model can be evaluated by prescribing fluctuations of any duration to study if the model prediction and experimental observations match. The benefit of basing the q_p-lifeline on large-scale predictions is that this ensures the yield loss is at least in the industrially relevant range; imposing unrealistically long cycle times to impose extreme changes in q_p may induce metabolic changes that are not relevant in modeling the large-scale response. By verifying model performance at a yield change that reflects the industrial scale process, it is likely that the metabolic responses captured in the scale-down simulator that contribute to this particular yield-change are the responses that act at the industrial scale.

Appendix C: Regime sensitivity

Fluctuation statistics are sensitive to parameter changes (geometry, N_s, K_s, $q_{s,max}$ and C_x) and modeling strategies. The RTDs are also influenced by the set regime boundaries and filtering strategy. The effect of physical regime changes is assessed by varying Da via the agitation rate N_s for the *P. chrysogenum* case. The effect of filter strength and the turbulent Schmidt number Sc_t is tested for the *S. cerevisiae* case.

Effect of changes in regime layout: P. chrysogenum The base CFD simulation had $\tau_{circ} = 18.2$ s; case $SENS-1$ has $\tau_{circ} = 25.6$ s (as experimentally observed), case $SENS-2$ has $\tau_{circ} = 42.8$ s, equal to the large-scale water-air result. Regime distributions are reported in figure C1. $SENS-1$ has a slightly larger excess zone due to slower mixing close to the feed, the starvation-limitation boundary is shifted slightly upward. For $SENS-2$, the excess zone is much larger, and the limitation-starvation boundary shifted further upwards. The change in RTDs was studied by tracking 4300 parcels over 3600 s. The RTDs are normalized for comparison and shown in figure C2. The increased regime volume and lower particle velocity lead to a broader RTD in the excess zone; stretching is not proportional to the change in N_s due to the superposed effects. The limitation RTDs are hardly affected; in all cases the mean RTD for a type C trajectory approaches the time required to move from $q_s/q_{s,max} = 0.95$ to $q_s/q_{s,max} = 0.05$ by consumption, which reads 8.13 s for $\tau_{circ} \rightarrow \infty$ for the current kinetics. The size of the limitation regime is q_s-controlled here, and while the zonal volume changes, the mean RTD remains roughly equal for highly non-ideal conditions.

Effect of Turbulent Schmidt number and boundary conditions: S. cerevisiae The influence of the top boundary condition and Sc_t is shown in figure C3. The higher τ_{95} for degassing leads to an overall steeper gradient, resulting in a larger region where

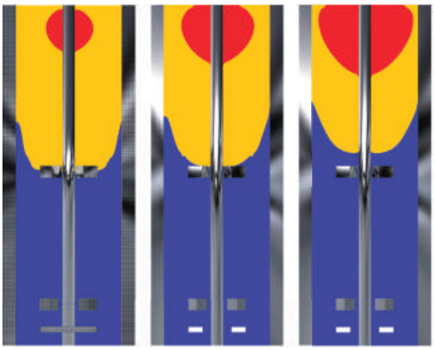

Figure C1: Variation of the regime layout as a function of the circulation time. Left: regular settings (τ_{circ} = 18.2 s). Middle: case $SENS-1$ (τ_{circ} = 25.6 s). Right: case $SENS-2$ (τ_{circ} = 18.2 s).

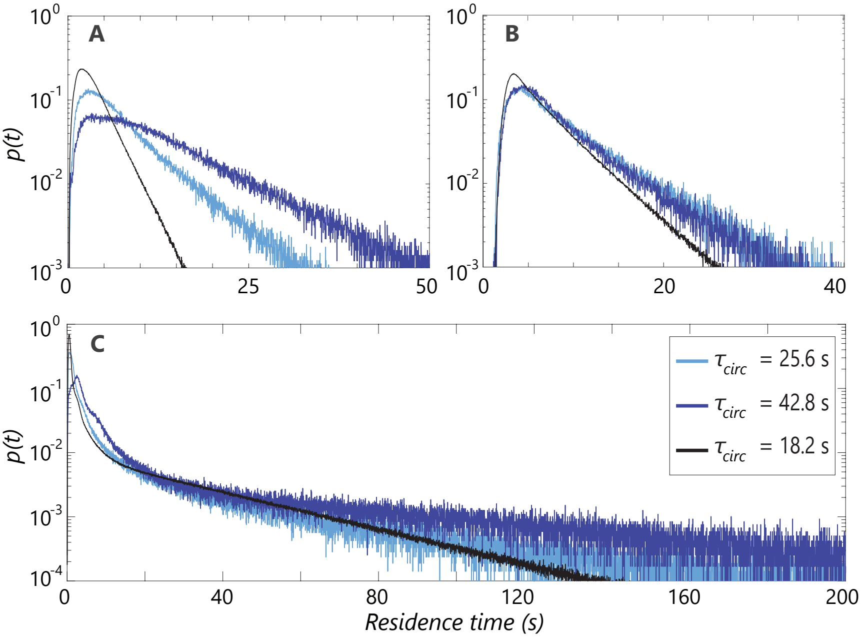

Figure C2: Sensitivity of the regime residence time distributions to the circulation time. A) type e-transition B) type c-transition C) type f-transition; changes in the distribution mainly occur due to the immersion of the top impeller in the starvation regime. Dark blue: $SENS-1$. Light blue: $SENS-2$. Black: Regular settings.

$c_s < 5$ mg/L near the bottom, and a larger region where $c_s > 80$ mg/L near the top. The differences have little effect on the regime distribution (figure C4). The per regime residence time distributions are not expected to differ significantly in terms of long term behavior, as the same circulation loops are enclosed in all cases.

Coupled metabolic model sensitivity: ideal mixing Coupled simulations were conducted with dilution rate $D_r = 0.033$ and feed concentration $C_f = 0.0895$ mol/kg, assuming ideal mixing. Four simulations were conducted: **1:** $q_{s,max} = 1.6$ mmol/g$_{dw}$/h and $K_s = 7.8 \cdot 10^{-6}$ mol/kg, **2:** $q_{s,max} = 1.6$ mmol/g$_{dw}$/h and $K_s = 9.8 \cdot 10^{-6}$ mol/kg, **3:** $q_{s,max} = 1.13$ mmol/g$_{dw}$/h and $K_s = 7.8 \cdot 10^{-6}$ mol/kg **4:** $q_{s,max} = 1.13$ mmol/g$_{dw}$/h and $K_s = 9.8 \cdot 10^{-6}$ mol/kg. The K_s change had negligible effect, whereas $q_{s,max}$ did significantly influence q_p and μ (fig. C5). Next we imposed feast-famine cycles of 360 s with $C_f = 0.0833$ mol/kg and $D_r = 0.05$ [44], and kinetic parameters $q_{s,max} = 1.6$ mmol/g$_{dw}$/h, $K_s = 7.8 \cdot 10^{-6}$ mol/kg and $q_{s,max} = 1.13$ mmol/g$_{dw}$/h, $K_s = 9.8 \cdot 10^{-6}$ mol/kg. For comparison, the model by Tang et al. (no simplified ATP pool) was included. The results are shown in figure C6. The higher $q_{s,max}$ mainly led to higher peaks in X_{gly} which reduce q_p via glycolytic inhibition, while most other pools remain unchanged. The different ATP formulation hardly affects q_p.

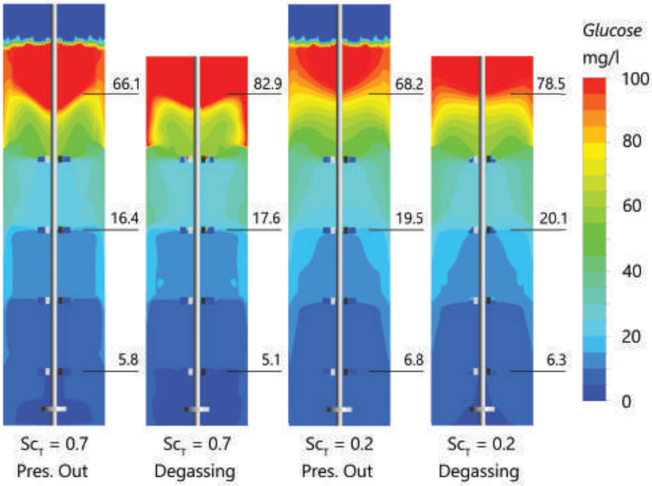

Figure C3: Comparison of concentration gradients for different outlet boundary conditions and values of the turbulent Schmidt number Sc_t. Concentrations at the probe location are presented right of every contour map.

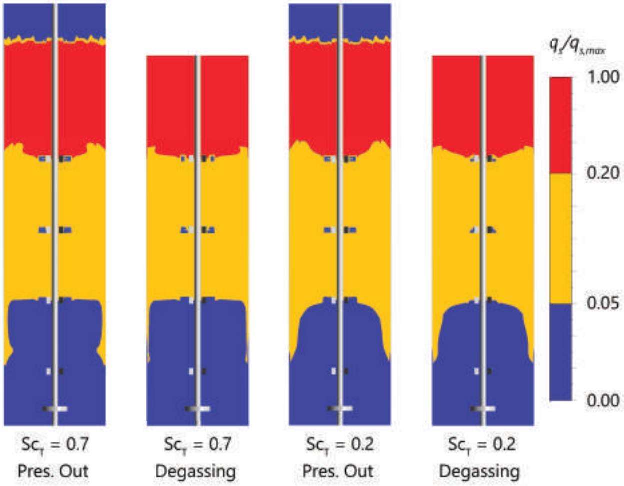

Figure C4: Comparison of the regime distribution for the different simulation setups.

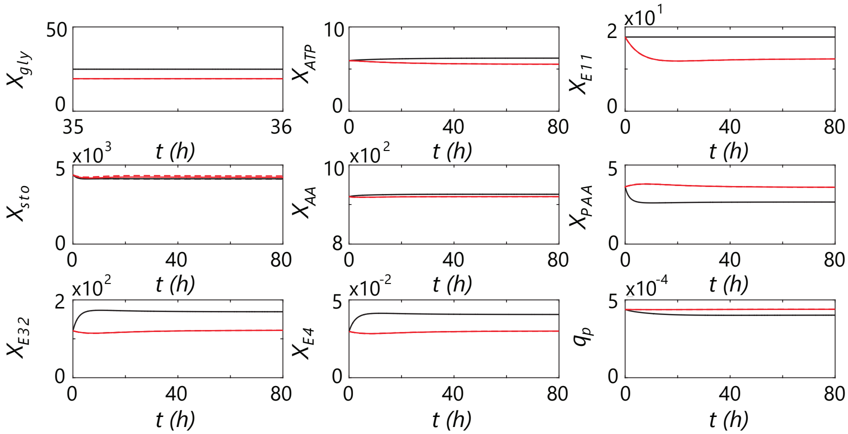

Figure C5: Sensitivity study for constant feed conditions, with with $C_f = 0.0895$ mol/kg and $D_r = 0.033$ h^{-1}. Black, solid: case 1. Black, dashed: case 2. Red, solid: case 3. Red, dashed: case 4. Intracellular pools X_{gly}, X_{AA}, X_{sto} and X_{PAA} have units μmol/g$_{dw}$. μ has units h^{-1}. q_p has units mol/Cmol$_x$/h. All other pools are dimensionless.

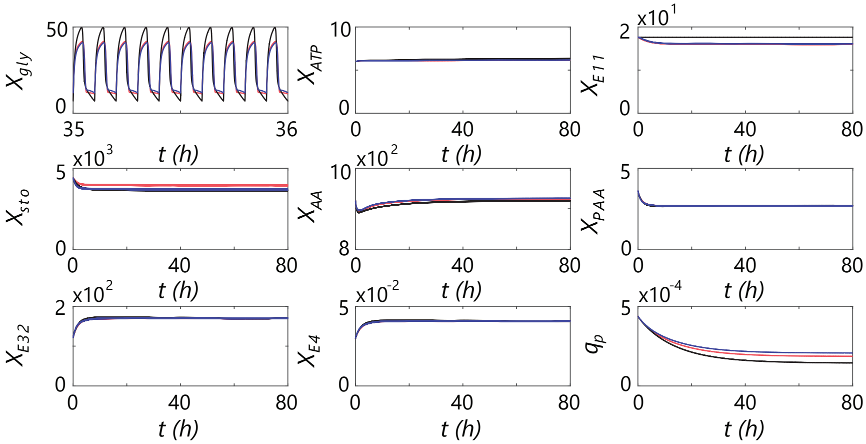

Figure C6: Sensitivity study for the simulation of 360 s feast-famine cycles, with $C_f = 0.0833$ mol/kg and $\mu = 0.05$ h^{-1}. Black: $q_{s,max} = 1.6$ mmol/g$_{dw}$/h, $K_s = 7.8 \cdot 10^{-6}$ mol/kg based on de Jonge et al. [44]. Red: $q_{s,max} = 1.13$ mmol/g$_{dw}$/h, $K_s = 9.8 \cdot 10^{-6}$ mol/kg, with patched ATP formulation ($X_{ATP} = 8.25X_{gly}^3/(10.5^3 + X_{gly}^3)$). Blue: original model of Tang et al. [226].

Appendix D: Lab scale setup and mixing

Mixing experiments were conducted in the 3 L laboratory setup used in ECUST, Shanghai. The tank geometry is shown in figure D2. Mixing experiments were conducted by registering the local conductivity change in response to a brine injection. The probe was placed in the outflow of the bottom rotor, attached to a baffle. Tracer is manually poured in via a tube at the top surface. 6 mL of brine solution was poured in each measurement, resulting in a conductivity change of approximately $15\mathrm{mS/cm^2}$; the probe resolution was $0.1\mathrm{mS/cm^2}$, with a time resolution of 0.4 s. The salt solution contained $5\mathrm{g/L}$ NaCl, which gives a density difference of 0.3% compared to tap water. Hence, buoyancy effects were considered negligible. Preliminary testing revealed the probe lag time is negligible. Mixing time determinations were conducted at $10-300$ RPM, the time resolution was insufficient for higher agitation rates. All measurements were resolved 5-fold, and the final conductivity averaged over 10 seconds was used to non-dimensionalize the results. The dimensionless mixing number θ_{95} as a function of Re is reported in figure D1.

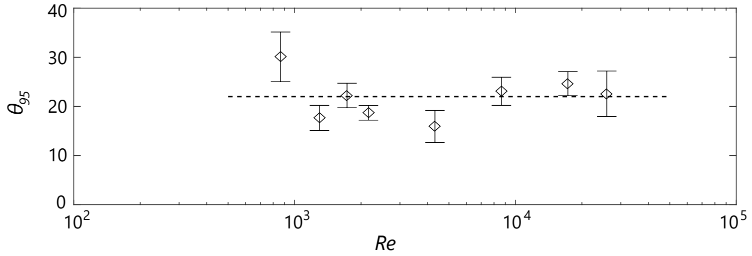

Figure D1: Mixing behavior in the lab scale fermentor at different Reynolds numbers in the transitional-turbulent range.

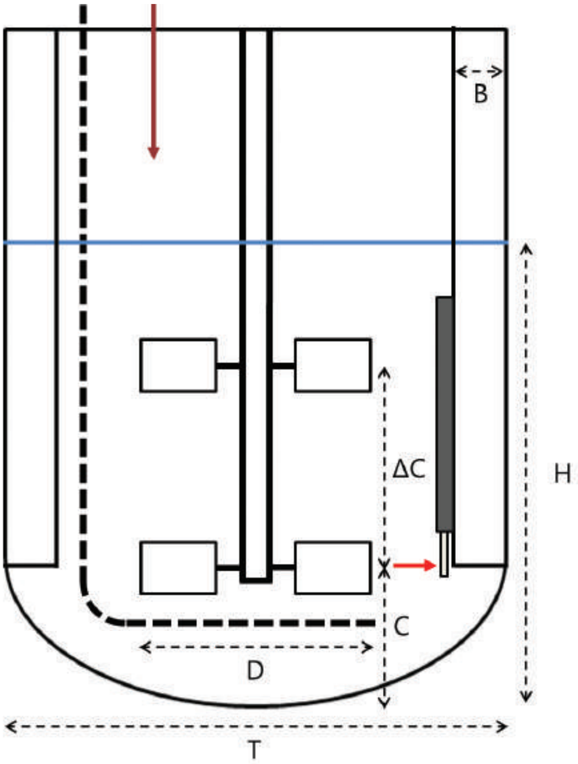

Label	Dimension (mm)
B	15
ΔC	84
C	40
T	160
H	165
D	72

→ Probe location

→ Injection location

Figure D2: Schematics of the laboratory scale reactor used in this study.

Appendix E: Airlift loop simulation

Simulations of an airlift loop reactor were conducted to further explore the use of Fourier analysis. Some data on a *S. cerevisiae* fermentation inside an airlift loop reactor is available [313–315, 315, 316], including data on a dissolved oxygen gradient [316]. However, an attempt to incorporate the oxygen consumption dynamics of Sonnleitner and Käpelli [268] did not yield satisfactory results. Instead, we opted to model a reactor only used for flow studies, based on a system for which sufficient CFD data was available, and added a dummy biological reaction model to this.

We modeled the reactor of Šimčík et al. [317], who conducted a combination of CFD and experiments in the setup. A single bubble size of 5 mm was used, with the Universal drag model and turbulent dispersion model by Simonin et al. [318]. The realizable $k-\epsilon$ model was used for turbulence. 2^{nd} upwind discretization was used for all equations except volume fraction, for which 1^{st} order upwind was used to ensure stability. Validation results are shown in table E1. As a dummy reaction model, we added the kinetics used for the *S. cerevisiae* simulations of chapter 5, with a biomass concentration of 30 g$_{dw}$/kg. The liquid has the properties of water, for gas, standard air at STP is assumed, with $\rho = 1.2$g/L, $\mu_l = 18.6 \cdot 10^{-6}$ Pa · s.

The feed is set to $F_s = 0.00194$ mol/s, which means under ideal mixing conditions $K_s = C_s$. Under the simulated conditions, the substrate gradient ranges from $0.45 < q_s/q_{s,max} < 0.8$. The feed is inserted as a source term at the bottom of the draft tube, as is visible from the high-q_s spot in figure E1. We added 7500 particles to the reactor and tracked them for 200 s. Figure E2, **A** shows a typical particle track, which has an obviously better defined structure than those recorded in stirred tanks. This is reflected in the Fourier spectra, reported in figure E2, **B**. There is still a wide residence time distribution, which we attribute to the shape of the headspace region, where particles may recirculate as in a stirred vessel. Two peaks nevertheless stand out, due to the plug-flow like behavior in the draft tube. The peak at 0.05 Hz reflects typical circulation behavior: this is the frequency of feed-point passings, reaching $q_s/q_{s,max} > 0.6$. The higher frequency peak at $0.1-0.12$ Hz reflects the peaks reaching $q_s/q_{s,max} > 0.52$. These peaks are attributed to headspace circulations.

These results hint at reasonably simple scale down strategies. One single-vessel option is to use a variable feed reactor, with total cycles of 20 s (0.05 Hz), imposing

Table E1: Validation of airlift loop simulations, compared with experimental data of Šimčík et al. [317].

Parameter	Simulation	Experimental
u_l (m/s) (draft tube)	0.7	0.75
u_l (m/s) (downcomer)	0.18	0.18
α (draft tube)	0.06	0.07
α (downcomer)	0	0.02

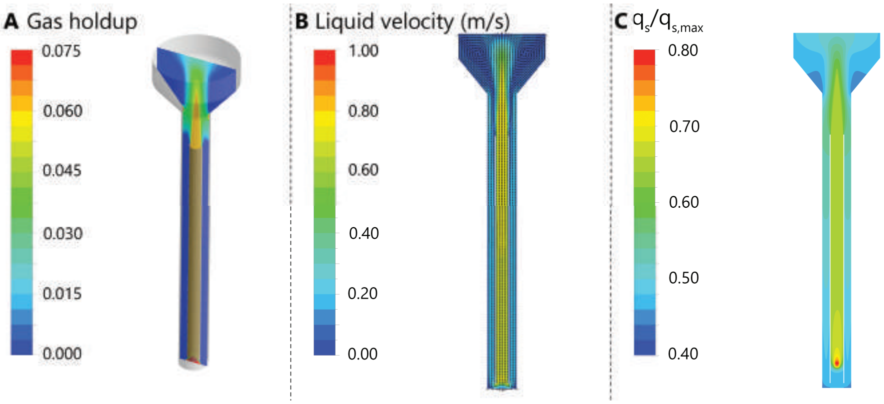

Figure E1: Eulerian results for the Airlift loop reactor. **A:** Gas holdup profile in the reactor. **B:** Liquid velocity profile. Vectors show direction, colors show magnitude. **C:** Uptake rate profile. Substrate is fed right above the sparger, leading to a high-uptake hotspot at this locations.

$q_s/q_{s,max} \approx 0.65$ at the cycle start, and using a secondary injection at $t = 10$ s to reach $q_s/q_{s,max} \approx 0.54$. Another option that takes the distribution in the top into account would be to combine a stirred tank for the headspace with a plug-flow reactor for the draft tube (feedpoint halfway the plug-flow). Of course, the here-simulated reactor is not an industrial scale fermentor, but the simulations provide an outline for how downscaling of an industrial scale draft-tube reactor might be approached.

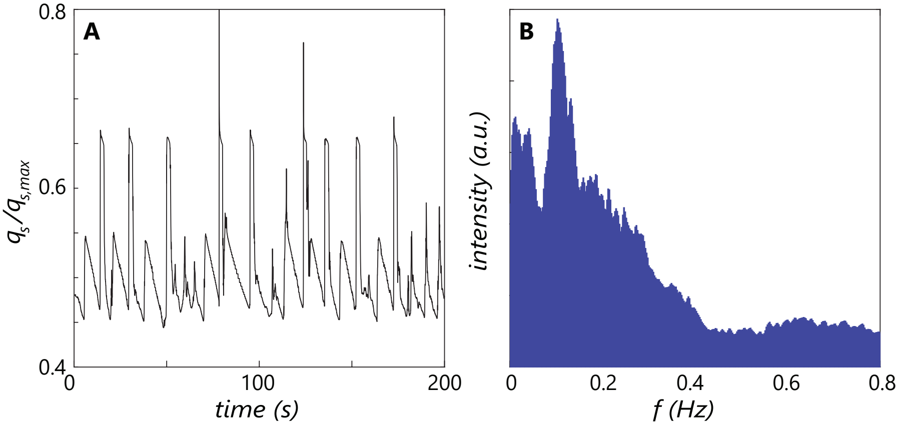

Figure E2: **A:** Example of a single Lagrangian particle track in the airlift-loop reactor. **B:** Composite Fourier spectrum of 7500 tracks, showing peak at 0.05 and 0.11 Hz, associated with reactor and headspace circulations respectively.

Appendix F: Microfluidic scale-down concept

When designing scale-down simulators based on industrial fermentation processes, the operational range offered by traditional bench-scale fermentors is limited. In order to obtain the duration and magnitude of variations observed in non-ideal industrial reactors, high biomass concentrations might be needed in the lab, which may lead to unfavorable rheology, causing poor mixing, mass transfer and pumping problems. Even when the requirements for replicating the duration and magnitude of variations can be met, this is only in the average sense; the most rapid perturbations can not be explicit imposed.

Micro-reactors offer an alternative methodology, that allows to impose very rapid, well controlled variations in the environment of micro-organisms. To our knowledge, no studies to date have aimed at imposing fluctuations in process parameters on the second scale, but micro-reactors have been used for detailed studies of cellular growth under controlled conditions [297, 307, 309, 310, 319], and to impose slow (minute-hour scale) environmental dynamics in order to study responses in protein activity [304, 306]. One major challenge associated with microfluidic scale-down is to probe the metabolic response on the single-cell level, but techniques in this area are subject to rapid development [13, 296, 311].

Imposing rapid (second-scale) variations in micro-reactors is absolutely possible from a theoretical perspective. As a proof-of-principle, we conducted a 2D CFD simulation of a very simple scale-down simulator, shown in figure F1 **A**, based on a simplification of the cell-trapping design of Probst et al. [320]. Note that the current design is by no means optimized; there may be better trap designs, channel designs, and so on. The current purpose is solely to get an indication considering the rate of change achievable in such a simulator. For this trial, we set a 40 µm diameter of the feed channels and main flow channel. A velocity inlet was used at both inlets, with $5-20\cdot10^{-4}$ m/s such that the main channel velocity is $1-4$ mm/s. The mixing path length was approx. 3 mm. The flowfield (laminar) was first solved in steady state with pure fluid B. At $t=0$, the fluid at inlet 1 is switched to pure A, with equal properties to B and a molecular diffusion coefficient $\mathcal{D}_m = 6\cdot10^{-10}$ m^2/s, for glucose in water. Figure F1 **A** shows a snapshot of the transition from pure B to $A+B$. After 3 s, the fluid was switched back to pure B. The surface-averaged concentration at the cell cluster was measured. The imposed step function is smeared out due to the laminar velocity profile and diffusive backmixing, as can be observed in figure F2, but still a step-like profile retrieved with $5-95\%$ saturation time of 0.46 s $-$ 1.15 s, for the highest and lowest inlet velocity. This shows that even this simple, unoptimized concept can serve as an excellent basis for imposing rapid extra-cellular dynamics. Using concepts from control theory, a transfer function describing the relation between feed (input) and fluctuation registration at the cell cluster (output) can be derived, which would allow

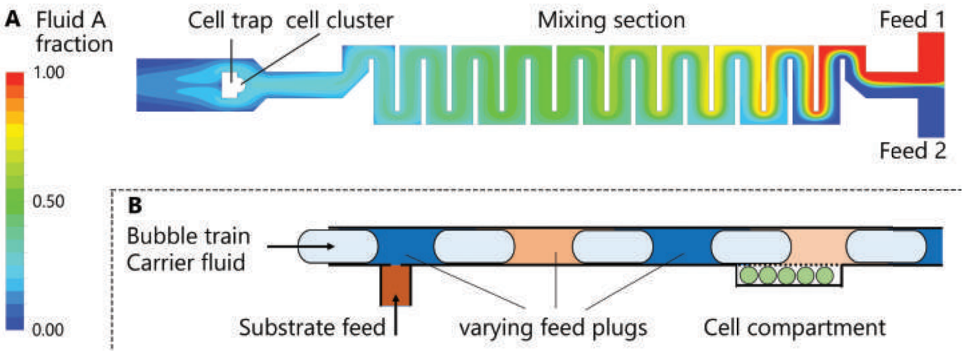

Figure F1: **A:** 2-D CFD simulation of a simple single-phase micro-reactor (channel diameter 40 μm) designed to impose rapid extra-cellular variations on micro-organisms, physically trapped in a cell chamber. Contour plot shows a switch from pure fluid B to fluid A fed via feed 1, while feed 2 constantly feeds fluid B. **B:** concept layout of a 2-phase microreactor designed to reduce backmixing in the substrate flow by introducing Taylor-flow.

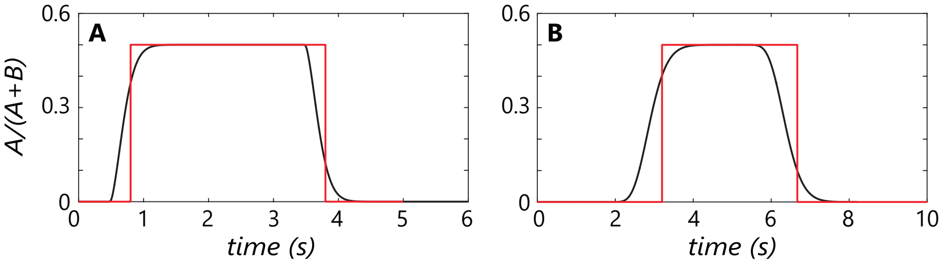

Figure F2: Response at the cell-trap (black) to a pulse of A inserted via one inlet. The pulse profile (red) has been visualized as the response for a perfect plug flow with the same superficial flow-rate. **A:** inlet velocity of 2 mm/s, **B:** inlet velocity of 0.5 mm/s per channel.

a desired response profile (possibly even a lifeline directly acquired from CFD, using deconvolution techniques to minimize the impact of the device) to be translated to the required feed profile to impose the desired lifeline.

If back-mixing due to the laminar flow and diffusion is too strong, an alternative may be to turn to a droplet-based scale-down simulator, sketched in figure F1 **B**. Using a variable-magnitude side-feed, the substrate concentration in every plug can be controlled separately, while the presence of bubbles or plugs reduces backmixing. The presence of this bubble train does imply the cells are not exposed directly to the main flow, but are placed in a separate compartment [321]. This means diffusion through the continuous phase film and separating membrane (or PDMS pillar array) induces a time delay, and may lead to some back-mixing. Designing optimal micro-reactors to directly impose lifelines with rapid fluctuations on micro-organisms requires further quantification of such phenomena, which is a project in and of itself.

List of Publications

Full papers

8. **C. Haringa**, W. Tang, G. Wang, A.T. Deshmukh, J. Xia, M. Reuss, J. Chu, W.M. van Gulik, J.J. Heijnen, R.F. Mudde, H.J. Noorman, *Computational fluid dynamics simulation of an industrial P. chrysogenum fermentation with a coupled 9-pool metabolic model: towards rational scale-down and design optimization.*, Chem. Eng. Sci., *accepted.*

7. G. Wang, B. Wu, J. Zhao, **C. Haringa**, J. Xia, J. Chu, Y. Zhuang, S. Zhang, J.J. Heijnen, W. van Gulik, A.T. Deshmukh, H.J. Noorman, *Power Input Effects on Degeneration in Prolonged Penicillin Chemostat Cultures: A Systems Analysis at Flux, Residual Glucose, Metabolite and Transcript Levels*, Biotechnology and Bioengineering, *accepted.*

6. W. Tang, A.T. Deshmukh, **C. Haringa**, G. Wang, W. van Gulik, W. van Winden, M. Reuss, J.J. Heijnen, J. Xia, J. Chu, H.J. Noorman, *A 9-pool metabolic structured kinetic model describing days to seconds dynamics of growth and product formation by Penicillium chrysogenum*, Biotechnology and Bioengineering, **114**, 1733 (2017).

5. **C. Haringa**, R.F. Mudde, H.J. Noorman, *Euler-Lagrange analysis towards representative down-scaling of a* 22 m^3 *aerobic S. cerevisiae fermentation*, Chemical Engineering Science **170**, 653 (2017).

4. **C. Haringa**, H.J. Noorman, R.F. Mudde, *Lagrangian modeling of hydrodynamic–kinetic interactions in (bio)chemical reactors: Practical implementation and setup guidelines*, Chemical Engineering Science **157**, 159 (2017).

3. **C. Haringa**, W. Tang, A.T. Deshmukh, J. Xia, M. Reuss, J.J. Heijnen, R.F. Mudde, H.J. Noorman, *Euler Lagrange computational fluid dynamics for (bio) reactor scale down: An analysis of organism lifelines*, Engineering in Life Sciences **16**, 652 (2016).

2. Y. Liu, Z.J. Wang, J. Xia, **C. Haringa**, Y. Liu, J. Chu, Y. Zhuang, S. Zhang, *Application of Euler Lagrange CFD for quantitative evaluating the effect of shear force on Carthamus tinctorius L. cell in a stirred tank bioreactor*, Biochemical Engineering Journal **114**, 209 (2016).

1. D.A. Hoang, **C. Haringa**, L.M. Portela, M.T. Kreutzer, C.R. Kleijn, V. van Steijn, *Design and characterization of bubble-splitting distributor for scaled-out multiphase microreactors*, Chemical Engineering Journal **236**, 545 (2014).

Conference papers

1. S. Mukherjee, A. Zarghami, **C. Haringa**, S. Kenjeres, H.E.A. van den Akker *A comparative assessment of Lattice Boltzmann and Volume of Fluid (VOF) approaches for generic multiphase problems*, 9^{th} International Conference on Multiphase Flow (2016).

Submitted and in preparation

1. S. Mukherjee, A. Zarghami, **C. Haringa**, K. van As, S. Kenjeres, H.E.A. van den Akker *Comparing a Pseudopotential Lattice Boltzmann method to the Volume of Fluid method for multiphase flows.*, Int. J. of Heat and Fluid Flow, *submitted.*
2. G. Wang, J. Zhao, **C. Haringa**, J. Xia, J. Chu, Y. Zhuang, S. Zhang, W. van Gulik, J.J. Heijnen, H.J. Noorman, *Comparative Performance of Different Scale-down Simulators of Substrate Gradients in Penicillium chrysogenum Cultures: The Need of a Biological Systems Response Analysis*, Biotechnology and Bioengineering, *submitted.*
3. **C. Haringa**, R. Vandewijer, R.F. Mudde, *working title: Inter-compartment interaction in multi-impeller mixing part 1: Experiments and Reynolds Averaged Navier Stokes simulations*, Chemical Engineering Research and Design, *in prep.*
4. **C. Haringa**, R. Vandewijer, R.F. Mudde, *working title: Inter-compartment interaction in multi-impeller mixing part 2: Large Eddy Simulations*, Chemical Engineering Research and Design, *in prep.*
5. **C. Haringa**, C. de Jong, L.M. Portela, M.T. Kreutzer, C.R. Kleijn and V. van Steijn, *Breakup of elongated droplets in microfluidic T-junctions*, Physical Review Fluids., *submitted*

Acknowledgements

Perhaps the most difficult chapter to write of a PhD thesis is this one. Over a period of four years, the amount of people that in one way or another contributes to a thesis project grows to epic proportions, and properly acknowledging all of them becomes a daunting task to say the least. I will try my very best attempt to thank all those that deserve it, but in case I did forget anyone, my sincere apologies.

I want to start expressing my gratitude to all teachers I encountered during my studies; too many to list individually. My MSc thesis supervisors do have to be named: Duong Hoang, Volkert van Steijn, Chris Kleijn and Michiel Kreutzer. I thoroughly enjoyed my MSc. project, in part due to the challenges you continually raised. Without it, I might never have converged towards undertaking a PhD. Volkert, our discussions have continued to this day, since we took some extra time to finish the final paper based on this MSc work. I still find them thoroughly challenging and inspiring, and even though the overall trajectory took slightly longer than anticipated, it has culminated in a nice piece of microfluidic work.

Rob Mudde, before I fully finished my MSc, you burst in my room proclaiming you had a PhD position available. I have never regretted the decision I made shortly after that. During the project you always stimulated me to look deeper into problems we encountered, back to basic understanding and the proverbial back of the envelope. The insights gained with this proved invaluable. Henk Noorman, with your industrial point of view you were instrumental in keeping up the pace. Furthermore, you were an indispensable source of suggestions regarding literature about industrial fermentations and scale-down processes. Thank you both for your supervision over the past four years.

I started this adventure, which combines flow physics and microbiology, as a chemical engineer. This basically meant I knew nothing about either subject. Luckily I was surrounded by people who were well trained in these fields, and never hesitated to share their knowledge. Walter van Gulik, you expanded my understanding about the functioning of micro-organisms, and setting up metabolic networks. Sef Heijnen, you advocated the philosophy of keeping things simple, and starting at the end. Hence, the acknowledgments were the first part of this thesis that I wrote. But in a way you also started at the end: some measurements conducted in your first job at DSM proved very valuable for this project, at the time of your retirement. This of course calls for the Dutch expression ”the circle is round”. Matthias Reuss, thanks for our frequent discussions over the years, and the valuable historic perspective and suggestions that you brought to the table. Rob van der Lans, you helped me a great deal with original ”Stavanger” data. Wouter van Winden, you regularly supplied details considering fermentor design and modeling, which proved of great value. Amit Deshmukh, your thesis was an indispensable starting point for biological details, and you played a major role in taking care of the logistics of this project. I hope our collaborations will continue within DSM. To all my new DSM colleagues, thank you for the warm welcome, and for the opportunity to show my research has more than just academic value. I'm greatly looking forward to many collaborations yet to come.

On the fluid dynamics side, I had the advantage of being part of the Transport Phenomena group. Of course, my fellow PhD students were always open to discuss the many little questions and issues that arose. Sasa Kenjeres, Luis Portela and Harrie van den Akker, your ideas contributed greatly to the single-phase, multi-impeller work which really came to fruition late in this PhD work. Many thanks for that. Especially near the start and the end of my project, I may have been a bit of a nuisance for the support staff of the group. Getting all the contracts and forms in order proved to be more of a hassle than normal, and from what I heard, my file within the TP archive outgrew that of the typical PhD student. Anita van Haren and Fiona Tuynman, thanks for all the effort you put into making everything work out smoothly, and for keeping the TP group running. Without you, things would surely end in chaos. Although most of my work was theoretical, some experimental sidetracks were pursued over the years by me and my students, which would not have been possible without the support of Evert Wagner, Stefan ter Hagen, Jos Thieme and Christiaan Schinkel. My gratitude for your help and flexibility, as our requests were not always very clear and timely. Thanks to Youp Goozen and Ruud van Tol for preparing our experimental setup.

My project offered the opportunity of working together with the State Key Laboratory for bioreactor engineering at *East China University of Science and Technology* in Shanghai. I've enormously enjoyed the months I spent there, as well as our discussions during Chinese visits to the Netherlands and virtual meetings. Ju Chu, thank you for your hospitality during my visits to China and for all the places you suggested I should visit while I was there. Jianye Xia, our early discussions guided me in setting up my first CFD simulations, and showed that even the lab scale may not be as ideal as people often think it is. Neil, Champion and Alice, you were of course my great collaborators in China and I'm proud of the work we did together. Thanks for all the good times we had in Delft and Shanghai; the dinners, discussions, excursions and more. Neil, you showed me some of the outskirts of Shanghai, where no typical tourist would ever visit. Champion, our daily lunch discussions, reaching from science to society, were great fun. The suit you helped me buy in Shanghai is still frequently used. Liu Yu, it was an honor to help writing your paper, and you showed me some of the best hot pot practices in Shanghai. And of course, all the other students and staff members that I met in Shanghai, thanks for making me feel part of the team.

Moving away from the project sphere, there is a long list of people within the Chemical Engineering department of TU Delft that have to be acknowledged. Robin, Rita, Diederik, Rafaela, Francisca, Catalin, Dries, Bengisu, Nicola and Leslie, thanks for the fun times we had organizing the DPTI summerschool together. TG, thanks for your above ChemE-average coffee, and for keeping the student community in ChemE lively. Eli, Ina, Tim, Shaurya, Maulik, Andreas Nygren, Tobias Perssoa, Durgesh and many others within the PPE and CE groups, the 'back of the (old) building' drinks and BBQ were fun. I hope the connection between the 'back of the building' groups lives on, even though the new building invalidates the name. During my time within TP I've seen many BSc and MSc students come and go, and each period had its own highlights.

In the early days, the Thursday market visits and friday drinks were going strong with many thanks to Matthijs Zweemer, Mathijs Koot and Jimmy Tjin. Corné, you kept those drinks lively during the 2014 season, all the best with your PhD in Limerick. Ruben Z., Ruiz, Simon, Jelle S. Zimo, Mattijs R., Pieter, Tjeerd, Gijs, Joost, Kelbij, Jaap, Sagar, Isabelle, Ivo, Lynn, Yingying and Kim, we frequently ran out of space during lunch and coffee breaks during the mid-period of my PhD due to your active participation. Sherwin, you nearly extended your stay here but fooled us in the end. Too bad, we would have loved to have you around for longer, I hope the nutritional business proves to be fun. Jelle M, Patrick, Frenk, Madelon, Shaikh, Kris, Joep, Boris, our daily table tennis breaks made the last weeks in old DelftChemTech much more intensive. The spatial constraints of the new building have unfortunately reduced the group feeling, but Johan, Sander, Joep, Jorrit, Amit, Ashwin, Katerina, Romana, Stefan, Doedo, Jorne, Wouter, you tried to keep the TP spirit alive against all odds. Of course, all the students that I did not name explicitly, thanks for being around.

My own students, of course, deserve a paragraph of their own. Agnes, Laurens, Lennart, Victor and Marenka, supervising your BSc projects was a very educating and entertaining experience. Your work provided me with useful insights in multi-phase and multi-impeller flow. Harm, you had a tough project on coupling hydrodynamics and kinetics, but in the end you managed to deliver a nice thesis and our discussions provided many insights. Ruben, spending time with you in China was a delight, although our evening at the Shanghai brewery was one to be remembered for the wrong reasons. Some better reasons for remembrance: the contributions you made to chapter 3 of this thesis. Conrad, your continuation of my MSc. project led to some great results, and the sensitivity of your experimental methods required some lengthy overnight measurement sessions which also kept my Mario kart skills sharp. Aside from a master student, you are also one hell of a general collaborator in terrible ideas, a role that you will surely fulfill for years to come. Koen, as my last student you took on one of the first challenges defined within this project, showing that well-mixed fermentors are not as well mixed as people believe. A piece of work to be proud of. Besides my BSc. and MSc. students, thanks to all the students that I encountered in the various courses that I had the pleasure to assist at over the years, those taking Computational Transport Phenomena in particular. You are the most convincing argument for the statement that the best way to understand a subject is to teach it.

Research is done in a highly dynamic environment as the number of MSc. and BSc. students clearly proves, but also in terms of direct colleagues I’ve had the pleasure of meeting many interesting individuals over the years. Duong, our appointments overlapped only briefly, but of course I had the pleasure of working with you before already. Annekatrien, Özgür, Edoardo, Xiaogang, Ahad, Hrushikesh, Chirag, Harish, Saidah, Snehal, Iman, Rita, Elin, Kevin, Fei, Jos, Andre and David, thanks for the fun during lunches, coffee breaks and all or other group outings. Being among such a diverse group of people means life is never boring. Rudi, Niels and Rajat, I only briefly had the opportunity of sharing a room with you at the beginning of my PhD, but of course had many more delightful encounters with you during the rest of my stay. Anand, it was fun sharing our duty as supervisors of the student ”fishtank” in the old building, all the best in Wageningen. Manu and Saeid, we surely had the best room in the new building,

your presence was as radiating as our view! Koen, your karting trip was legendary and surely requires follow-up, and your presence during TP events was always much appreciated. Bernhard, Laurens, Anton and Michiel, the times I spent as your roommate were certainly turbulent; bouncing increasingly improper jokes around the room was a delight, although it may not always have contributed to overall productivity. Wenjie, being present at your wedding in China was an honor. All the best in the future. Anton and Dries, you were always open for ideas - good and bad - and organizing all sorts of activities. I am sure there are many adventures yet to be had, and my life will not be complete before I finally beat you in a game of civilization. Manas, you are great at keeping the TP group lively, but really, you have some work ahead of you in remembering the proper times for lunch and coffee! Siddhartha, you are truly TP's renaissance man. Our discussions regarding the universe, life and everything were awesome, may the future hold many more. All of you, thank you for the great times, I dearly cherish all the memories.

Matthijs, Maurice, Margje, Tobias, somehow you knew I was going to engage in a PhD before I did. Our yearly holiday has turned out to be a great break from work, to be continued for many years I hope. Tobias, our adventures in China were sublime, whether we were conducting a slightly underestimated 50km hike, or roaming Lijiang's nightlife. Of course, I value our infrequent Friday night discussions concerning the state of science and industry as highly. Tim and Mathijs, any event involving you is ensured to have an unexpected ending - for the better, typically. Johannes and Coby, Jasper and Terence, Wim and Henk, we may not see each other too frequently as we ended up all over the country, but those times that we do manage to meet up are always memorable. Luckily, there are always those events that draw everyone back to Terschelling, to enjoy the good old times.

Harry and Louise, thanks for always making me feel at home when I visit Leidschendam and for the interest you have always showed in my work. Finn and Julia, Marie and Reinier, thanks for all the good times, from summer BBQs to beergartens at Lichtjesavond. And of course thanks to the rest of your family for the warm welcome. To my family, many thanks for the interest you've always shown towards my work. Due to the distance we don't see each other frequently, but I'm sure my parents keep you all well up to date.

Jelle, while we both have the privilege of being engineers you are certainly the more practical of the two; I will always be jealous of your mechanical skills (and your skills on the guitar, for that matter). Luckily I can still teach you a thing or two about Reynolds numbers, and so far I'm ahead in monopoly victories. Thanks to you and Tessa for all the fun times at Terschelling. Jan and Reina, your continuing support has always been most valuable. And of course, there's the benefit of you living in one of the finest places on this planet. Going home always is a most welcome escape from city (and research) life. I can never express enough praise for all that you have provided over the years, bringing me where I am today. And last, Anne Sophie. You hopped on board pretty much at the same time that I started this endeavor, and you've been with me every step of the way. I am endlessly grateful for the moments we've shared so far, and while this PhD journey is nearing an end, there are so many more journeys we have yet to make. Whatever our next steps will be, I am sure they will be wonderful.

Curriculum Vitæ

Cornelis (Cees) Haringa was born in Harlingen, the Netherlands, on May 14, 1988. He spent his chidhood on the island of Terschelling and obtained his high-school diploma in Harlingen. In 2006 he started the BSc programme ”Molecular Science and Technology”, a shared programme between Delft university of Technology and the University of Leiden. Here, he majored in Chemical engineering and took a minor in management of industrial operations. In 2009-2010, he interrupted his studies to be on the board of study association ”Technologisch Gezelschap”. His BSc., obtained in 2011, was followed by an MSc. degree in Chemical Engineering at TU Delft. During his MSc. he did a 4 month internship in Conceptual Design Engineering in BASF Ludwigshafen (Germany). He obtained his MSc. in April 2013, with the thesis ”the breakup behavior of droplets in microfluidic T-junctions”, for which he was awarded the Unilever research prize 2013. He continued his academic career with a PhD project on hydrodynamic-kinetic interaction in large scale bioreactors under supervision of Prof. Dr. Robert F. Mudde and Prof. Dr. Ir. Henk J. Noorman, which resulted in this thesis. During his PhD project, he collaborated with East China University of Science and Technology (ECUST) and DSM Sinochem pharmaceuticals. He currently continues his work as a CFD expert in the DSM Biotechnology Center. Besides his research work, he enjoyed being involved in teaching various theoretical and practical courses related to transport phenomena. Outside of his research work, he enjoys traveling, music and reading on a wide range of scientific and political issues.